

Sustainable solar energy conversion with defined ferrite nanostructures

Dissertation

zur Erlangung des akademischen Grades

„doctor rerum naturalium“

(Dr. rer. nat.)

eingereicht am Fachbereich

Biologie und Chemie

der

Justus-Liebig-Universität Gießen

von

Kristin Kirchberg, M.Sc.

Gießen, den 02.11.2018

1. Gutachter und Betreuer:

Prof. Dr. Roland Marschall

2. Gutachter:

Prof. Dr. Bernd M. Smarsly

Prüfer:

Prof. Dr. Peter J. Klar

Prüfer:

Prof. Dr. Bernhard Spengler

Declaration

The present thesis was prepared at the Institute of Physical Chemistry of the Justus-Liebig-University Giessen in the period of 1st November 2015 – 31st October 2018 under the supervision and guidance of Prof. Dr. Roland Marschall.

I declare that I have completed this dissertation single-handedly without the unauthorized help of a second party and only with the assistance acknowledged therein. I have appropriately acknowledged and cited all text passages that are derived from or are based on the content of published work of others, and all information relating to verbal communications. I consent to the use of an anti-plagiarism software to check my thesis. I have abided by the principles of good scientific conduct laid down in the charter of the Justus Liebig University Giessen „Satzung der Justus-Liebig-Universität Gießen zur Sicherung guter wissenschaftlicher Praxis“ in carrying out the investigations described in the dissertation.

Erklärung

Ich erkläre: Ich habe die vorgelegte Dissertation selbstständig und ohne unerlaubte fremde Hilfe und nur mit den Hilfen angefertigt, die ich in der Dissertation angegeben habe. Alle Textstellen, die wörtlich oder sinngemäß aus veröffentlichten Schriften entnommen sind, und alle Angaben, die auf mündlichen Auskünften beruhen, sind als solche kenntlich gemacht. Ich stimme einer evtl. Überprüfung meiner Dissertation durch eine Antiplagiat-Software zu. Bei den von mir durchgeführten und in der Dissertation erwähnten Untersuchungen habe ich die Grundsätze guter wissenschaftlicher Praxis, wie sie in der „Satzung der Justus-Liebig-Universität Gießen zur Sicherung guter wissenschaftlicher Praxis“ niedergelegt sind, eingehalten.

Gießen, 23. April 2019

(Kristin Kirchberg)

Danksagung

Zunächst möchte ich meinem Doktorvater, Prof. Dr. Roland Marschall, für die Möglichkeit zur Promotion über dieses interessante Thema danken. Zudem danke ich ihm für die vielen Möglichkeiten zum wissenschaftlichen Austausch im Rahmen von Konferenzen oder Forschungsaufenthalten, die mir immer wieder Anregungen für neue wissenschaftliche Blickwinkel gegeben haben.

Mein besonderer Dank gilt auch Prof. Dr. Bernd M. Smarsly, der freundlicherweise das Zweitgutachten für diese Arbeit übernimmt und mich überdies auch in seine Arbeitsgruppe integriert hat.

Bei Prof. Dr. Lianzhou Wang und der restlichen Arbeitsgruppe von der University of Queensland (UQ) in Brisbane möchte ich mich ganz herzlich für die Gastfreundschaft während meines Forschungsaufenthalts bedanken.

Außerdem bedanke ich mich bei Dr. Kristina Kvashnina für Ihre Unterstützung als Beamline-Operatorin während der Messzeit an der European Synchrotron Radiation Facility (ESRF).

Diese Arbeit wäre nicht zustande gekommen ohne die Hilfe vieler Kollegen, die mir verschiedenste Messmethoden beigebracht, mich bei Fragen unterstützt und teilweise sogar komplette Messungen für mich durchgeführt haben.

Aus der AG Smarsly-Marschall: Danke an Rüdiger Ellinghaus, Kevin Turke, Sebastian Werner, Dr. Jana Timm und Felix Badaczewski, die viel Zeit für Physisorptionsmessungen investiert haben. Außerdem vielen Dank an Hubert Wörner, Kevin Turke und Felix Badaczewski für die zahlreichen TG-MS-Messungen. Pascal Cop danke ich für die ToF-SIMS-Messungen und seinen Rat im Hinblick auf das Rotationsbeschichtungsverfahren. Bei Dr. Christian Suchomski möchte ich mich für seine Einweisung in die Raman-Spektroskopie und die vielen Diskussionen zum Thema Ferrite und mesoporöse Materialien bedanken. Julia Migenda und Morten Weiß danke ich für ihre Hilfsbereitschaft bei Fragen zu DLS-Messungen.

Aus der AG Janek danke ich Dr. Joachim Sann für die teilweise sehr kurzfristigen XPS-Messungen und seine Hilfe bei deren Auswertung sowie Dr. Klaus Peppler und Dr. Boris Mogwitz für ihre Hilfe bei den REM- und EDX-Messungen. Ein besonderer Dank gilt auch Dr. Bjoern Luerßen, der immer ein offenes Ohr hatte und ohne zu zögern seine Hilfe angeboten hat.

Auch außerhalb des Physikalisch-Chemischen Instituts hatte ich tatkräftige Unterstützung: Der AG Spengler und insbesondere Florian Lotz danke ich für die Möglichkeit, die Feinwaage nutzen zu dürfen, ohne die ich die Masse der Dünnschichtbeschichtungen nicht hätte bestimmen können. Dr. Anne Schulze möchte ich für die Einweisung am TEM und ihre konstante Unterstützung bei

allen dazugehörigen Fragen danken. Für die Messung von IR-Spektren möchte ich mich bei Dr. Dennis Gerbig und Brigitte Weinl-Boulakhrouf aus der Organischen Chemie bedanken. Max Kracht danke ich für die Einweisung ins Dünnschicht-Diffraktometer und seine Geduld mit mir.

Außerdem möchte ich mich beim Team der Feinmechanischen Werkstatt sowie der Chemikalienausgabe und Glasbläserei, insbesondere Hans-Jürgen Wolf und Anja Beneckenstein, sowie Harald Weigand herzlich bedanken für die Anfertigung verschiedenster Geräte, die einige Experimente erst möglich gemacht haben.

Weiterer Dank gebührt allen Studenten, die ich im Rahmen ihrer Spezialisierungs-, Bachelor- und Masterarbeiten sowie Hiwi-Tätigkeiten betreuen durfte und die zum Erfolg dieser Promotion beigetragen haben: Allen voran Anna Becker, deren Arbeiten zu Magnesioferrit-Nanopartikeln Grundlage sowohl für eine Publikation^[1] waren und einen großen Beitrag zum Verständnis dieses Systems geliefert haben; außerdem Phillip Timmer, Christopher Simon und Marius Eckert, die sich ausgiebig mit Zinkferrit in verschiedenen Erscheinungsformen beschäftigt haben.

Für die finanzielle Unterstützung in Form der Finanzierung meiner Stelle möchte ich mich bei der Deutschen Forschungsgesellschaft (DFG) bedanken. Des Weiteren gilt mein Dank dem Deutschen Akademischen Austauschdienst (DAAD), der meinen Forschungsaufenthalt in Australien und die Konferenzreise zur International Solar Fuels Conference in San Diego ermöglicht hat.

Natürlich möchte ich mich auch bei meinen Bürokollegen Tobias, Christopher, Morten und Natalia sowie der gesamten AG Smarsly und Marschall bedanken sowie bei den fleißigen Korrekturlesern Maren, Christoph, Giuli, André und Morten. Der Zusammenhalt in der Arbeitsgruppe war super, sowohl bei der Arbeit als auch bei anschließenden Feierabend-Aktivitäten.

Auch meinen Studienkollegen aus Hannover, insbesondere Mandy, Jana, Janine, Steffi, Marianne, Daniel und Vanessa möchte ich für die schöne Zeit, die vielen langen Lern- und Praktikumstage und die tollen Ausflüge in die britische Kultur danken. Ich werde immer mit viel Freude an die Zeit mit euch zurückdenken.

Zu guter Letzt möchte ich mich bei meiner Familie bedanken, allen voran meiner Schwester Lina, die mir gezeigt hat, dass auch riesige Hürden überwindbar sind. Ich bin sehr stolz darauf, was du alles schon geschafft hast und du motivierst mich dazu, immer mein Bestes zu geben. In ganz besonderem Maß will ich mich auch bei meinem Freund Sebastian bedanken, der mich während der Promotion und insbesondere in der Schlussphase unterstützt hat, wo er konnte – ohne dich hätte ich den Stress nur schwer bewältigen können.

Table of Contents

1	Introduction.....	1
1.1	Motivation.....	1
1.2	Overview.....	4
2	Theoretical Background.....	6
2.1	Present Challenges in Energy Supply.....	6
2.2	Solar Energy Conversion.....	8
2.2.1	Photocatalysis and Photoelectrochemistry.....	9
2.2.2	Semiconductor Characteristics.....	13
2.2.3	Influences on Photoactivity.....	18
2.2.3.1	Nanostructuring.....	19
2.2.3.2	Co-Catalysts.....	24
2.2.3.3	Sacrificial Agents.....	25
2.2.4	Characterization of the Photocatalyst Performance.....	27
2.3	Photoactive Materials.....	31
2.3.1	Non-Noble Transition Metal Absorber Materials.....	31
2.3.2	Iron Oxide Semiconductors as Photocatalysts.....	33
2.3.3	Ferrite Materials.....	34
3	Experimental Section.....	39
3.1	Chemicals.....	39
3.2	Synthesis Techniques.....	42
3.2.1	Nanoparticle Synthesis.....	42
3.2.1.1	High-Temperature Reflux Synthesis.....	42
3.2.1.2	Microwave-Assisted Nanoparticle Synthesis.....	43
3.2.1.3	Post-Synthetic Heat Treatment.....	44
3.2.2	Nanoparticle Functionalization.....	44
3.2.2.1	In situ Steric Stabilization.....	44
3.2.2.2	Post-synthetic Steric Stabilization.....	45
3.2.2.3	Post-synthetic Electrostatic Stabilization.....	45
3.2.3	Mesoporous Thin Film Preparation.....	46

3.2.3.1	Sol-Gel Assisted Thin Film Synthesis	46
3.2.3.2	Infiltration with SiO ₂ Scaffold	48
3.2.4	Thin Films Derived from Nanoparticles	48
3.2.5	Mesoporous Powder Preparation	49
4	Characterization Techniques	50
4.1	X-Ray Methods	50
4.1.1	Powder X-Ray Diffraction	50
4.1.2	Grating Incidence X-Ray Diffraction	50
4.1.3	Rietveld Refinement	50
4.1.4	X-Ray Photoelectron Spectroscopy	51
4.1.5	Synchrotron-Based X-Ray Excitation Experiments	52
4.1.5.1	X-Ray Absorption Near Edge Spectroscopy	54
4.1.5.2	X-Ray Emission Spectroscopy	57
4.1.5.3	Valence-to-Core X-Ray Emission	59
4.1.5.4	Resonant Inelastic X-Ray Scattering	60
4.2	Spectroscopic Methods	62
4.2.1	Vibrational Spectroscopy	62
4.2.1.1	Infrared Spectroscopy	65
4.2.1.2	Raman Spectroscopy	65
4.2.2	UV-Vis Spectroscopy	66
4.3	Thermogravimetry	66
4.4	Electron Microscopy	67
4.4.1	Scanning Electron Microscopy	67
4.4.2	Transmission Electron Microscopy	67
4.4.3	Energy-Dispersive X-Ray Spectroscopy	67
4.5	Physisorption	67
4.5.1	N ₂ Physisorption	71
4.5.2	Kr Physisorption	72
4.6	Characterization of Colloidal Solutions	73
4.6.1	Dynamic Light Scattering	76

4.6.2	Zeta Potential measurements	76
4.7	Photocatalytic Degradation Experiments.....	76
4.8	TOC Analysis	77
4.9	Photoelectrochemical Methods	78
4.9.1	Mott-Schottky Measurements	78
4.9.2	Photocurrent Measurements	79
4.9.3	Incident Photon-to-Current Conversion Efficiency	79
4.10	Time of Flight Secondary Ion Mass Spectrometry.....	79
5	Results and Discussion	80
5.1	Nanoparticles	80
5.1.1	Ferrite Nanoparticles.....	80
5.1.1.1	Microwave-Assisted Synthesis of Ferrite Nanoparticles	80
5.1.1.2	Variation of Synthesis Period	83
5.1.1.3	Variation of the Reaction Setup	84
5.1.1.4	Post-synthetic Calcination of Zinc Ferrite Nanoparticles	86
5.2	Surface Functionalization	87
5.2.1.1	Non-Polar Colloidal Solutions	88
5.2.1.2	Polar Colloidal Solutions.....	92
5.2.2	XAS Investigation of Ferrite Nanoparticles.....	98
5.2.2.1	XAS Investigation of Reference Compounds	98
5.2.2.2	XAS Investigation of ZnFe ₂ O ₄ Nanoparticles	101
5.2.3	Photocatalytic Degradation of Model Compounds.....	108
5.3	Sol-Gel Derived Mesoporous Ferrite Thin Films.....	113
5.3.1	Mesoporous Zinc Ferrite Thin Films	115
5.3.1.1	Polymer-Templated Zinc Ferrite Synthesis	115
5.3.1.2	PEC Performance of Sol-Gel Derived Mesoporous Zinc Ferrite Thin Films	122
5.3.1.3	Morphology Conservation via SiO ₂ Infiltration.....	126
5.3.2	Mesoporous Magnesium Ferrite Thin Films.....	129
5.3.2.1	Polymer-Templated Magnesium Ferrite Thin Film Synthesis	129

5.3.2.2	PEC Performance of Sol-Gel Derived Magnesium Ferrite Thin Films	131
5.3.3	Mesoporous Calcium Ferrite Thin Films	135
5.3.3.1	Polymer-Templated Calcium Ferrite Thin Film Synthesis.....	135
5.3.3.2	PEC Performance of Sol-Gel Derived Calcium Ferrite Thin Films	144
5.4	Nanoparticle-Derived Zinc Ferrite Thin Films.....	149
5.5	Mesoporous Zinc Ferrite Powders	153
5.5.1	XAS Investigation of Mesoporous Zinc Ferrite Powders	157
6	Conclusion	163
7	Outlook.....	166
8	References.....	168
9	Appendix.....	179
10	List of Abbreviations and Symbols	189
11	List of Tables.....	194
12	List of Figures.....	195
13	List of Publications, Contributions and Research Visits	202
13.1	Peer-Reviewed Journals	202
13.2	Poster and Talk Contributions	202
13.3	Research Visits.....	203

Abstract

The present thesis deals with the synthesis and characterization of nanostructured, phase-pure ferrite materials (MFe_2O_4) concerning their potential use in photocatalysis and photoelectrochemistry. The cubic spinel magnesium and zinc ferrite ($MgFe_2O_4$ and $ZnFe_2O_4$) and the orthorhombic calcium ferrite ($CaFe_2O_4$) were chosen as photocatalyst materials due to their composition of earth-abundant and non-toxic elements. They exhibit band gaps of 1.9 eV – 2.0 eV^[2,3], which allows to perform photocatalytic reactions under visible light excitation. While $MgFe_2O_4$ and $CaFe_2O_4$ are reported to be n-type and p-type semiconductors, respectively, contradictory reports were published on the band positions and semiconducting behavior of $ZnFe_2O_4$. Thus, this thesis aims to clarify these characteristics for the three chosen compounds.

Solution-based synthesis procedures were selected on the basis of literature reports^[4,5] to produce nanoparticles and mesoporous thin films of the selected ferrite compounds. For nanoparticle synthesis, a microwave-assisted approach was chosen. Furthermore, methods for post-synthetic and *in situ* production of colloidal solutions were developed. This offers the possibility to study the interplay of colloidal stability, the nature of surfactants and the resulting efficiency for photocatalytic degradation processes.

To create mesoporous thin films, a dip-coating approach was applied investigating different block-copolymers used as porogens. The synthesis procedure was optimized with regard to the activity under visible light. By this means, conclusions on the connection between the pore morphology and crystallinity of mesoporous thin films and their photoelectrochemical performance was possible.

Special focus was put on the phase purity of the synthesized ferrites, which was checked not only by X-ray diffraction (XRD), but also by Raman spectroscopy. Besides, various analytical methods such as spectroscopic tools, physisorption, photoelectrochemistry or synchrotron-based X-ray absorption techniques (XES, XANES, RIXS) were employed to achieve a detailed characterization and a deeper understanding of the photocatalytic and photoelectrochemical properties of the chosen ferrite materials.

Kurzfassung

Die vorliegende Arbeit beschäftigt sich mit der Synthese und Charakterisierung von nanostrukturierten, phasenreinen Ferritmaterialien (MFe_2O_4) in Hinblick auf ihre potentielle Anwendung in der Photokatalyse und Photoelektrochemie. Die kubischen Spinelle Magnesium- und Zinkferrit ($MgFe_2O_4$ und $ZnFe_2O_4$) und das orthorhombische Calciumferrit ($CaFe_2O_4$) wurden als photokatalytische Materialien ausgewählt aufgrund ihrer ressourcenreichen und ungiftigen Elemente. Die Materialien weisen Bandlücken zwischen 1.9 eV und 2.0 eV^[2,3] auf, was die photokatalytische Anwendung unter Verwendung von sichtbarem Licht als Anregungsquelle ermöglicht. Während $MgFe_2O_4$ und $CaFe_2O_4$ als n-typischer bzw. p-typischer Halbleiter identifiziert wurden, gibt es in der Literatur widersprüchliche Berichte über die Bandpositionen und Halbleitercharakteristika des $ZnFe_2O_4$. Daher zielt diese Thesis auf die Aufklärung dieser Charakteristika für alle drei ausgewählten Verbindungen.

Es wurden Synthesemethoden aus homogener Lösung anhand von Literaturstellen^[4,5] ausgewählt, um Nanopartikel sowie mesoporöse Dünnschichten der ausgewählten Ferritmaterialien herzustellen. Für die Nanopartikelsynthese wurde ein mikrowellengestützter Ansatz gewählt. Außerdem wurden Methoden zur direkten und post-synthetischen Erzeugung kolloidaler Lösungen entwickelt. Dies ermöglicht die Erforschung der Zusammenhänge zwischen Kolloidstabilität, Art der Oberflächenreagenzien und der resultierenden Effizienz in photokatalytischen Abbaureaktionen.

Um mesoporöse Dünnschichten herzustellen, wurde ein Tauchbeschichtungsverfahren verwendet und der Einfluss verschiedener Block-Copolymere als Poren-template untersucht. Die Synthese wurde hinsichtlich der Aktivität der Materialien bei Bestrahlung mit sichtbarem Licht optimiert. Dadurch konnten Rückschlüsse auf den Zusammenhang zwischen Porenmorphologie und Kristallinität mesoporöser Dünnschichten und deren photoelektrochemischer Leistungsfähigkeit getroffen werden.

Besonderer Fokus wurde auf die Phasenreinheit der synthetisierten Ferrite gelegt, was mittels Röntgendiffraktion (XRD) und Raman-Spektroskopie überprüft wurde. Außerdem wurden verschiedene Analysemethoden wie beispielsweise spektroskopische Methoden, Physisorption, Photoelektrochemie oder synchrotrongestützte Röntgenabsorptionstechniken (XANES, XES, RIXS) genutzt, um eine umfassende Charakterisierung der synthetisierten Proben zu ermöglichen und ein tieferes Verständnis über die photokatalytischen und photoelektrochemischen Eigenschaften der ausgewählten Materialien zu erhalten.

1 Introduction

1.1 Motivation

The impact of climate change due to global warming is indisputable in the scientific community.^[1-3] The main reason for the increase of the global average temperature – approx. 0.2 °C per decade during the past 30 years – are greenhouse gases produced due to the human consumption behavior, *e.g.* widely established use fossil energy sources and intensive animal farming.^[6,9,10] The sustainable generation and storage of energy from renewable sources is one of the major topics of recent research to cover the worldwide demand for energy in the present and the future and to avoid further increase of greenhouse gas emissions. Energy supplied by photocatalytic and photoelectrochemical generation of renewable fuels presents an environmentally friendly opportunity to use the most abundant sustainable energy source – the sun. For a good cost-to-value efficiency, suitable semiconductor materials need to be found for optimum use of the energy input *via* sunlight by conversion into electrical energy and storage in form of solar fuels.

In the past, research focused on binary oxide photocatalysts such as TiO₂ (3.0 eV (rutile), 3.2 eV (anatase))^[11,12], Ta₂O₅ (4.0 eV)^[13] and Nb₂O₅ (3.4 eV)^[13]. But also ternary compounds like CaTiO₃ (3.5 eV)^[13], SrTiO₃ (3.25 eV)^[14], Y₂TiO₇ (3.5 eV)^[15] and Ba₅Ta₄O₁₅ (4.5 eV)^[16] have attracted more attention. Due to their large band gaps, the use of the sunlight spectrum is limited to the small region of UV and near-UV light. Because of this, the overall efficiency is still too poor to design comprehensive systems for industrial application in sustainable energy generation.

Recently, ferrites (MFe₂O₄) have been widely discussed as potential materials for photocatalysis and photoelectrochemistry.^[17-19] With their variety of possible metal cations, numerous ferrite materials can be synthesized having band gaps around 2.0 eV for visible light absorption, which increases the total sunlight energy input compared to the aforementioned oxides. Depending on the metal cation M, ferrites can consist of non-toxic and inexpensive because earth-abundant elements. Most commonly, ferrites exhibit a cubic spinel type crystal structure, but other structures are reported as well, *e.g.* for copper ferrite (CuFe₂O₄, tetragonal)^[20,21], barium ferrite (BaFe₂O₄, orthorhombic)^[22] or calcium ferrite (CaFe₂O₄, orthorhombic)^[23].

Cubic spinel ferrites are often reported to be n-type semiconductors possessing a favorable band bending for oxygen evolution reaction.^[17] A change in crystal structure prevalently leads to a p-type semiconducting behavior, which makes those ferrites interesting for photoreduction reactions such as conversion of CO₂ to methanol^[24] or hydrogen evolution reaction during photoelectrochemical water splitting^[17]. As there is a limited number of oxide-based p-type semiconductors known so far^[25], the fabrication of p-type ferrite photoelectrodes gained a lot of attention during the past few years.

A variety of synthesis approaches for ferrite nanoparticles and thin film electrodes have been reported so far, *i.e.* high-temperature reflux synthesis, mechanochemical and hydrothermal approaches, solid state reactions, chemical vapor deposition (CVD) or atomic layer deposition (ALD) thin film techniques.^[5,26–31]

As part of this doctoral thesis, ferrite compounds magnesium ferrite, zinc ferrite and calcium ferrite (MFe_2O_4 ; $M = Zn, Mg, Ca$) were synthesized and investigated concerning their photoelectrochemical behavior for solar fuel production. The fabrication of ferrite nanoparticles and nanostructured thin films of the aforementioned ferrites was aimed by development of solution-based synthesis procedures. Extensive characterization was performed using various analytical methods such as X-ray diffraction and absorption techniques, spectroscopic tools and photoelectrochemistry.

Magnesium ferrite and zinc ferrite ($MgFe_2O_4$ and $ZnFe_2O_4$) are cubic spinel-type ferrites with different tendencies for inversion. Their band gaps were reported to be 2.0 eV^[3] and 1.9 eV^[2], which makes visible light absorption possible. In literature, especially the band positions of zinc ferrite have been discussed controversially, as many contradictory reports were published. This is why special focus was put on the determination of their semiconducting behavior (n-type or p-type) and band positions to evaluate, if overall water splitting or only one half-reaction – hydrogen evolution reaction (HER) or oxygen evolution reaction (OER) – is possible. Calcium ferrite ($CaFe_2O_4$) is reported to show p-type semiconducting behavior alongside a band gap of 1.9 eV.^[32] In contrast to $MgFe_2O_4$ and $ZnFe_2O_4$, it has an orthorhombic crystal structure due to distortion of the oxygen coordination sphere. The conduction and valence band edges reported in literature (-0.6 V and 1.3 eV vs. NHE)^[32] are suitable for simultaneous solar hydrogen and oxygen evolution. The p-type conducting behavior, band positions and photoelectrochemical response of mesoporous $CaFe_2O_4$ were illuminated in detail.

By synthesis optimization combined with detailed analyses, an optimum procedure for production of nanostructured ferrites, *i.e.* nanoparticles and mesoporous thin films, was realized.

For mesoporous thin films, a sol-gel approach was chosen and two different block-copolymers as porogens were chosen. These two thin film synthesis approaches were aimed to be compared concerning their porosity and photoelectrochemical performance, as differences in surface area, interconnection of crystallites and intrinsic defect concentration were expected. Furthermore, mesoporous thin films from a nanoparticle-containing solution were desired.

For synthesis of nanoparticle-based photoelectrodes, phase-pure ferrite nanoparticles are necessary. Therefore, a microwave-assisted reaction was selected developing suitable synthesis techniques to obtain well-dispersible ferrite nanoparticles in polar and non-polar solvents by direct and post-synthetic surface functionalization.

Special focus was put on the phase purity of the synthesized ferrites, which was checked not only by X-ray diffraction (XRD), but also by Raman spectroscopy being a powerful tools to trace by-phases since it is very sensitive to different iron oxide species.^[33] In this work, $MgFe_2O_4$ and $ZnFe_2O_4$

nanoparticles and mesoporous MgFe_2O_4 , ZnFe_2O_4 and CaFe_2O_4 thin films are presented, exhibiting a high grade of phase purity.

1.2 Overview

The next chapter (chapter 2) will elucidate the theoretical background on the challenges of energy supply and the opportunity of solar energy conversion. In this context, the process of photocatalysis and photoelectrochemistry and the possibilities of improvement of these processes by nanostructuring or application of sacrificial agents and co-catalysts will be explained. After discussion of non-noble transition metal oxide absorber materials for potential use in photoelectrochemistry and photocatalysis, the discussion will focus on iron-oxide-based materials with special focus on ZnFe_2O_4 , MgFe_2O_4 and CaFe_2O_4 as earth-abundant, non-toxic and cost-effective absorber materials.

In the following part (chapter 3), the experimental conditions for synthesis of ZnFe_2O_4 , MgFe_2O_4 and CaFe_2O_4 in form of nanoparticles, colloidal solutions and mesoporous thin films and powders will be explained.

Subsequently, in chapter 4 the experimental methods used for analysis of the synthesized samples will be discussed including theoretical background of several special analysis techniques.

In chapter 5, the results on the synthesis and characterization of ZnFe_2O_4 and MgFe_2O_4 nanoparticles and colloidal solutions, sol-gel and nanoparticle-based mesoporous ferrite thin films and mesoporous ZnFe_2O_4 powders will be discussed. This includes the microwave-assisted and solvent-reflux-based synthesis of ZnFe_2O_4 and MgFe_2O_4 nanoparticles with regard to the influence of the synthesis period, setup and post-synthetic heat treatment. Consecutively, the preliminary experiments on the surface functionalization of microwave-derived ZnFe_2O_4 and MgFe_2O_4 nanoparticles for generation of non-polar and polar colloidal solutions will be presented. Afterwards, the characterization of the synthesized and post-synthetically treated samples by X-ray absorption methods will be discussed and the photocatalytic activity of non-functionalized and surface-capped ZnFe_2O_4 and MgFe_2O_4 nanoparticles will be shown. The results of microwave-assisted synthesis and surface functionalization of MgFe_2O_4 nanoparticles have been published in *The Journal of Physical Chemistry C* in 2017.^[1]

The preliminary experiments on sol-gel-derived mesoporous thin films of ZnFe_2O_4 , MgFe_2O_4 and CaFe_2O_4 will be elucidated in chapter 5.3. Here, the effect of different block-copolymers, maximum calcination temperature and period as well as the infiltration with SiO_2 on the photoelectrochemical performance of mesoporous ZnFe_2O_4 thin films will be presented (chapter 5.3.1). The results of this work were published in 2018 in *ChemPhysChem*.^[34] Based on these findings, the synthesis of mesoporous MgFe_2O_4 was approached in connection with photoelectrochemical investigations (chapter 5.3.2). Furthermore, the development of a reliable synthesis approach for formation of CaFe_2O_4 thin film electrodes with hierarchical pore structure at temperatures below 800 °C for possible application as photocathodes will be discussed (chapter 5.3.3).

In addition, a synthesis method for mesoporous nanoparticle-based ZnFe_2O_4 photoanodes *via* spin-coating was developed (see chapter 5.4) and the results on mesoporous ZnFe_2O_4 and the characterization using synchrotron-based X-ray absorption methods will be illustrated (chapter 5.5).

The next two chapters summarize the results discussed in chapter 5 concerning their optimization for photocatalytic and photoelectrochemical application. An outlook will give perspectives on possible future research topics in this context.

The main part (chapter 2 and 7) is followed by a list of references, tables, figures, publications and conference contributions related to this work. Furthermore, it includes supplementary data supporting the discussion of the main part (see chapter 9).

2 Theoretical Background

2.1 Present Challenges in Energy Supply

As the discussion about global warming has heated up recently, alternative ways of energy production and storage are more necessary than ever to limit the greenhouse effect caused by greenhouse gases.

Here, carbon dioxide (CO₂) and methane (CH₄) have to be emphasized as gases relevant for the greenhouse effect, which are mainly produced by human consumer behavior, e.g. fossil fuel consumption and extensive animal breeding.^[10] Avoiding the fossil combustion product CO₂,

which is said to be responsible for up to 80 % of global warming, would be the most important goal in climate politics.^[36] An increase in CO₂ emission from combustion by 100 % from 1971 to 2015 becomes apparent from Figure 2.1. Scientists have stated a clear correlation between the increase of greenhouse gases and global warming for decades, but so far, the annual energy consumption is still mainly based on CO₂-critical sources as shown in Figure 2.2. Even though 42 years are in between the two statistics, the percentage of fossil-based resources has declined only slightly from 86.7 % (1973) to 81.4 % (2015), showing that the energy consumption behavior has not changed significantly during the past decades.

Concerning the total amount of CO₂ emission, the consumption of non-renewable energy has even increased, underlining the importance of change in energy supply to prevent further damage to the world climate. The consequences of strong rise in the world's average temperature is already noticeable today, as droughts, floods and rapid weather breaks are frequently reported.^[7-9] The increase of such extreme weather conditions can

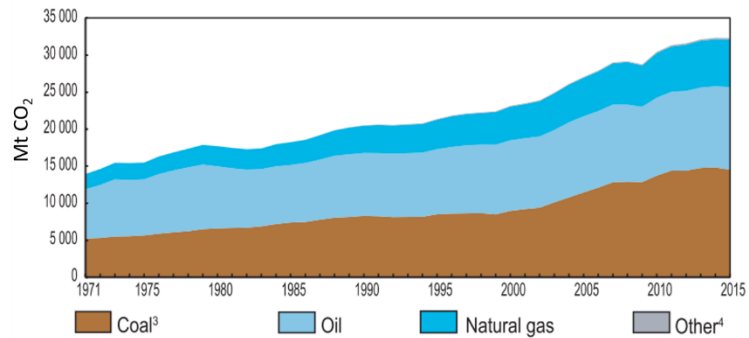


Figure 2.1: Worldwide CO₂ emission from fuel combustion in between 1971 and 2015.^[35]

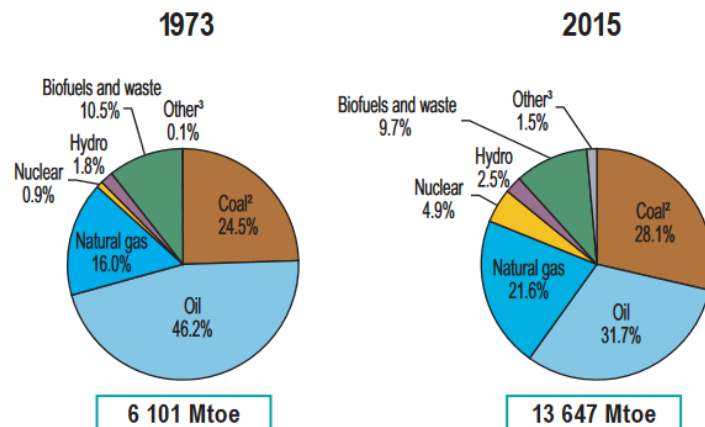


Figure 2.2: World's total energy supply by fuels in 1973 (left) and 2015 (right).^[35]

lead to bad harvests, extension of desert regions and shortages in drinking water. Therefore, the global community agreed to limit global warming by all possible means, committing to a decrease of emissions of 80 % by 2050.^[37] Furthermore, the Paris agreement was signed, to keep the rise of global average temperature below 2 °C.^[38]

To achieve this, “green” alternatives to widely used fossil fuels and fossil-fuel-derived products are needed and a variety of possibilities is already used. Commercially available techniques of sustainable electricity generation are, for example, wind energy (838 TWh in 2015), solar photovoltaics (247 TWh in 2015) or geothermal energy (3978 TWh in 2015).^[35] Compared to the global coal production of around 7.3 billion tons in 2015, the amount of renewable energy is vanishingly low (compare also Figure 2.2). With a still growing world population, a rising demand in energy is expected, which cannot be satisfied solely from sustainable sources so far. Nevertheless, widely established fossil fuel resources are finite, and their reserves decline every year. In Figure 2.3, the energy reserves for different resources are shown. For renewable sources, a yearly potential is shown, which exceeds the total reserves of finite energy sources (*e.g.* natural gas or petroleum). As evident from this graph, solar energy exhibits the highest potential to satisfy and even exceed the world’s annual energy needs, which is why current research aims to make use of this almost infinite energy resource.

So far, the most popular way to harvest solar energy is the application of photovoltaic (PV) cells. 95 % of the commercial modules are made from mono- or multi-crystalline silicon wafers with record efficiencies of 26.7 % and 22.3 %, respectively.^[40] In 2017, PV cells contributed to the global electricity by 1.7 %^[40], which is not yet competitive to fossil fuels and nuclear energy generation. Nevertheless, there is

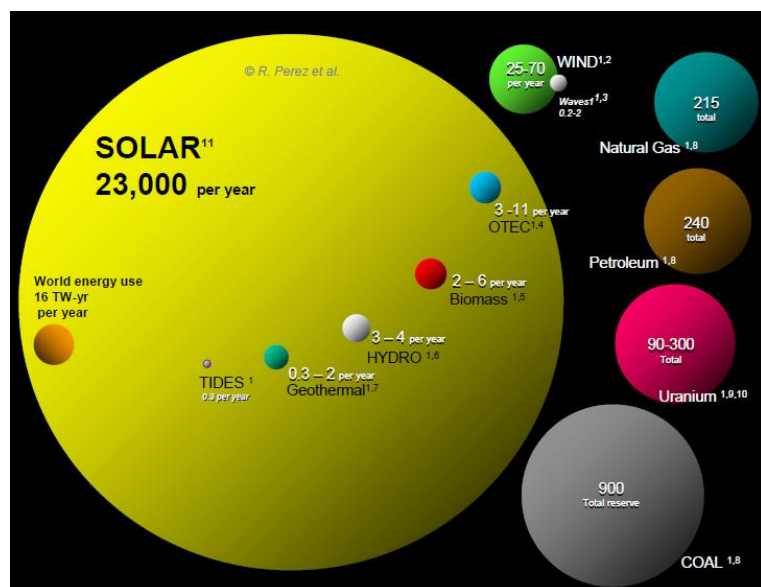


Figure 2.3: Potential energy reserves of renewable and finite resources.^[39]

a fast growing market for PV cells with an annual increase of 24 % between 2010 and 2017.^[40] As direct use of the generated energy is not always possible and night times need to be bridged, too, storage facilities for solar energy are necessary. With electrical energy from solar cells, solar fuels can be produced such as hydrogen (H₂) from electrolysis of water. In solar fuels, the energy harvested from sunlight is conserved and can be stored or transported. This way, low-sunlight regions could be supplied with solar-derived energy and variations of the solar input due to weather conditions and seasons can be compensated. By combustion of H₂, the stored energy is released and only H₂O occurs

as combustion product, which can be converted into H₂ again. This is a major advantage compared to common fossil fuels with high CO₂ emission. Besides, the high gravimetric energy density and an abundant source of H₂ generation (water) are reasons why solar H₂ production plays a key role in scientific research during the last decades.^[41]

2.2 Solar Energy Conversion

With solar cells, energy from sunlight is not used directly but converted into electrical energy. During this conversion process, energy losses within the system occur. Possible alternatives to use solar energy directly for H₂ generation from water are photocatalysis and photoelectrochemistry. For utilization of sunlight, semiconductors with band gaps in the range of the sun's emission spectrum are needed in both, PV-based electricity generation and photocatalysis. The incident photons need to match or exceed the band gap energy barrier to generate separated charge carriers, namely electrons and holes. The energy E is connected to the frequency ν , the wavenumber ω and the wavelength λ by:

$$E = h\nu = \frac{hc}{\lambda} = hc\omega \quad (2.1)$$

According to this equation, with a larger band gap E_g , only higher-energetic light is suitable to excite charge carriers, creating electrons and holes. Especially band gaps in the range of the UV light use only a very small part of the solar spectrum.

In contrast, smaller band gaps around 2 eV (equal to 620 nm) would be suitable to use a larger part of the solar spectrum. This is also emphasized by Figure 2.4, which shows the dependence of solar-to-hydrogen (STH) efficiency and photocurrent density on the band gap. With optical band gaps of 400 nm or less, not even 5 % STH conversion efficiency can be reached. For comprehensive systems, a minimum STH conversion efficiency of 10 % is discussed.^[43,44] This can only be achieved with absorber materials having band gaps of ≤ 2.3 eV, which is equal to an absorption ≤ 530 nm (compare Figure 2.4). Taking into account also overpotentials, which need to be generated for gas evolution reactions, a band gap of ≤ 2 eV would be desirable. Therefore, visible light active

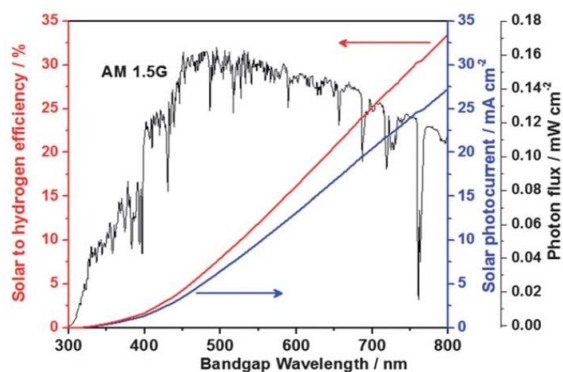


Figure 2.4: STH efficiency and solar photocurrent density generated under AM1.5G illumination correlated to the semiconductor band gap.^[42]

semiconductors should be preferred for solar light driven processes. For comprehensive PEC cells, semiconductor photoelectrodes are aimed showing sufficient H_2 and O_2 evolution rates in aqueous solution at large current densities ($10 - 15 \text{ mA cm}^{-2}$) under 1 sun illumination for hundreds of hours.^[45] For this purpose, efficient light harvesting and performance without degradation is necessary, outlining the need for materials research and characterization in this field. In the following chapters, the processes occurring during photocatalysis and photoelectrochemistry will be illuminated in detail.

2.2.1 Photocatalysis and Photoelectrochemistry

In photocatalysis, chemical processes are induced by charge carriers, which are generated within semiconductor compounds *via* light irradiation. The general term of photocatalysis is widely used for endergonic photocatalytic reactions ($\Delta_{\text{R}}G^\circ > 0$) as well as for exergonic, photosynthetic reactions ($\Delta_{\text{R}}G^\circ < 0$).^[46] In a recent review by F. E. Osterloh, the differences in reaction course for surface-sensitive photocatalytic reactions and charge-separation-sensitive photosynthetic reactions were discussed in detail.^[47] Currently, homogeneous and heterogeneous systems are under review for photocatalytic applications. Homogeneous systems, which are designed to mimic nature's solutions, *e.g.* photosystem II present in chlorophyll, show high turnover numbers (TON) indicating highly efficient redox processes.^[48] Furthermore, enantioselective processes can be performed by photocatalytic reactions.^[49,50]

Unfortunately, homogeneous systems are less resistant against photocorrosion than heterogeneous photocatalysts, which is the main reason for insufficient long-term stability.^[13,51] Additionally, recovery of the homogeneous photocatalyst is usually difficult, while heterogeneous photocatalysts can be easily separated from reaction solution by filtration, sedimentation or centrifugation. The general process of heterogeneous photocatalysis is displayed in Figure 2.5. When light with photon energy larger than the band gap of the semiconductor is used, electrons (e^-) can be excited from the semiconductor's valence band (VB) into the conduction band (CB), leaving a hole (h^+) in the VB. Then, the separated e^- and h^+ , which are called charge carriers, can either diffuse to the surface or they can recombine, which means the loss of absorbed solar

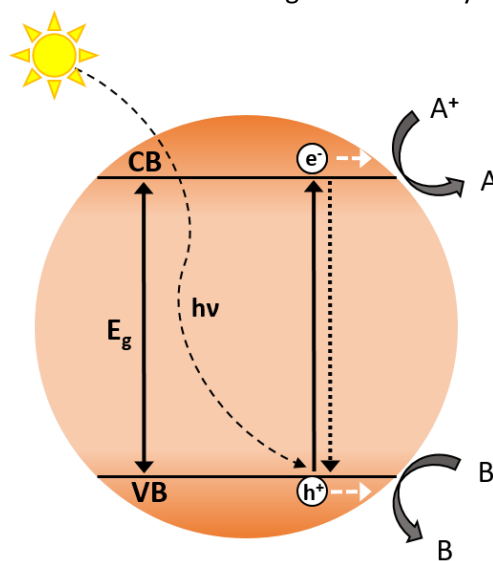
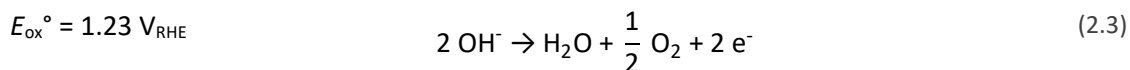
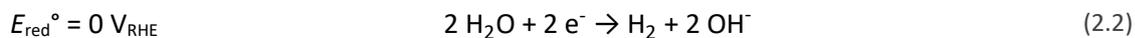


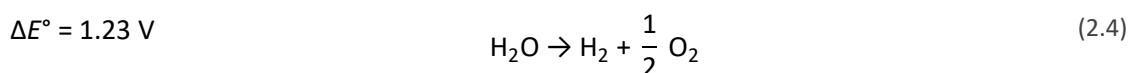
Figure 2.5: Schematic illustration of the photocatalytic process.

energy. For efficient photocatalytic processes, recombination of charge carriers needs to be reduced to a minimum. For this, several methods are applicable, which will be discussed later on (see chapter 2.2.3). Due to charge carrier accumulation at the semiconductor surface, reduction (by e^-) and oxidation (by h^+) of compounds can occur. More precisely, a reduction reaction is possible if the CB minimum of the semiconductor is more negative (on the electrochemical potential table) than the redox potential of the substance which is supposed to be reduced. Accordingly, the oxidation of a substance is possible if its redox potential is energetically beneath the VB of the semiconductor. However, not only band gap size and band positions determine the photocatalytic efficiency of a semiconductor. Also the defect density and charge carrier concentration within the bulk material as well as the interfaces between the semiconductor and the electrolyte have a major influence.^[46]

As discussed earlier, photocatalytic water splitting by solar light is an economically and environmentally highly interesting reaction, which is investigated intensively by the photocatalysis community. It is widely considered to be artificial photosynthesis^[52], as the production of solar fuels by photocatalytic process shows many similarities to nature's photosynthesis including the thermodynamic aspects (1.23 eV for water splitting and 1.24 eV for glucose formation).^[46] The half reactions for oxygen evolution reaction (OER) and hydrogen evolution reaction (HER) under alkaline conditions are given in equations (2.2) and (2.3).



The overall water splitting reaction follows as:



Due to the high number of holes, which need to be accumulated for OER, this half-reaction is nowadays considered to be the limiting step.^[53] Another challenge is the large Gibbs free energy of $\Delta_{\text{R}}G^{\circ} = 237 \text{ kJ mol}^{-1}$ for the water splitting process.^[54] This makes overall water splitting a photosynthetic process. For efficient water splitting, both, the HER and OER, need to be optimized as the overall efficiency is limited by the low-performing half-reaction. Alternatively, also oxidation of other compounds instead of OER is possible. For example pollutants can be degraded, *e.g.* 4-chlorophenol or benzophenone.^[55] In this manner, a cleaning water treatment could be coupled with solar hydrogen production. During photoelectrochemistry, the same basic processes are triggered as discussed for photocatalysis. As peculiarity, the half-cell reactions are spatially separated from each

other at two single photoelectrodes, which are connected to each other within a tandem cell, which is shown in Figure 2.6.

The oxidation reaction (OER in case of water splitting) is performed at the photoanode side, while the reduction reaction (HER in case of water splitting) occurs at the photocathode side. The first photoelectrochemical (PEC) cell for overall water splitting was already reported in 1972 by Fujishima and Honda.^[56] Since then, many approaches for photoelectrochemical solar fuels production have been made to improve the overall performance.

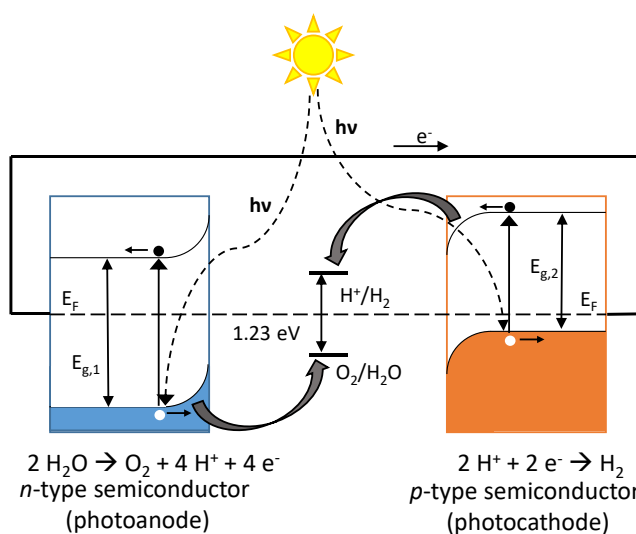


Figure 2.6: PEC water splitting in a semiconductor tandem cell.

When designing a photoelectrochemical device for production of solar fuels, cost, toxicity, durability and performance need to be considered to gain a system being an economic alternative to photovoltaic-coupled electrolyzer approaches. These PV-electrolyzer systems usually operate at 1.8 V, as entropic increase and overpotentials for gas evolution need to be added to the bias of 1.23 V theoretically necessary for overall water splitting.^[57] As the external bias is generated solely by the PV unit, it is subject to fluctuation of the incident light intensity, which can be affected by weather conditions and daytime. Due to this dependence, large energy losses up to 50 % are possible.^[44] Furthermore, the complex combination of PV module and electrolyzer is susceptible to construction errors and transfer losses inside the system.

As an alternative, photoelectrochemical cells have been developed, which use a more direct approach for light-driven water splitting, reducing the potential loss channels compared to the more complex PV-electrolyzer systems. Also in PEC systems, the open circuit voltage generated by photoexcitation of charge carriers needs to exceed the bias of 1.23 V and additional overpotentials for the HER and OER. Here, single-absorber cells with a photocathode and a photoanode fabricated from the same absorber material, or a side-by-side combination of two materials with different band gaps as separate electrodes can be applied. Even more sophisticated is the synthesis of two photoabsorbers with different band gaps on top of each other, which is called dual absorber tandem cell. A restriction concerning the band gaps of the applied semiconductor materials arises from the fact, that a part of the solar light must still be absorbable by the bottom layer to construct a working device.^[58]

Already 30 years ago, scientists tried to evaluate the maximum expectable efficiency of different PEC devices. Weber and Dignam calculated the theoretical conversion efficiencies of semiconductor photoelectrodes for solar water splitting.^[59] They stated a maximum STH efficiency of approx. 12 % for

single absorber PEC devices. Construction of a p-n-junction PEC cell, where an n-type and a p-type semiconductor with a band gap of 1.4 eV are aligned side by side can theoretically improve the STH efficiency up to 16.6 % under AM 1.2 illumination. For an integrated tandem PEC device, the authors calculated possible STH efficiencies up to 22 %. Bolton and co-workers improved the assessment by taking into account a high loss of 1.0 eV per photon.^[60] With this, they calculated maximum STH efficiencies of 12.7 % for single absorber PEC cells with a band gap of 2.23 eV and 21.6 % for a tandem PEC cell with absorbers having band gaps of 1.89 eV and 1.34 eV. The improvement for tandem cells can be attributed to the optimized absorption of the incident solar light due to combination of materials exhibiting different band gaps. Another theoretical approach from 2013 by the group of Nathan Lewis states a maximum STH efficiency of around 30 % when absorber materials with band gaps of 1.60 eV and 0.95 eV are used as photoanode and photocathode.^[61] This already points out, that small band gap semiconductors like silicon would be very suitable for application in tandem PEC devices.

In fact, silicon-based tandem cells in combination with various absorber materials have been studied intensively during the last years, but also perovskite-based tandem cells gained much interest.^[62–69] The dependence of the maximum STH efficiency and the maximum photocurrent density

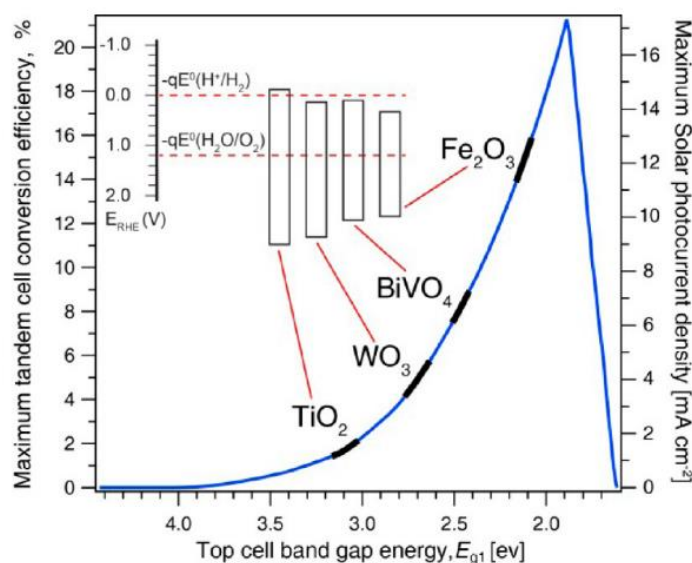


Figure 2.7: Maximum theoretical STH efficiencies and photocurrent densities under solar irradiation correlated to the band gap of the applied photoanode material in combination with a photocathode exhibiting a band gap of < 1.5 eV; inset shows the band positions of the exemplary absorber materials with respect to the redox potentials for OER and HER in water (from Prévot et al.)^[44]

of tandem devices is depicted in Figure 2.7. In PEC tandem cells, the photocurrent density is directly related to the rate of water splitting. Thus, improving the PEC performance of the single absorber materials can improve the tandem device. In many cases, improvement of the photoanode side for the 4-hole-accumulation-process of OER is necessary. Typical shortcomings are a high overpotential, slow water oxidation kinetics, a low degree of light absorption or a low mobility of the photo-generated charge carriers.^[44] All

of these points can be addressed to improve the photocurrent density of the photoanode. Prospects for improvement of the photocatalytic and photoelectrochemical performance of absorber materials will be discussed in chapter 2.2.3.

2.2.2 Semiconductor Characteristics

The energy bands of a semiconductor are based on the interaction of separate orbital levels of the individual atoms, which are periodically arranged. The resulting band structure depends on the contributing elements, their configuration and coordination.

In a semiconductor, the highest occupied levels form the VB and the lowest unoccupied levels form the CB, both separated by a “forbidden” gap called band gap (E_g). Depending on the local density of

states, different valence and conduction band structures can form. The band gap, which is the shortest distance between the occupied and the unoccupied states, can therefore be at the same wave vector k or show a k offset. Band gaps with $\Delta k = 0$ are called direct band gaps, whereas $\Delta k \neq 0$ results in an indirect band gap. In Figure 2.8, the band structure of a direct and an indirect semiconductor are illustrated.

For optoelectronic applications, direct semiconductors are preferred, as the excitation of electrons into the CB and their relaxation under photon emission is fast. Concerning photocatalysis, long-lived excited charge carriers are desirable, which is why indirect semiconductors are considered preferential. The energy level occupation of the valence band and the conduction band can be described by a Fermi Dirac function $f(E)$, depending on the Fermi energy E_F , the Boltzmann constant k_B and the temperature T . The occupation probability of the energy levels by electrons $f(E)$ is large for $E < E_F$ and decreases rapidly for $E > E_F$. At the Fermi energy, the occupation probability becomes 0.5 by definition. For an ideal, undoped semiconductor, the Fermi energy is located in the middle of the VB and the CB.

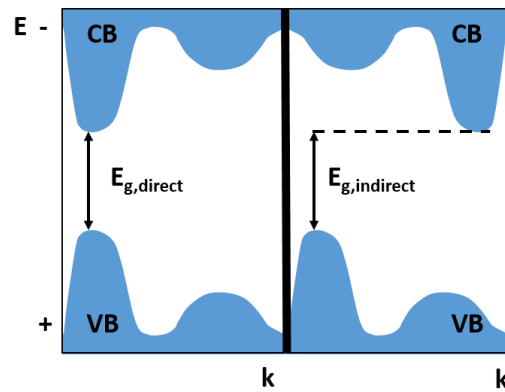


Figure 2.8: Direct and indirect band gap semiconductors.

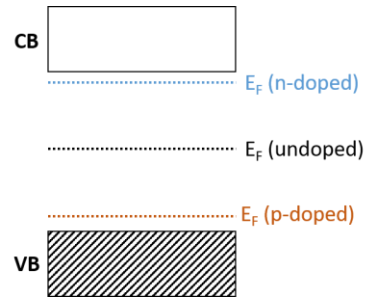


Figure 2.9: Fermi level positions in case of undoped, p-doped and n-doped semiconductor.

$$f(E) = \frac{1}{1 + e^{\frac{E - E_F}{k_B T}}} \tag{2.5}$$

In non-ideal materials, doping occurs in form of impurity atoms or vacancies. This introduces electron acceptor or donor levels, which leads to p-type or n-type semiconductors. In case of donor doping, the Fermi energy depends on the number of donors in the system, *i.e.* the donor density N_b .

Novel donor levels are introduced by additional density of states from the impurity atoms. For n-doping, the donor levels are located just beneath the CB, marking the new position of the Fermi level. In case of p-doping, acceptor levels above the valence band are created, which locate the Fermi level position in p-type semiconductors. This is also shown in Figure 2.9.

When a semiconductor is immersed into an electrolyte, a solid-liquid junction forms. Applying a potential to the system leads to the migration of majority charge carriers out of the interface region. The minority charge carriers, which are less mobile, are therefore accumulating in the junction region, creating a space charge (SC) region. The change in the concentration of majority carriers between the bulk and the solid-liquid interface causes a local difference in their energy levels, which is depicted as an upward bending of the CB in case of n-type semiconductors. The VB is behaving accordingly to maintain a constant difference between CB and VB. The band bending results from the charge q of the minority carriers and potential drop across the SC region $\Delta\Phi_{SC}$. In Figure 2.10, the connection between the SC region, its electrical field, the potential drop and the resulting band bending is shown. Depending on the amount of doping and the material itself, different sizes w_{SC} of the SC region can be found. This can be described by equation (2.6).

$$w_{SC} = \left(\frac{2 \Delta\Phi_{SC} \varepsilon \varepsilon_0}{q N_D} \right)^{1/2} \quad (2.6)$$

Here, ε_0 is the vacuum permittivity and ε is the dielectric constant of the material. The SC region caused by the local potential drop attracts oppositely charged ions from the electrolyte to compensate the local charge at the solid interface. In concentrated electrolytes, this opposite charge is located outside the Helmholtz layer and can be taken as local capacity C_{SC} . From this, the Mott Schottky equation ((2.7)) derives.

$$\frac{1}{C_{SC}} = \frac{2}{N_D \varepsilon \varepsilon_0} \left(\Delta\Phi_{SC} - \frac{k_B T}{q} \right) \quad (2.7)$$

For materials with low doping concentration ($< 10^{24} \text{ m}^{-3}$)^[70], the potential drop $\Delta\Phi_{SC}$ is assumed to only occur in the SC region, which is why absolute potential values U can be used. The flat band potential U_{FB} is the electrode potential, where constant (flat) valence and conduction bands are present, as the electrical field in the semiconductor at the solid-liquid junction becomes zero.

The surface, which is a crystal defect in the crystal lattice, breaks the periodicity of the bulk material, intrinsic states are introduced, which are called surface states.^[71] For materials with a high number of surface states, charging can occur due to electron exchange between the semiconductor and the electrolyte.

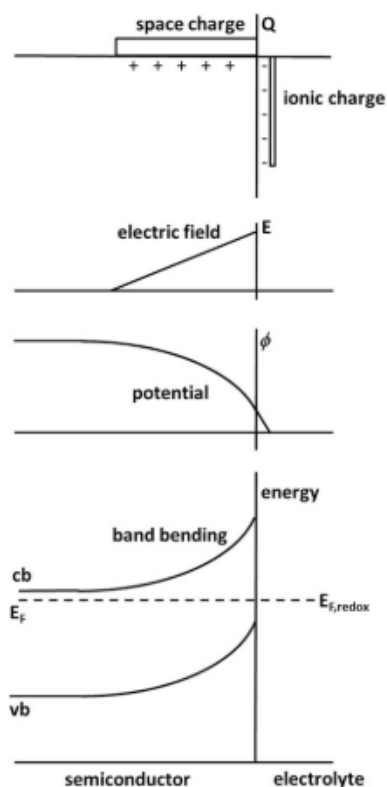


Figure 2.10: Schematic illustration of the interplay between space charge, electrical field, potential and band bending.^[71]

In case of extremely high number of surface states, this can lead to metal-like character causing Fermi level pinning.^[72,73] This can also appear under illumination independently from the number of surface states, when minority charge carriers are heavily accumulated in the SC region due to slow transfer kinetics. The electron transfer from the depletion layer to the electrolyte is described by the Gärtner equation.^[74] As it is not valid for slow electron transfer kinetics and does not consider charge carrier recombination in the SC region, it was extended by Reichmann^[75] and El Guibaly and Colbow^[76] to a more accurate but highly complex model.

In small features such as nanoparticles, almost no electrical field is build up, leading to neglectable band bending. Therefore, also no defined SC region can be found. Thus, charge carrier transport is fully diffusion controlled. As the depletion force from the electrical field is missing, the overall carrier transfer is slowed down. A special case of nanostructuring are mesoporous systems, where the electric field can be either present or absent, depending on the feature

size. This complicates their correct description.^[71]

As the band bending depends on the evolution of an electrical field within the solid, with mesoporous and nanostructured photoelectrodes the development of substantial band bending is not possible, thus leading to a fully diffusion controlled charge carrier transport. If the feature size would match or deceed the minority carrier diffusion length, recombination could be reduced. However, several aspects need to be considered. There is a linear dependence between the concentration of minority and majority charge carriers. In mesoporous semiconductors, the Fermi level diverges from the respective band (*e.g.* CB for n-type), which leads to lower majority carrier concentration. At certain critical sizes, equal concentrations of electrons and holes are found and recombination does not follow pseudo-first order kinetics anymore.^[70] Furthermore, scattering and unfavorable minority carrier accumulation in multistep redox processes are not incorporated in state-of-the-art theoretical descriptions for macroscopic systems. Due to this, no adequate description for recombination processes in nanostructured semiconductors have been found yet.^[70]

In an illuminated semiconductor, the amount of e^- and h^+ can be described according to equations (2.8) and (2.9).^[77] $E_F(e^-)$ and $E_F(h^+)$ are the quasi Fermi levels of photo-generated electrons and holes, and N_e and N_h are the respective densities of states. E_{CB} and E_{VB} are the conduction and the valence band energy.

$$e^- = N_e \left(\frac{1}{1 + e^{\left(\frac{E_{CB} - E_F(e^-)}{k_B T} \right)}} \right) \quad (2.8)$$

$$h^+ = N_h \left(\frac{1}{1 + e^{\left(\frac{E_F(h^+) - E_{VB}}{k_B T} \right)}} \right) \quad (2.9)$$

In n-type semiconductors under dark conditions, majority carriers are responsible for the semiconductor electrode reaction, as the equilibrium density of the minority carriers is much smaller. Their potential-dependent accumulation leads to a dark current. Under illumination, an equal excess of photo-generated electrons and holes can be found.

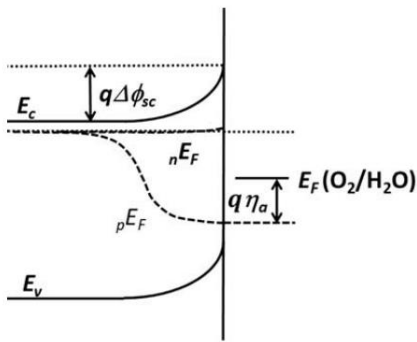


Figure 2.11: Energy diagram of a biased n-type photoelectrode with Fermi level splitting.^[70]

In Figure 2.11, the interplay of changing quasi Fermi levels and emerging overpotential in case of an n-type semiconductor with slow electron kinetics under external bias is shown. Then, photo-generated minority carriers reign the electrode reaction. In n-type semiconductors, the number of photo-generated electrons is still much smaller than the original number of electrons under dark conditions.^[70] Therefore, the overall electron concentration does not change significantly. This is why $E_F(e^-)$ remains close to E_F for the dark equilibrium. In contrast, the photo-generated holes drastically increase the hole density, thus

shifting $E_F(h^+)$ towards the valence band. When $E_F(h^+)$ drops below the oxidation potential of the electron-donating species in solution, this creates a driving force for oxidation reactions like OER. This driving force can be expressed as ΔE_F and is directly related to the overpotential η_a by equation (2.10).

$$\eta_a = \frac{\Delta E_F}{q} \quad (2.10)$$

The diffusion of charge carriers to the surface of a semiconductor is limited by their effective masses, which depend on the crystal orbitals forming the band structure of the semiconductor. With narrow bands, the electrons and holes generated in those bands are highly localized (large E_i) and exhibit large effective masses according to the dispersion relation.^[78–80] According to Brus^[80], charge carriers can be treated as pseudo-particles having a quantum localization energy E_i , which is dependent on the effective mass m^* of the charge carrier and the particle radius r . In a quantum-mechanical approach it can be described as

$$E_i \cong \left(\frac{1.8e^2}{\varepsilon \cdot r} \right) + \left(\frac{\pi^2 \cdot h^2}{2m_r^* \cdot r^2} \right) \quad (2.11)^{[81]}$$

This takes into account the dielectric constant ε of the material and the reduced effective mass m_r^* , which is the sum of the effective mass of electrons (m_e^*) and holes (m_h^*). The experimental determination of effective masses was described by Kormann *et al.*^[81] With the charge carrier mobility μ defined as

$$\mu = \frac{q \cdot \tau_L}{m^*} \quad (2.12)$$

the effective mass m^* is connected to the charge q and the lifetime τ_L of the charge carriers. In combination with the charge carrier mobility, the mean free diffusion length L of charge carriers can be calculated. In an n-type semiconductor holes are the minority charge carriers and their diffusion length L_h is described as

$$L_h = \sqrt{\frac{k_B T}{q} \mu_h \tau_h} \quad (2.13)$$

Here, μ_h is the hole mobility and τ_h is the lifetime of the holes. The larger the effective mass, the smaller the mean free diffusion path to another lattice site. Desirably, the value for the minority carrier diffusion length would be in the range of the light penetration depth.

Related to quantum localization energy E_i , this means, that the mean length of average diffusion without recombination is larger, when the bands comprising the respective crystal orbitals are more diffuse resulting in lower effective masses. The mean free diffusion path limits the charge separation efficiency and therefore also the expectable photoactivity. This relation is known as the photo-Dember effect, which determines the charge carrier transport if no external electric field is applied.^[82,83] In the following chapter 2.2.3, possibilities to influence the photocatalytic activity will be discussed.

2.2.3 Influences on Photoactivity

The main challenges for high efficiency photocatalyst materials are a broad light absorption, *i.e.* narrow band gaps, in combination with efficient charge carrier separation and transport to the semiconductor surface to prevent recombination.^[84] Furthermore, charge transfer at the solid-liquid interface is a crucial step. Surface, electronic and bulk properties influence these critical processes.

With band gaps and band positions showing major influence on the photoactivity, adjusting these parameters is one critical point. Band gap engineering is a widespread field.^[13,41] For instance, doping with metal and non-metal atoms leads to tailored band gaps and band positions.^[84] The VB maximum in metal oxide semiconductors can be shifted to more negative relative potentials by nitrogen doping. Introduction of transition metal ions can lead to new CB levels within a semiconductor, which can be more positive than the original CB levels, *e.g.* when doping TiO₂ with transition metals Cu and Zn.^[85] Besides, due to quantum confinement effect, also the crystallite size can influence the band positions, which is widely known for quantum dots like CdS or CdSe nanoparticles.^[86] Furthermore, dye sensitization of UV-active photocatalysts can improve the overall photoactivity.^[87]

Another important factor is the number of crystal defects within a solid photocatalyst, which have different dimensional expansion. They act as recombination sites, lowering the photocatalytic activity. Common 0D defects, also called point defects, are vacancies or interstitials within the crystal lattice, while 1D defects are for example dislocations. Grain boundaries and the surface of a semiconductor represent 2D defects. In 3D expansion, inclusions, *e.g.* of by-phases, represent crystal defects. Therefore, uncontrolled formation of by-phases within a material can suppress its photocatalytic performance. As crystal defects are considered bulk properties, they can be influenced by thermal treatment. Thermal annealing can heal intrinsic crystal defects, leading to large monocrystalline areas.^[88]

Another way to improve the charge carrier separation is the specific formation of heterojunctions. In composite photocatalysts consisting of two semiconductors with suitable band positions, charge carriers can be transferred from the respective bands of component of one system to the other one. As this charge injection is very fast, electrons are accumulated in one semiconductor, while holes are transferred to the other one, leading to efficient charge carrier separation. A detailed description is provided in a review by R. Marschall.^[25]

In the following sections, prospects for improvement of the photocatalytic and photoelectrochemical performance by nanostructuring or application of co-catalysts and sacrificial agents will be given.

2.2.3.1 Nanostructuring

Diffusion of photo-generated charge carriers to the electrode-electrolyte interface of a heterogeneous photocatalytic system is a crucial step, as most charge carriers exhibit diffusion lengths much smaller than the average film thickness or particle size of the photocatalyst. Especially in n-type oxide materials, photo-generated minority charge carriers (holes) exhibit mean diffusion lengths of only few nanometers before recombination in the bulk material occurs.^[53] Nanostructuring can reduce the size of the semiconductor to the range of the mean free diffusion length of the charge carriers, thus reducing recombination.^[89,90] In the optimum case, the particle size would be twice the dimension of the mean free diffusion length to allow charge carriers, which are generated in the center of the particle, to diffuse to the surface without recombination. For α - Fe_2O_3 photoanodes, it was already shown that nanostructuring can drastically improve the PEC performance.^[91] Furthermore, small nanocrystals are often monocrystalline. With the absence of grain boundaries, recombination can be reduced even further.

A variety of methods can be used to obtain semiconductor materials with features in the nanoscale regime. Generally, creation of nanosized materials can be achieved by top-down and bottom-up approaches.^[92,93] Top-down synthesis starts with a macroscopic material, which is reduced in size, usually by mechanical force. One of the most popular top down methods is ball milling for nanoparticle synthesis, but also electron beam techniques or etching of macroscopic thin films can create nanosized features.^[94–96] With bottom-up synthesis approaches, creation of nanoparticles starts from molecular, atomic or ionic precursors. By thermal or electrochemical activation, the precursors are degraded, forming new compounds of nanometer size. The mechanism of nanoparticle synthesis by nucleation and consecutive growth from solution has been described by LaMer in 1950 (see Figure 2.12).^[97]

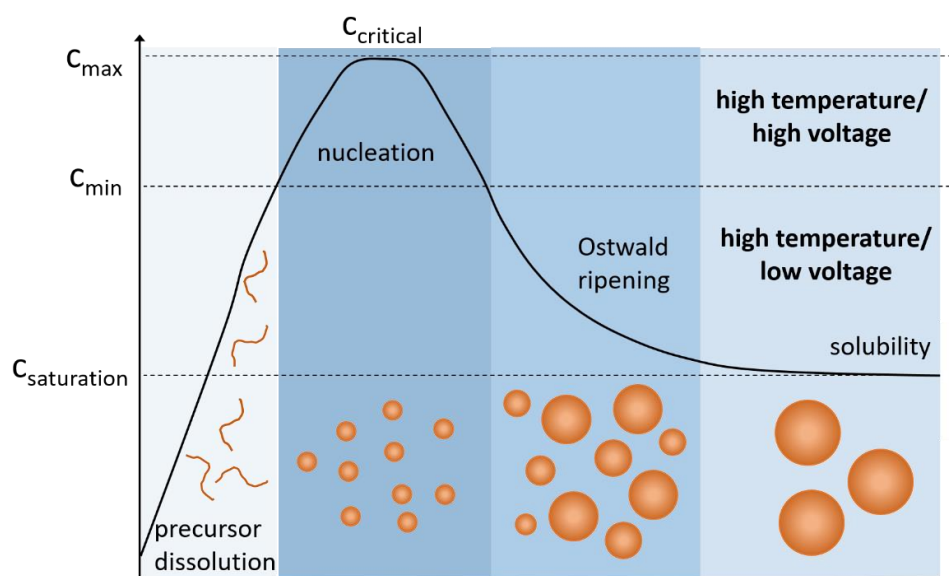


Figure 2.12: LaMer diagram showing nanoparticle evolution during bottom-up synthesis.

At the beginning, the precursor is dissolved in the solution, which increases the overall concentration. At the saturation concentration $c_{\text{saturation}}$, no spontaneous nucleation occurs, as this process would consume energy. Therefore, a higher critical concentration c_{critical} is necessary for formation of solid nuclei. When nucleation occurs, the precursor concentration in solution is lowered. Falling below the minimum nucleation concentration c_{min} stops the nucleation process, but nanoparticle growth is still possible due to an oversaturation in the solution. Here, larger particles grow on the cost of smaller particles, which dissolve again due to higher surface tension. This is known as Ostwald ripening.^[98] When the precursor concentration in solution drops below $c_{\text{saturation}}$, also particle growth stops and the final product is obtained.

A number of synthesis techniques is based on this principle mechanism, such as electrodeposition^[99], electrospinning,^[100,101] sol-gel synthesis,^[21,102] solvothermal approaches^[103,104], co-precipitation^[105] as well as solution-based microwave and high temperature synthesis.^[26,27,106] By this means, a variety of morphologies from nanoparticles in different shapes to nanofibers^[100,101] and nanorod arrays^[107] can be designed. With bottom-up approaches targeted faceting is possible, where the most active facets for the desired reaction can be created, thus supporting the reaction course.^[85-87]

Furthermore, the generation of mesoporous materials can be achieved by various synthesis routes, *e.g.* hard templating^[111-113], soft templating^[114-119] or sintering of nanoparticulate layers^[120,121].

In hard templating, a rigid mesostructured scaffold is infiltrated with a precursor solution. After the formation of the desired compound, the hard template is removed by etching or heat treatment. Here, a partial destruction of the formed compound by aggressive etching or high temperatures opposes the incomplete removal of the template. Thus, the removal of the template is a crucial and the most complicated step in many hard-templating syntheses. Furthermore, with small pore features a complete infiltration with the precursor solution can be challenging.

Using soft templating, *in situ* formation of the scaffold from micelles of the structure-directing agent occurs. As there is no rigid structure pre-defined, the precursor solution can encapsulate the soft template completely. As soft templates, ionic surfactants, organic matrices and polymers have been reported.^[5,122,123]

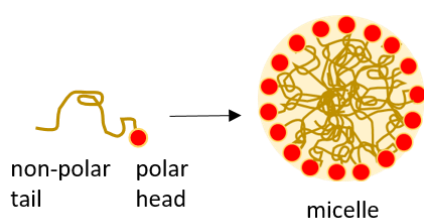


Figure 2.13: Schematic illustration of micelle formation.

Soft templates used for solution-based synthesis of mesoporous compounds are amphiphilic with a polar head group and a larger non-polar tail. In polar solvents, at a certain concentration – the critical micelle concentration (CMC) – the molecules arrange their hydrophobic parts towards each other, which leads to the formation of micelles with a polar surface depicted in Figure 2.13. In this work, different polymers were used as soft templates, which are

listed in Table 3.4. The two most-used of these polymers are shown exemplarily, namely Pluronic® F127 (Figure 2.14a) and the poly(isobutylene)-*b*-poly(ethylene oxide) PIB3000 (Figure 2.14b). Both are block-copolymers containing hydrophilic and hydrophobic units. For tri-block-copolymers with polyethylene oxide (PEO) and polypropylene oxide (PPO) units, a variety of combinations is known. Their physical properties (viscosity, hydrophilicity, thermal stability) can be influenced by tailored choice of PEO and PPO units. This leads to the “Pluronic grid” of commercially available PEO-PPO block-copolymers, which is shown in Figure 2.14c.

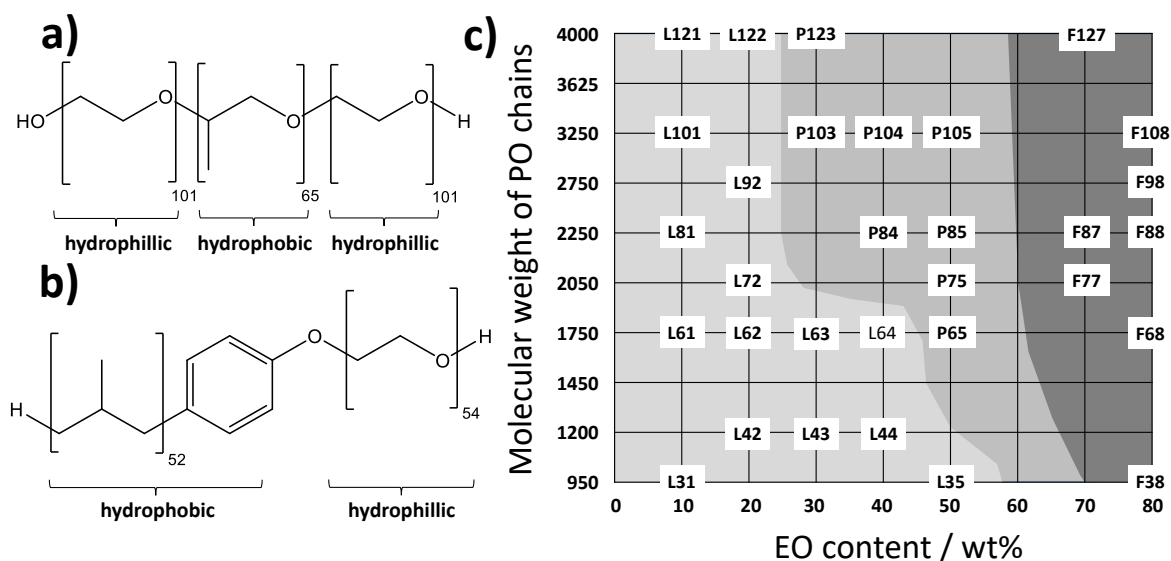


Figure 2.14: a) Pluronic F127, b) PIB3000, c) “Pluronic grid” illustrating the variation in composition of PEO-PPO-PEO block-copolymers and their state of matter with a liquid phase (L, pale grey), a paste-like phase (P, grey) and a solid phase (F, dark grey) adapted from literature^[124–126].

A precursor solution containing a block-copolymer or surfactant can be used for creation of porous thin films from homogeneous or colloidal solution by various coating application.^[5,127] In this work, mostly sol-gel-based dip coating is used for generation of mesoporous metal oxide thin films, which is why this process will be discussed in more detail. Typically, a mixture of metal precursors dissolved in well-chosen solvents is mixed with a certain amount of surfactant. During dip coating, a solid substrate with a surface matching the wettability properties of the chosen solvent mixture is immersed in the precursor solution. For polar solvents, the surface should be polar to achieve sufficient wetting. Surface treatment prior to the dip coating can improve the wettability, *e.g.* by (electro-)chemical or plasma-etching or ion sputtering.^[128–130] The withdrawal speed and surrounding atmosphere determine the thickness of the thin film, leading to thinner films at slower withdrawal rates due to increased draining of the liquid film. During withdrawal of the wetted substrate from the precursor solution, the solvent starts to evaporate changing the concentration of the surfactant inside the liquid film. When the concentration reaches the CMC, micelles are formed within the liquid film and start to assemble, which

is called evaporation induced self-assembly (EISA).^[131,132] The metal precursors fill the spacing between the assembled micelles, which determines the arrangement of pores in the resulting gel. Depending on the speed of solvent removal, which is influenced by the saturation of the surrounding atmosphere, an ordered or irregular packing of the polymer micelles can occur.

Furthermore, the mechanism of solid compound formation has to be taken into account. In this work, the most prominent synthesis approach for porous thin films is based on a sol-gel mechanism. Here, metal precursors are dissolved in a polar solvent to generate solvated metal ions. These solvated metal ions react with traces of water present in the mixture, which is called hydrolysis.^[133]



Hydrolysis can proceed, leading to stepwise exchange of the original ligands with OH-groups. This process is followed by condensation of the hydrolyzed metal ions forming metal-oxygen-metal bonds.^[133]



This includes the elimination of either water (dehydration, equation (2.15) or alcohol (dealcoholation, equation (2.16) molecules.^[133] After dehydration, the released water molecules can lead to hydrolysis of additional precursor. By this means, a colloidal dispersion of partially condensed metal oxide clusters is created, which is called sol. With ongoing condensation, also called syneresis or aging, a three-dimensional network of metal oxide/metal hydroxide clusters is formed, which is much more rigid than the dispersed single clusters. This non-fluid network within a still present liquid phase is called gel.^[134] In 1996, Kakihana *et al.* defined five types of gels, which are formed by sol-gel synthesis of materials, *i.e.* colloidal gels, metal-oxane polymer gels, metal complex gels and two types of polymer complex gels.^[133,134] These gel-types differ in the nature of their building blocks and bonding types, but all yield a homogeneous, metal-containing precursor for synthesis of metal oxide compounds. In comparison to many other reaction techniques, this solution-based approach offers metal precursor mixing on an atomic level, which is very important for generation of ternary oxides.^[133,134] The gel is dried to remove the remaining solvent, forming a xerogel or aerogel. In the final step, the metal-hydroxide groups are removed by calcination, which leads to a crystalline metal oxide compound.^[134]

Lately, research focusses on the synthesis of mesoporous solid compounds, as mesopores (2 – 50 nm) combine the advantages of a high surface area and well-accessible pores. Here, silica has been well-investigated in terms of ordered and non-ordered mesopores. Starting from common alcoxide precursors like tetraethyl orthosilicate (TEOS) or tetramethyl orthosilicate (TMOS), the

hydrolysis and condensation in the presence of structure-directing surfactants leads to highly porous materials with defined pore sizes and a narrow pore size distribution. By variation of the surfactant or block-copolymer concentration, tailoring of the pore morphology is possible. Hereby, ordered micropores (zeolites) and mesopores of 2D hexagonal (MCM-41, SBA-15) or cubic gyroid (KIT-6) shape can be created.^[135,136] These mesoporous silica compounds can be used as hard template to generate mesoporous structures from other compounds, *e.g.* mesoporous carbon.^[137,138] Besides, a variety of other mesoporous metal oxides has been synthesized by template-tailored approaches for utilization in catalysis, drug delivery, or energy storage, *e.g.* WO₃, TiO₂, Ta₂O₅, CsTaWO₆, ZrO₂, ZnO, α-Fe₂O₃ and others.^[112,118,137,139–141] In comparison with nanoparticle systems, mesoporous materials do not suffer from agglomeration effects and therefore maintain a large accessible surface area, which is a crucial parameter in surface-dependent photocatalytic and photoelectrochemical processes.

In terms of porous compounds for various applications, a differentiation between ordered and non-ordered porosity has emerged. A multiplicity of silica compounds with ordered porosity has been reported over the years, being the most prominent material class of ordered porous compounds.^[135,142] Besides, many other materials with ordered pores have been developed for catalytic and photocatalytic applications.^[137,143,144] Due to homogeneous pore size and pore walls thickness, ordered porosity leads to excellent model systems for development or validation of theoretical predictions and novel analysis techniques.^[123,145] But not only pore ordering, but also interconnectivity and accessibility of the pores is important for the reactivity of porous compounds as pore blocking can occur.

From the application point of view, systematic comparison of ordered and non-ordered porous systems is scarce. In a study by Limnell *et al.*, mesoporous silica were loaded with a poorly soluble model drug to investigate the influence of pore ordering on the drug release properties of a material.^[146] Here, the ordered MCM-41 was compared to the non-ordered Syloid® 244. The authors report faster drug release from non-ordered mesoporous silica, which they accounted to the larger pore size and smaller particle size of Syloid® 244. With MCM-41, similar values for drug release were achieved when a more sophisticated drug loading process was applied.

Lately, non-ordered, hierarchical pore structures have gained attention as they combine the large surface area of the smaller pores, which are well accessible *via* larger pores allowing effective mass transport. This has been shown to effectively improve the performance in catalysis and photocatalysis.^[147,148]

To summarize, the tailored design of nanosized photocatalysts by choice of synthesis technique can enhance their performance in photocatalytic and photochemical reactions.

2.2.3.2 Co-Catalysts

Decoration of the photoactive semiconductors with so-called co-catalysts can increase the overall performance, too. Co-catalysts are additional compounds deposited on the surface of the actual photocatalyst, which are able to collect and accumulate charge carriers. Furthermore, they can show lower overpotentials for gas evolution reactions, which further supports the reaction course. Co-catalysts can be metals (e.g. Au, Rh)^[90,149], transition metals oxides (e.g. RuO₂, IrO₂)^[150] or amorphous metal-based compounds, (e.g. Co-Pi, CoO(OH)_x)^[151,152]. Also, complex morphologies and combination of different materials for reaction support is possible, e.g. core-shell structures.^[16] In case of metal co-catalysts on semiconductor photocatalysts, a Schottky contact is generated inducing charge carrier migration. As metal co-catalysts usually exhibit lower Fermi energies than the absorber materials on which they are deposited, an efficient electron transfer from the CB of the semiconductor towards the metal sites is possible.^[25,153]

Therefore, the metal co-catalyst becomes the active center for reduction processes, e.g. proton reduction (Figure 2.15 left). Furthermore, the metal sites can act as recombination centers for hydrogen atoms (H[•]), which were created by proton reduction

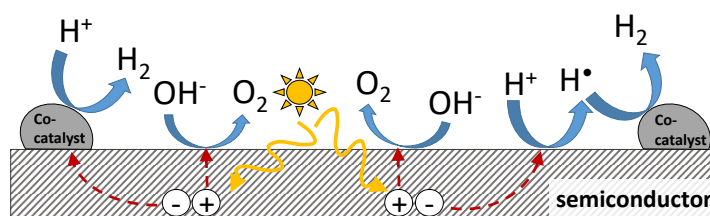


Figure 2.15: Mechanisms of hydrogen evolution on a semiconductor surface decorated with HER-co-catalysts acting as electron trap (left) and hydrogen atom recombination site (right).

at the semiconductor surface (Figure 2.15 right) as proposed by Joo and co-workers.^[154] At the same time, charge carrier recombination is suppressed. By performing electrocatalytic reactions, the co-catalyst supports the overall reaction course. As electrocatalytic reactions occur at longer time scales compared to pure photochemical processes, also complex reactions with multiple electron transfer steps can be performed, such as HER or OER.^[155] There are various methods for deposition of co-catalysts onto a photocatalyst surface, e.g. co-precipitation, thermal deposition or impregnation. An effective method for deposition of co-catalysts is the *in situ* growth initiated by light excitation. This is called photodeposition and has found widespread application, e.g. for deposition of Pt on TiO₂^[156], CoPi on TiO₂^[152] or Pt on CaFe₂O₄^[157]. By this approach, the deposition occurs at the active sites of the photocatalyst and small, well-distributed co-catalyst particles are created.^[158] The optimum amount of co-catalyst for enhanced photoactivity depends on the type of co-catalyst, its particle size and the quality of co-catalyst/photocatalyst contact.^[159,160] In a systematic study, Fu *et al.* reported the enhancement of the photoactivity depending on the metal type of the co-catalyst deposited on TiO₂.^[160] Here, Pt on TiO₂ showed the largest enhancement, which was attributed to the large work function of Pt increasing the Schottky barrier effect.

2.2.3.3 Sacrificial Agents

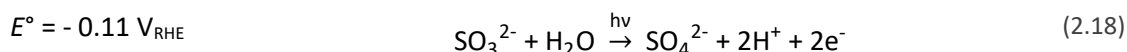
By addition of substances with suitable redox potentials and fast redox kinetics, recombination of charge carriers can be suppressed by fast electron exchange with the redox agent. Furthermore, the endergonic process of overall water splitting can be transformed into an exergonic process. These substances are called sacrificial agents. In case of water splitting, depending on the nature of the sacrificial agent (electron donor or acceptor) either the evolution of O₂ or H₂ can be eliminated. Therefore, the back reaction to water is suppressed, which further increases the yield of gas evolution. For absorber materials with band positions enclosing the HER and OER redox potentials, the choice of sacrificial agent can drive only one half-reaction selectively on the same material. In combination with a two-compartment reactor setup, both half-reactions can be driven in the same system spatially separated by a cation exchange membrane. Multiple designs were reported in literature.^[142,156,161] By this, the complex separation of the H₂/O₂ gas mixture evolving during photocatalytic water splitting can be avoided.

For the OER, electron acceptors like metal cations (Ag⁺, Fe³⁺), sodium iodate (NaIO₃) or sodium persulfate (Na₂S₂O₈) have been reported.^[156,162] A majority of studies reports AgNO₃ as the sacrificial agent for water oxidation.^[163,164] One issue, which needs to be addressed when using AgNO₃ is the formation of elemental silver simultaneously to the OER, as shown in equation (2.17).

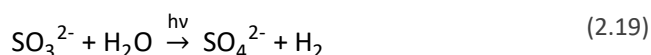


The formation of elemental silver on the semiconductor surface changes the optical and catalytic properties of the system and therefore affects the analyzed process.^[165] To avoid this impact, alternative sacrificial agents should be used, *e.g.* S₂O₈²⁻ or NO.^[79,165]

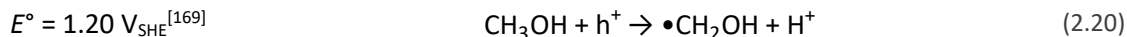
Another widely used sacrificial agent is sodium sulfite (Na₂SO₃) with a redox potential of SO₃²⁻/SO₄²⁻ of -0.11 V_{RHE}^[71], which is more negative than the standard reduction potential for HER (0 V_{RHE}). Therefore, the proton reduction from water molecules becomes an exergonic photocatalytic process (0 < Δ_RG°) in the presence of SO₃²⁻. The oxidation of SO₃²⁻ is shown in equation (2.18).^[166]



In combination with proton reduction, the overall reaction is:



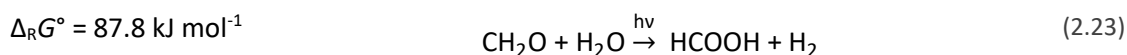
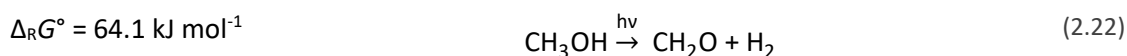
Similar to electron-donating species, with electron-accepting sacrificial agents the OER half-reaction turns exergonic.^[71] Another prominent sacrificial agent is methanol (MeOH).^[167] By fast insertion of an electron into the VB of the semiconductor, MeOH is photo-oxidized and the α -hydroxy-methyl radical is created (equation (2.20)).^[168]



The α -hydroxy-methyl radical has a very cathodic electrochemical potential, thus injecting a second electron into the CB according to equation (2.21). This effect is known as photocurrent doubling.^[168]

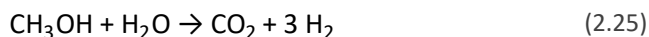


Formaldehyde can be further decomposed to formic acid and CO_2 , subsequently, which means complete mineralization of the sacrificial agent. The consecutive steps for methanol mineralization are shown in equations (2.22) to (2.24).^[170]



The third reaction step, having a negative Gibbs free energy, prevents the evolved H_2 from undergoing undesired back reactions.^[165]

The overall process for photocatalytic hydrogen generation in the presence of MeOH would be



with a Gibbs free energy of $\Delta_{\text{R}}G^\circ = 16.1 \text{ kJ mol}^{-1}$.^[168] This is much smaller than the Gibbs free energy for overall water splitting ($\Delta_{\text{R}}G^\circ = 237 \text{ kJ mol}^{-1}$)^[54], which means a lower energy barrier for H_2 generation and the HER is highly promoted due to the presence of methanol as sacrificial agent. By now, a variety of alternative sacrificial agents for the hydrogen evolution half-reaction has been explored, *e.g.* different alcohols, amines, carboxylic acids or glucose.^[160,165,171] They show different oxidation potentials for their decomposition as exemplarily shown in Figure 2.16.

With bio-available organic sacrificial agents, a nearly carbon-neutral process is possible due to the reconversion of the released CO_2 into the sacrificial agent by photosynthesis, increasing the sustainability of the photocatalytic process.^[159,172]

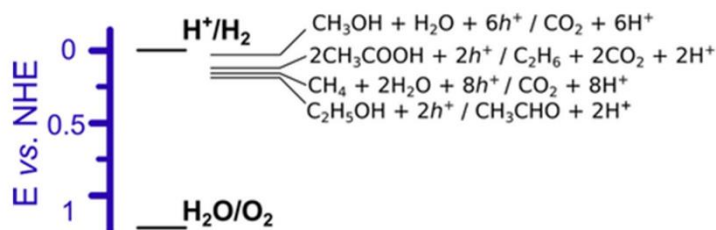


Figure 2.16: Oxidation potentials for different organic sacrificial agents in regard to the redox potentials for the water splitting half reactions.^[159]

The use of sacrificial agents helps to estimate the ability for light-driven water reduction or oxidation, respectively. On the other hand, the ability to perform OER and HER in the presence of sacrificial agents does not guarantee successful overall water splitting without sacrificial agents.^[173] In the following chapter, possibilities for characterization of the photocatalyst performance in the presence and absence of sacrificial agents will be discussed.

2.2.4 Characterization of the Photocatalyst Performance

The suitability of a semiconductor material for photocatalytic and photoelectrochemical applications can be evaluated by different techniques and analytical parameters. Basic characterization of the flat band potential U_{FB} and the donor density N_{D} is possible by detection of the capacitance in relation to an externally applied potential and application of the Mott Schottky equation (equation (2.7)). Several photoelectrochemical methods have been developed during the past decades, such as photocurrent measurements with detection of the overall current under dark and illuminated conditions while a defined potential range is scanned, or the determination of the incident photon to current conversion efficiency (IPCE), where at a constant potential, the wavelength dependent photocurrent is measured. The principles of these techniques will be discussed here.

Bulk lifetimes for minority carriers are usually very short (picoseconds for polycrystalline materials).^[70] With short minority carrier lifetimes, the minority carriers have only short diffusion paths before recombination in the bulk takes place. When charge carriers recombine within the SC region before they interact with electron-donating species from the solution, a non-ideal shape of the photocurrent is found with a delayed onset as shown in Figure 2.17 (see also Figure 2.18). A high recombination rate within the SC region leads to a shift of the onset potential compared to the flat band potential obtained by Mott Schottky measurement.

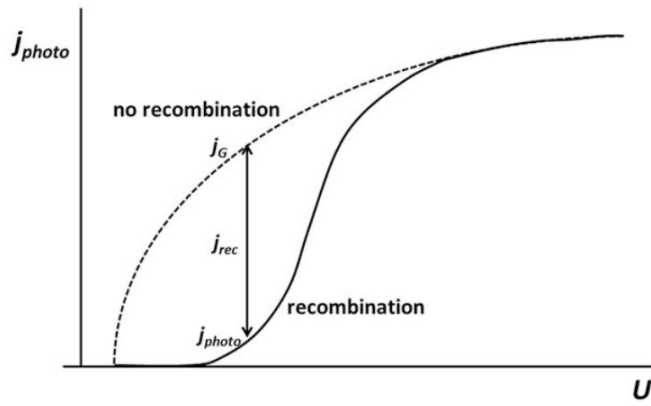


Figure 2.17: Shape of photocurrent curves under ideal conditions and with recombination in the SC layer (from S. Giménez *et al.*).^[71]

Typically, the relaxation time of minority carriers in an n-type semiconductor is around one nano-second. For water splitting, large energy barriers for the multistep process lead to much higher relaxation times (milliseconds to seconds).^[70] When intermittent light is used, transient effects can reveal if the electron transfer from the electrolyte is slow. The measured

photocurrent depends on the charging current J_{charge} , the recombination current J_{rec} and the charge transfer current J_{tr} , which is displayed in Figure 2.18 for an n-type photoelectrode.

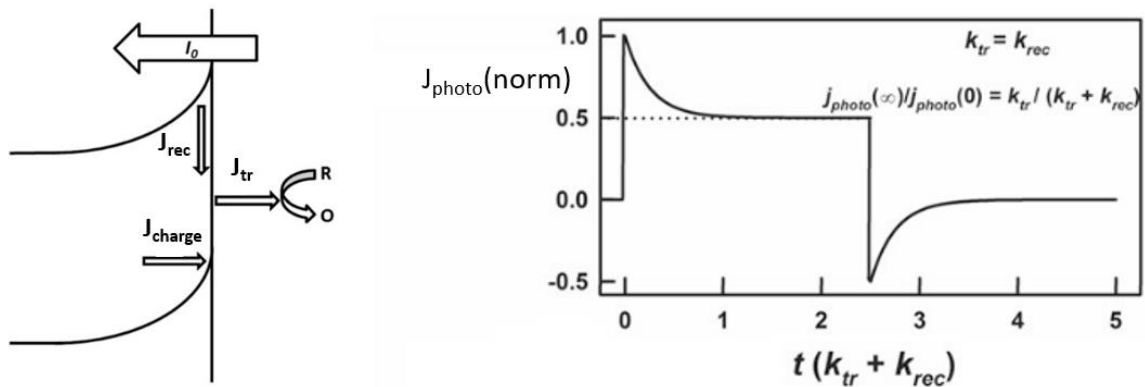


Figure 2.18: Current flowing at the semiconductor-electrolyte interface during illumination (left) and resulting transient photocurrent response (from Giménez *et al.*).^[71]

In case of an n-type semiconductor, the photocurrent is governed by hole transport and transfer processes. When the illumination starts, the number of holes at the surface h_{surf} is still low, which is why no recombination occurs. Due to slow electron transfer from the solution into the bulk J_{tr} has also not build up. This is why the initial photocurrent is determined by J_{charge} , which results from SC charging due to hole accumulation in free and also trapped states. With increasing h_{surf} , J_{rec} and J_{tr} increase, too. This changes C_{SC} and manifests in “spikes” with exponential decay until a steady state is reached, where the rate of holes diffusing into the SC region is in equilibrium with the rate of recombination and charge transfer into the electrolyte. The shape of such a transient photocurrent response is shown in Figure 2.18 in the right.

The currents flowing due to recombination (J_{rec}) and interfacial transfer (J_{tr}) are in equilibrium. They both proceed at the surface and depend on the concentration of holes near the surface h_{surf} . They can be described according to equations (2.26) and (2.27).

$$J_{\text{tr}} = q k_{\text{tr}} h_{\text{surf}} \quad (2.26)$$

$$J_{\text{rec}} = q k_{\text{rec}} h_{\text{surf}} \quad (2.27)$$

The rate constants for transfer and recombination reaction (k_{tr} and k_{rec}) follow (pseudo) first-order kinetics. They determine the steady state photocurrent J_{S} and the initial photocurrent J_0 . The mathematical context is given in equation (2.28).

$$\frac{J_{\text{S}}}{J_0} = \frac{k_{\text{tr}}}{k_{\text{tr}} + k_{\text{rec}}} \quad (2.28)$$

As the number of electrons at the surface depends on the band bending, with increasing bias the recombination decreases, leading to a higher steady state current. Theoretically, from transient photocurrent responses the rate constants for charge transfer and recombination can be calculated. Because side-effects during intermittent illumination can affect the practical measurement, intensity-modulated measurements on a DC current are recommended to obtain reliable values for k_{tr} and k_{rec} .^[70] Based on the Gärtner equation, the ideal external quantum efficiency (EQE), also known as incident photon-to-current conversion efficiency (IPCE), can be described.^[70]

$$\text{IPCE} = \frac{J_{\text{photo}}}{q I_0} = 1 - e^{-\left(\frac{w_{\text{sc}} \alpha}{1+L}\right)} = \frac{|J_{\text{photo}}| \cdot h \cdot c}{P_{\lambda} \cdot \lambda} \quad (2.29)$$

This takes into account the total electron amount generated by all incident photons, allowing an estimation of the maximum efficiency, which is possible under certain illumination conditions. As can be seen from equation (2.29), the IPCE depends on the incident photon flux I_0 , the absorption coefficient α , the minority carrier diffusion length L , the power of the light source P_{λ} and the wavelength λ . Minority carrier diffusion is usually dependent on the efficiency of removing the majority carriers from the system. If the electron transfer is too slow, both charge carrier transfer and recombination compete in the space charge region. For complex multistep reactions, where charge carrier accumulation is necessary (e.g. HER and OER), recombination is the limiting factor for high IPCE. Sacrificial agents (compare chapter 2.2.3.3) can be applied during IPCE measurements, which leads to a decreased recombination of charge carriers at the semiconductor surface due to a faster reaction course of the sacrificial agent compared to water molecules. Therefore, the overall detectable

photocurrent increases, which leads to higher IPCE values. This approach is used in photoelectrochemistry to identify the impact of hole accumulation and surface recombination on the PEC performance of absorber materials.

Furthermore, photocatalytic degradation of model compounds is a very common method for nanoparticle samples. Here, colored compounds like methylene blue or rhodamine B have been reported frequently, but also colorless systems like 4-chlorophenol are established model compounds.^[174–176] As the interactions between photocatalysts and model compounds influence the determined activity, it is advisable to perform more than one test reaction for assessment of the light-induced activity of absorber materials.

With colored model compounds, several issues need to be considered, such as the overlap in absorption of the model compound and the photocatalyst or electrostatic interaction.^[177] When using colored systems for degradation experiments under simulated solar light, a light-induced decomposition of the colorant can occur independently from photocatalytic processes. This is why reference experiments in the absence of the photocatalyst should be performed when colored compounds are photocatalytically degraded. Furthermore, most model compounds tend to adsorb on the photocatalyst surface, which is why an equilibration period in the dark should be preceded before the actual decomposition experiments. Besides, partial decomposition can already lead to a discoloration although a complete decomposition to CO₂ (mineralization) has not been achieved. Additional analysis techniques should support the optical detection to determine the degree of mineralization. The same principle applies to the degradation of model compounds under high energy UV light. Therefore, the activity of photocatalysts under visible light irradiation is recommended to be tested with model compounds, which do not absorb visible light, *e.g.* dichloroacetic acid.^[177] At the moment, there are only few standardized methods for determination of the photocatalytic activity. The ISO 10678:2010 test standard is based on the decomposition of methylene blue, which is not advisable as sole test reaction as discussed above.^[178] Nevertheless, the proposed values for model compound concentration and reactor setup can be used as guideline for the development of more suitable test reactions, as all these parameters influence the reaction course of model compound degradation as well. Furthermore, depending on the morphology of the photocatalyst and its applied amount, light scattering inside the reactor vessel can vary. To determine the efficiency of degradation experiments and allow comparison between different absorber materials, a reference value needs to be defined. For photocatalysis, the number of incident photons can be compared to the number of degraded molecules, resulting in the photonic efficiency ξ (equation (2.30)).

$$\xi = \frac{\text{degradation rate}}{\text{photon flux}} = \frac{k \cdot c_0 \cdot V}{A \cdot I_0} \quad (2.30)$$

The number of incident photons is highly dependent on the illuminated area A , the rate constant k , the initial dye concentration c_0 , and the volume of the reactor V . Therefore, the photon flux I_0 needs to be separately determined for every experimental setup and each light source due to changing light intensity Φ .

$$I_0 = \frac{\Phi \cdot \lambda}{N_A \cdot h \cdot c} \quad (2.31)$$

Here, several methods for actinometric analysis are known. For solid systems (*e.g.* solar cells), physical actinometers can be applied such as thermopiles, bolometers or photodiodes.^[179] For experiments in solution, chemical actinometers are more suitable. These need to exhibit a known quantum yield, a decomposition behavior directly proportional to the amount of incident photons and the decomposition products must be easily quantifiable.^[179] Since the development of chemical actinometry in 1825 by John Herschel, several compounds have been used, *e.g.* leucocyanides, uranyl oxalate, vanadium iron oxalate or malachite green, but as they are either toxic or already react in the dark, their application is rather complicated.^[179] Nowadays, ferrioxalate is the most common chemical actinometer and is recommended by the International Union of Pure and Applied Chemistry (IUPAC).^[180] Its decomposition can be followed by complexation with phenantroline.

2.3 Photoactive Materials

2.3.1 Non-Noble Transition Metal Absorber Materials

Since the first light-driven water splitting was reported, many years have passed, in which a strong interest in light-active semiconductors has developed. A very prominent photoactive semiconductor is titanium dioxide (TiO_2), which shows many modifications, of which the most prominent are rutile, anatase and brookite having slightly different band gaps and band positions.^[181] TiO_2 was already used in the first photoelectrochemical cell reported by Fujishima and Honda.^[56] Since then, intensive research on the photocatalytic properties of single-phase TiO_2 ^[182], multi-phase TiO_2 ^[183] and TiO_2 -based composites^[184] has been performed. Also, nanostructuring^[121,185], application of co-catalysts^[186], metal and non-metal doping^[85,187,188] have been studied. Although TiO_2 has been investigated intensively, its application for highly efficient solar water splitting is questionable because of its large band gap, reducing the amount of absorbable light from the solar spectrum. In addition, WO_3 was investigated as alternative material due to its non-toxicity, high chemical stability under acidic conditions and strong oxidizing power of its photogenerated holes.^[189,190] It exhibits a band gap of 2.5 – 2.8 eV^[189], which is

still quite large. Therefore, photocatalytic application is only possible under UV light and near-visible light illumination, which limits the application and solar light irradiation as well. Furthermore, no H_2 generation is possible with WO_3 without bias. Other well-investigated semiconductor systems are Cd-based chalcogenides. Here, studies especially focused on colloidal stability and faceting. A large variety of nanoparticle shapes and sizes, as well as core-shell structures and advanced hetero structures have been reported.^[191–194] The adjustability of the band gap due to the quantum size effect offers the possibility of tailor-made semiconductor systems. Furthermore, non-spherical and core-shell systems show more than one excitation maximum, making those systems also interesting for imaging and sensing applications. Despite the variety of accessible modifications, Cd-based materials are considered as harmful for health and environment and incur strong photocorrosion. Consequently, a widespread application of cadmium chalcogenides for solar water splitting is highly unlikely.

Another compound of interest is $BiVO_4$ with a band gap in the visible light regime and suitable band positions for OER (see Figure 2.19). Already 20 years ago, it was reported as potential candidate for photocatalytic OER.^[164] Just recently, there was a revival for $BiVO_4$ in the materials scientist community, as it is considered a highly promising photoanode material. Many studies showed that modification of the pure $BiVO_4$ material is needed for significant activity. The application in heterojunction and composite materials^[68,195–198], doping^[199], electrochemical treatment^[200] and decoration with co-catalysts^[201] or passivating surface layers^[202] was reported to improve the performance in photoelectrochemical and photocatalytic water splitting experiments. A study of Zachäus *et al.* revealed a significant grade of surface recombination being responsible for low-performing bare $BiVO_4$.^[203]

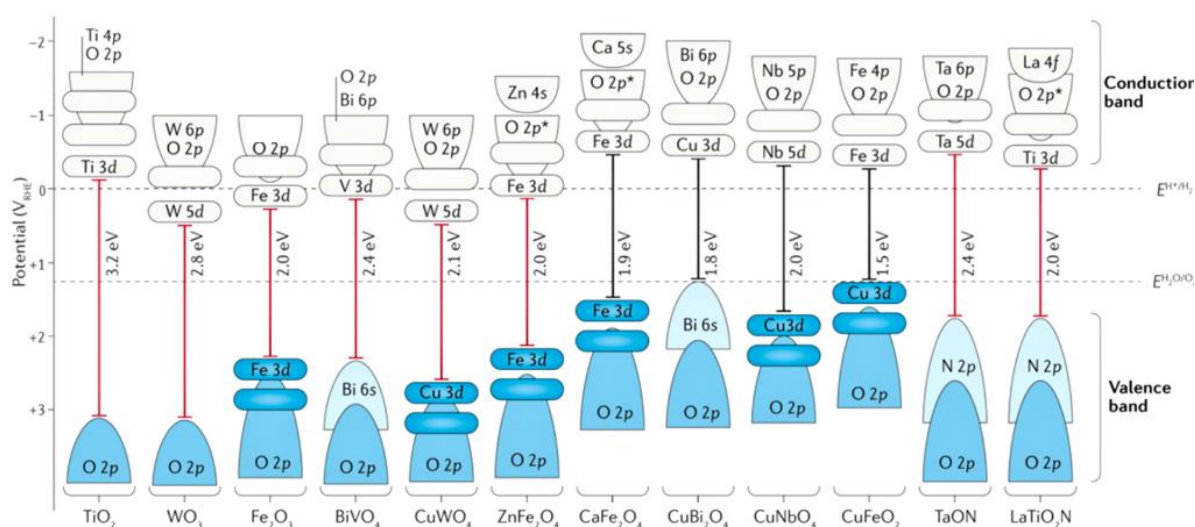


Figure 2.19: Band positions of various metal oxide semiconductors in relation to the redox potentials for water splitting (adapted from K. Sivula & R. van de Krol).^[204]

In Figure 2.19, the band positions of different metal oxide semiconductor materials are shown. Most semiconductors show only small overpotentials for hydrogen evolution reaction (HER), which would require additional bias under real reaction conditions. Some materials, such as WO_3 or $\alpha\text{-Fe}_2\text{O}_3$ are only suitable for oxygen evolution reaction (OER) without external bias. In contrast to TiO_2 or WO_3 , some metal oxide semiconductors, especially ternary systems, show smaller band gaps giving rise to visible light activity. Here, TaON , LaTiO_2N , CuNbO_4 and CaFe_2O_4 show matching band positions for overall water splitting. Non-metal nitrogen doping in TaON and LaTiO_2N introduced additional N 2p orbitals, shifting the valence band potentials to more negative values. This is an example of classical band gap engineering as discussed in chapter 2.2.3.

As the number of small band gap semiconductors already considered for solar water splitting is still limited, materials research is focusing on the discovery of novel suitable compounds. Furthermore, as ideal band positions for overall water splitting are rare, the interest in tandem devices covering both, OER and HER, has increased, as already discussed in chapter 2.2.1. Due to abundant elemental resources and low toxicity, iron-based materials have gained more and more attention during the past years in terms of photocatalytic applications. Already in Figure 2.19, the suitable orbital configurations of $\alpha\text{-Fe}_2\text{O}_3$ and ZnFe_2O_4 for OER and for overall water splitting in case of CaFe_2O_4 is displayed. In the following chapters, iron oxide semiconductors and ferrites in particular will be discussed in detail.

2.3.2 Iron Oxide Semiconductors as Photocatalysts

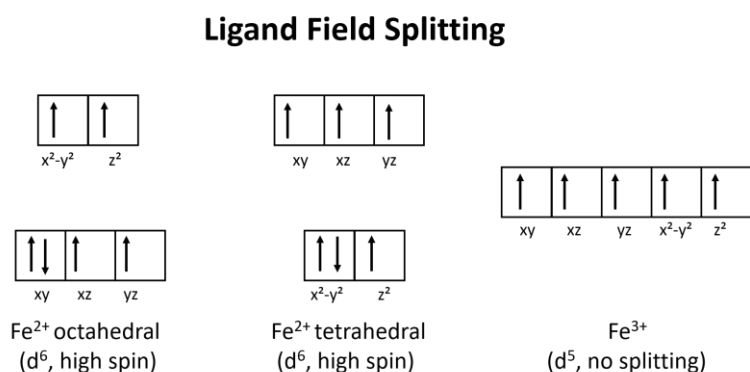


Figure 2.20: Ligand field splitting of Fe^{2+} and Fe^{3+} 3d orbitals.

In the elementary form, Fe has $3d^64s^2$ electron configuration. At its most common oxidation states of +2 and +3, a d^6 or d^5 configuration is the result. In many iron oxide materials, an octahedral coordination of oxygen around the iron ion is found, *e.g.* in hematite ($\alpha\text{-Fe}_2\text{O}_3$), maghemite ($\gamma\text{-Fe}_2\text{O}_3$) and goethite ($\alpha\text{-FeOOH}$). In some cases, also tetrahedral coordination can be found, *e.g.* in magnetite (Fe_3O_4 , spinel-type). In Figure 2.20, the preferred ligand field splitting of octahedral and tetrahedral complexes of Fe^{2+} or Fe^{3+} is shown.

During the past 20 years, mostly $\alpha\text{-Fe}_2\text{O}_3$ was discussed as photoactive material and potential candidate for solar water splitting due to its small band gap and non-toxic, low cost precursor

materials.^[53] Hematite has been tested for many applications *e.g.*, photocatalytic pollutant degradation, sensing, energy storage or in tandem cells.^[65,205–209]

However, several properties of $\alpha\text{-Fe}_2\text{O}_3$ limit its photocatalytic performance. Morin *et al.* and Bosman *et al.* found a low charge carrier mobility in $\alpha\text{-Fe}_2\text{O}_3$.^[210,211] Cherepy and co-workers reported very short diffusion pathways and lifetimes for α - and $\gamma\text{-Fe}_2\text{O}_3$.^[212] Furthermore, strong Fermi level pinning and passivation of the surface states combined with an unfavorable hole accumulation decrease the efficiency of $\alpha\text{-Fe}_2\text{O}_3$ photocatalyst.^[53,213] Therefore, single-compound $\alpha\text{-Fe}_2\text{O}_3$ devices are widely seen as unsuitable for solar water splitting. Nevertheless, a suitable combination with other materials in order to form heterojunctions or its application as sensitizer is still investigated.^[151,214] Recently, other iron oxide compounds called ferrites (MFe_2O_4) have gained interest in the photocatalysis community and will be discussed in the following chapter.^[17,18]

2.3.3 Ferrite Materials

Generally, ferrites with the chemical formula MFe_2O_4 (M = bivalent metal cation) can be divided into two classes: spinel-type ferrites with a cubic structure, where the oxygen atoms are packed in a cubic closed package (*ccp*) and the metal ions occupying tetrahedral and octahedral sites, and non-spinel type ferrites, which can have various geometries, *e.g.* tetragonal^[21] or orthorhombic^[22,157]. Both types show narrow band gaps < 2.2 eV, which makes them visible light active semiconductors.^[18] The general structure of cubic and orthorhombic spinel ferrites is shown in Figure 2.21. For cubic spinel

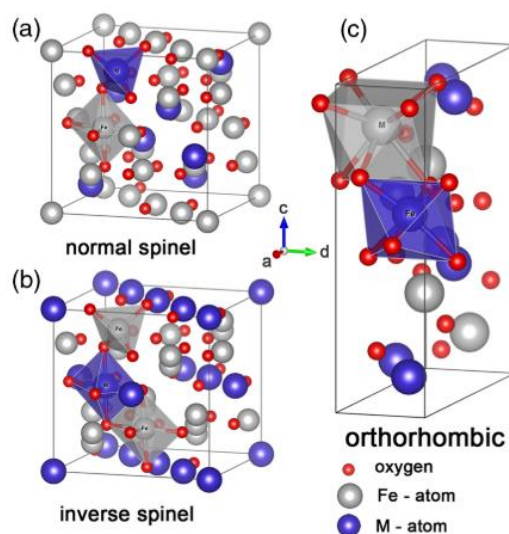


Figure 2.21: Structure of (a) normal spinel, (b) inverse spinel and (c) orthorhombic ferrites.^[18]

ferrites, the space group O_h^7 ($Fd3m$) describes the crystal structure.^[215,216] Due to electroneutrality, $\frac{1}{8}$ of all tetrahedral sites and $\frac{1}{2}$ of all octahedral sites are filled. As Fe^{3+} has a d^5 configuration and higher oxidation state, it favors octahedral coordination, which is why in a normal spinel, the Fe^{3+} occupy half of the octahedral sites and M^{2+} are located in the tetrahedral sites ($[\text{M}]^{\text{T}}[\text{Fe}_2]^{\text{O}}\text{O}_4$). In some cases, an inverted filling of $\frac{1}{4}$ of the octahedral sites with M^{2+} ions occurs, leading to Fe^{3+} ions in tetrahedral coordination ($[\text{Fe}]^{\text{T}}[\text{M}]^{\text{O}}[\text{Fe}]^{\text{O}}\text{O}_4$). These spinels are called inverse spinels. Most spinels show either mainly normal character or mainly inverse character. For ferrites, the degree of inversion δ is defined

2.3 Theoretical Background – Photoactive Materials

as the amount of Fe^{3+} located in tetrahedral coordination and described as $(\text{M}_{1-\delta}\text{Fe}_\delta)^{\text{T}}(\text{M}_\delta\text{Fe}_{2-\delta})^{\text{O}}\text{O}_4$.^[217] For Zn^{2+} , a normal spinel structure was reported in combination with Fe^{3+} ($\delta \approx 0$), while other ions like Ni^{2+} or Co^{2+} tend to form inverse spinels ($\delta \approx 1$). There are several factors, which influence the degree of inversion, namely the radii quotient ($r_{\text{cation}}/r_{\text{anion}}$), the Madelung constant and the ligand-field splitting energy. The ligand field splitting energy in tetrahedral geometry is smaller than for octahedral configuration ($\Delta_{\text{T}} \approx 4/9 \Delta_{\text{O}}$). Ions with d^{10} or d^5 configuration (e.g. Zn^{2+} , Fe^{3+}) have equal energies for tetrahedral and octahedral ligand fields. In the case of iron-based cubic spinels, a normal spinel is found when the M^{2+} has either d^5 or d^{10} , and to an inverse spinel if the M^{2+} has another d-orbital configuration. For bulk ZnFe_2O_4 , this predicts a normal spinel structure, which was also reported in literature.^[218] Furthermore, partial inversion ($0 < \delta < 1$) is possible and reported for MnFe_2O_4 , MgFe_2O_4 and nanosized ZnFe_2O_4 , which becomes partly inverse due to increasing disorder and number of oxygen vacancies in the nanoparticle.^[218] The degree of inversion in spinel ferrites can be influenced by choice of synthesis method, precursor components or post-synthetic annealing treatment.^[217–219]

A special feature of ferrites is their magnetic behavior resulting from Fe^{3+} ions in different ligand field splitting. In partially inverse spinels, the number of spin up Fe^{3+} on octahedral sites and spin down Fe^{3+} on tetrahedral sites is not equal, leading to ferromagnetic behavior. This makes ferrites also interesting for applications in medicine and microelectronics.^[220] When ferrites appear in nanosize, also superparamagnetic behavior is observed, as the particle size is in the range of the Weiss domains ($\approx 10^{-14} \text{ m}^3$).^[218,219,221,222] This leads to a magnetic response also in ferrite materials, which do not show magnetic behavior in the bulk material.^[219]

For decades, ferrite materials were investigated for their magnetic properties due to crystal field splitting (compare Figure 2.20). Just recently, they were also considered as photoactive materials, as they show small band gaps, which are dependent on the metal cation M within the compound.^[18,223]

Consulting different literature

sources, various sometimes even contradictory reports can be found for the band positions and semiconducting nature of MgFe_2O_4 and ZnFe_2O_4 .^[17,18] For ZnFe_2O_4 , variations up to 1 eV between different reports can be found, which is also visible from Figure 2.22.

ZnFe_2O_4 , MgFe_2O_4 and CaFe_2O_4 consist of non-toxic, cheap and earth-abundant elements, which makes them interesting for multiple commercial applications. For years, they have been investigated

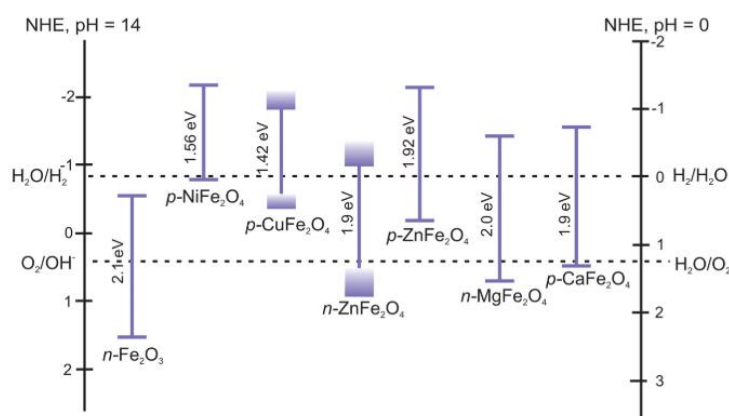


Figure 2.22: Band positions reported for different ferrite compounds.^[18]

in terms of biomedical applications^[224,225], electrical devices^[226], high-density information storage^[227], catalysis^[228], sensing^[205,229] and energy storage^[206,230,231]. Due to their band gaps in the visible light regime (1.9 eV – 2.0 eV)^[2,3,32], corresponding to a theoretical STH conversion efficiency of around 20 % (compare Figure 2.4)^[30,232], they have been in the focus of photocatalytic and photoelectrochemical research lately, especially with respect to photoelectrochemical water splitting.^[17,18]

The photocatalytic properties of bare and surface-functionalized MgFe₂O₄ and ZnFe₂O₄ nanoparticles have been reported for photocatalytic pollutant degradation of dyes (*e.g.* methylene blue, rhodamine B, crystal violet)^[233–236], organic compounds (*e.g.* 4-chlorophenol, acid orange)^[119,176] and heavy metal ions^[237] under illumination with UV or visible light. However, studies on the photocatalytic performance of stable aqueous colloids linked to the nature of the surfactant had not been reported at the beginning of the thesis work.

Besides, ZnFe₂O₄, MgFe₂O₄ and CaFe₂O₄ have been applied for PEC water splitting, but most reports are based on heterostructures of these ferrites combined with other semiconductor materials for photocatalytic and photoelectrochemical application. Here, porous thin films structures showed promising PEC performance. For example, Tingting *et al.*^[238] prepared highly ordered, inverse-opal-based nanostructure of ZnO/ZnFe₂O₄, and She and co-workers^[196] synthesized ZnO nanorod films decorated with BiVO₄/ZnFe₂O₄, to highlight some recent ZnFe₂O₄-based porous thin film approaches. Additionally, research on various p-n-heterojunction photoanodes containing CaFe₂O₄ has been performed lately, *e.g.* CaFe₂O₄/ZnFe₂O₄^[2], CaFe₂O₄/TaON^[239] and CaFe₂O₄/BiVO₄^[195] and CaFe₂O₄/α-Fe₂O₃^[151]. For CaFe₂O₄/BiVO₄ it was possible to demonstrate that the p-n-heterojunction formation reduces charge carrier recombination on the electrode surface, while the charge carrier recombination within the *bulk* material remains unchanged.^[195]

Investigations of single-phase ZnFe₂O₄, MgFe₂O₄ and CaFe₂O₄ thin films are still limited. A variety of sometimes quite expensive techniques has been explored for synthesis of phase-pure ZnFe₂O₄. These extend from synthesis of 3 μm ZnFe₂O₄ films by Tahir *et al.*^[240] and below 500 nm thick porous ZnFe₂O₄ films by Peeters *et al.*^[31], which were both synthesized using chemical vapor deposition (CVD), to high performing ZnFe₂O₄ nanorod arrays obtained after post-synthetic microwave-annealing and H₂ reduction treatment by Kim *et al.*^[107,232], and only 70 nm thick, dense ZnFe₂O₄ thin films obtained by Hufnagel *et al.*^[30] *via* atomic layer deposition.

Already in 1987, Matsumoto *et al.*^[241] described CaFe₂O₄ as a possible photocathode material for H₂ evolution. Since then, usually high temperatures (1100 – 1200 °C) were needed for synthesis of CaFe₂O₄ thin films made by solid state reaction (SSR).^[32,241] CaFe₂O₄ thin films on FTO-coated glass substrates were produced by pulsed laser deposition (PLD) at a much lower temperature of 550 °C by Cao *et al.*^[242], but the CaFe₂O₄ targets necessary for PLD were synthesized by SSR at 1100 °C. The

authors observed Fermi level pinning within bulk-CaFe₂O₄ and decomposition of the CaFe₂O₄ electrode during water splitting experiments.

In 2016, Shaheen^[243] and co-workers reported the synthesis of MgFe₂O₄/reduced graphene oxide composite for photocatalytic and photoelectrochemical application. They investigated methylene blue decomposition under visible light irradiation (420 nm) and observed 85 % mineralization after 30 min confirmed by TOC analysis. The higher PEC performance of the composite in comparison to single MgFe₂O₄ was attributed to suppressed charge carrier recombination. In the group of Weidong Shi, MgFe₂O₄ nanofibers and nanowires were investigated.^[244,245] Synthesis of the nanostructures was performed by electrospinning. They reported enhanced photocatalytic degradation of tetracycline under visible light with the as-prepared rod-in-tube nanofibers. By CVD-coating with MoS₂, a 1D heterostructure with enhanced charge carrier mobility was created, which showed 92 % photoelectrochemical tetracycline degradation after two hours. A photoelectrochemical hydrogen evolution rate of 5.8 mmol h⁻¹ g⁻¹ was found at 0.5 V bias under Xe arc lamp irradiation.

Just recently, Guijarro *et al.*^[246] used a β-FeOOH nanostructure as a solid precursor for MgFe₂O₄, CuFe₂O₄ and ZnFe₂O₄ thin films. The infiltration with metal nitrate solutions and subsequent calcination at 800 °C led to the formation of MgO, CuO and ZnO impurities, which were etched under highly acidic (7 M HNO₃ for CuFe₂O₄, MgFe₂O₄) or alkaline (5 M NaOH for ZnFe₂O₄) conditions. They were able to improve the performance by NiFe₂O_x deposition and post-synthetic calcination in H₂ atmosphere. Promising faradaic efficiencies (97 %), but also a high degree of bulk recombination and Fermi level pinning at 0.9 V_{RHE} were reported.

Not only mesoporous thin films, but also mesoporous powders show improved photocatalytic performance, *e.g.* higher hydroxyl radical formation for mesoporous hematite (α-Fe₂O₃)^[122] and improved removal of atrazine for magnetite (Fe₃O₄)^[247] mesoporous powders. Furthermore, mesoporous ferrite powders synthesized by hard and soft templating methods have shown improved reactivity towards As³⁺ and Cr⁶⁺.^[237,247,248] It was shown, that controlled porosity exceeds the efficiency of non-templated aggregated nanoparticle networks because of highly accessible pores and increased electron-hole separation.^[237]

The synthesis of ferrite nanoparticles has been reported employing numerous different techniques, *e.g.* sol-gel^[21,249,250], mechanochemical^[217,251–253], hydrothermal^[254–258], co-precipitation^[105], microwave-assisted^[106,219,251,259] and high-temperature^[26,27,260] routes, mostly under inert gas atmosphere, but only few authors take account of minor impurities of iron oxide by-phases within their samples using Raman spectroscopy in addition to X-ray diffraction (XRD) analysis.

The stabilization of magnetic nanoparticles, such as ferrite nanoparticles, in non-aqueous and aqueous solution could improve their handling due to lower risk of exposure to nanoparticle dusts. Furthermore, ferrofluids have proven to be interesting for application in exclusion seals, sensors,

dampers and shock absorbers, for magnetic resonance imaging contrast enhancement and as cell labelling agent because of their superparamagnetic behavior and easy liquid handling.^[261–265]

For direct synthesis of stable colloidal solutions of magnetic nanoparticles, a variety of approaches was used. Many stabilizing agents have been applied such as long-chain-organic molecules (oleylamine, oleic acid, dimercaptosuccinic acid, sodium dodecylsulfate, citric acid)^[27,236,260,266–272] and different polymers (polyvinylpyrrolidone, polyvinyl alcohol, Igepal® CO 520, polyethylene glycol).^[273–275] Again, most reports lack a closer look onto the phase purity of their materials. Some researchers reported impurities of α -Fe₂O₃ and ZnO or MgO after synthesis of ferrite colloids.^[275] These impurity compounds can act as recombination sites and suppress the photoactivity of the prepared ferrite materials, or could even boost the activity due to heterojunction formation.

Based on the promising literature reports concerning ferrite nanostructures in photocatalytic and photoelectrochemical applications, in this thesis a synthesis technique for highly mesoporous ZnFe₂O₄, MgFe₂O₄ and CaFe₂O₄ thin films directly from solution and in a nanoparticle-based approach *via* dip coating was developed. As basis for mesoporous thin films directly from solution, the report of Haetge and co-workers was chosen.^[5] They reported the formation of ordered mesopores in MFe₂O₄ thin films (M = Cu, Ni, Zn, Co, Mg) by application of a polymer soft template. With the poly(ethylene-co-butylene)-block-poly(ethylene oxide) di-block copolymer, polymer micelles form in solution, which arrange during evaporation induced self-assembly (EISA) to build ordered spherical pores. The pore walls are crystallized at relatively low temperatures (T < 660 °C). However, the photoelectrochemical properties of the synthesized films were not investigated.

The selected synthesis approaches for mesoporous ferrites and ferrite nanoparticles will be optimized and their application in photocatalysis and photoelectrochemistry will be elucidated in the following chapters.

3 Experimental Section

3.1 Chemicals

All chemicals used for synthesis, stabilization or analysis purposes are listed below. They were used without further purification and were stored under proper conditions according to the supplier's notes.

Table 3.1: List of organic solid chemicals.

Chemical name	Abbreviation	Chemical Formula	Purity grade	Supplier	CAS-number
1,2-dodecanediol	-	C ₁₂ H ₂₆ O ₂	> 90 %	TCI	1119-87-5
betaine hydrochloride	BETA	C ₅ H ₁₂ NO ₂ Cl	> 98 %	TCI	590-46-5
calcium acetylacetonate	Ca(acac) ₂	C ₁₀ H ₁₄ CaO ₄	> 98 %	TCI	19372-44-2
cetyltrimethyl ammonium chloride	CTAC	C ₁₉ H ₄₂ NCl	-	SIGMA ALDRICH	112-02-7
citric acid monohydrate	CIT	C ₆ H ₁₀ O ₈	> 99.5 %	CARL ROTH	5949-29-1
iron(III) acetylacetonate	Fe(acac) ₃	C ₁₅ H ₂₁ FeO ₆	> 99 %	ACROS	14024-18-1
magnesium acetylacetonate	Mg(acac) ₂	C ₁₀ H ₁₄ MgO ₄	> 98 %	TCI	14024-56-7
zinc acetylacetonate	Zn(acac) ₂	C ₁₀ H ₁₄ ZnO ₄	> 96 %	TCI	14024-63-6

Table 3.2: List of inorganic solid chemicals.

Chemical name	Chemical Formula	Purity grade	Supplier	CAS-number
boron nitride	BN	98 %	SIGMA ALDRICH	10043-11-5
calcium nitrate tetrahydrate	$\text{Ca}(\text{NO}_3)_2 \cdot 4 \text{H}_2\text{O}$	99.98 %	ALFA AESAR	13477-34-4
iron(III) nitrate nonahydrate	$\text{Fe}(\text{NO}_3)_3 \cdot 9 \text{H}_2\text{O}$	99.99 %	SIGMA ALDRICH	7782-61-8
lanthanum hexaboride	LaB_6	99.5 %	ALFA AESAR	12008-21-8
magnesium nitrate hexahydrate	$\text{Mg}(\text{NO}_3)_2 \cdot 6 \text{H}_2\text{O}$	99 %	SIGMA ALDRICH	13446-18-9
sodium chloride	NaCl	99.5 %	CARL ROTH	7647-14-5
sodium hydroxide	NaOH	> 90 %	SIGMA ALDRICH	1310-73-2
sodium sulfate	Na_2SO_4	> 99 %	J.T. BAKER	7757-82-6
sodium sulfite	Na_2SO_3	> 98.5 %	ACROS	7757-83-7
zinc nitrate hexahydrate	$\text{Zn}(\text{NO}_3)_2 \cdot 6 \text{H}_2\text{O}$	> 99 %	CARL ROTH	10196-18-6

Table 3.3: List of inorganic and organic liquid chemicals.

Chemical name	Abbreviation	Purity grade	Supplier	CAS-number
1,2-dichlorobenzene	DCB	> 99 %	MERCK	95-50-1
1-phenylethanol	1-PE	> 99 %	SIGMA ALDRICH	98-85-1
2-methoxyethanol	2-ME	>99.3 %	ABCR	109-86-4
acetone	-	99 %	VWR	67-64-1
ammonia	-	28 wt%	FLUKA	7664-41-7
dibenzyl ether	DBE	>98 %	SIGMA ALDRICH	103-50-4
diethyl ether	Et_2O	99.9 %	VWR	60-29-7
ethanol	EtOH	>99.8 %	ACROS	64-175
hydrogen peroxide	H_2O_2	30 wt%	SIGMA ALDRICH	7722-84-1
methanol	MeOH	> 99.85 %	CHEMSOLUTE	67-56-1
N,N-dimethylformamide	DMF	99 %	ACROS	68-12-2
oleic acid	OA	90 %	ABCR	112-80-1
oleylamine	OLA	70 %	SIGMA ALDRICH	112-90-3
tetraethyl orthosilicate	TEOS	99.99 %	VWR	78-10-4
toluene	-	99 %	ABCR	108-88-3

Table 3.4: List of polymers.

Abbreviation	Chemical name	Chemical Formula	Molar Weight	Supplier	CAS-number
PVP	poly(vinylpyrrolidone)	$H-(C_6H_9NO)_{92}-H$	10000	ALFA AESAR	9003- 39-8
Pluronic® F127	poly(ethylene oxide)- <i>b</i> - poly(propylene oxide)- <i>b</i> -poly(ethylene oxide)	$H-(C_2H_4O)_{101}-(C_3H_6O)_{65}-$ $(C_2H_4O)_{101}-H$	12600	SIGMA ALDRICH	9003- 11-6
PIB3000	poly(isobutylene)- <i>b</i> - poly(ethylene oxide)	$H-(C_4H_8)_{52}-(C_6H_4)-O-$ $(C_2H_4O)_{54}-H$	3000	BASF SE	-
PIB6000	poly(isobutylene)- <i>b</i> - poly(ethylene oxide)	$H-(C_4H_8)_{107}-(C_6H_4)-O-$ $(C_2H_4O)_{100}-H$	6000	BASF SE	-
PIB10000	poly(isobutylene)- <i>b</i> - poly(ethylene oxide)	$H-(C_4H_8)_{178}-(C_6H_4)-O-$ $(C_2H_4O)_{227}-H$	10000	BASF SE	-

3.2 Synthesis Techniques

3.2.1 Nanoparticle Synthesis

3.2.1.1 High-Temperature Reflux Synthesis

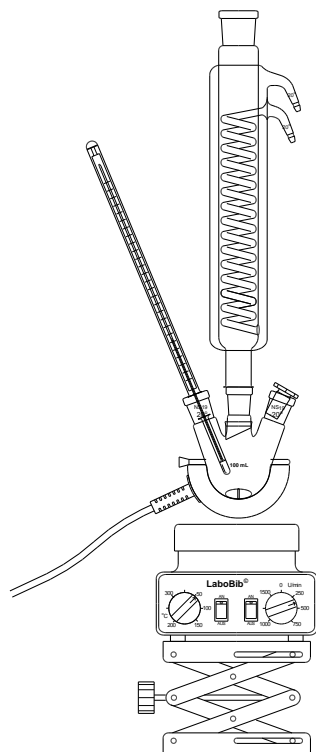


Figure 3.1: Reaction setup for standard reflux synthesis.

To synthesize ferrite nanoparticles under established reflux conditions (so-called batch conditions), a 3-neck-roundbottom flask was equipped with a condenser, temperature sensor and a magnetic stirring bar (see Figure 3.1). The used amount of acetylacetonate (acac) precursors, reaction times and temperatures can be found in Table 3.5. In a typical synthesis, $A(\text{acac})_2$ ($A = \text{Zn}, \text{Mg}$) was pre-dissolved in 15 mL 1-PE under ultrasonic treatment for 15 min resulting in a concentration of $0.033 \text{ mmol mL}^{-1}$. Then, the clear solution was added to an adequate amount of $\text{Fe}(\text{acac})_3$ to obtain the molar ratio A:B as 1:2. The solution was vigorously stirred at $40 \text{ }^\circ\text{C}$ under ambient conditions until the solid compounds were fully dissolved. Afterwards, the reaction mixture was heated to reflux ($206 \text{ }^\circ\text{C}$) as fast as possible and was kept at this temperature for one hour. After the reaction time, the solution was allowed to cool down to room temperature. Then, the solution was mixed with excess of diethyl ether (Et_2O) and centrifuged at 7000 rpm for 10 min to precipitate the synthesized nanoparticles. The supernatant was discarded and the sediment was redispersed in 15 mL of

ethanol (EtOH). Then, another 20 mL of Et_2O were added and the mixture was centrifuged at 7000 rpm for 10 min to wash off unreacted precursor residues from the nanoparticles' surface. This washing procedure was repeated three times before the solid was dried in an oven at $100 \text{ }^\circ\text{C}$ for 12 hours. The resulting dry solid was grinded to obtain a fine powder.

Table 3.5: Reaction conditions for batch synthesis of AFe_2O_4 nanoparticles.

Desired Compound	$T / ^\circ\text{C}$	$t_{\text{syn}} / \text{min}$	V / mL	n_A / mmol	$n_{\text{Fe}} / \text{mmol}$
ZnFe_2O_4	206 (reflux)	60	15	0.5	1
MgFe_2O_4	206 (reflux)	60	15	0.5	1

3.2.1.2 Microwave-Assisted Nanoparticle Synthesis

Parallel to the nanoparticle synthesis under reflux conditions, synthesis was also investigated under microwave irradiation. With microwaves the solution mixture is heated directly, which allows better heat penetration and faster reactions courses. In Figure 3.2, both heating principles are compared. The used amount of precursors, reaction times and temperatures can be found in Table 3.6.

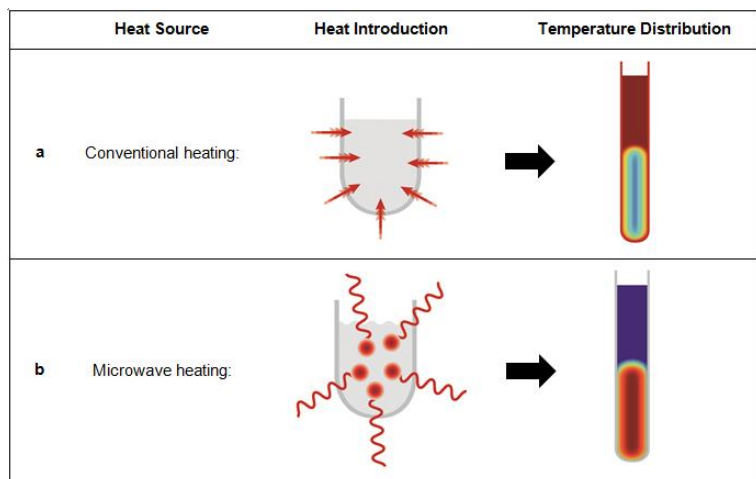


Figure 3.2: Heat distribution in conventional heating and microwave heating.^[276]

For this purpose, $A(acac)_2$ ($A = Zn, Mg, Ca$) was pre-dissolved in 12 mL of *rac*-1-phenylethanol (1-PE) under ultrasonic treatment. The solution was transferred into a second vessel containing a defined amount of $B(acac)_3$ ($B = Fe, Cr$). The vessel of compound $A(acac)_2$ was rinsed with another 3 mL of 1-PE, which were added to the main solution. The reaction

mixture was treated in an ultrasonic bath for another 10 min to dissolve all solid components. Then, the solution was transferred into a borosilicate glass microwave vessel equipped with a stirring bar and was sealed with a Teflon[®]-lined cap (ANTON PAAR). The reaction vessel was placed inside a *Monowave 400* (ANTON PAAR), was heated to the desired reaction temperature as fast as possible under vigorous stirring (300 rpm) and was kept at this temperature for 30 min. After the reaction time, the mixture was allowed to cool down to room temperature. The work up was pursued as described in 3.2.1.1.

Table 3.6: Reaction conditions for microwave-assisted synthesis of AB_2O_4 nanoparticles.

Desired Compound	$T / ^\circ C$	t_{syn} / min	V / mL	$n_A / mmol$	$n_B / mmol$
$ZnFe_2O_4$	275	30	15	0.5	1.0
$MgFe_2O_4$	275	30	15	1.0	1.0
$CaFe_2O_4$	275	30	15	0.5	1.0

3.2.1.3 Post-Synthetic Heat Treatment

Post-synthetic calcination in air of as-prepared microwave-derived ZnFe_2O_4 nanoparticles was performed in a muffle furnace (NABERTHERM L311). Grinded powder samples were filled into a ceramic crucible and placed inside the muffle furnace at room temperature. The samples were heated to either 400 °C, 500 °C or 600 °C, respectively, with a heating rate of 10 °C min^{-1} . After maintaining the maximum temperature for one hour, samples were allowed to cool down to room temperature inside the muffle furnace. The calcined samples were grinded in a mortar to obtain fine powders.

3.2.2 Nanoparticle Functionalization

3.2.2.1 In situ Steric Stabilization

To obtain stable nanoparticle colloids, surface functionalization of the ferrite surface is necessary. This way, stable colloids in polar or non-polar solvents can be obtained.

For non-polar colloidal stabilization, the *in situ* functionalization with common ligands oleylamine (OLA) and oleic acid (OA) was investigated. One approach was the adaption of a procedure reported by Sun and co-workers for microwave synthesis.^[27] For this, a mixture of zinc acetylacetonate ($\text{Zn}(\text{acac})_2$, 158.0 mg) or magnesium acetylacetonate ($\text{Mg}(\text{acac})_2$, 133.5 mg), iron(III)-acetylacetonate ($\text{Fe}(\text{acac})_3$, 423.4 mg), 1,2-dodecanediol (2.0 g), oleylamine (OLA, 2 mL), oleic acid (OA, 2 mL) and dibenzyl ether (20 mL) was prepared, which gave a molar ratio of 1:2:15.2:27:28.5:286. This mixture was treated in an ultrasonic bath, resulting in a dark red solution. The mixture was processed either under reflux conditions or under microwave heating conditions as described above (see chapters 3.2.1.1 and 3.2.1.2). In a typical batch reaction, the solution was heated to 280 °C under vigorous stirring and was kept at this temperature for three hours before cooling down. In a microwave-assisted approach, 15 mL of the reaction solution were treated according to the heating program described under 3.2.1.2. After the reaction, excess of methanol (MeOH) was added to the turbid black solution to precipitate the nanoparticles. Centrifugation at 6000 rpm was followed by redispersion in toluene. The resulting colloid was washed another three times before a final redispersion in toluene resulted in stable colloidal solutions ($\approx 40 \text{ mg mL}^{-1}$).

Another approach to perform *in situ* surface functionalization with OLA and OA was taken by modification of the procedure described under 3.2.1.1. Here, addition of 4.5 mL of OLA and 4.5 mL of OA to the synthesis mixtures was performed. The work up was done as described above for OLA/OA-functionalized nanoparticles.

For direct synthesis of polar stable colloidal solutions, the microwave-assisted synthesis (3.2.1.2) was modified again. Aqueous colloidal solutions were produced by addition of polyvinylpyrrolidone

(PVP) to the reaction mixtures. The PVP-containing reaction mixture was fully dissolved by ultrasonic treatment. A PVP amount of 1.5 g (100 mg mL^{-1}) was chosen as standard value. For production of PVP-encapsulated ZnFe_2O_4 nanoparticles, also lower PVP amount of 0.15 g (10 mg mL^{-1}), 0.5 g (33 mg mL^{-1}) and 1.0 g (66 mg mL^{-1}) were applied to investigate the influence of polymer amount on the colloidal stability.

3.2.2.2 *Post-synthetic Steric Stabilization*

Post-synthetic functionalization was realized by reflux treatment of as-synthesized nanoparticles in the presence of OLA and OA. In detail, 20 mg ferrite nanoparticles were mixed with 10 mL of toluene, 1 mL of OLA and 1 mL of OA. The solution was kept at $110 \text{ }^\circ\text{C}$ for 48 hours before allowing to cool down. The nanoparticles were precipitated by addition of excess EtOH. The redispersion in 5 mL of toluene followed by washing with MeOH was repeated three times to remove excess ligands. The nanoparticles were then redispersed to obtain stable colloids in toluene (8 mg mL^{-1}).

3.2.2.3 *Post-synthetic Electrostatic Stabilization*

By modifying a procedure by Patil *et al.*^[277], a direct stabilization of nanoparticles in water can be achieved. For this purpose, an aqueous solution of betaine hydrochloride (BETA, 2 wt%) was prepared. The solution was mixed with dry nanoparticles in the ratio of 8 mg mL^{-1} . The mixture was mixed on a shaker for at least 10 hours to obtain a stable colloid. By careful precipitation with acetone under magnetic attraction, the functionalized nanoparticles were washed three times and redispersed in distilled water.

Another approach for electrostatic stabilization was developed according to the report of Lattuada *et al.*^[270] Here, a solvent mixture of N,N-dimethylformamide, 1,2-dichlorobenzene and citric acid monohydrate in the molar ratio of 1:162:111 was prepared. Then, nanoparticles were added in the ratio of 8 mg mL^{-1} solution. The mixture was kept at $100 \text{ }^\circ\text{C}$ for 24 hours before precipitation with Et_2O . To remove excess surfactants, the nanoparticles were washed three times with acetone before being redispersed in distilled water (8 mg mL^{-1}).

3.2.3 Mesoporous Thin Film Preparation

3.2.3.1 Sol-Gel Assisted Thin Film Synthesis

Mesoporous AFe_2O_4 thin films ($A = Zn, Mg, Ca$) were prepared via sol-gel-based dip coating taking advantage of the evaporation induced self-assembly of polymeric micelles. The polymer was varied, using either block-copolymer poly(ethylene oxide)-*b*-poly(propylene oxide)-*b*-poly(ethylene oxide) (Pluronic® F127, abbr. PLU, SIGMA ALDRICH), or block-copolymer poly(isobutylene)-*b*-poly(ethylene oxide) in three molecular weights of the polyisobutylene unit ($MW_{PIB} = 3000$, $MW_{PIB} = 6000$ or $MW_{PIB} = 10000$; abbr. either PIB3000, PIB6000 or PIB10000, BASF SE). Thin films were coated on various substrates, namely silicon (100) wafers (SILTRONIC), fluorine-doped tin oxide (FTO) coated Pilkington TEC glass slides (XOP GLASS) and indium tin oxide (ITO) coated quartz glass slides (PRÄZISIONS GLAS & OPTIK). The schematic procedure of mesoporous thin film preparation is shown in Figure 3.3.

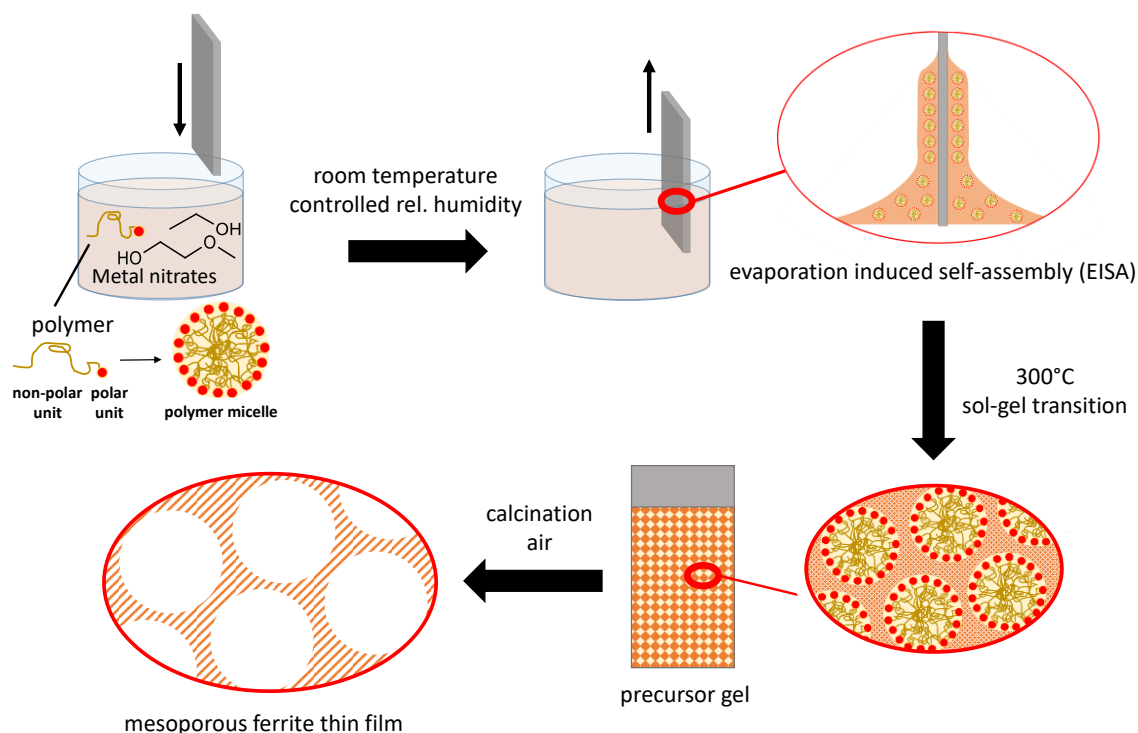


Figure 3.3: Schematic dip coating synthesis of mesoporous ferrite thin films.

Typically, metal nitrate hydrate salts of $A(NO_3)_2$ ($A = Ca, Mg, Zn$) were dissolved in 0.6 mL ethanol (EtOH) by mixing on a shaker for 30 min (for exact amounts see Table 3.7, Table 3.8 and Table 3.9). In the same fashion, iron(III) nitrate nonahydrate was dissolved in 0.2 mL EtOH and 0.4 mL 2-methoxyethanol (2-ME) in a second vessel. Parallel to this, 45 mg of polymer was dissolved in 0.2 mL 2-ME and 0.9 mL EtOH under ultrasonic treatment for 30 minutes. After all precursors were fully dissolved, the solutions were mixed and the mixture was treated in an ultrasonic bath for another

3.2 Experimental Section – Synthesis Techniques

5 min. The precursor solution was filtered with a syringe filter (PTFE, 0.2 μm) into a dip coating vessel to remove large solid components. The vessel was then placed inside a closed, humidity controlled chamber to achieve constant conditions of the surrounding atmosphere for the dip coating procedure. The relative humidity was set to 10 %, but varied until the end of the dip coating process between 10 – 15 %. Thin films were coated on various substrates by dipping them into the precursor solution and direct withdrawal from it, both with a constant speed of 8 mm s⁻¹. The as-coated substrates remained inside the chamber for three minutes before being transferred into a muffle furnace (NABERTHERM L311), which was pre-heated to 130 °C. The temperature was kept for three hours to guarantee well-dried thin films and aging of the formed sol. Subsequently, the films were heated to 300 °C with a heating rate of 0.5 °C min⁻¹. During heat treatment at 300 °C for 12 hours, the precursor sol formed into a solid metal oxide hydroxide gel. This gel was then calcined at various temperatures to obtain the desired mesoporous AFe₂O₄ thin films.

Table 3.7: Precursor mixture for mesoporous ZnFe₂O₄ film synthesis.

Precursor	m / mg	n / mmol	Solvent
Zn(NO ₃) ₂ · 6 H ₂ O	128.2	0.439	0.6 mL EtOH
Fe(NO ₃) ₃ · 9 H ₂ O	348.3	0.862	0.2 mL EtOH, 0.4 mL 2-ME
polymer	45	-	0.9 mL EtOH, 0.2 mL 2-ME

Table 3.8: Precursor mixture for mesoporous MgFe₂O₄ film synthesis.

Precursor	m / mg	n / mmol	Solvent
Mg(NO ₃) ₂ · 6 H ₂ O	98.9	0.439	0.6 mL EtOH
Fe(NO ₃) ₃ · 9 H ₂ O	348.3	0.862	0.2 mL EtOH, 0.4 mL 2-ME
Pluronic® F127	45	-	0.9 mL EtOH, 0.2 mL 2-ME

Table 3.9: Precursor mixture for mesoporous CaFe₂O₄ film synthesis.

Precursor	m / mg	n / mmol	Solvent
Ca(NO ₃) ₂ · 6 H ₂ O	203.6	0.431 or 0.560	0.6 mL EtOH
Fe(NO ₃) ₃ · 9 H ₂ O	348.3	0.862	0.2 mL EtOH, 0.4 mL 2-ME
polymer	45	-	0.9 mL EtOH, 0.2 mL 2-ME

3.2.3.2 Infiltration with SiO₂ Scaffold

To stabilize the mesopores, which were originally formed during short term calcination, and enabling crystal defect healing during long term calcination at the same time, PLU- and PIB-derived mesoporous ZnFe₂O₄ thin films, which had been calcined at 600 °C without holding time, were infiltrated with SiO₂ according to procedures reported by Ogawa *et al.*^[278] and Brillet *et al.*^[138] For this, 100 mL of MeOH were mixed with 0.21 g of hexadecyltrimethyl ammonium chloride (C₁₆TAC), 17.7 g of deionized water, 9 mL of ammonia (25 %) and 0.37 mL of tetraethyl orthosilicate (TEOS) to achieve a molar ratio of 1500:0.4:774:72:1. After cooling the infiltration solution to 0 °C, the mesoporous thin films were immersed in the solution for 18 hours at 0 °C. Afterwards, the thin film samples were removed from the turbid solution, extensively rinsed with MeOH and subsequently dried at room temperature. Then, the samples containing SiO₂ scaffold were calcined for 12 hours at 600 °C in air with a heating rate of 10 °C min⁻¹. Removal of the hard template after calcination was achieved by storing the SiO₂-containing samples in 5 M NaOH for 10 min. Afterwards, the samples were washed thoroughly with deionized water and dried at room temperature.

3.2.4 Thin Films Derived from Nanoparticles

For preparation of mesoporous thin films derived directly from nanoparticles, spin coating of PVP- coated nanoparticles under humidity control was employed. This is schematically shown in Figure 3.4.

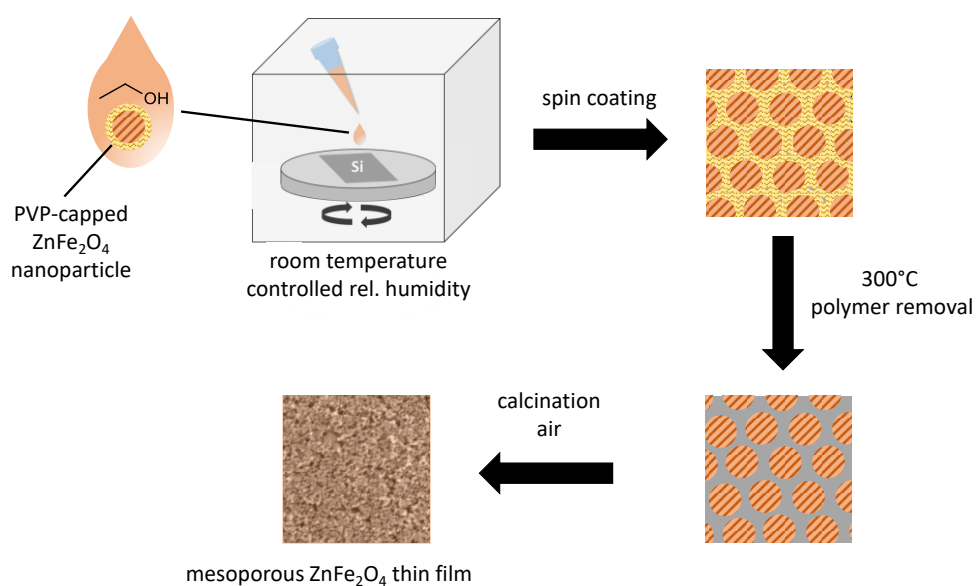


Figure 3.4: Schematic spin coating synthesis of mesoporous ZnFe₂O₄ thin films.

As-prepared, PVP-coated ZnFe₂O₄ nanoparticles were dispersed in EtOH in a defined concentration (18.5 mg mL⁻¹). The desired substrate was fixated on the rotation disk inside the spin coating chamber. The relative humidity was set to 10 %. Then, 200 μL of the solution was drop-casted when the rotation of the substrate was started. After rotation with 1500 rpm for 60 seconds, the rotation was stopped. The coated substrate remained inside the chamber for two more minutes before being transferred into a pre-heated muffle furnace (130 °C). After four hours at 130 °C, the substrate was heated to 300 °C (2 °C min⁻¹) and kept at the maximum temperature for 3 hours. The subsequent calcination was performed at 500 °C, 600 °C or 700 °C with a heating rate of 10 °C min⁻¹ and a holding time of 3 or 12 hours.

3.2.5 Mesoporous Powder Preparation

The synthesis of the precursor mixture for preparation of mesoporous powders was performed identically to 3.2.3.1. Block-copolymers Pluronic® F127 (abbr. PLU, SIGMA ALDRICH) or poly(isobutylene)-*b*-poly(ethylene oxide) (PIB3000, abbr. PIB, BASF SE) with a molecular weight of MW_{PIB} = 3000 for the polyisobutylene unit was used as porogens. The prepared precursor solution was filled into a ceramic crucible and placed inside a muffle furnace (NABERTHERM L311) at room temperature. The furnace was slowly heated (5 °C min⁻¹) to 75 °C and maintained at this temperature for 2 hours to remove the ethanol solvent. Then, the temperature was increased to 130 °C by 0.3 °C min⁻¹. For 3 hours, the mixture was kept at 130 °C to form the precursor sol. Afterwards, the temperature was increased by 0.5 °C min⁻¹ to 300 °C and kept for 12 hours to receive the precursor gels. In a second step, the obtained gels were calcined with a heating rate of 10 °C min⁻¹ for 12 hours at 500 °C, 550 °C or 600 °C, respectively.

4 Characterization Techniques

4.1 X-Ray Methods

4.1.1 Powder X-Ray Diffraction

X-ray powder diffraction (XPRD) analysis was performed using a *X'Pert Pro diffractometer* (PANALYTICAL) with Cu K α radiation ($\lambda = 1.5406 \text{ \AA}$) and Bragg-Brentano geometry. The patterns were recorded from 15° to 75° 2θ with a step size of 0.033° , an emission current of 40 mA and an acceleration voltage of 40 kV. For data evaluation regarding phase purity PANALYTICAL *X'Pert HighScore Plus* software (Version 3.0.5) in combination with reference patterns from the *Crystallography Open Database* (COD)^[279] was used. For quick estimation of the average crystallite size L_a , the Scherrer equation was employed.^[280]

$$L_a = \frac{K_{\text{Bragg}} \cdot \lambda}{FWHM \cdot \cos \theta} \quad (4.1)$$

Here, $K_{\text{Bragg}} = 0.93$ is the Bragg constant, $FWHM$ is the full width at half maximum and θ is the Bragg angle, both used in radian measure.

4.1.2 Grating Incidence X-Ray Diffraction

Grating incidence X-ray diffraction (GIXRD) analysis was done on a *X'Pert Pro MRD* (PANALYTICAL) equipped with a parallel plate collimator (0.27°) and Cu W/Si mirror using an Empyrean Cu LFF HR X-ray tube (Cu K α radiation, $\lambda = 1.5406 \text{ \AA}$). For all measurements, a 1.4 mm anti-scatter slit, a 0.04 rad soller slit, a $1/16^\circ$ divergence slit and a 2 mm mask were mounted. Patterns were recorded from 25° to 65° with an emission current of 40 mA and an acceleration voltage of 40 kV. *In situ* measurements at elevated temperatures in synthetic air (80 % N $_2$, 20 % O $_2$) were realized by using a domed hot stage (*DHS 1100*, PANALYTICAL). Samples were heated to the desired temperatures with a heating rate of $10 \text{ }^\circ\text{C min}^{-1}$.

4.1.3 Rietveld Refinement

To perform Rietveld refinement, an instrumental resolution file (IRF) is needed to include instrumental line broadening effects into the calculations. For this purpose, XRD patterns of a highly-pure lanthanum hexaboride (LaB $_6$) standard substance were recorded.

The crystallite sizes and strains of samples can be evaluated using Rietveld refinement. For this purpose, the free software *FullProf*, Version 2.05 (2011) was used.^[281] The refinement procedure was performed in accordance with the guidelines formulated by the International Union of Crystallography Commission on Powder Diffraction.^[282] Peaks were fitted with a Thompson-Cox-Hastings Pseudo-Voigt profile function, which consists of Gaussian and Lorentzian contributions to the fit function. A 6-coefficient polynomial background function was used for background determination. Gaussian parameter U_{Gauss} describing the full width at half-maximum (FWHM) and parameter Y_{Gauss} describing the Lorentzian part of the peak shape, were refined to determine the line broadening caused by crystal size effects. As IRF-files were provided, no refinement of Gaussian and parameters V_{Gauss} and W_{Gauss} was performed. Due to very small crystallite sizes, Lorentzian parameter X_{Gauss} was not refined. Crystallographic Information Files (CIF)^[283] obtained from the crystallographic open database (COD) were used for $ZnFe_2O_4$ (COD ID 2300615)^[284] and $MgFe_2O_4$ (COD ID 9007273)^[285]. All shift relaxation factors were chosen to be 0.8.

In a typical procedure, first the instrumental zero offset, background (6-coefficient polynomial) and scale coefficient were fitted all at once until convergence. Then, the Y_{Gauss} and U_{Gauss} values were fixed and fitted alternately until convergence, starting with Y_{Gauss} . Afterwards, the lattice constant a was refined. In a second cycle, line shaping parameters U_{Gauss} and Y_{Gauss} were refined again in turns. When a , Y_{Gauss} and U_{Gauss} reached a minimum in least square deviation, the Debye-Waller factors B for every elemental site were alternately refined. As for the $Fd\bar{3}m$ structure, no fractional atom parameters are found, x , y and z were not refined. Finally, microstrain was fitted using the refinement of the Lorentzian line broadening parameters K41, K61 and K81 of the $m3m$ Laue class.

In the following, obtained lattice constants a , microstrain values η , average crystallite sizes L_a and goodness-of-fit parameters χ^2 for all refined samples are given (see Table 9.1).

4.1.4 X-Ray Photoelectron Spectroscopy

X-ray photoelectron spectroscopy (XPS) measurements were performed on *PHI Versaprobe II Scanning ESCA Microprobe* (PHYSICAL ELECTRONICS) equipped with an Al K_α X-ray source. The X-ray beam with a power of 50 W was sized to 0.1 x 1.3 mm. 23.5 eV was chosen as analyzer pass energy for detail spectra, which were recorded with a step size of 0.2 eV and a step time of 50 ms. The C 1s line signal was fixed to 284.8 eV for charge correction.^[286] All data was processed using *CasaXPS* software.

4.1.5 Synchrotron-Based X-Ray Excitation Experiments

Hard X-ray experiments with high-energy X-rays were performed at the Rossendorf Beamline (BM20) at the European Synchrotron Radiation Facility (ESRF) using the 6 GeV storage ring. The experimental station RCH-II was used for all experiments, which is equipped heavy-duty 6-circle goniometer (HUBER). The energy of the monochromatic beam was tuned between 7090 eV and 7220 eV with 0.3 eV step size to excite Fe K-edge features. A water-cooled Si/Rh/Pt mirror collimator, a double crystal monochromator (Si(111)) with a spectral resolution of 0.2 eV and a toroid (Rh/Pt) mirror focusing on a flat Si surface were employed. The general optics used for the experiments are shown in Figure 4.1.

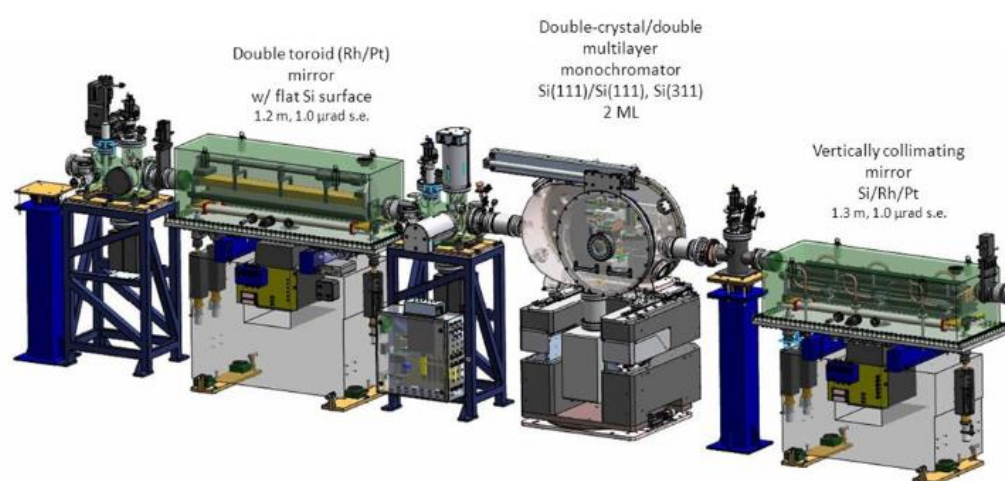
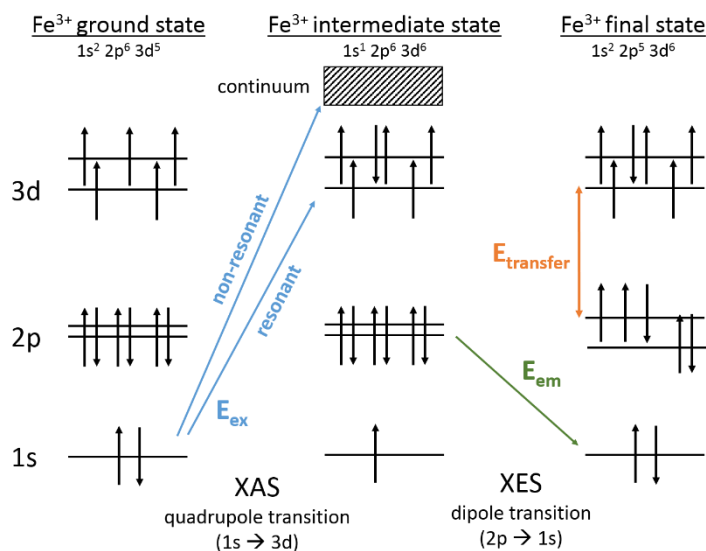


Figure 4.1: Beamline optics of the Rossendorf beamline (BM20) at ESRF.^[287]

For XANES measurements, samples were diluted with boron nitride ($\approx 1 \mu\text{m}$). In XES, RIXS and V2C measurements, the pure samples were analyzed. Samples were sealed in Kapton[®] foil, mounted on an x-y-z-stage, which is adjustable by stepper motors and gearboxes, and measured at room temperature under ambient pressure. In all experiments (HRFD-XANES, site-selective XES, RIXS, V2C-XES) a 5-crystal Johann-type emission spectrometer was employed.

The measurements were performed on ZnFe_2O_4 and MgFe_2O_4 nanoparticles and ZnFe_2O_4 mesoporous powders. Reference substances of nanosized hematite and magnetite were analyzed equally to the ferrite samples. The calibration of the monochromator was performed with an Fe foil, which was corrected to E_0 for the iron K-edge at 7112 eV.^[288] The calibration of the monochromator was checked after each change of the analysis technique. Obtained data were processed using *PyMca* software.^[289] All experiments were performed under the experimental number CH5027.


 Figure 4.2: X-ray absorption and emission processes for Fe^{3+} .

X-ray absorption spectroscopy (XAS) and X-ray emission spectroscopy (XES) are synchrotron-based analysis techniques applicable to various materials, such as metals, transition metal oxides and metal complexes.^[290–295] Both methods are complimentary to each other, with the transition processes being connected as shown in Figure 4.2. The energy for excitation can be delivered in form of soft X-rays (< 1 keV) or hard X-rays (> 3 keV).^[296] Hard X-rays show wavelengths comparable or shorter than the spacing of crystalline planes, while soft X-rays correspond to larger distances.^[296] Absorption of soft X-ray by materials is much higher than for hard X-rays, which is why most soft X-ray experiments are carried out under vacuum conditions. This makes the experimental design and sample handling more difficult compared to hard X-ray experiments, which can also be performed under ambient conditions or in different gas atmospheres.^[296] The absorption of X-rays can be described equivalently to Lambert-Beer's law^[297] as

$$I = I_0 \cdot e^{-\alpha D} \quad (4.2)$$

where I_0 is the incident X-ray intensity, I is the intensity of the transmitted energy, α is the linear absorption coefficient and D is the sample thickness. Theory of XAS is based on the independent particle approximation, reducing a complex theory to an effective independent electron approximation.^[297] By this, Fermi's golden rule equation (4.3) can be applied.^[297,298]

$$I_{\text{XAS}} \sim |\langle \Phi_f | d | \Phi_i \rangle|^2 \delta(E_f - \hbar\omega - E_i) \quad (4.3)$$

Here, the X-ray absorption intensity I_{XAS} is proportional to the dipole coupling d of the initial state of the deep core hole Φ_i to the final state Φ_f representing the unoccupied final quasi-particle states. The dipole momentum implies, that the spin during transition is conserved and the orbital momentum between the initial and the final state differs by $\Delta J = \pm 1$. The delta function, guaranteeing energy conservation, describes the photon energy defined as

$$\hbar\omega + E_i \equiv E_f \quad (4.4)$$

When the photon energy matches or exceeds the 1s binding energy, excitations of deep core 1s electrons into unoccupied p-states are triggered. The resulting spectra are called K-edge spectra. For transition metals, the K edges are found between 5 keV and 10 keV of absorption energy.^[296]

A disadvantage of hard X-ray spectroscopy is the signal broadening as a consequence of core-hole lifetime broadening. Because of Heisenberg's uncertainty relation, the core-hole lifetime τ_{hole} is connected to the Lorentzian shape broadening with the width Γ by

$$\tau_{\text{hole}} \cdot \Gamma = \hbar = 6.6 \cdot 10^{-16} \text{ eVs} \quad (4.5) \text{ [296]}$$

For hard X-rays, Γ is reported to be 1.0 eV – 1.3 eV at transition metal K-edges, while for soft X-rays it is only 0.4 eV – 0.5 eV at the transition metal L-edges.^[296] Due to this, K-edge line shapes are about three times broader than L-edge features.^[298] On the other hand, soft X-ray experiments usually need to be performed under vacuum, which makes *in situ* experiments under ambient conditions impossible. With a resolution of ≈ 1 eV, K edge spectroscopy offers the possibility to characterize orbital splitting and electron-electron interaction.^[299]

4.1.5.1 X-Ray Absorption Near Edge Spectroscopy

X-ray absorption spectroscopy (XAS) offers materials characterization in form of X-ray absorption near-edge spectroscopy (XANES, around 50 eV around the absorption edge) and extended X-ray absorption fine structure (EXAFS), which is the region above 10 – 20 eV.^[297,300,301] In this work, for X-ray absorption only XANES measurements will be discussed. XANES probes the full density of states around the absorbing atom or ion, including multiple scattering phenomena induced by the final excited states. As the absorbed energy depends on the core electron binding energy, this technique allows to obtain information characteristically for the analyzed element. Detailed conclusions on the unoccupied states of the electronic structure of unknown compounds can be drawn from comparison with known reference systems of the same element.

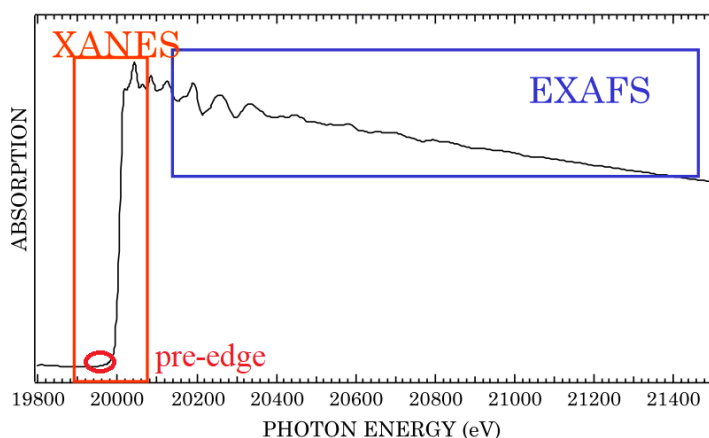


Figure 4.3: X-ray absorption spectrum with marked XANES and EXAFS regions (adapted from S. Bare).^[301]

XANES spectra are divided into three regions, which are shown in Figure 4.3: 1) a pre-absorption region with a pre-edge structure, 2) a distinct absorption edge in an element-specific energy range, and 3) a multiple-scattering region. The absorption edge of XANES is shifted to higher energies with higher valences, which can be

used to determine the valence state of the metal cation. For Fe^{2+} and Fe^{3+} ions, this has been shown in an extensive study by Westre *et al.*^[290] Furthermore, in transition metal oxides the absorption edge energy is also determined by the metal-oxygen distance as shown by De Vries *et al.* for manganese oxides.^[291]

The pre-edge structure in K-edge spectra is caused by 1s core electron excitation into 3d orbitals of the transition metal, which is why no pre-edge structure is observed for elements with d^{10} configuration. Due to less probability of electron transition into d orbitals, pre-edge features of weak intensity are created.^[297] The overall excitation probability into the 3d band and strongly depend on the number of 3d vacancies.^[300,302] The pre-edge is sensitive to crystal field splitting, site symmetry and metal oxidation state.^[299] As these parameters also control the structure of chemical compounds, from XANES spectra conclusions on the local structure around X-ray scattering atoms can be drawn.

If a 3d transition metal atom has octahedral coordination with six identical ligands, this coordination sphere shows inversion symmetry. Therefore, no 3d-4p orbital mixing is possible and the 3d valence orbitals show only quadrupole transition, while dipole transitions are “Laporte” forbidden.^[298,299] In tetrahedral coordination, the local mixing of 4p and 3d nature is symmetry allowed, as these systems do not show inversion symmetry, leading to p-d hybrid orbitals.^[290,298] These hybrid orbitals apply to the dipole selection rule, which is why not only quadrupole transitions from 1s to 3d orbitals, but also dipole transitions from 1s into 4p-3d hybrid orbitals are observed in the pre-edge region of tetrahedral complexes.^[300,303] With a distorted octahedral coordination, the original inversion symmetry is broken. As more p character will be added to the 4p-3d hybrid orbitals, this allows 1s electron excitation into the hybrid orbitals.^[297,303] Because the amount of p character is still quite small in those hybrid orbitals, only a limited amount of “allowed” transitions can occur. Therefore, in tetrahedral systems the pre-edge intensity is larger than in distorted octahedral symmetry.^[300,303] This has already been shown for different iron oxides and titanium compounds with different coordination geometry.^[295,298] Furthermore, multiplet splitting occurs due to electron-electron repulsion and ligand

field splitting, which leads to multiple final states. Therefore, the local coordination number and coordination symmetry around the absorbing metal determine the shape and intensity of the pre-edge structure.^[302]

In 2005, de Groot and co-workers^[298] investigated divalent and trivalent iron oxides with different coordination geometry, observing a pre-edge center at 7113 eV for the Fe²⁺ iron oxides and at 7114.5 eV for the Fe³⁺ iron oxides. Additionally, they located the absorption edge at 7122 eV for Fe³⁺.^[298] The results give an average energy position of Fe³⁺ pre-edges at 7113.5 eV for both for tetrahedral and octahedral symmetry, whereas their relative intensities are 0.35 for tetrahedral and 0.06 for octahedral symmetry, respectively. Westre and co-workers proved, that oxidation state, spin state, local geometry and the nature of the ligand interaction affect the pre-edge feature of iron-based complexes.^[290] For octahedral Fe³⁺ complexes they found the split to vary depending on the ligand binding strength between 1.7 eV and 3.5 eV, which was attributed to allowed electric quadrupole transition causing the 1s-3d pre-edge feature.

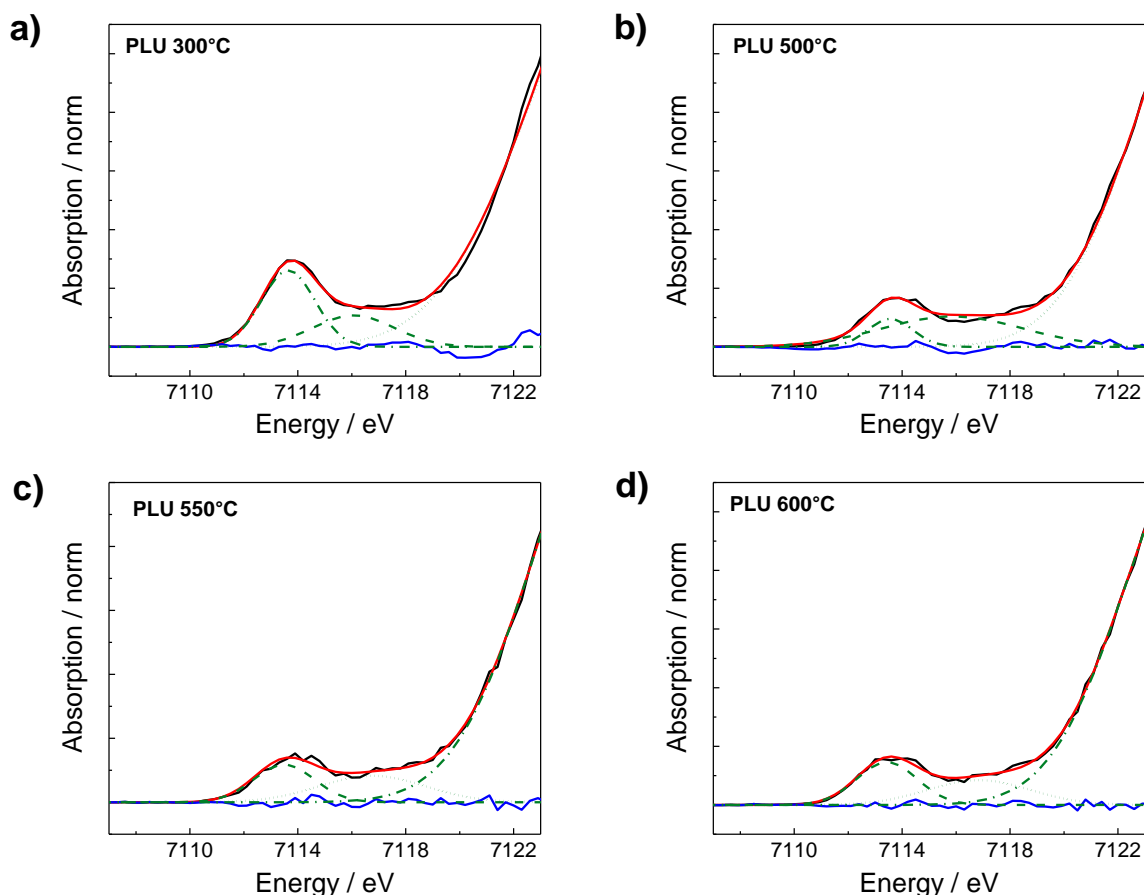


Figure 4.4: XANES pre-edge fits of mesoporous ZnFe₂O₄ powders.

For high-resolution fluorescence detected XANES (HRFD-XANES) measurements, three single spectra were collected. They were merged and normalized by the average absorption intensity at around 7200 eV. The pre-edge region of all spectra was fitted using *Athena* software^[304] to allow a detailed comparison of the samples. Examples of fitted spectra are shown in Figure 4.4.

4.1.5.2 X-Ray Emission Spectroscopy

X-ray Emission Spectroscopy (XES) investigates the reversed process described for XAS, *i.e.* relaxation of an excited electron into the initial valence band state. By filling the deep core hole created during XAS with an electron from a higher orbital, energy of an element characteristic signature is emitted. While XAS probes the density of states of the unoccupied orbitals which are lowest in energy, XES gives insights into the density of states of the highest occupied energy levels.^[296]

If the core hole was created in the 1s shell (K-edge absorption) by electron excitation, the emitted fluorescence is called K fluorescence. The K fluorescence can show lines of different intensities referred to as α , β or γ , where $K\alpha$ is the most intense emission line at the lowest energy resulting from 1s core hole filling with a 2p electron.^[296] All K emission lines show a fine structure, which results from the interaction of the orbital spin with its momentum on the one hand, and the interaction between the electrons on the other hand. The emission processes resulting in different emission signals are shown in Figure 4.5. For $K\alpha$ -lines, were 2p spin-orbit splitting ($K\alpha_1$, $K\alpha_2$) can be observed.^[296] Approx. 25 % of the absorbed energy is emitted in form of $K\alpha$ fluorescence.^[305]

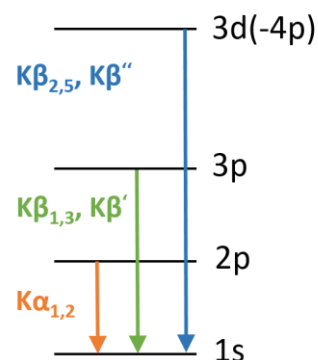


Figure 4.5: Origin of XES emission lines.

In the second case, which is typical for $K\beta$ -lines, the interactions can occur either between valence shell electrons or between a core electron and a valence shell electron, leading to a splitting into $K\beta_{1,3}$ and $K\beta'$.^[296] $K\beta$ main lines were reported to be 8 times less intense than $K\alpha$ fluorescence.^[305] Weak satellite signals created in the $K\beta$ -line are due to relaxation from the valence orbitals into the 1s shell. These valence-to-core (V2C) transitions are labeled $K\beta_{2,5}$ and $K\beta''$.^[296] The strong interaction of 2p and 3p electron-spin with electron-electron interaction result in a chemical sensitivity of $K\alpha$ - and $K\beta$ -lines for the electronic structure.^[292] On the other hand $K\alpha$ - and $K\beta$ -lines are less sensitive towards the atomic structure, which has been shown by Peng and co-workers.^[292] Despite the $K\alpha_1$, $K\alpha_2$ emission having about 8 times the intensity of $K\beta_{1,3}$ and $K\beta'$, this fluorescence is least sensitive to local structure changes. Here, $K\beta_{1,3}$ and $K\beta'$ are much more sensitive concerning the oxidation and spin state of 3d metals.^[306,307] It should be mentioned, that none of the discussed transitions directly describes the 3d states.

Two types of XES are distinguished: resonant XES, where an excitation into the valence band was triggered first, and non-resonant XES, where the core electron was excited into the continuum state (see Figure 4.2). Non-resonant XES can be performed with every X-ray source connected to an X-ray spectrometer, as it is based on excitation into continuum state.^[308] For resonant XES, high-energy monochromatic X-rays are required.

Two types of XES are distinguished: resonant XES, where an excitation into the valence band was triggered first, and non-resonant XES, where the core electron was excited into the continuum state (see Figure 4.2). Non-resonant XES can be performed with every X-ray source connected to an X-ray spectrometer, as it is based on excitation into continuum state.^[308] For resonant XES, high-energy monochromatic X-rays are required.

The shape of the spectral line is determined by the final state, where the deep core hole has been filled. When the core hole was created due to energy absorption close to the absorption edge, both X-ray emission and absorption correlate and can be described by the Kramers-Heisenberg formula being the basis of all resonant X-ray processes. Emission energies much higher than the resonance cause normal X-ray emission (fluorescence). In contrast to XANES, XES signals do not show any shift, if the metal-to-ligand distance changes, but a variation in total intensity. However, the peak positions are sensitive to the ligand type. This was reported in an extensive study by Smolentsev *et al.*^[309]

When a 2p or 3p core hole is present, the single particle approximation is not suitable anymore to describe the underlying processes, as multiplet effects dominate the resulting states. This is also the case for the final state of XES (compare Figure 4.2).^[310]

In most pre-edge features of transition metals, both dipole and quadrupole excitations occur causing more than one peak in the pre-edge region. These relate to excitations into different final states. Due to this, by selected excitation and emission detection of these transitions, conclusions of the respective final states can be drawn. This approach is called site-selective XES. For Fe^{3+} in $\alpha\text{-Fe}_2\text{O}_3$, the excitation and emission process has been described by Caliebe and co-workers.^[303,310] There, excitations from the ground state (with half-filled 3d orbitals) to quadrupole ($1s3d^6$) and dipole ($1s3d^54p$) intermediate states are described. Using 7113 eV, 7114 eV and 7118 eV, they addressed the 1s transition to t_{2g} and e_g orbitals formed due to crystal field splitting. The dipolar decay along 1s2p leads to $2p3d^6$ and $2p3d^54p$ final states. The pre-edge peaks (a) and (b) in Figure 4.6 relative to the t_{2g} projected and e_g projected final states, which are separated by crystal field splitting. Peak (c) is caused by the quadrupole excitation. As the decay only involves 1s and 2p orbitals, the 3d states remain unchanged during decay. When measuring the $K\alpha$ -emission at the different peak position, information on either the t_{2g} or e_g character of the final states can be obtained. They were able to reveal different peak shapes for the resulting XES plots, which revealed a narrower line width and additional spectral features in contrast to the non-resonant XES.

Site-selective XES spectra were recorded at 7113 eV, 7114 eV and 7118 eV excitation energy, respectively, with a step size of 0.2 eV. These energy values were chosen according to a report by Caliebe *et al.*^[303] The obtained spectra were fitted using a split pseudo-Voigt function provided by

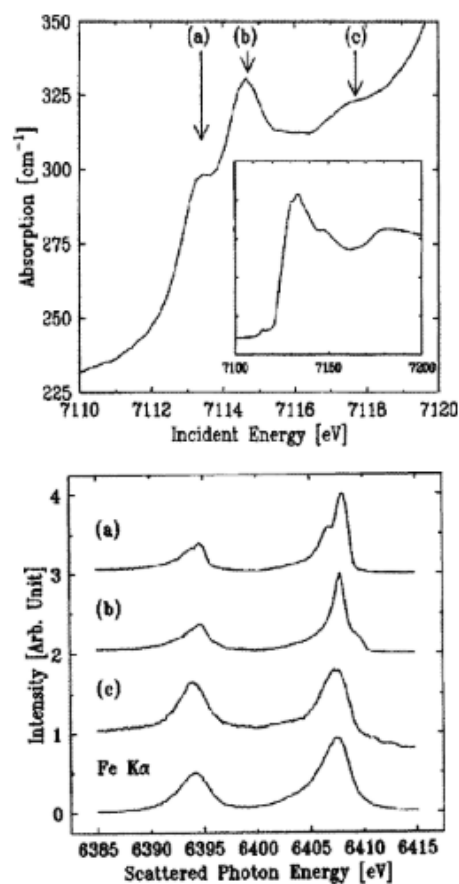


Figure 4.6: K-edge absorption spectrum (top) and corresponding $K\alpha$ XES of $\alpha\text{-Fe}_2\text{O}_3$.^[303]

PyMca software.^[289] The general fit quality is exemplarily shown for the hematite nanoparticle sample in Figure 4.7.

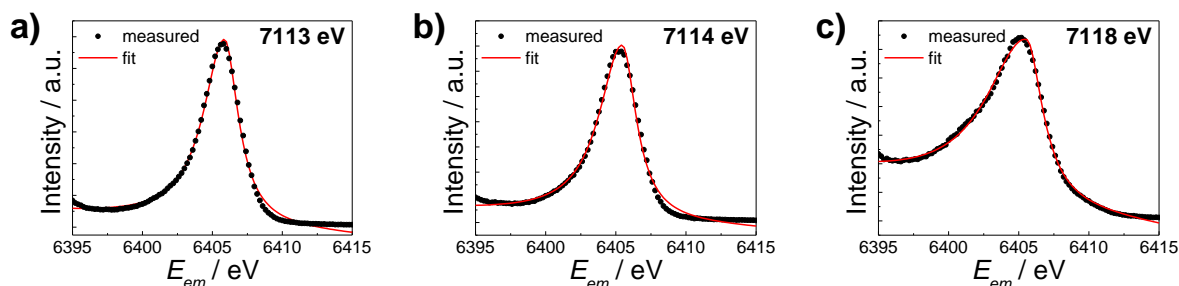


Figure 4.7: Measured XES spectra of Fe_3O_4 and respective fits.

RIXS planes were obtained by exciting the samples with energies between 7108 eV and 7122 eV, matching the 1s pre-edge energy of Fe. Parallel to this, the 1s2p emission energy was scanned. The data was processed using the built-in *Matplotlib* graphic tool of *PyMca* software.^[289]

V2C spectra of the $\text{K}\beta_{2,5}$ feature of ZnFe_2O_4 was obtained by detection of the emission energy in the range of 7085 eV to 7130 eV.

4.1.5.3 Valence-to-Core X-Ray Emission

Weak satellite signals created in the high-energy region of the $\text{K}\beta$ XES line arise from the relaxation of electrons from the ligand valence orbitals into the metal 1s shell, filling the 1s core hole. These valence-to-core (V2C) transitions are labeled $\text{K}\beta_{2,5}$ and $\text{K}\beta''$ and are very sensitive to both, electronic structure and local coordination, which is complementary information to XANES spectra.^[296] This is why they provide valuable insights into chemical structures despite their very weak intensity (several hundred times weaker than $\text{K}\alpha_1$ and $\text{K}\alpha_2$)^[296]. The core hole lifetime broadening determines the width of the V2C signals.^[308] For basic principles of V2C measurement setup, the reader is referred to an article by E. Gallo and P. Glatzel.^[308] The probability of the V2C excitation depends highly on the incident X-ray energy.^[308] The lines originate from transitions involving the 2s and 2p orbitals of the ligands, which is why they are element-sensitive and present in metal oxide samples but absent in metallic samples.^[311] Due to the sensitivity to the ligand and the metal electronic state, V2C-XES can provide insights into the changes of the electronic structure, if the spectra are recorded under *operando* conditions.^[308]

In the case of $\alpha\text{-Fe}_2\text{O}_3$, the $\text{K}\beta''$ line is caused by electron transition between the hybrid orbitals formed of Fe d and O 2s orbitals, which are called cross-over transitions. As V2C is a sub-category of XES, the position of the $\text{K}\beta''$ line is highly sensitive to the ligand type but not to the bond length. As in

ferrites, all Fe^{3+} are coordinated by oxygen, no energy shift of the $\text{K}\beta''$ line is expected when comparing V2C XES spectra of ZnFe_2O_4 and MgFe_2O_4 with those of hematite or magnetite.

The $\text{K}\beta_{2,5}$ line originates from electron transitions of hybrid orbitals of Fe 3d and O 2p orbitals with metal p character to the 1s metal orbital.^[308] They can provide information on the nature of the chemical bond. The high energy side of the $\text{K}\beta_{2,5}$ line can show multi-electron features.^[308] For distinct interpretation of the origin of the $\text{K}\beta_{2,5}$ line, quantum mechanical calculation are necessary. A one-electron approach can be used to describe the spectral features and gain insight into the nature of the chemical bonds.

Interpretation of V2C XES spectra is possible by either quantum chemical calculations or comparison to V2C XES spectra of reference substances containing elements in a comparable chemical environment. For normal spinel ZnFe_2O_4 , where the Fe K-edge emission was studied, comparison with hematite V2C XES reports from literature would be suitable as in both substances, Fe^{3+} ions are in octahedral oxygen coordination.

The report by Nowakowski *et al.*^[312] from 2017 showed, how resonant XES of the $\text{K}\beta''$ signal in combination with XANES can be used to determine the band gap of different iron-based materials. They calculated both spectra types from RXES planes of Fe, $\alpha\text{-Fe}_2\text{O}_3$ and $\text{Fe}(\text{NO}_3)_3 \cdot 9\text{H}_2\text{O}$ and determined the valence and conduction band position from the inflection points of these spectra. They calculated a band gap energy of 2.1 eV for $\alpha\text{-Fe}_2\text{O}_3$ and 1.1 eV for Fe metal, which is contradictory to the metal character itself. Furthermore, they reported an edge shift of 10.8 eV for $\alpha\text{-Fe}_2\text{O}_3$ in comparison to the Fe metal edge at 7112 eV.

Bergmann and co-workers^[305] studied the sensitivity of $\text{K}\beta''$ signal to ligand type, bond distance and metal oxidation state in Mn compounds. They found the energy of the signal to depend strongly on the ligand characteristics, while its intensity decreased with increasing metal-to-ligand distance. With change of oxidation state of the Mn, the $\text{K}\beta_{2,5}$ peak shifts by ≈ 1 eV per oxidation unit. This proves the applicability of V2C for determination of structural configuration in transition metal complexes.

4.1.5.4 Resonant Inelastic X-Ray Scattering

Resonant inelastic X-ray scattering (RIXS; sometimes also resonant X-ray emission spectroscopy RXES) is frequently considered as photon-in-photon-out spectroscopy. It is a second order process, where the 1s core hole is filled by a shallow electron, creating a core hole in the 2p shell as the final state.

In 1s2p RIXS, the sample is resonantly excited to create a 1s core hole. Due to the resonant excitation close to the absorption edge, no ionization of the studied atoms occurs as the excited electron stays bound in the excited state, but a direct probing of the atoms and their photo-excited

electrons in bound states is possible. The 1s core-hole is then filled by an electron from the 2p shell, which creates a secondary core-hole in the 2p shell. As the resulting state with a 2p core hole is identical to the $L_{2,3}$ edge spin-orbit split, this allows probing of soft X-ray features with hard X-ray excitation. The RIXS plane consists of a set of scans at constant emission energy, which were produced by varying excitation energy. The observed energy transfer reflects the energy, which remains in the sample after the final state is reached. The second order process of RIXS measurements is described by the Kramers-Heisenberg equation (equation (4.6), which is applicable for all resonant processes.^[300]

$$F(\Omega, \varphi) = \sum_f \left| \sum_n \frac{\langle f | T_2 | n \rangle \langle n | T_1 | g \rangle}{E_g - E_f + \Omega - i \frac{\Gamma_K}{2}} \right|^2 \cdot \frac{\frac{\Gamma_L}{2\pi}}{(E_g - E_f + \Omega - \varphi)^2 + \frac{\Gamma_L^2}{4}} \quad (4.6)$$

Here, E_g is the energy of the ground state $|g\rangle$, E_f is the energy of the final state $|f\rangle$, Ω is the excitation energy and φ is the emission energy. The intermediate state $|n\rangle$ is reached by transition operator T_1 from the ground state. From this intermediate state, a decay process T_2 leads to the final state. In 1s2p RIXS, a resonant excitation occurs from the ground state before photon absorption, which is $1s^2 2p^6 3d^5$ for Fe^{3+} , creating an intermediate state with a 1s core hole ($1s^1 2p^6 3d^6$), which is equal to the final state in K-edge XAS. Consecutively, the 1s core hole is filled by a 2p electron, which leads to the final state of $1s^2 2p^5 3d^6$. This final state is equal to L-edge XANES, were a direct excitation of 2p electron into the 3d valence is triggered. Because the final state is not identical with the ground state (compare Figure 4.2), local phenomena such as d-d or charge transfer transitions can be studied from the energy difference.^[303]

The Kramers-Heisenberg equation contains two Lorentzian line shapes for the absorption and the decay process, which have different line broadenings Γ . Due to this, spectra of K-edge like character are created during excitation, as this is dependent on the 1s core-hole lifetime, and spectra of L-edge like character along the energy transfer $\Omega - \varphi$, which depicts the 2p core-hole lifetime broadening. The circular broadening of the RIXS plane maximum results from lifetime broadening of the 1s core hole in the intermediate state (for E_{ex}) and the 2p hole in the final state (for $E_{transfer}$) (compare Figure 4.2).^[313]

As the final state shows smaller lifetime broadening, sharper features are obtained compared to conventional XAS. The effect is called “line shaping effect” and helps to better separate pre-edge features. Because the L-edge-like final state is reached *via* the intermediate state, RIXS spectra may contain more information than L-edge XAS spectra, but theoretical tools developed for L-edge absorption might not be applicable. The 1s2p RIXS decay corresponds to $K\alpha_{1,2}$ fluorescence line in non-resonant XES.^[296] Usually, RIXS spectra are presented as 2D contour plots allowing a qualitative comparison between 1s X-ray absorption and 1s2p X-ray emission processes in different substances.

The report of de Groot and co-workers^[300] from 2005 presented a comprehensive study on 1s2p RIXS for Fe²⁺ and Fe³⁺ iron oxide materials with octahedral or tetrahedral coordination, respectively. For α -Fe₂O₃, a diagonal structure was found, which indicates that the emission in this compound appears at a constant emission energy indicating that only one final state arises. They attributed this to the conservation of the electronic excitation during the decay step, *i.e.* the replacement of a 1s core hole with the 2p core hole.^[300] The authors discussed the possibilities to obtain different cross-section 1D plots for quantitative analysis from 2D RIXS planes. They showed, that a cross-section with constant incident energy is related to resonant XES spectra, whereas a cross-section with constant energy transfer implies, that for different excitation energies the same final states was reached. A diagonal line would be equivalent to a constant emission energy, which results in K-edge like XANES spectra with removed lifetime-broadening.

For magnetite with Fe³⁺ in tetrahedral sites, significant 3d-4p orbital hybridization is allowed due to missing inversion symmetry. This leads to large 1s \rightarrow 4p dipole transition contributions in the pre-edge feature. A 1.5 eV K-edge shift for magnetite was reported by Sikora *et al.*^[313] The maximum of incident and transfer energy in the RIXS plane of Fe₃O₄ was observed at 7113.6 eV, 708.8 eV, which was attributed to tetrahedral Fe³⁺.^[313] They ascribed the diagonal structure in the RIXS plane to non-resonant fluorescence.

4.2 Spectroscopic Methods

4.2.1 Vibrational Spectroscopy

Infrared and Raman spectroscopy are complementary analytical methods, which can provide valuable information on the strength of chemical bonds as well as the symmetry of compounds. They are based on vibrations of atomic bonds within molecules or solid compounds. In all systems having electron pairs shared between different atoms, a vibration of these bonds is possible.

Depending on the nature of the bond, different amounts of energy are needed to excite the vibrations. For IR-active vibrations, the absorbed photon needs to match the resonance frequency of the vibration, which is described by the energy frequency relation (see equation (2.1)). Furthermore, the overall dipole moment of a molecule or periodic unit needs to change during vibration (see Figure 4.8). This is the case for non-symmetric vibrations.^[314] When the electron density of a molecule or periodic unit is changed during

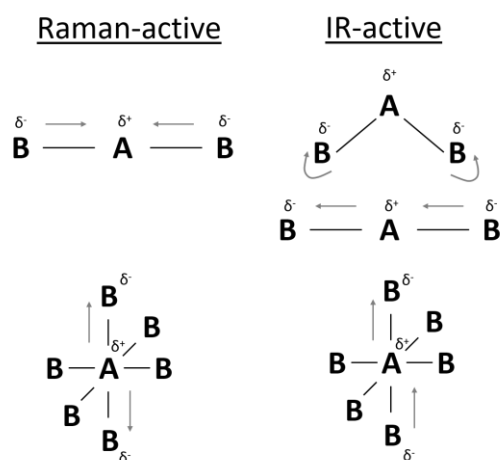


Figure 4.8: Examples of IR-active and Raman-active vibrations.

vibration, which means the polarization of the electronic shell, then this vibration is Raman-active (see Figure 4.8). Symmetric stretching vibrations are common examples for this. The deflection of the bonding partners is proportional to the oscillation energy by the proportional constant k . This constant includes the influence of the vibrational frequency ν_{osc} and the atomic masses of the bonding partners, which are described as reduced mass m_{red} . The vibrational frequency ν_{osc} of a molecule consisting of two atoms can be described as:

$$\nu_{\text{osc}} = 2\pi \sqrt{\frac{k}{m_{\text{red}}}} \quad (4.7)$$

According to equation (4.7), the vibrational frequency of a bond is high, if the bond energy described by k is large. In addition, with lightweight binding partners the oscillation frequency is high. Due to these bonding specific circumstances, IR- and Raman-active vibrations are characteristic for certain functional groups or building blocks within a molecular structure. This is also the case for geometrical units inside a solid compound. Depending on the geometry, bond lengths and bonding partners, different resonant frequencies are needed for vibrational excitation.^[314]

In IR spectroscopy, excitation with a broad spectral region of IR radiance ($4000 - 400 \text{ cm}^{-1}$) triggers various vibrations within a molecular or solid compound. The loss of intensity compared to the incident beam intensity is detected, resulting in transmission spectra. The more complex the connectivity and functionality within a molecule, the more complex the resulting IR pattern due to a high number of resonant vibrations, which can also overlap. Most vibrations can be assigned to typical functional groups or building blocks inside a molecule and are literature-known. The model of the harmonic oscillator is applicable for rough estimation of vibrational modes, but it is not sufficient to include also the complexity of higher vibrational modes or even dissociation of molecules due to absorption of a photon with high energy E_{diss} . For this purpose, the inharmonic oscillator resulting from the Schrödinger equation is more suitable (equation (4.8)).

$$E_{\text{osc}} = h \cdot \nu_{\text{osc}} \left(n + \frac{1}{2} \right) - \frac{h^2 \nu^2}{4 E_{\text{diss}}} \left(n + \frac{1}{2} \right)^2 \quad (4.8)$$

Here, a non-symmetric potential curve considers also the weakening of bonds with higher atomic distance. In addition, the quantization of energy absorption needs to be considered. This means, that absorption of energy quants is only possible if

$$E_{\text{osc}} = h \cdot \nu_{\text{osc}} \left(n + \frac{1}{2} \right) = \frac{h}{2\pi} \sqrt{\frac{k}{m_{\text{red}}}} \left(n + \frac{1}{2} \right) \quad (4.9)$$

is fulfilled. At $n = 0$, the molecule vibrates with a ground state energy. Higher n are called overtones. The number of fundamental vibrations z (at $n = 0$) can be calculated according to the following equations.

$$\text{linear molecules:} \quad z = 3N - 6 \quad (4.10)$$

$$\text{non-linear molecules:} \quad z = 3N - 5 \quad (4.11)$$

Here, z is the number of vibrational degrees of freedom and N is the number of atoms within a molecule. Vibrations can be divided into stretching vibrations, which go along with a change in bond length, and bending vibrations, which result from changing bond angles (compare Figure 4.8).

Raman spectroscopy is based on the Raman effect, named after Chandrasekhara Raman, who was awarded with the Nobel prize in physics for his discovery in 1930.^[315] The Raman effect is based on the influence of incident light on the polarization within molecules and periodic units. Excitation to a virtual energetic level is caused by high-energy monochromatic light due to change in the polarization of the electron cloud. This creates a short-lived virtual state. The incident photon energy does not necessarily need to match the energy of the excited state.

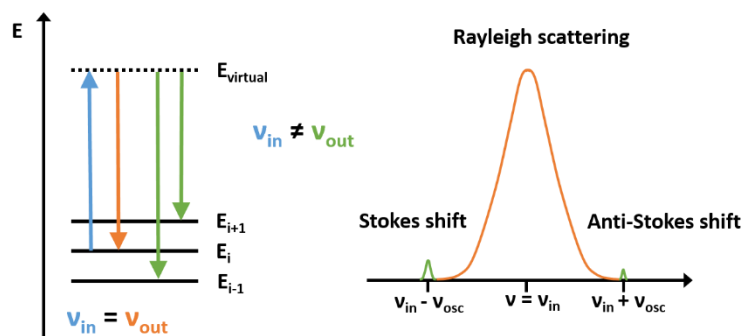


Figure 4.9: Processes during Raman spectroscopy.

The underlying principle is the scattering of photons at the distorted electron clouds, which can be divided into two species: elastic scattering, so called Rayleigh scattering, and inelastic scattering, which is the basis of Raman spectroscopy. The inelastic scattering results from absorption or emission of energy

in form of phonons, which transfers a molecule from its ground state into a higher or lower energetic state than before the scattering process. This can be described as:

$$\Delta E = E_{i+1} - E_i = h(\nu_{in} - \nu_{osc}) \quad (4.12)$$

$$\Delta E = E_{i-1} + E_i = h(\nu_{in} + \nu_{osc}) \quad (4.13)$$

The loss of energy due to phonon excitation creates a scattered photon with a lower frequency. This energy shift is called Stokes shift. In the opposite case, the photon gains energy from interaction with an oscillating molecule in its excited state, leading to a shift to higher frequencies, which is called Anti-Stokes shift. These processes are depicted in Figure 4.9. Here, E_{i+1} , E_i and E_{i-1} are the respective energy levels involved in absorption and emission of the photon, ν_{in} is the frequency of the incident photon and ν_{osc} is the triggered oscillation due to inelastic scattering. As the amount of inelastically scattered phonons is small (only one in $10^6 - 10^8$ electrons)^[316], the Stokes and Anti-Stokes shift is very weak (see Figure 4.9). Therefore, intense light sources (lasers) are needed to achieve detectable Raman signals. As the energetic change due to scattering is very small, the Stokes and Anti-Stokes lines are located close to the Rayleigh scattering. The Anti-Stokes shift need already excited states for increase of scattered photon energy, which is dependent on the thermal energy in the system. Because of this, at room temperature the Anti-Stokes signals are very weak compared to the Stokes signals. This is why for standard measurements, signals caused by Stokes scattering are detected.

Raman-active vibrations in solids are characteristic values for a compound and can be predicted by group theory. The so-called lattice modes result from longitudinal and transversal propagation of the triggered vibrations throughout the whole crystal lattice. During this vibration, inter-atomic angles and distances change, causing a polarization of the electron shell of each atom, which can then trigger Stokes and Anti-Stokes scattering. The lattice modes are very sensitive towards crystal defects in solid compounds, as this changes the periodicity of the crystal lattice.

4.2.1.1 Infrared Spectroscopy

Fourier transformed infrared spectra (FTIR) were collected on an *IFS25 FTIR spectrometer* (BRUKER). Samples were pressed with KBr to obtain pellets, which were analyzed between 400 and 4000 cm^{-1} with a step width of 4 cm^{-1} . The obtained spectra were processed using *OPUS 7.5* software (BRUKER) and *OriginPro® 2016G* (ORIGINLAB).

4.2.1.2 Raman Spectroscopy

Identification of the cubic spinel structure and the degree of inversion is possible via Raman spectroscopy. Cubic spinels typically show five first order Raman-active modes ($E_g + 3 F_{2g} + A_{1g}$).^[216] Raman spectroscopy is especially suitable for detection of $\alpha\text{-Fe}_2\text{O}_3$, of which even traces show intense characteristic features, namely the A_{1g} mode at 225 cm^{-1} and E_g mode at 298 cm^{-1} .^[317] But also iron

oxide materials with very high structural similarity can be distinguished due to a shift in their Raman signals.^[33,317] This makes Raman spectroscopy a powerful tool for iron oxide based materials.

Raman spectra of all samples were obtained on a *Senterra* Raman microscope (BRUKER) equipped with a Nd:YAG laser ($\lambda = 532$ nm). Most thin films and nanoparticle samples were analyzed with a laser power of 2 mW. Sensitive samples were analyzed with 0.2 mW laser power. The magnification was set to 50x. Other parameters were adjusted in regard to the sample characteristics for generation of optimum spectra. A spectral resolution of either $3 - 5$ cm^{-1} or $9 - 12$ cm^{-1} was used, depending on the signal quality. In general, 40 co-additions and 20 seconds integration time were used. For low emission samples, 250 co-additions and 3 seconds integration time were chosen. The obtained spectra were processed using *OPUS 7.5* software (BRUKER) and *OriginPro® 2016G* (ORIGINLAB). For samples coated on silicon wafers, the Si substrate Raman signal was subtracted.

4.2.2 UV-Vis Spectroscopy

Ultraviolet-visible light (UV-Vis) spectroscopy was conducted on a *Lambda 750 UV/Vis-NIR* spectrometer from PERKIN ELMER in either diffuse reflectance (DR) or transmission (TR) mode. For DR mode, the spectrometer was equipped with a Praying-Mantis mirror unit. BaSO_4 was used as a white standard in DR mode. DR spectra were recorded between 2300 – 200 nm with 1 nm step width. To convert the reflection R into absorption spectra, the Kubelka-Munk equation was used (equation (4.14)).

$$F(R) = \frac{(1 - R)^2}{2R} \quad (4.14)$$

From this, band gaps of solid samples were calculated from their Tauc plots.^[318] Here, $(F(R)h\nu)^{\frac{1}{n}}$ is plotted against the excitation energy (in eV). Linear fitting of the absorption increase gave indirect band gaps $n = 2$ and direct band gaps for $n = \frac{1}{2}$. For solution TR mode, blank solutions of the corresponding solvent mixture were used. Non-coated glass substrates were utilized as blank samples in solid TR mode.

4.3 Thermogravimetry

For thermogravimetric analyses (TGA), a *STA409PC* thermo-scale (NETZSCH) equipped with a *QMG421* quadrupole mass spectrometer (MS, 70 eV ionization energy, BALZERS) was used. Samples were heated from 30 °C to 800 °C with a heating rate of 5 °C min⁻¹ in synthetic air (80 % N₂, 20 % O₂).

4.4 Electron Microscopy

4.4.1 Scanning Electron Microscopy

Scanning electron microscopy images (SEM) were collected on a *MERLIN field emission scanning electron microscope* (FE-SEM, ZEISS) with an accelerating voltage of 3 keV, a sample current of 90 pA and a working distance of 2.5 ± 1 mm.

4.4.2 Transmission Electron Microscopy

For transmission electron microscopy (TEM) and Selected Area Electron Diffraction (SAED) analysis, samples were dissolved in ethanol or toluene in low concentrations and subsequently drop casted on carbon-coated copper grids (PLANO). TEM images were taken on a *CM30* (PHILLIPS) with 300 kV acceleration voltage and analyzed using *ImageJ* software.^[319]

4.4.3 Energy-Dispersive X-Ray Spectroscopy

Energy-dispersive X-ray (EDX) spectra were collected on an *X-Max 50* energy dispersive X-ray spectroscopy analyzer (OXFORD INSTRUMENTS) with an accelerating voltage of 10 keV, a sample current of 1000 pA and a working distance of 5 mm.

4.5 Physisorption

The benefit of gas physisorption is the profound characterization of porosity in solid materials, which allows determination of the specific surface area S , average pore volume V_p , average pore size d_p and pore size distribution from only one measurement by application of suitable analysis models. The International Union of Pure and Applied Chemistry (IUPAC) divides between three pore sizes: micropores with diameters smaller than 2 nm, macropores with diameters larger than 50 nm and mesopores covering the pore sizes between micro- and macropores.^[320]

For surface analysis, the mechanism of adsorbing gas molecules on solid surfaces is used. Gas molecules are taken as rigidly shaped spheres occupying a defined area σ_m inside a monolayer. The amount of adsorbing gas (adsorbent) necessary to cover the surface area (S) of a certain compound (adsorbate) with a monolayer of gas molecules can be described as monolayer capacity n_m^a , which includes also the Avogadro constant N_A .

$$n_m^a = \frac{S}{N_A \cdot \sigma_m} \quad (4.15)$$

Due to this, the amount of adsorbed molecules per surface at a certain temperature and pressure is constant. By variation of the gas pressure, different amounts of gas can be adsorbed. This volumetric approach allows the characterization of porosity by systematic analysis of the increased gas adsorption. During gas adsorption, the adsorption branch of an isotherm is recorded and weak dipole-dipole interactions and Van der Waals forces appear. During desorption, these forces need to be overcome, leading to a desorption branch, which might not be identical to the adsorption branch depending on the sort of porosity within the analyzed sample. The IUPAC defines different kinds of physisorption isotherms, which are depicted in Figure 4.10.

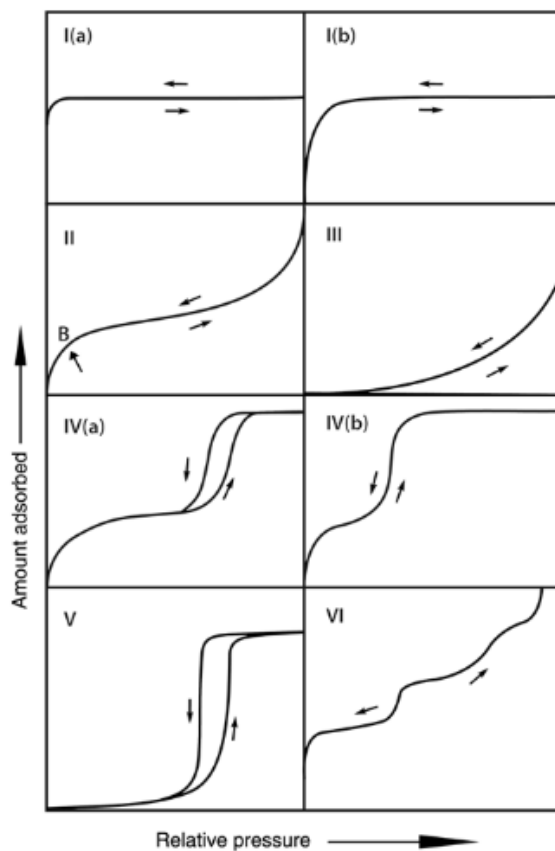


Figure 4.10: Different types of physisorption isotherms according to the IUPAC classification.^[321]

Reversible type I isotherms are typical for microporous materials with small external surfaces. In contrast, type II and type III isotherms, also being reversible, are usually found for non-porous and macroporous materials with monolayer formation (type II) or without monolayer formation (type III). Type IV isotherms typically appear in mesoporous samples with large mesopores (> 4 nm for N_2 , type IV(a)) or smaller mesopores (type IV(b)). Type V isotherms appear for mesoporous materials with weak adsorbent-adsorbate interactions and reversible type VI isotherms is typical for layer-by-layer adsorption on non-porous materials. As seen for type IV(a) and type V isotherms, hysteresis occurs due to multilayer adsorption and therefore capillary condensation of the adsorbent inside the mesopores. Different types of hysteresis are classified by IUPAC in Figure 4.11.

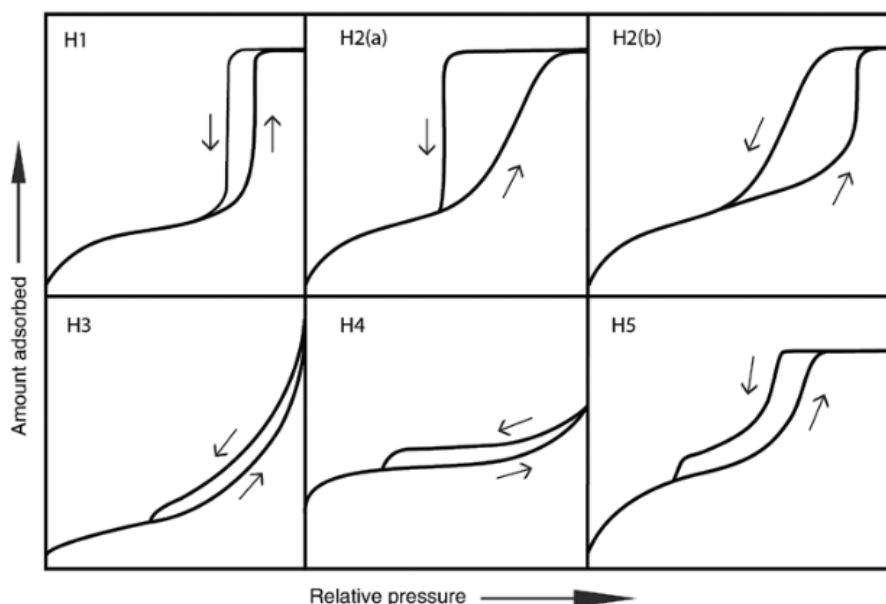


Figure 4.11: Different types of hysteresis loops according to the IUPAC classification.^[321]

For mesoporous materials with uniform pores, H1 hysteresis is typical. In more complex pore structures, network effects become prominent influencing the hysteresis. Pore blocking can occur, which lead to type H2(a) (narrow size distribution of the pore necks) and type H2(b) loops (wider size distribution of the pore necks). H3 loops can be found for nanoparticle agglomerates and pore networks with partially filled macropores, whereas H4 loops are typical for aggregated microporous-mesoporous materials, *e.g.* zeolites. Samples containing both open and partially blocked mesopores show H5 hysteresis loops. Especially in complex pore structures, network effects and bottle-neck pores

can affect the desorption path of a physisorption isotherm, which is why in such samples, the adsorption branch should be considered for further analysis.

Based on the assumptions made in equation (4.15), the adsorbed volume V_{ads} of gas can be directly correlated to the gas pressure p . At low relative pressures p/p_0 , surface area determination by BET model (equation (4.16), named after S. Brunauer, P. H. Emmett and E. Teller) is applicable.^[322] This widely used model incorporates multimolecular adsorption layers by respecting, that the forces being active during gas adsorption are also responsible for multimolecular adsorption.

$$\frac{p}{V_{\text{ads}}(p_0 - p)} = \frac{1}{V_m C} + \frac{C - 1}{V_m C} \left(\frac{p}{p_0} \right) \quad (4.16)$$

The linearized form allows to construct a plot of $p/(V_{\text{a}}(p_0-p))$ vs. p/p_0 , which can lead to a straight line, from which the BET constant C and the volume of a monolayer V_m can be obtained. The value of C is indicative for the quality of the BET fit. If C is < 5 , the BET model cannot be applied.^[321,323] From the volume of the monolayer V_m , the specific surface area S_{BET} can be calculated by assuming a closed packing of gas molecules (of mass m) within the monolayer, which is expressed by

$$S_{\text{BET}} = V_m \cdot N_A \cdot \frac{\sigma_m}{m} \quad (4.17)$$

As evident from (4.17), the specific surface area is proportional to the atomic mass of the adsorbent. Nitrogen is traditionally used for physisorption experiments at 77 K due to its abundance and well-defined adsorption behavior on many materials. At 77K, σ_m for N_2 in a closely packed monolayer is assumed to be 0.162 nm^2 . But because of the quadrupole moment within the N_2 molecule, it was recently found, that molecule's orientation of a surface is strongly dependent on the adsorbent-adsorbate interactions leading to an uncertainty of σ_m up to 20 %.^[324]

Argon (Ar) and krypton (Kr) seem to be suitable alternatives to N_2 , as they do not obtain a quadrupole moment. But at 77 K both gases are below the bulk triple point temperature, which is why their bulk reference state is not well-defined at this temperature. For Ar, gas adsorption at 87 K can overcome this problem resulting in a constant σ_m of 0.142 nm^2 . For Kr, the cross-sectional value is still not well defined at this temperature. Commonly used values vary between $0.17 - 0.23 \text{ nm}^2$.^[321] Nevertheless, due to a large molecular mass and much lower saturation pressures compared to Ar and N_2 , Kr physisorption is very sensitive and advantageous for analysis of samples with low specific surface areas, which is the case for porous thin films on non-porous substrates.

In case of C values < 5 from BET analysis, the Langmuir data reduction model should be applied.^[323] This is more applicable to the case of chemisorption, assuming the formation of gas monolayers on solid surfaces. The linearized form (4.18) is plotted as p/V_{ads} versus p , enabling a linear fit of

measurement data in low pressure range. In this equation, K_L is an empirical constant called Langmuir sorption coefficient. The correlation coefficient is aimed to be > 0.99 to achieve reliable values.^[323]

$$\frac{p}{V_{\text{ads}}} = \frac{1}{V_m K_L} + \frac{p}{V_m} \quad (4.18)$$

The specific surface area resulting from Langmuir approach S_L is described in (4.19), where V_{mol} is the molar volume of the gas.

$$S_L = \frac{V_m N_A \sigma}{m V_{\text{mol}}} \quad (4.19)$$

For many years, estimation of the pore size was performed using the Kelvin equation. From this, further specification led to more developed methods. Nowadays, the model from Barrett, Joyner and Halenda (BJH) is widely used. It combines the Kelvin equation with a standard isotherm (t -plot), considering the desorption of pre-adsorbed multilayer films in cylindrical pores. However, BJH method significantly underestimates the pore size of mesopores smaller than 10 nm by up to 30 %.^[321] Furthermore, as only the desorption branch of the isotherm is taken into account, network effects and bottle-neck pores can lead to misleading results. Alternatively, density functional theory (DFT) methods are on the rise. They describe the adsorption and phase behavior of fluids in confined solid spaces on a molecular level and are therefore also valid for small pores.^[325] The liquid-solid interaction potential of the molecules strongly depends on the pore shape, which is why various pore shapes (*e.g.* slit, cylindrical, spherical) and different adsorbates can be chosen (carbon, zeolites, silica). With DFT based methods, which are already commercially available and also mentioned in ISO standard (15901-1), a wide range of micro- and mesopore sizes can be characterized yielding reliable pore size distributions.^[325]

4.5.1 N_2 Physisorption

N_2 physisorption measurements of nanoparticle and mesoporous powder samples were performed on a *Quadrasorb evo* (QUANTACHROME) at 77 K. All samples were degassed at 120 °C prior to the measurement. Data analysis was performed using *ASiQWin* software (Version 4.0, QUANTACHROME).

A first evaluation of N_2 physisorption data using BET method revealed C values lower than zero, indicating a non-ideal adsorption behavior of nitrogen on the samples surfaces. Instead, surface area of ferrite nanoparticle and powder samples was determined by Langmuir model with linear fit of the

adsorption isotherm below $p/p_0 = 0.35$. The correlation coefficient was found > 0.99 for all analyzed samples. The adsorption branch was chosen, as desorption can overshadow pore blocking effects in porous samples.

In this work, non-local DFT (NLDFT) was chosen for pore volume and pore size analysis of all reported samples. For pore analysis, a suitable model needs to be applied. As there was no model for iron oxide materials, NLDFT model of gas adsorption on silica (cylindrical pores) was chosen for analysis of nanoparticle and powder samples. To exclude effects of pore blocking, only the adsorption branch of N_2 physisorption isotherms was analyzed. To see if this a suitable model system, NLDFT fits were evaluated first. In Figure 4.12, selected fits are shown.

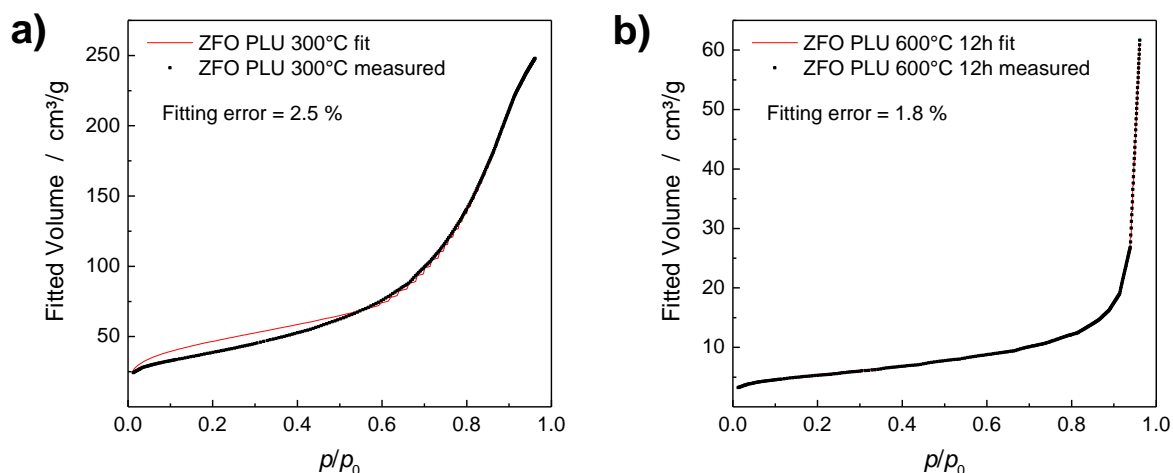


Figure 4.12: Fitting comparison (NLDFT adsorption model) of N_2 physisorption data for $ZnFe_2O_4$ porous powders calcined at a) 300 °C and b) 600 °C.

The fitting errors vary between 1.8 % and 2.5 %, indicating reasonably well fitted isotherms. For higher relative pressures, the fitting is very accurate but in the range of $p/p_0 = 0.1 - 0.5$, the fitting has lower quality. As this area has only negligible influence on the calculation of the pore diameter d_p , all NLDFT fits were accepted for data analysis.

4.5.2 Kr Physisorption

Krypton physisorption measurements at 77 K were conducted with an *AUTOSORB-iQ* setup (QUANTACHROME). All thin films were degassed prior to the physisorption measurements at 120 °C for 60 hours or 300 °C for 5 hours, respectively. Data analysis was performed using *ASiQWin* software (Version 4.0, QUANTACHROME). The BET model was used for surface area determination, as C constant values showed sufficient quality (all > 20). The cross-sectional area was chosen to be σ_m of 0.205 nm² per Kr atom.

4.6 Characterization of Colloidal Solutions

Wolfgang Ostwald was one of the first researchers to investigate the features of nanosized colloidal compounds. With his publication in 1948, he created the basis for modern nanomaterials and colloid research.^[326] Nobel laureate Hermann Staudinger divided colloids into three groups: dispersoid colloids (lyophobic), micellar colloids (lyophilic, *e.g.* surfactants), and molecular colloids (lyophilic, *e.g.* polymers).^[327]

A theory to describe the stability of lyophobic colloids was described by Derjaguin, Landau, Verwey and Overbeek and is widely known as DLVO theory.^[329,330] It describes an energy course depending on the particle-particle distance and is shown in Figure 4.13. Evraers *et al.* described all interactions within a colloidal system as sum of the individual Lennard-Jones-potentials of each nanoparticle.^[331] The Lennard-Jones-potential ϕ_L is the sum of attractive and repulsive forces ϕ_A and ϕ_R , which depend on the permittivity of the solvent ϵ and the particle size a . As attractive forces, Van der Waals, London and dipole-dipole interactions need to be mentioned. Typical repulsive forces are Born repulsion and bilayer repulsion. Generally, the attractive interaction ϕ_A between two particles is described as

$$\phi_A = -4\epsilon \left(\frac{a}{D}\right)^6 \quad (4.20)$$

and the repulsive forces ϕ_R due to Born repulsion are defined as

$$\phi_R = 4\epsilon \left(\frac{a}{D}\right)^{12} \quad (4.21)$$

Here, a different dependence on the interparticle distance D becomes evident. The attractive interactions are proportional to D^{-6} , while the repulsive ones are proportional to D^{-12} . Therefore, a critical distance between the particles can be found, where the attractive forces exceed the repulsive

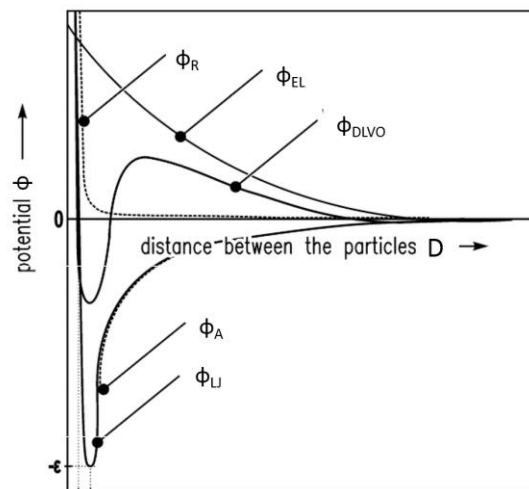


Figure 4.13: Potential curve according to DLVO theory adapted from Sahabi *et al.*^[328]

forces and agglomeration occurs. For DLVO theory, an additional term for electrostatic repulsion is added.

$$\phi_{EL} = \frac{2\pi r \epsilon_0 \epsilon \kappa \psi^2}{\kappa} e^{-\kappa(D-2r)} \quad (4.22)$$

Here, ψ is the surface potential, ϵ is the permittivity of the solvent, and κ is the inverse screening length. The resulting potential ϕ_{DLVO} (4.23) and its components are depicted in Figure 4.13.

$$\phi_{DLVO} = \phi_A + \phi_R + \phi_{EL} = \phi_L + \phi_{EL} \quad (4.23)$$

Due to the interplay of the different forces, minima and maxima occur. The secondary minimum at large particle distances is the region of colloidal stability. When the interparticle distance decreases, a maximum is reached due to repulsive forces, which marks the energy barrier for coagulation. With a large energy barrier, coagulation is unlikely and the colloid is referred to as stable. With low energy barriers close to zero, the interparticle distance shortens easily, shifting the energy into the primary minimum. Then, coagulation appears, which is irreversible.

Two forms of stabilization of dispersoid colloids are common, namely steric and electrostatic stabilization, which are schematically shown in Figure 4.14. Steric stabilization appears, when

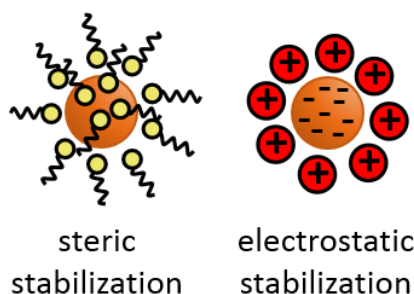


Figure 4.14: Steric and electrostatic stabilization in dispersoid colloids.

nanoparticles are functionalized with long-chain organic molecules or polymers. The organic functionalities bound to the nanoparticle surface show repulsive effects due to steric interaction. Therefore, the distance cannot fall below the length of the organic moieties, which prevents coagulation. This mechanism is only active, if the surrounding solvent matches the polarity of the steric units, as only this allows them to unfold to their full length.

When particles are immersed in a solvent, different attractive and repulsive forces occur. In aqueous solution, OH groups are formed at the surface of metal oxide nanoparticles. Depending on the pH value of the solution, these OH groups will be protonated or deprotonated, resulting in a charged surface of the bare nanoparticle.

With electrostatic stabilization, the stabilizing ligand accumulates at the nanoparticle surface due to attractive interactions between the oppositely charged surface and the ligand ions. As a result, an electric double layer is generated (see Figure 4.15).^[332] Due to the stronger repulsion of these highly-charged nanoparticles, the energy barrier is increased, which leads to more stable colloids. In close proximity to the solid surface, an immobile double layer of ligand ions is formed, which is called Stern layer (after Otto Stern)^[333], followed by a diffuse layer of ligand ions. This diffuse layer is mobile, but still strongly attracted by the charged

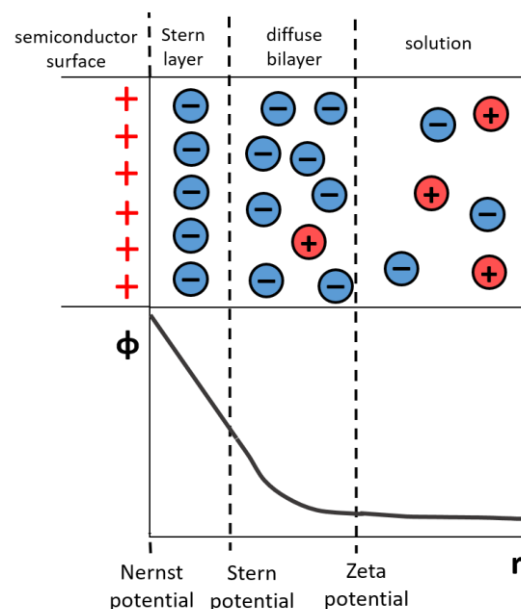


Figure 4.15: Formation of electric double layer.

solid surface. The interface between the diffuse layer and the solution, where all ions are statistically distributed, is called slipping plain. The interfaces between the layers have specific potentials, which are the Nernst potential at the solid-liquid interface, the Stern potential between the Stern layer and the diffuse layer, and the Zeta potential ξ at the slipping plane, which is defined as

$$\xi = \frac{z \cdot e}{4\pi \epsilon_0 \epsilon a} \quad (4.24)$$

Colloidal solutions are called stable, when their zeta potential is either larger than 30 mV or lower than -30 mV.^[332] With zeta potentials in between these values, coagulation or agglomeration can occur, depending on the zeta potential strength. At a zeta potential of 0 mV, the isoelectric point (IEP) is reached. The potentials caused by the ions are dependent on the ionic strength and their concentration in solution. The minimum concentration to prevent coagulation is called critical coagulation concentration (ccc), which is described by the Schulze-Hardy-rule.^[334]

As the energy barrier is large when attractive forces are low and repulsive forces are high, several parameters can increase this barrier. Mainly, the surfactant concentration has a strong influence. It can increase the zeta potential and therefore also the repulsive interactions. In addition, the particle size plays an important role concerning the attractive and repulsive interactions according to equations (4.20) and (4.21). This is one reason, why stable colloids of small nanoparticles can be obtained more easily, whereas large particles (several micrometers) heavily tend to agglomerate.

When nanoparticles, which are functionalized with non-polar ligands, are exposed to polar solvents, the organic molecules constrict and the steric repulsion is lost, leading to coagulation. If only coagulation occurred, then exposure to non-polar solvents leads to unfolding of the steric units, resulting in stable non-polar colloids again. This can be used to purify freshly synthesized non-polar

colloids from synthesis residues, as this is a common washing procedure for sterically stabilized colloids and was also applied in the present work.

Destabilization of electrostatically stabilized colloids is caused by dilution of the solution or addition of strong ionic substances, as this changes the potential of the solution. Usually, this destabilization is non-reversible. For soft destabilization, a polar organic solvent (*e.g.* acetone) can be carefully added, which would allow redispersion in the original solvent after removal of the precipitation agent. This technique was used for purification of electrostatically stabilized ferrite nanoparticles in this work.

4.6.1 Dynamic Light Scattering

The hydrodynamic radius of surface-functionalized nanoparticles was analyzed using dynamic light scattering (DLS). Diluted solutions of stabilized nanoparticles in suitable solvents (*e.g.* water, toluene) were measured at a *Zetasizer Nano ZS* (MALVERN) at a temperature of 25 °C. The scattered laser beam (He/Ne, $\lambda = 633$ nm) was detected in an angle of 173°. Every sample was measured five times to calculate average hydrodynamic diameters according to the particle number distribution. A refractive index of 2.39 for MgFe_2O_4 and 2.36 for ZnFe_2O_4 was assumed.^[335]

4.6.2 Zeta Potential measurements

For information on their zeta potential, aqueous solutions of electrostatically stabilized nanoparticles were measured at a *Zetasizer Nano ZS* (MALVERN). Samples were filled into a polycarbonate DTS capillary cuvette (MALVERN) and placed into the device at a temperature of 25 °C at the original pH value of the investigated solution (8 mg mL^{-1}). Every sample was measured three times to calculate an average zeta potential.

4.7 Photocatalytic Degradation Experiments

For photocatalytic degradation experiments, aqueous solutions of rhodamine B ($c = 10^{-5} \text{ mol L}^{-1}$) and tetracycline ($c = 10^{-4} \text{ mol L}^{-1}$) were prepared. A defined volume of 20 mL of model compound

solution was transferred into a glass vessel, which was wrapped with aluminum foil to exclude scattered light. For blank experiments, only the freshly-synthesized solutions were used. For all other experiments, 10 mg of photocatalyst was added to the solution, leading to a nanoparticle concentration of 0.5 mg mL^{-1} . Sufficient homogenization was achieved by permanent treatment inside an ultrasonic bath operated at 100 % power and 37 kHz, which was equipped with a cooling system to maintain the temperature at $20 \text{ }^\circ\text{C}$. The experimental setup is shown in Figure 4.16.

Before the samples were exposed to solar light, the reaction mixtures were treated in an ultrasonic bath in the dark for 30 min to achieve an adsorption-desorption equilibrium. Then, the solutions were placed underneath the solar simulator (150 W, NEWPORT ORIEL Sol 1A). The photon flux of $9.246 \cdot 10^{-7} \text{ mol s}^{-1}$ was determined by ferrioxalate actinometry prior to the experiments.

Of each sample, 3 mL of solution were taken at the start of the experiment, after 30 min equilibration in the dark and every 30 min during the illumination period. These solutions were then centrifuged for 5 min at 10000 rpm to remove the solid photocatalyst, before measuring UV-Vis spectra as described in chapter 4.2.2.

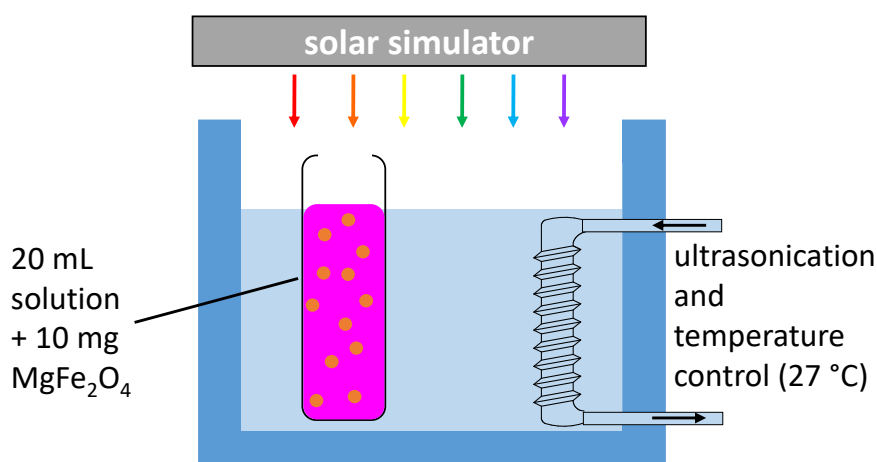


Figure 4.16: Experimental setup used for photocatalytic degradation of model compounds.

4.8 TOC Analysis

The analysis of total organic carbon (TOC) is based on the combustion of organic compounds, which are dissolved in aqueous solutions. The evolving carbon dioxide (CO_2) is detected via IR photometry. By this means, conclusions on the degree of mineralization during degradation experiments can be drawn.

All measurements were performed on a 2010 K1 model (DIMATOC). The samples were acidified to convert inorganic carbonates into CO₂. This inorganic CO₂ is then removed by degassing with synthetic air. Afterwards, 100 μL of the aqueous sample are injected into a reactor at 850 °C to burn the sample in O₂ atmosphere. The emerging CO₂, which results from all organic compounds contained in the sample, was detected using a non-dispersive IR detector.

4.9 Photoelectrochemical Methods

All photoelectrochemical measurements were performed on a *Zennium* potentiostat (ZAHNER) using a three electrode combination. Samples were mounted as working electrodes in a PTFE cell with quartz window (ZAHNER, Figure 4.17), which was also equipped with a platinum wire counter electrode. The reference electrode was Ag/AgCl in 3 M NaCl solution. A glass junction filled with 3 M NaCl was used to protect the reference electrode from corrosive electrolyte solution. For experiments under illumination, the illuminated area was fixed to 1 cm².

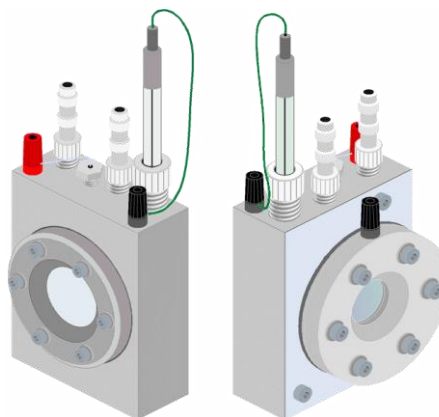


Figure 4.17: PEC cell (adapted from ZAHNER).^[336]

4.9.1 Mott-Schottky Measurements

Mott Schottky measurements were performed in the dark, sweeping the potential by 50 mV s⁻¹. The analysis range and scanning direction were chosen in regard to the estimated band positions and semiconductor doping type of the analyzed samples. For ZnFe₂O₄ mesoporous photoanodes, the potential was changed from 1.63 V_{RHE} to 0.18 V_{RHE} with a sweep of 50 mV s⁻¹, for MgFe₂O₄ it was changed from 1.63 V_{RHE} to 0.18 V_{RHE} with a sweep of 10 mV s⁻¹ and for CaFe₂O₄ it was changed from 0.20 V_{RHE} to 1.40 V_{RHE} with a sweep of 10 mV s⁻¹. The frequency was set to 100 Hz and the potential amplitude was 5 mV. Flat band potentials and donor densities were calculated using the Mott Schottky

equation (equation (2.7)). The relative permittivity of the absorber materials were assumed to be $\epsilon(\text{ZnFe}_2\text{O}_4) = 150^{[337]}$, $\epsilon(\text{MgFe}_2\text{O}_4) = 32^{[274]}$ and $\epsilon(\text{CaFe}_2\text{O}_4) = 10^{[338]}$.

4.9.2 Photocurrent Measurements

For photocurrent measurements under continuous and discontinuous irradiation, two different light sources were used. On the one hand, a white light LED (1000 W/m², $\lambda \geq 400$ nm, ZAHNER) was used for evaluation of the photoactivity during visible light excitation. On the other hand, one sun illumination was used employing a Xe arc light source (300 W, LOT-QUANTUMDESIGN) equipped with an AM 1.5 G filter operated in a distance of 16 cm from the working electrode surface. The potential range was chosen in regard to the analyzed compound. For p-type semiconductor CaFe₂O₄, the potential was shifted from more negative values to more positive values with a slew rate of 5 mV s⁻¹. For n-type semiconducting MgFe₂O₄ and ZnFe₂O₄, the potential range was scanned *vice versa* with the same sweep rate. For discontinuous illumination experiments, a period of 5 s illumination time followed by 5 s of dark conditions was chosen. In some cases, 10 s of illumination and 10 s of dark conditions was used for better identification of the equilibrium state.

4.9.3 Incident Photon-to-Current Conversion Efficiency

For IPCE measurements, the TLS unit from ZAHNER was used. The measurements were conducted at a constant potential of 0.1 V and a frequency of 100 mHz. For front side illumination, the installed LEDs with wavelengths at $\lambda = 292, 308, 318, 339, 358, 368, 385, 397, 408, 429, 455, 479, 523, 532, 574,$ and 593 nm were utilized. The measurements were performed in the presence as well as in the absence of suitable sacrificial agents to characterize the photoelectrode materials.

4.10 Time of Flight Secondary Ion Mass Spectrometry

Time of Flight Secondary Ion Mass Spectrometry (ToF-SIMS) measurements were performed with a 5-100 model (ION-TOF GMBH) in the negative mode. Bismuth ions (Bi⁺) were accelerated with 25 keV and with a cycle time of 60 s. Depletion of a 200 x 200 nm² large area of the solid compound was realized with Cesium ions (Cs⁺, 1 keV). From this, an inner area of 100 x 100 nm² was analyzed. After 0.5 s of delay, 1 s in 10 s sputter time was used to record a mass spectrum.

5 Results and Discussion

5.1 Nanoparticles

5.1.1 Ferrite Nanoparticles

5.1.1.1 Microwave-Assisted Synthesis of Ferrite Nanoparticles

Synthesis efforts to produce phase-pure ZnFe_2O_4 and MgFe_2O_4 nanoparticles were based on a procedure reported by Suchomski and co-workers.^[106] This approach was developed for microwave-assisted synthesis of very small ZnFe_2O_4 nanoparticles. Adjustment regarding the synthesis temperature alongside adaption for synthesis of MgFe_2O_4 were made prior to the start of this work.^[339] The optimized conditions (30 min 275 °C) under microwave-assisted synthesis were used as basis for all further experiments described in this thesis. For both, ZnFe_2O_4 and MgFe_2O_4 , spherical crystalline nanoparticles were obtained after 30 min of microwave-assisted synthesis at 275 °C according to chapter 3.2.1.2. Phase purity was checked using XRD and Raman analysis.

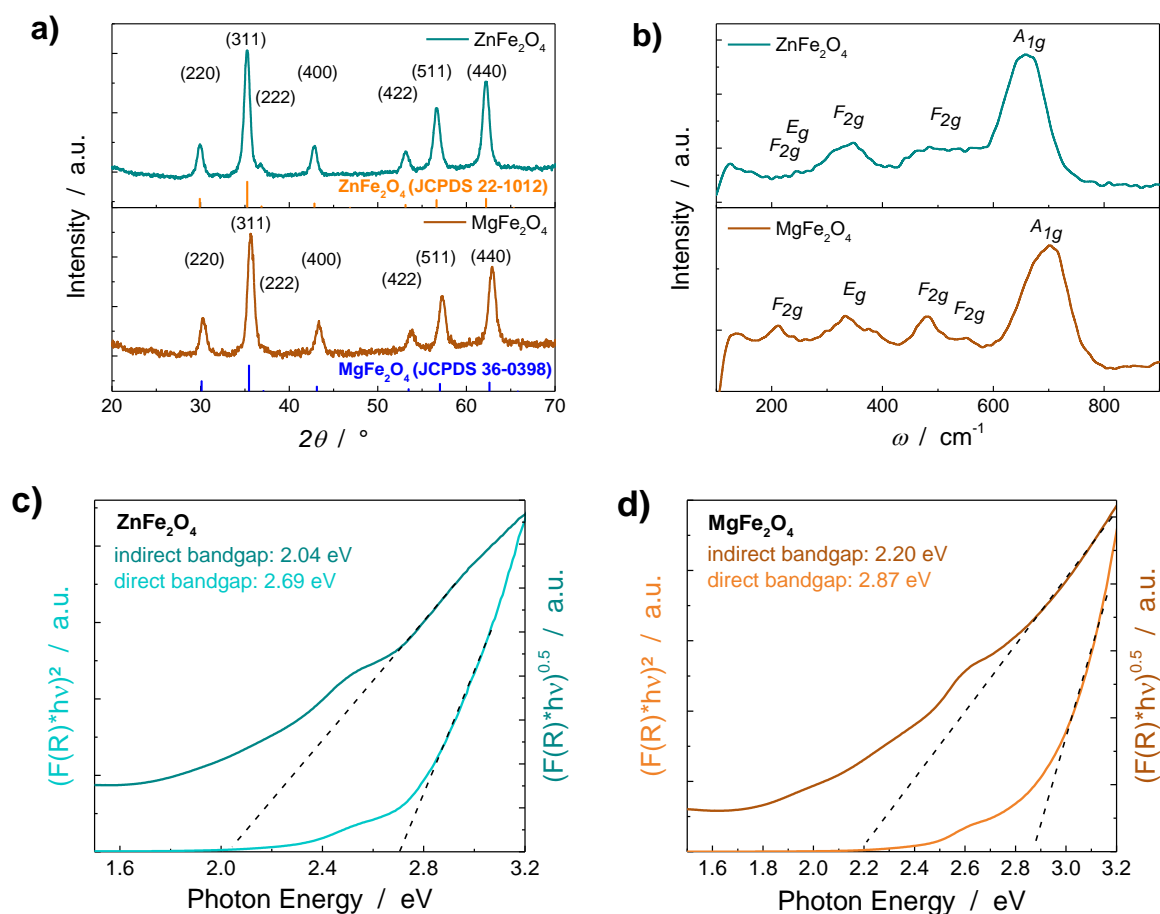


Figure 5.1: a) XRD patterns, b) Raman spectra and c-d) DR-UV/Vis spectra recorded for ZnFe_2O_4 and MgFe_2O_4 nanoparticles obtained from microwave-assisted synthesis (d) adapted from literature^[1].

As shown in Figure 5.1a, all reflections detectable in the XRD patterns can be assigned to reference patterns (JCPDS card no. 22-1012 for ZnFe_2O_4 and JCPDS card no. 36-0398 for MgFe_2O_4). An average crystallite size of 8.6 nm for ZnFe_2O_4 and 3.2 nm MgFe_2O_4 was achieved according to Rietveld refinement (Table 9.1). For cubic spinel (AB_2O_4) compounds, five Raman active modes originate from lattice vibrations in tetrahedral (AO_4) or octahedral (BO_6) coordination.^[216] The predicted modes were found in the Raman spectra (see in Figure 5.1b). All vibrations found below 600 cm^{-1} result from BO_6 vibrations. For ZnFe_2O_4 , a very distinct F_{2g} mode can be seen. Additionally, two F_{2g} and an E_g modes of rather weak intensity match literature reports.^[216] The A_{1g} mode, which originates from tetrahedral lattice vibrations, consists of a mode at 702 cm^{-1} and a shoulder at 653 cm^{-1} due to partial inversion of the normal spinel structure. This was already reported by Thota *et al.*^[340] A similar pattern can be seen for MgFe_2O_4 . A qualitative difference between MgFe_2O_4 and ZnFe_2O_4 is visible. Especially the F_{2g} and E_g modes are more intense for MgFe_2O_4 , while ZnFe_2O_4 shows only one prominent F_{2g} . This difference occurs due to different degree of inversion. ZnFe_2O_4 is reported to be a normal spinel with only very low degree of inversion, while nanosized MgFe_2O_4 is reported to have random cation distribution.^[219,341] Therefore, in both ferrites the octahedral and tetrahedral lattice sites are not equally occupied by B^{3+} and A^{2+} ions.

Tauc plots from DR-UV/Vis spectra are shown in Figure 5.1c-d. The direct band gaps are found to be 2.69 eV and 2.87 eV for ZnFe_2O_4 and MgFe_2O_4 , respectively, which arise from charge transfer excitation from oxygen ligands to Fe^{3+} . The indirect band gaps, being smaller, were found to be 2.04 eV and 2.20 eV. They are attributed to the Fe^{3+} d-d transition. This suggests that both ferrite compounds are indirect band gap semiconductors (compare Figure 2.8), which makes them suitable for photocatalytic applications due to longer-lived charge carriers. The values match well with reports from literature.^[246,342–344] As the average crystallite size of MgFe_2O_4 is much smaller compared to ZnFe_2O_4 , the larger band gap values might be due to a quantum size effect.

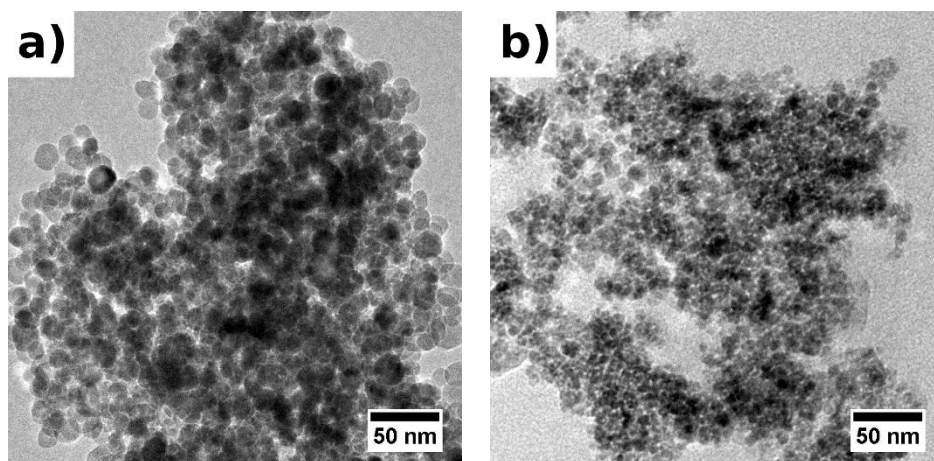


Figure 5.2: TEM images of microwave-derived a) ZnFe_2O_4 and b) MgFe_2O_4 nanoparticles.

TEM images depicted in Figure 5.2 reveal the spherical, monocrystalline nature of ZnFe_2O_4 and MgFe_2O_4 . The difference in particle size is consistent with average crystallite sizes obtained by Rietveld refinement. For ZnFe_2O_4 , an average particle size of 10 nm was estimated according to TEM analysis. MgFe_2O_4 nanoparticles were found to be significantly smaller (around 5 nm). Besides, a strong tendency for agglomeration can already be estimated from the size of agglomerates shown in TEM images.

In contrast to magnesium and zinc derived spinel compounds, it was not possible to synthesize CaFe_2O_4 *via* the microwave-assisted approach. One reason for this is the significantly different thermal stability of the chosen precursors. The thermal decomposition of different acetylacetonate precursors can be seen in Figure 5.3.

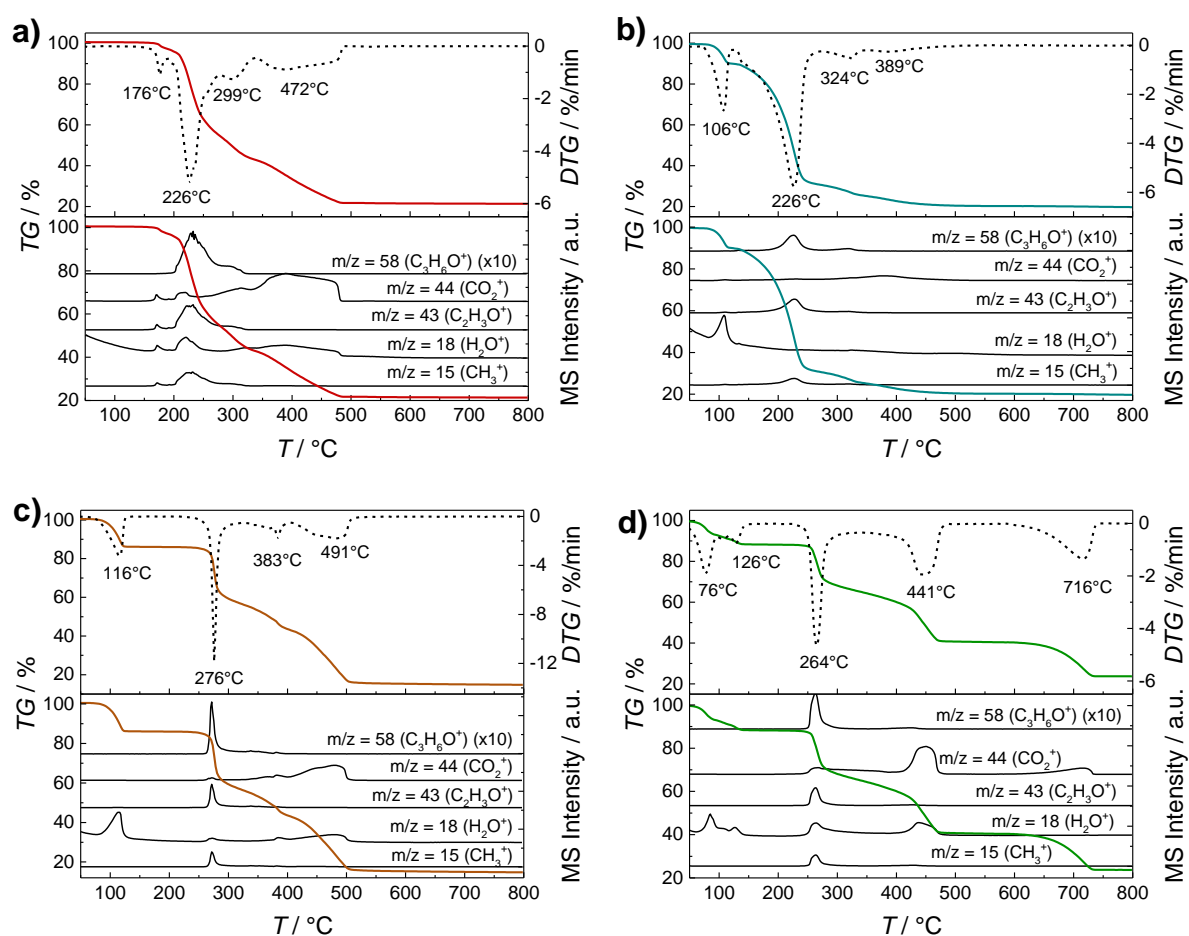


Figure 5.3: TG, DTG and MS traces of a) $\text{Fe}(\text{acac})_3$, b) $\text{Zn}(\text{acac})_2$, c) $\text{Mg}(\text{acac})_2$ and d) $\text{Ca}(\text{acac})_2$.

From TG and DTG data, it becomes evident, that $\text{Fe}(\text{acac})_3$ and $\text{Zn}(\text{acac})_2$ show similar decomposition behavior with main mass losses at 226 °C, which are due to decomposition of the acetylacetonate backbone indicated by MS traces of organic fragments ($m/z = 15; 43; 44; 58$). With $\text{Mg}(\text{acac})_2$, this decomposition occurs at 276 °C, which meets the reaction temperature. For all samples, mass losses around 110 °C can be assigned to water desorption ($m/z = 18$). Further MS traces

detected for $\text{Fe}(\text{acac})_3$, $\text{Zn}(\text{acac})_2$ and $\text{Mg}(\text{acac})_2$ at higher temperatures up to 491 °C indicate complete mineralization of the acetylacetonate precursor to CO_2 and H_2O ($m/z = 15; 18$). In contrast, $\text{Ca}(\text{acac})_2$ shows a very different thermal decomposition pattern with a multistep weight loss profile in TG analysis (Figure 5.3d). Although the main decomposition step at 264 °C meets the temperature of 275 °C used in a typical synthesis, the complexity of decomposition might lead to slower reaction kinetics compared to $\text{Fe}(\text{acac})_3$, therefore inhibiting calcium incorporation. The microwave-assisted synthesis with very fast reaction course might not be beneficial for synthesis with precursors showing delayed decomposition behavior. Furthermore, the synthesis path with choice of precursors, solvent and maximum synthesis temperature was designed for fabrication of spinel type ferrites. As already discussed, CaFe_2O_4 obtains an orthorhombic structure with distorted octahedra. With this more complex structure, the synthesis path developed for ZnFe_2O_4 by Suchomski *et al.*^[106] and adapted for MgFe_2O_4 ^[1] might not be applicable for CaFe_2O_4 . Due to this, synthesis of CaFe_2O_4 under microwave-assisted synthesis conditions was not pursued any further.

5.1.1.2 Variation of Synthesis Period

As already mentioned, prior to this work the optimization of MgFe_2O_4 nanoparticle synthesis in terms of reaction temperature was investigated and discussed^[339]. Consequently, in this work the influence of synthesis time on the formation of ZnFe_2O_4 and MgFe_2O_4 nanoparticles will be elucidated. For this, the synthesis time at 275 °C was varied between 10 min and 30 min. Development of crystallite formation was followed by XRD analysis (Figure 5.4a). Again, after all reaction periods, phase pure ferrite nanoparticles were obtained as comparison with reference patterns suggests.

The data was evaluated using Rietveld refinement to obtain average crystallite sizes and microstrain values of all samples (Figure 5.4b, for details see Table 9.1). As evident, ZnFe_2O_4 nanoparticles show significantly larger crystallite sizes compared to MgFe_2O_4 . This might be assigned to the lower decomposition temperature of $\text{Zn}(\text{acac})_2$ (226 °C), which leads to higher free Zn^{2+} concentration in solution, when the reaction is performed at 275 °C. Due this higher oversaturation, larger particles can grow. The crystallite size increases only slightly when comparing samples obtained after 10 min and 30 min of synthesis time. The same trend can be seen for microstrain, which slightly decreases with increasing nanoparticle size. Inhomogeneous microstrain, which causes peak broadening in XRD reflections, is an indicator of crystal defects such as interstitials or vacancies. As the value stays almost constant for all synthesis periods, there was no influence found on the defect concentration of microwave-derived MgFe_2O_4 and ZnFe_2O_4 nanoparticles.

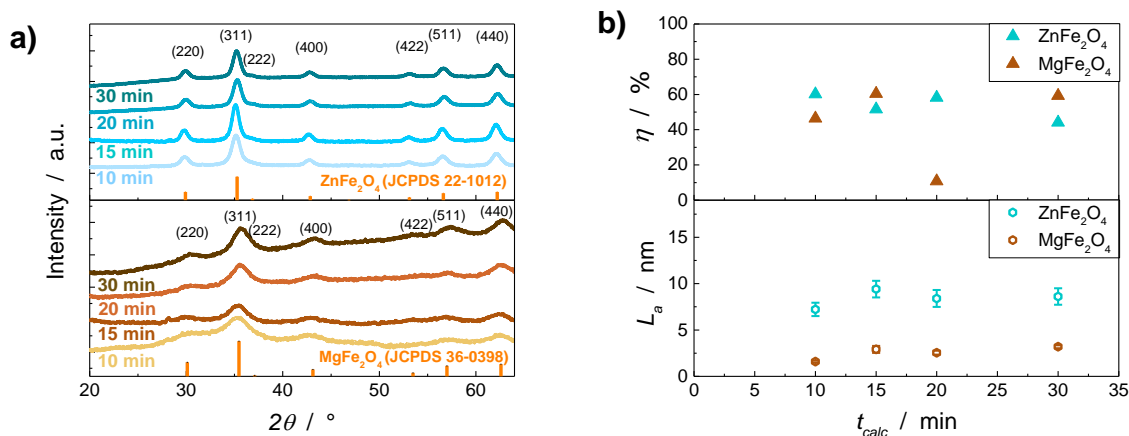


Figure 5.4: a) XRD patterns as well as b) crystallite sizes (above) and microstrain values (below) of microwave-derived ZnFe₂O₄ and MgFe₂O₄ nanoparticles obtained after different synthesis periods.

The minor influence on the average crystallite size and microstrain of the obtained ferrite nanoparticles underlines the very fast reaction course of microwave-assisted synthesis, which is beneficial if highly crystalline materials are desired after short synthesis time.

5.1.1.3 Variation of the Reaction Setup

The aforementioned synthesis approach was developed and optimized for microwave-assisted synthesis. To evaluate, whether this approach is also applicable for standard high temperature synthesis, ZnFe₂O₄ nanoparticles were produced after the procedure described in chapter 3.2.1.1. The resulting nanoparticles are compared to microwave-derived nanoparticles.

Phase purity was confirmed using XRD and Raman analysis. The results depicted in Figure 5.5 show as-synthesized ZnFe₂O₄ from microwave-assisted (microwave) and high temperature reflux (batch) reaction paths. All reflections in the XRD patterns shown in Figure 5.5a-b match well with the reference pattern (JCPDS card no. 22-1012). An additional reflection detected at 32° 2θ for the batch-derived sample was assigned to an artefact caused by the sample holder and is marked with * in Figure 5.5b. Rietveld refinement gave comparable average crystallite sizes and microstrain values. Besides, all Raman vibrations (Figure 5.5c) were attributed to pure ZnFe₂O₄ phase.^[216] IR spectra recorded for both samples (Figure 5.5d) show vibrations at 554 cm⁻¹ for tetrahedral stretching and 420 cm⁻¹ for octahedral stretching assignable to ZnFe₂O₄.^[345] In addition, weak aliphatic C-H stretching and bending vibration signals at 2917 cm⁻¹ and 1017 cm⁻¹ as well as clear signals for carbonyl group stretching vibrations at 1555 cm⁻¹ and 1418 cm⁻¹ can be assigned to organic precursor residues and solvent molecules still present at the surface. The broad vibration around 3400 cm⁻¹ typical for O-H stretching vibrations with hydrogen bridging interaction indicates adsorbed water molecules.^[314]

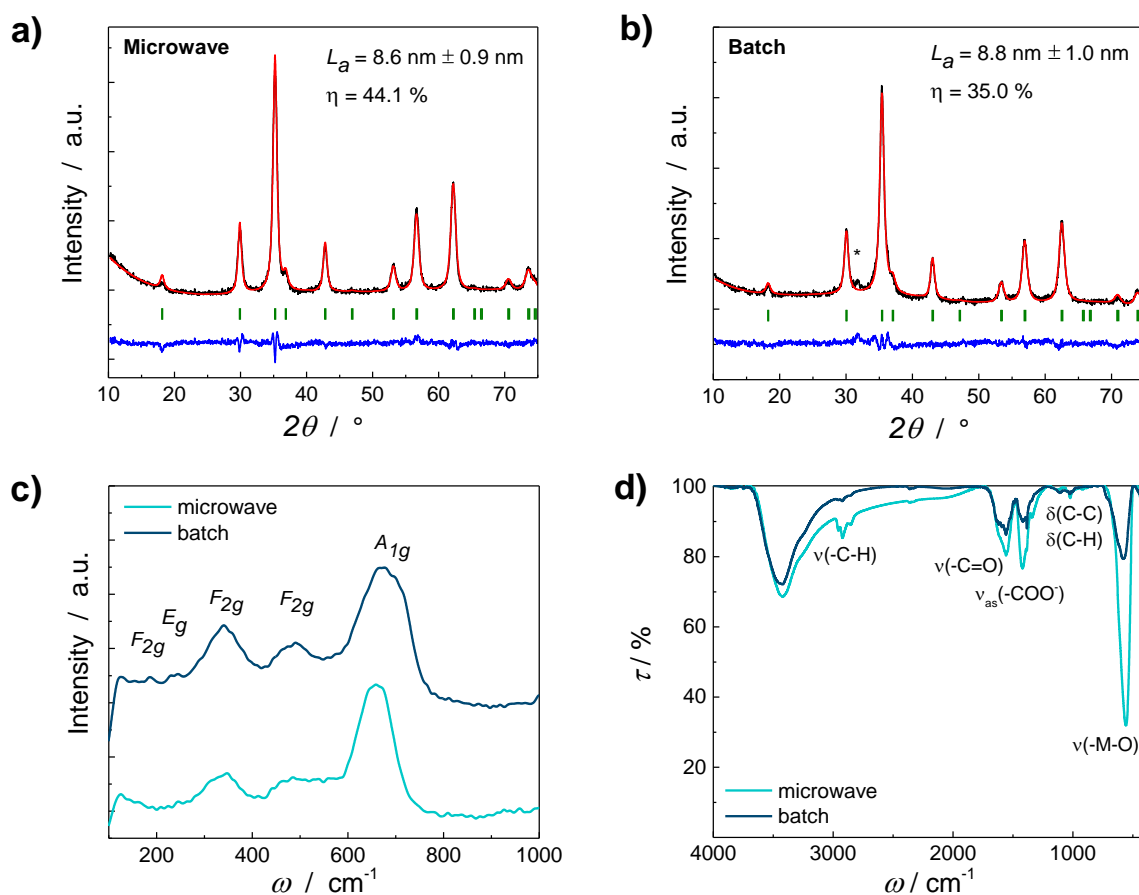


Figure 5.5: Rietveld refinements of a) microwave-derived and b) batch-synthesized ZnFe_2O_4 (* marks a reflection caused by the sample holder) as well as their c) Raman spectra and d) IR patterns.

TEM images (Figure 5.6) show spherical nanoparticles of rather uniform size, which are monocrystalline. Both, shape and size, found for batch-synthesized ZnFe_2O_4 nanoparticles match the results from microwave-assisted synthesis (compare Figure 5.2a). The heavily agglomerated sample suggests that the obtained nanoparticles do not form stable dispersions.

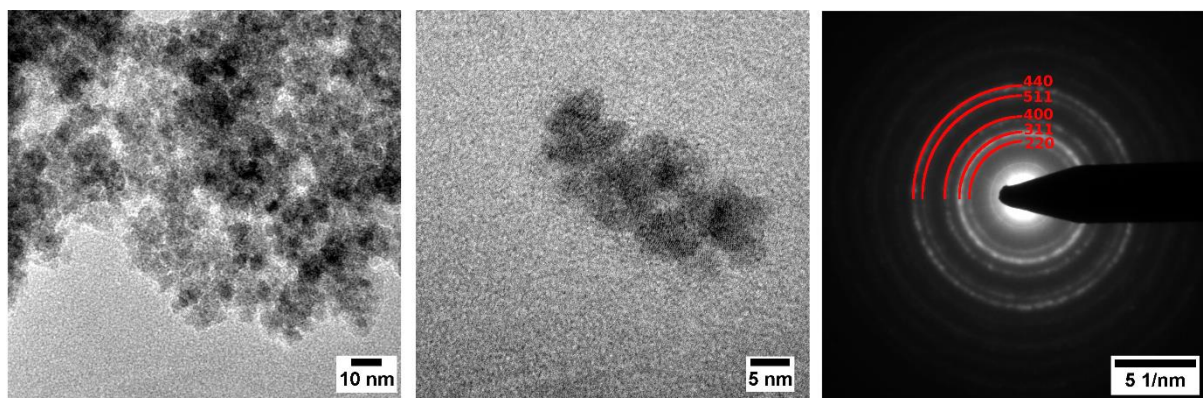


Figure 5.6: TEM images of batch-synthesized ZnFe_2O_4 nanoparticles.

For well-dispersed nanoparticles, surface functionalization would be necessary, which will be discussed later on (see chapter 5.2). In general, both samples exhibit comparable crystallite sizes, microstrain values and surface agents alongside their highly phase pure nature. This allows the conclusion, that high temperature reflux synthesis according to the developed synthesis (chapter 3.2.1.1) is well suitable for production of phase pure, crystalline ZnFe_2O_4 nanoparticles, if there is no microwave reactor available.

However, the attempt to produce MgFe_2O_4 nanoparticles via reflux synthesis was not successful, as the $\text{Mg}(\text{acac})_2$ used as magnesium precursor was not decomposable at the maximum reflux temperature. Therefore, only microwave-derived nanoparticles are subject of this thesis.

5.1.1.4 *Post-synthetic Calcination of Zinc Ferrite Nanoparticles*

As neither the synthesis time nor the synthesis setup influences the size, a post-synthetic heat treatment was applied for ZnFe_2O_4 nanoparticles to identify the impact of calcination on the crystallite size and phase purity. For the influence of post-synthetic thermal treatment on microwave-derived MgFe_2O_4 nanoparticles, the reader is referred to a report by A. Becker, which investigated this aspect in detail prior to the work presented here.^[339]

Microwave-derived ZnFe_2O_4 nanoparticles were heat treated after synthesis for one hour in air in a temperature range between 400 °C and 600 °C (for details see 3.2.1.3). In Figure 5.7, a sample analyzed directly after synthesis (as-syn) is compared to samples calcined at 400 °C, 500 °C and 600 °C. The XRD patterns (Figure 5.7a) indicate a fully crystalline nature of all samples, as there was no amorphous underground detected. No additional reflections originating from phase impurities are visible. Rietveld refinement of the XRD patterns gave the average crystallite sizes and microstrain values of all samples, which are shown in Figure 5.7b (for details see Table 9.1). No significant difference in crystallite size was found for the sample calcined at 400 °C, but the microstrain decreased. This was attributed to thermal healing of intrinsic defects. The almost linear decrease of microstrain due to loss of crystal defects and lower surface area goes along with the increase of crystallite size at 500 °C and 600 °C due to sintering at higher calcination temperature.^[88] Using N_2 physisorption and Langmuir equation (equation (4.19)), the surface area of calcined ZnFe_2O_4 nanoparticles was determined. As shown in Figure 5.7c (details given in Table 9.2), with increasing calcination temperature the surface area reduces from $118 \text{ m}^2 \text{ g}^{-1}$ for the as-synthesized sample to $26 \text{ m}^2 \text{ g}^{-1}$ after calcination at 600 °C. This is due to increased sintering leading to particle growth and therefore decrease of the surface area. Overall, post-synthetic calcination of ZnFe_2O_4 nanoparticles leads to larger crystallites, but on the cost of surface area. The phase purity of the material is not affect.

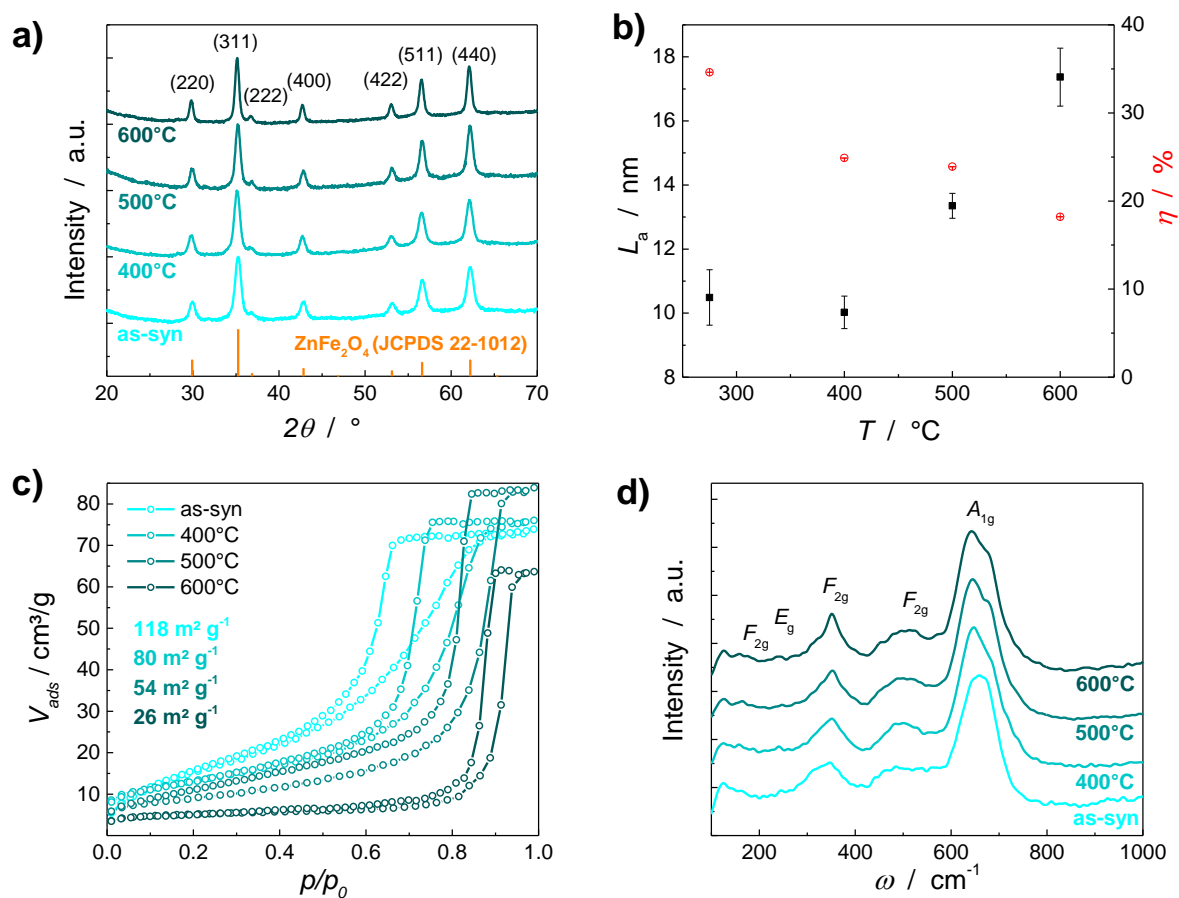


Figure 5.7: a) XRD patterns, b) average crystallite size and microstrain, c) physisorption isotherms and d) Raman spectra of microwave-derived, as-synthesized and calcined ZnFe_2O_4 nanoparticles.

5.2 Surface Functionalization

As previously mentioned, the synthesized ferrite nanoparticles tended to heavily agglomerate in both, polar and non-polar solvents. As dispersion stability was expected to improve surface accessibility with regards to potential applications, various approaches for synthesis of colloidal ferrite nanoparticles were taken. Figure 5.8 gives an overview on the methods successfully developed to achieve this. They will be illuminated in detail further on.

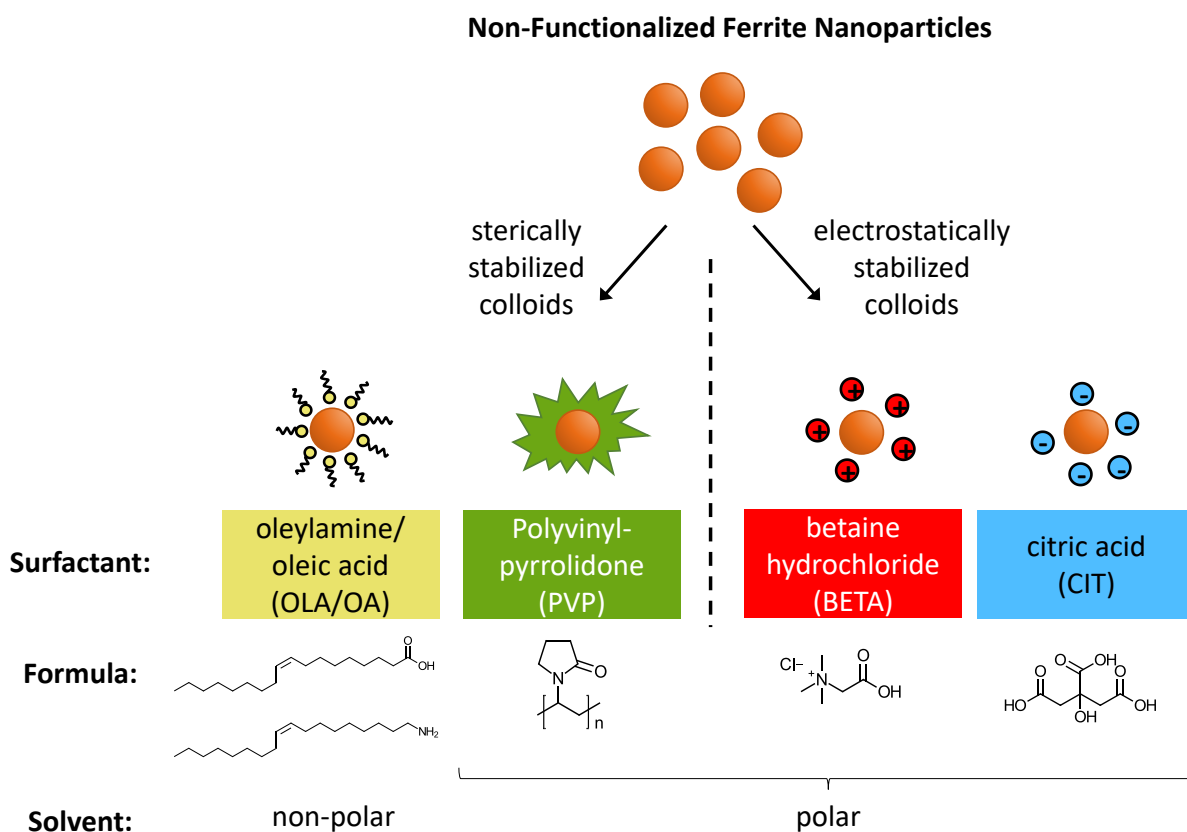


Figure 5.8: Surface functionalization approaches for ferrite nanoparticles.

5.2.1.1 Non-Polar Colloidal Solutions

In situ Surface Functionalization

For direct synthesis of oleylamine (OLA) and oleic acid (OA) functionalized ZnFe_2O_4 nanoparticles to obtain non-polar colloids, a procedure reported by Sun and co-workers was chosen.^[27] This method was used in reflux synthesis (Sun Batch) and was also adapted for microwave-assisted synthesis (Sun MW). As OLA and OA are very common capping agents for non-polar colloids and have been applied in various solvents during synthesis,^[268,277,346] a third approach was applied. There, the reaction mixture described in chapter 3.2.1.2 was mixed with 1.5 mL of OLA and 1.4 mL OA before microwave-assisted synthesis was performed (STD + OLA/OA).

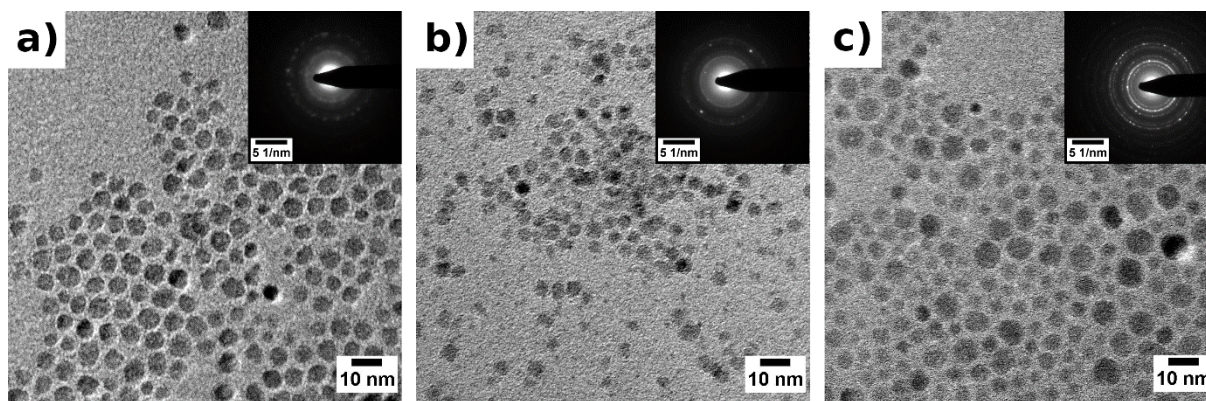


Figure 5.9: ZnFe_2O_4 nanoparticles obtained after a) Sun reflux approach, b) Sun microwave approach and c) addition of OLA/OA to the standard microwave synthesis.

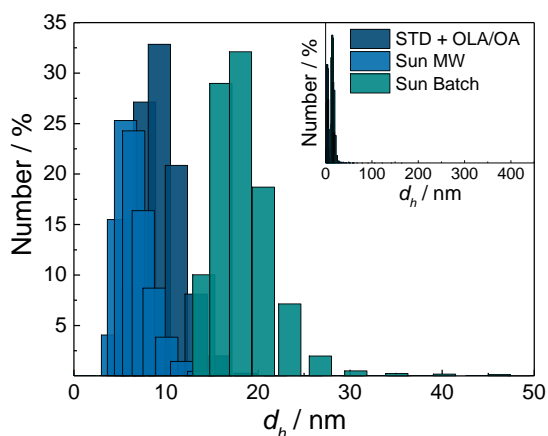


Figure 5.10: DLS measurements of *in situ* OLA/OA-capped ZnFe_2O_4 nanoparticles in toluene.

The batch synthesis was performed according to chapter 3.2.2.1. With this approach, a stable colloidal solution in toluene containing very uniform, spherical nanoparticles of around 8 nm was obtained as can be seen in Figure 5.9a. Synthesis of an identical reaction mixture under microwave heating at 275 °C yielded spherical nanoparticles with a broader size distribution (see Figure 5.9b). This might be caused by rapid heating and cooling combined with the missing ripening step, which is usually performed

during batch synthesis. When adding OLA and OA to the reaction mixture previously used for synthesis of phase-pure ZnFe_2O_4 nanoparticles, a stable colloidal solution of spherical nanoparticles with a rather broad size distribution was obtained (Figure 5.9c), which supports the theory of non-ideal reaction course to form monodisperse nanoparticles. All samples were found to be stable non-polar colloids with a small distribution of their hydrodynamic diameters according DLS measurement (Figure 5.10). Unfortunately, no phase pure ZnFe_2O_4 materials were prepared, as phase analysis using XRD and Raman spectroscopy revealed. In Figure 5.11a, XRD patterns of samples obtained from the three OLA/OA-assisted synthesis approaches are shown. These still match well with the reference pattern (JCPDS card no. 22-1012), not showing any impurity phases. However, when Raman spectra were collected, they revealed by-phases of maghemite ($\gamma\text{-Fe}_2\text{O}_3$) and ferrihydrite ($\delta\text{-FeOOH}$) formed during synthesis.^[33] The main A_{1g} mode of ZnFe_2O_4 at 647 cm^{-1} shows broadening and shifting due to the appearance of A_{1g} modes of $\gamma\text{-Fe}_2\text{O}_3$ (655 cm^{-1}) and $\delta\text{-FeOOH}$ (710 cm^{-1}).^[33,216] As Raman spectroscopy is a very sensitive technique for iron oxide analysis, even low amounts of phase impurities can be

detected in contrast to XRD, where amounts below 3 wt.% do not show reflections. This underlines the necessity of Raman analysis, if phase pure iron oxide based materials are desired and phase impurities are longed to be identified.

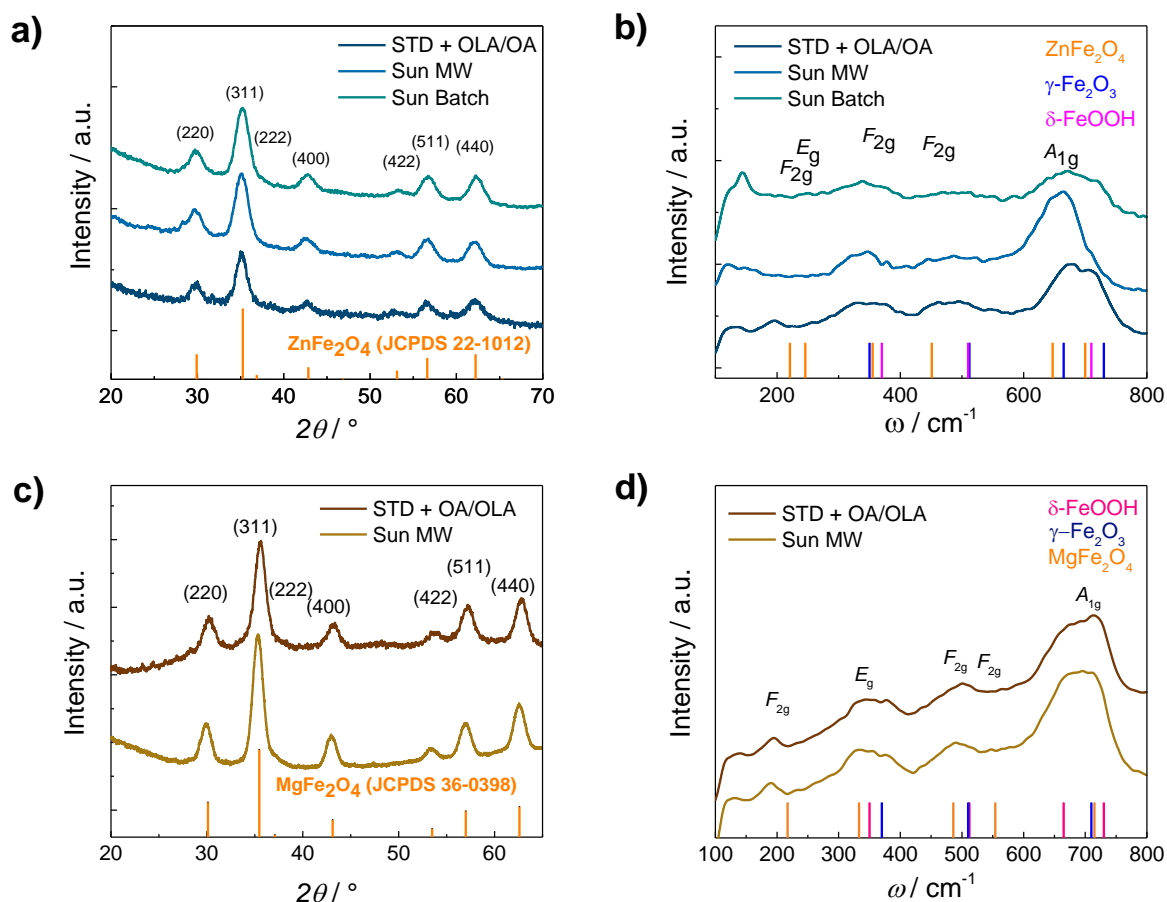


Figure 5.11: XRD patterns of *in situ* OLA/OA- functionalized a) ZnFe₂O₄ and b) MgFe₂O₄ nanoparticles and Raman spectra of *in situ* OLA/OA- functionalized c) ZnFe₂O₄ and d) MgFe₂O₄ nanoparticles synthesized by different approaches (c and d adapted from literature).^[1]

Comparable results were found, when *in situ* OLA/OA-stabilized MgFe₂O₄ nanoparticles were desired to be synthesized by a microwave-assisted heating approach (compare chapter 3.2.2.1). DLS measurements (Figure 9.1) showed well dispersed nanoparticles with a hydrodynamic diameter of 6.5 nm (after Sun et al.) and 10.8 nm (addition of OLA and OA), which is comparable to the nanoparticle size obtained by TEM analysis (Figure 9.2). XRD patterns appeared to be phase-pure, as no additional reflections from the expected signals for MgFe₂O₄ (JCPDS card no. 36-0398) were found (see Figure 5.11c). However, Raman analysis revealed the presence of impurity phases, which were formed during synthesis (see Figure 5.11d). In the *in situ* functionalized MgFe₂O₄ samples, especially δ -FeOOH is very prominent according to Raman analysis.

The formation of γ -Fe₂O₃ and δ -FeOOH is accounted to the presence of OLA and OA within the synthesis mixture, which apparently perform redox reactions during high temperature synthesis

leading to iron oxides apart from ZnFe_2O_4 and MgFe_2O_4 formation. Therefore, the idea of *in situ* functionalization of ZnFe_2O_4 and MgFe_2O_4 nanoparticles with OLA and OA was discarded.

Post-Synthetic Surface Functionalization

Instead of synthesis in the presence of OLA and OA, a post-synthetic functionalization of as-prepared, phase pure ZnFe_2O_4 and MgFe_2O_4 nanoparticles was performed according to the procedure described in chapter 3.2.2.2.

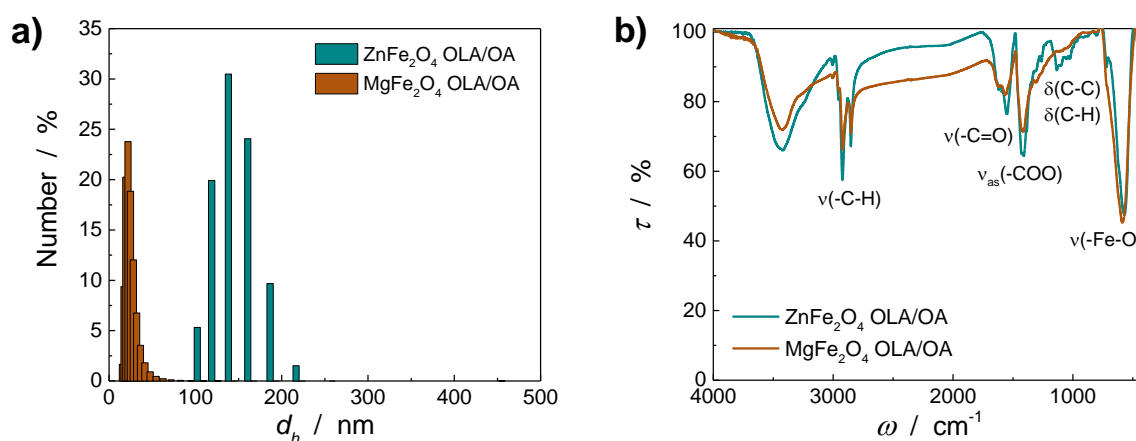


Figure 5.12: a) IR and b) DLS of post-synthetically OLA/OA-capped ZnFe_2O_4 and MgFe_2O_4 nanoparticles (data for MgFe_2O_4 adapted from literature).^[1]

The average size distribution obtained by DLS measurement (Figure 5.12a) reveals a larger average hydrodynamic diameter compared to *in situ* functionalized ZnFe_2O_4 and MgFe_2O_4 nanoparticles of 24.3 nm and 115 nm, respectively. This exceeds the nanoparticle size measured for non-functionalized nanoparticles of approx. 12 nm and 5 nm, respectively. Thus, the post-synthetic stabilization did not lead to agglomerate-free dispersions. Nevertheless, the average size distribution obtained by this approach shows rather small agglomerates and is therefore still acceptable for further sample processing.

Successful surface functionalization of ZnFe_2O_4 and MgFe_2O_4 nanoparticles was verified by IR analysis shown in Figure 5.12b. The obtained spectra contain all characteristic vibrations expected for OLA and OA.^[347] At 2924 cm^{-1} and 2855 cm^{-1} asymmetric and symmetric stretching vibrations of aliphatic and olefinic C-H bonds of the long alkyl chains of OA and OLA were found. The corresponding deformation vibrations are found between 1150 cm^{-1} and 990 cm^{-1} . Furthermore, two bands for asymmetric and symmetric stretching vibrations of COO^- are observable at 1544 cm^{-1} and 1415 cm^{-1} , which indicate the absorption of deprotonated oleic acid on the nanoparticle surface. Moreover, bands for stretching vibrations of O-H groups of oleic acid and adsorbed water around at 3424 cm^{-1} were detected.

5.2.1.2 Polar Colloidal Solutions

In situ Surface Functionalization

Because as-prepared MgFe_2O_4 and ZnFe_2O_4 did not form stable aqueous dispersions, which would be desirable for photocatalytic applications in water, a modification of the microwave-assisted synthesis was done to gain water-stable nanoparticles directly from the synthesis (see 3.2.2.1). Briefly, to the precursor solution containing acetylacetonate precursors and 1-phenylethanol, the hydrophilic polymer polyvinylpyrrolidone (PVP) is added, which encapsulates the growing ferrite nanoparticles. The PVP shell with its long polymer chains leads to steric stabilization of the nanoparticles in polar solvents such as ethanol or water. Analogous to MgFe_2O_4 , stabilized ZnFe_2O_4 nanoparticles can be synthesized thereby. In Figure 5.13, PVP-coated MgFe_2O_4 and ZnFe_2O_4 nanoparticles are compared.

Rietveld refinement (Figure 5.13a-b) gave larger average crystallite sizes for both samples compared to bare, microwave-derived nanoparticles (compare Table 9.1). Alongside this, the microstrain decreases. Again, ZnFe_2O_4 developed much larger crystallites than MgFe_2O_4 . Raman spectra of both compounds prove their phase purity. The minor reflection in the MgFe_2O_4 XRD pattern (marked with *) is an artefact of the sample holder. All Raman active vibrations, which were discussed previously, were also detected for PVP-coated samples (see Figure 5.13c-d). No additional signals indicating the presence of undesired by-phases can be found. This matches results from EDX analysis, where stoichiometric ratios of 1:2.01 for Zn:Fe of PVP-coated ZnFe_2O_4 and 1:1.80 for Mg:Fe of PVP-coated MgFe_2O_4 nanoparticles were found (see Figure 9.3). In Figure 5.13e, IR spectra are shown. The typical vibrations already described for non-functionalized nanoparticles were found. Additionally, typical bands for aliphatic C-H stretching vibrations (3000 cm^{-1} – 2820 cm^{-1}), the C=O stretching vibration of the lactam-carboxylic group (1659 cm^{-1} and 1597 cm^{-1}), aliphatic C-H bending vibrations (1424 cm^{-1} and 1351 cm^{-1}) and the C-N stretching vibrations of the lactam ring (1287 cm^{-1}) prove the encapsulation with PVP polymer.^[348] Most remarkably is the colloidal stability in water, which is shown in Figure 5.13f. Both samples show constant long-time stability without sedimentation. The size distribution according to the hydrodynamic diameters obtained from DLS measurements (see Figure 5.13f) of PVP-coated nanoparticles are 50.7 nm (ZnFe_2O_4) and 37.8 nm (MgFe_2O_4).

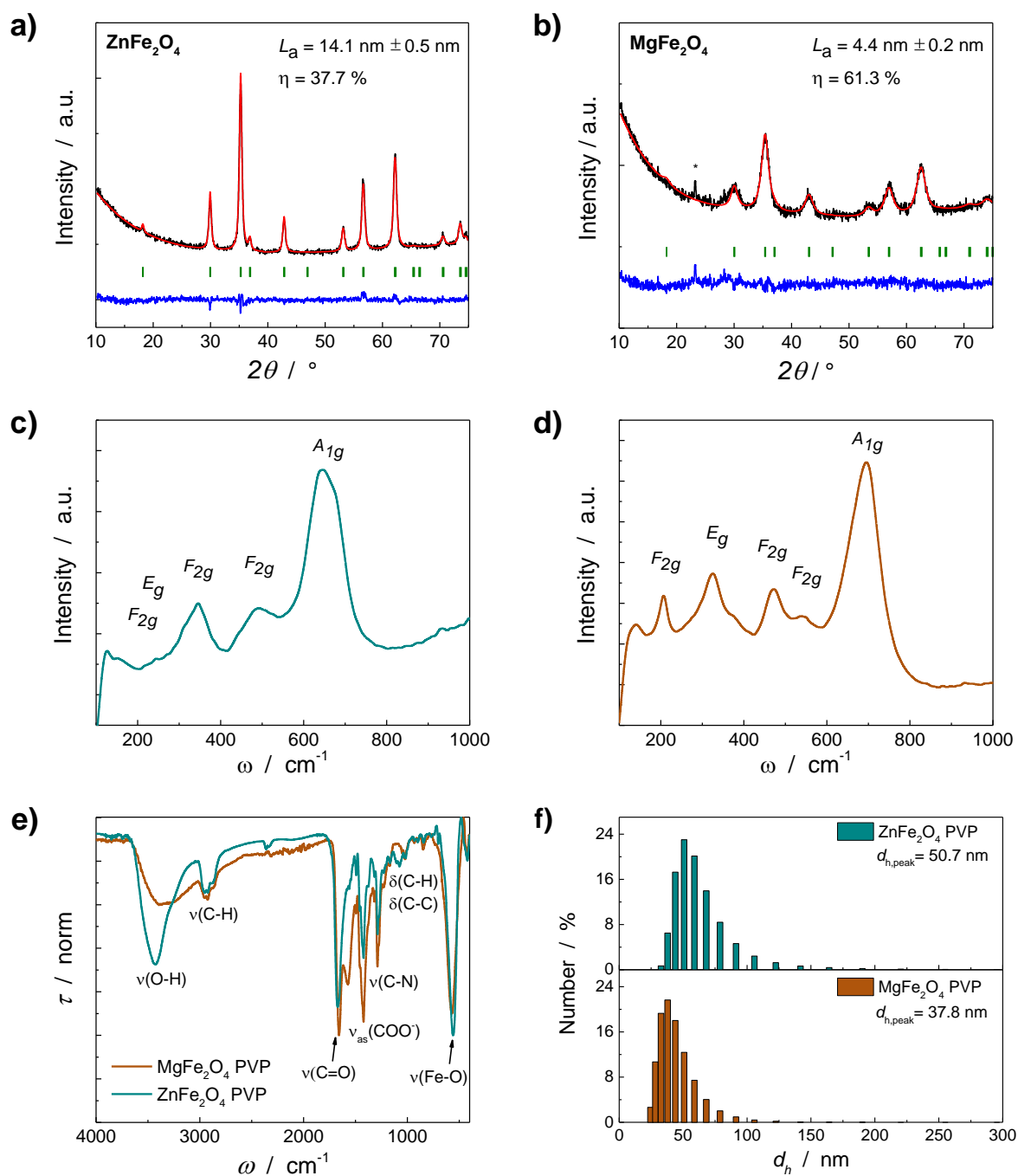


Figure 5.13: a-b) Rietveld refinements (* marks artefact of sample holder), c-d) Raman spectra, e) IR spectra and f) DLS measurements of PVP-encapsulated MgFe_2O_4 and ZnFe_2O_4 nanoparticles.

This is larger than the nanoparticle size observed during TEM analysis (18 nm for PVP-coated ZnFe_2O_4 , 7 nm for PVP-coated MgFe_2O_4 , compare Figure 5.14) indicating the formation of small agglomerates. Possibly, the PVP shell formed *in situ* during synthesis, encapsulates more than one particle, leading to larger hydrodynamic diameters.

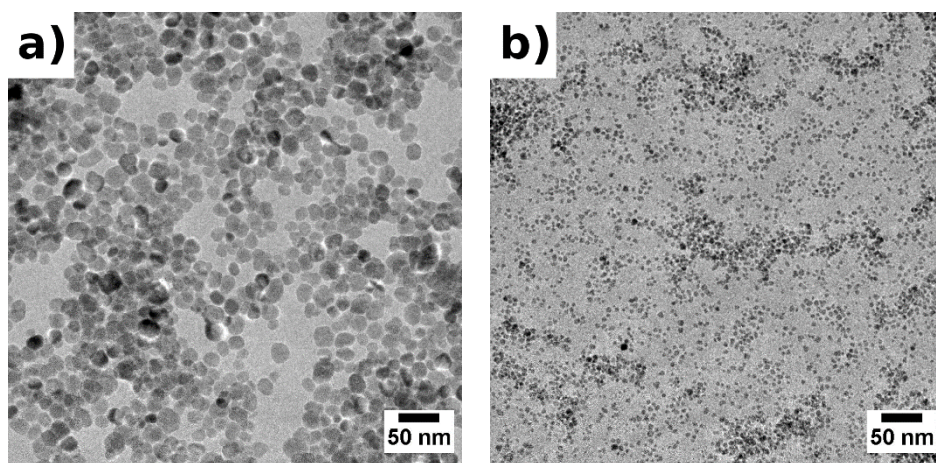


Figure 5.14: TEM images of PVP-coated a) ZnFe_2O_4 and b) MgFe_2O_4 nanoparticles.

To see the influence of polymer amount on the hydrodynamic radius obtained by DLS measurement, the PVP concentration for synthesis of PVP-encapsulated ZnFe_2O_4 and MgFe_2O_4 nanoparticles was subsequently lowered. The results of DLS analysis, which are shown in Figure 5.15a, clearly link a higher PVP concentration to the hydrodynamic diameter in the analyzed samples. More PVP in the synthesis mixture leads to thicker polymer shells and therefore larger hydrodynamic diameters. The IR patterns (Figure 5.15b) were recorded to prove a lower loading of PVP on the synthesized nanoparticles. Here, for samples produced with higher PVP amounts show much stronger characteristic vibrations in the region of 1800 cm^{-1} to 1000 cm^{-1} , which originate from the PVP shell of the encapsulated nanoparticles. The lower the amount of PVP, the weaker these vibrations. Especially the intensity of the signal at 2800 cm^{-1} resulting from the hetero-aromatic units of PVP decreases drastically. This proves a lower PVP loading, if the PVP amount added to the synthesis solution is reduced.

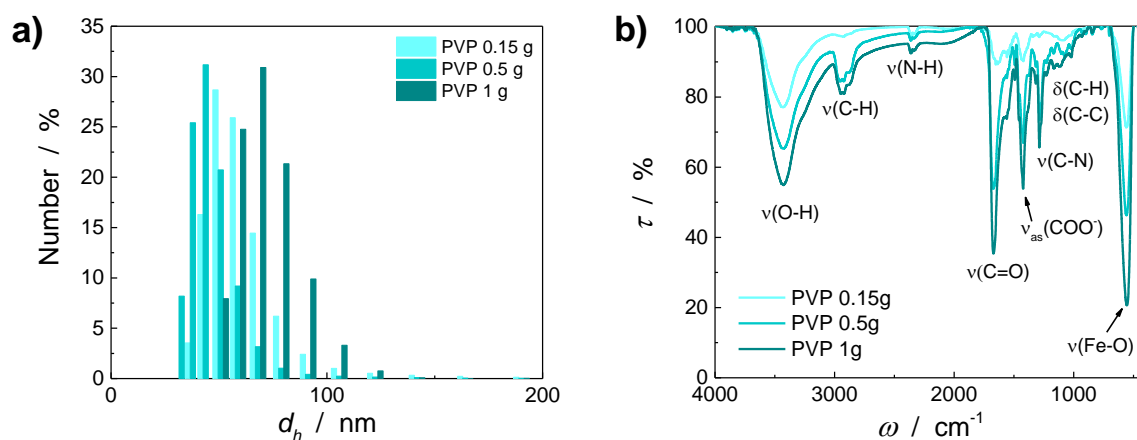


Figure 5.15: a) Hydrodynamic radii and b) IR spectra of PVP-encapsulated ZnFe_2O_4 nanoparticles with different amounts of PVP added to the synthesis mixture.

Post-Synthetic Surface Functionalization

To create aqueous colloidal solutions of ferrite nanoparticles from chapter 5.1.1.1, the samples were treated with betaine hydrochloride by adaption of a procedure described by Patil *et al.*^[349] Instead of a phase transfer as described in the original work, direct functionalization of as-synthesized, microwave-derived ZnFe_2O_4 and MgFe_2O_4 nanoparticles was achieved by shaking the nanoparticles in an aqueous betaine hydrochloride solution. The easy procedure and short treatment time is extremely advantageous for production of water-stable ferrite colloids.

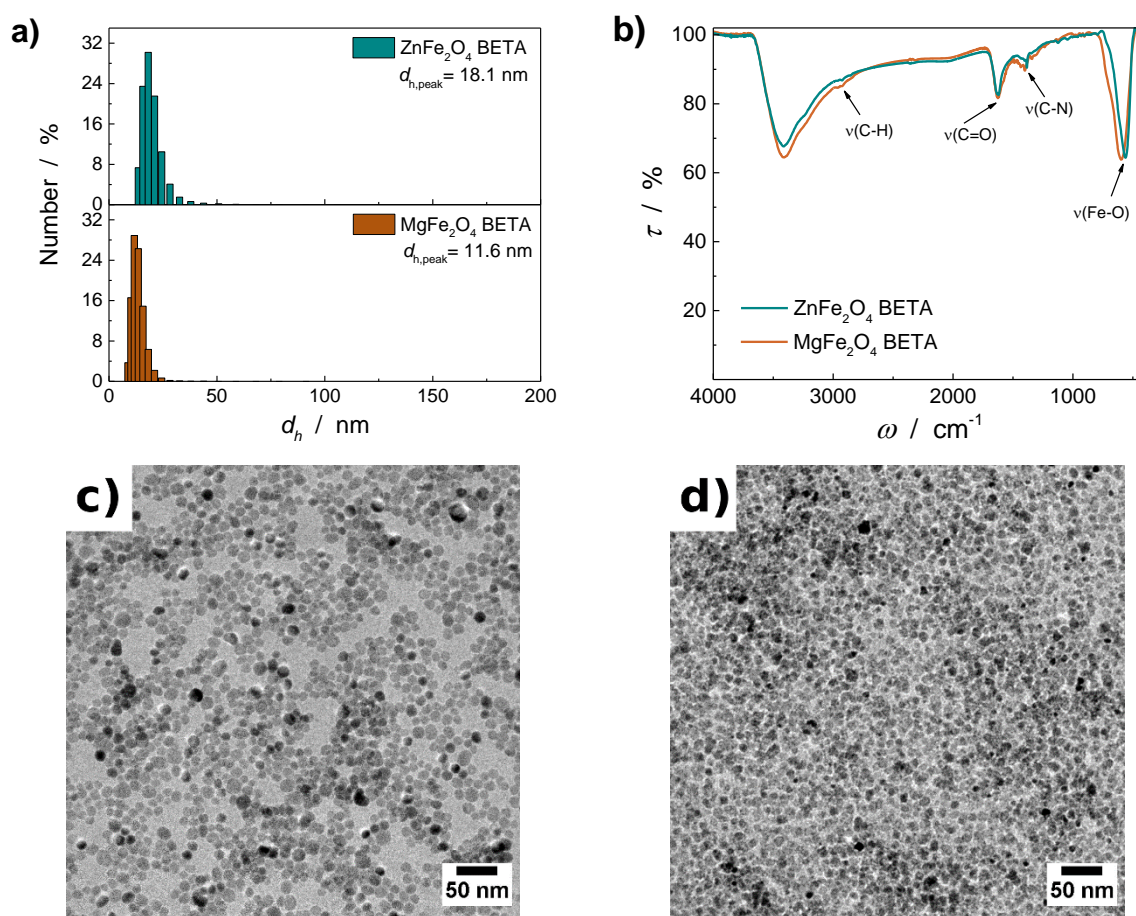


Figure 5.16: a) ZnFe_2O_4 and b) MgFe_2O_4 betaine hydrochloride functionalized nanoparticles.

After surface functionalization (described in chapter 3.2.2.3) with betaine ions (BETA), stable colloids were received with a narrow size distribution according to DLS measurements (Figure 5.16a). In general, the average hydrodynamic diameter d_h is slightly larger than the nanoparticle size estimated from TEM images. As d_h also includes the surface agents and solvent shell of solvated colloidal nanoparticles, it is expected to exceed the bare nanoparticle size. The hydrodynamic diameter d_h of BETA- ZnFe_2O_4 nanoparticles was found to be larger than for BETA- MgFe_2O_4 nanoparticles, which is consistent with the average particle sizes of monocrystalline nanoparticles before surface functionalization. The adsorption of positively charged ions was confirmed by zeta potential

measurements, yielding 48.5 mV and 42 mV for ZnFe_2O_4 and MgFe_2O_4 . The very high zeta potential values underline the superior colloidal stability. From IR analysis shown in Figure 5.16b, surface coverage with betaine ions was confirmed. Typical stretching vibrations at 2925 cm^{-1} , 1623 cm^{-1} and 1388 cm^{-1} were attributed to CH_3 , C-N and C=O functionalities, respectively. The values match well with literature reports for betaine hydrochloride functionalized magnetite nanoparticles.^[349] In TEM images (Figure 5.16c-d) the spherical shape of the original particles is still visible. This proves that no change in shape or size was caused by treatment with betaine hydrochloride. As the nanoparticles are widely spread on the copper grids, this underlines their colloidal stability and low tendency for agglomeration.

By varying the amount of betaine hydrochloride and nanoparticles, conclusions on the ideal ligand to nanoparticle ratio can be drawn. Therefore, a sample of MgFe_2O_4 nanoparticles was treated with betaine hydrochloride solution of only 0.5 wt% concentration, which is 75 % lower than the previously used. The amount of nanoparticles was the same as in the previous example to yield a ratio of 16 mg wt^{-1} of betaine hydrochloride to MgFe_2O_4 nanoparticles. In the other case, half the amount of nanoparticles and a betaine hydrochloride concentration of 4 wt% was used to achieve a ratio of 4 mg wt^{-1} of betaine hydrochloride to MgFe_2O_4 nanoparticles, which is identical to the ratio used for the sample presented in Figure 5.16. In Figure 5.17, the results for variation the ratio of betaine hydrochloride to MgFe_2O_4 nanoparticles is shown. From the DLS measurements, a change in hydrodynamic diameter becomes clearly visible when the ratio is changed to 16 mg wt^{-1} (Figure 5.17b). When a lower concentration of betaine hydrochloride solution is used with a lower amount of MgFe_2O_4 nanoparticles at the same time to maintain the nanoparticle-to-surfactant-ratio (4 mg wt^{-1}), a comparable stability for the colloidal solution was achieved. This leads to the conclusion, that the ligand to nanoparticle ratio is crucial for successful synthesis of betaine hydrochloride stabilized aqueous colloids.

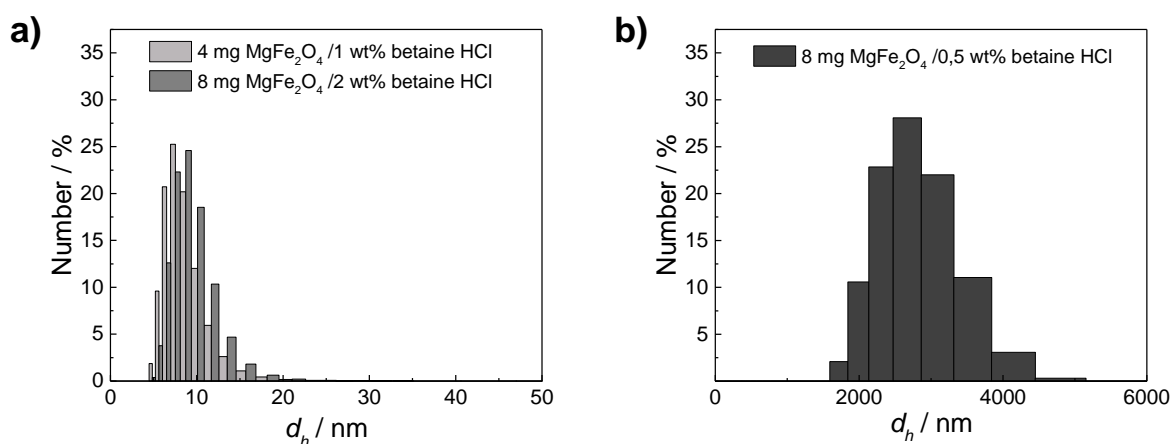


Figure 5.17: DLS measurements of a) betaine-capped MgFe_2O_4 nanoparticles with a molar ratio of 4 mg wt^{-1} and b) betaine-capped MgFe_2O_4 nanoparticles with a molar ratio of 16 mg wt^{-1} (adapted from A. Becker).^[350]

A second approach was developed for phase transfer of non-polar colloids into polar solvents by using citric acid. For this a report by Lattuada and co-workers^[270] was adjusted for post-synthetically OLA/OA-coated ferrite nanoparticles.

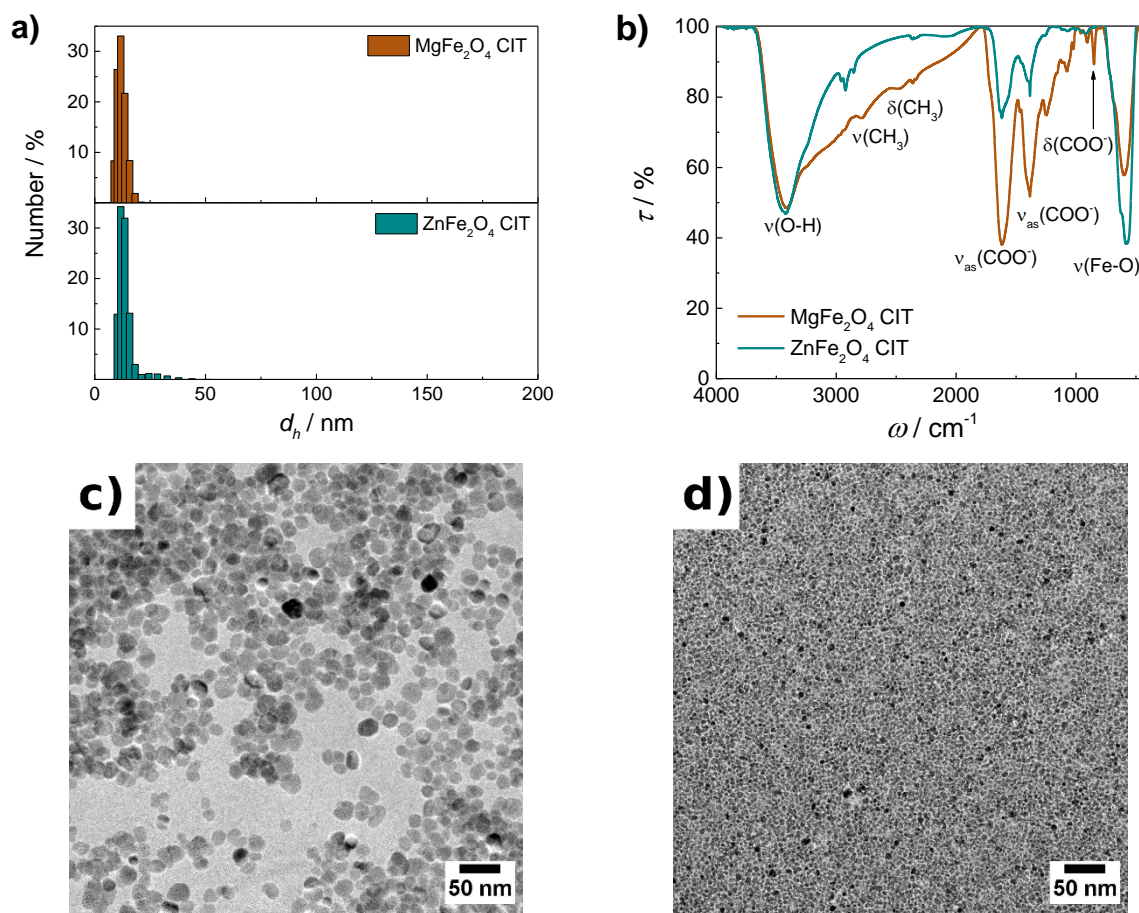


Figure 5.18: a) DLS size distributions and b) IR patterns as well as TEM images of citrate-functionalized c) ZnFe₂O₄ and d) MgFe₂O₄ nanoparticles (data for MgFe₂O₄ adapted from literature)^[1].

By this method, stable aqueous colloids with small variation of the hydrodynamic diameter were achieved as proven by DLS measurements (Figure 5.18a). Zeta potential was found to be -27 mV and -16 mV for ZnFe₂O₄ and MgFe₂O₄, respectively, indicating a negatively charged surface layer. IR patterns collected for citrate-capped ZnFe₂O₄ and MgFe₂O₄ nanoparticles both show characteristic vibrations of the surface agent (Figure 5.18b). As the IR spectrum matches well with iron(III) citrate reports from literature^[351], this indicates the attachment of not citric acid but citrate (CIT) on the nanoparticle surface because of highly alkaline conditions during the functionalization. This is in agreement with zeta potential measurements. Additionally, to the characteristically broad -OH stretching vibration around 3400 cm⁻¹ resulting from adsorbed water molecules, weak signals found at 2900 cm⁻¹ and 2500 cm⁻¹ result from aliphatic C-H stretching and deformation vibrations of CIT. Furthermore, intense symmetric and asymmetric stretching vibrations of the carboxylate group

coordinated to the surface metal ions were found at 1617 cm^{-1} and 1388 cm^{-1} .^[272] Also, the vibration band at 598 cm^{-1} and 434 cm^{-1} can be attributed to Fe–O stretching vibration of Fe^{3+} in tetrahedral and octahedral site.^[249] CIT-stabilized nanoparticles maintained the original size and shape of the microwave-derived nanoparticles as can be seen in TEM images in Figure 5.18c-d. Just as BETA-stabilized ferrite nanoparticles, they are finely distributed on the copper grid and do not show particle agglomerates, which matches the findings from DLS.

Betaine-capped and citrate-capped samples showed superior long-term colloidal stability (see Figure 9.4).^[1,350] After one week, a slight shift to larger hydrodynamic diameters was observed for both stabilization approaches. As there is only a minor increase in average hydrodynamic diameter, it is still in the range of agglomerate-free colloidal solutions. Even after 4 weeks, no agglomeration was found, as the distribution of hydrodynamic diameters did not change. Therefore, long-term stable aqueous colloids of ZnFe_2O_4 and MgFe_2O_4 nanoparticles can be synthesized by surface functionalization with betaine hydrochloride. The prepared colloidal solutions can be utilized for many applications, *e.g.* in photocatalytic pollutant degradation or for preparation of aerogels, which can also be used in catalytic applications.^[194,352,353]

5.2.2 XAS Investigation of Ferrite Nanoparticles

5.2.2.1 XAS Investigation of Reference Compounds

The reference substances Fe_3O_4 and $\alpha\text{-Fe}_2\text{O}_3$ in form of nanoparticles were used, as these two compounds show Fe^{3+} in octahedral and tetrahedral coordination, which is similar for partly inverse ferrite systems. Additionally, Fe_3O_4 exhibits Fe^{2+} in both coordination spheres, which would be a suitable reference concerning energy shift effects.

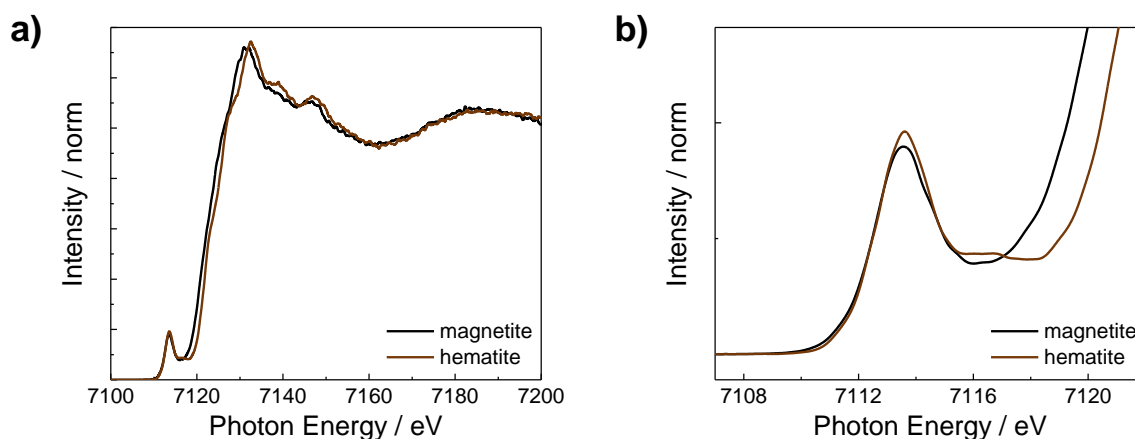


Figure 5.19: a) Full and b) pre-edge XANES spectra of Fe_3O_4 and $\alpha\text{-Fe}_2\text{O}_3$ nanoparticles.

The obtained XANES spectra and XANES pre-edge regions of the reference substances are depicted in Figure 5.19. At first, a very similar shape of the XANES spectra is visible. Both samples show multiple scattering in the post-edge region and a distinct pre-edge feature. Besides, difference in edge-energy between Fe_3O_4 and $\alpha\text{-Fe}_2\text{O}_3$ was found. XANES spectra were fitted in the pre-edge region using *Athena* software. The obtained values are listed in Table 5.1.

Table 5.1: XANES fits of reference compounds.

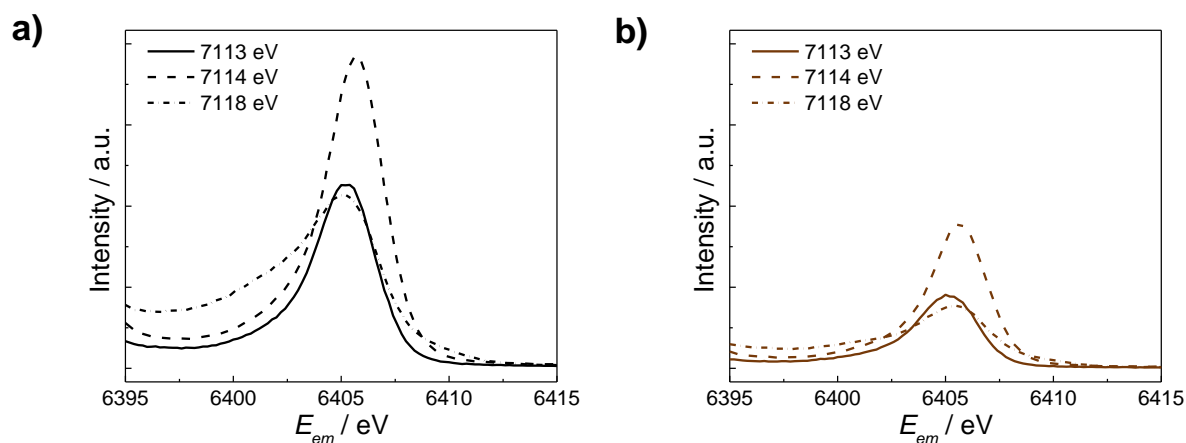
Sample	x_1 / eV	$FWHM_1$ / eV	A_1	x_2 / eV	$FWHM_2$ / eV	A_2	E_0 / eV
Fe_3O_4	7113.5	1.02	0.38	7116.4	1.35	0.15	7120.8
$\alpha\text{-Fe}_2\text{O}_3$	7113.6	2.14	0.36	7116.3	0.82	0.06	7121.7

x – peak position / $FWHM$ – full width at half maximum / A – peak area / E_0 – edge energy

A similar intensity in the pre-edge feature was not expected, as these from allowed transition involving the 3d states. As in the reference samples, the coordination of Fe^{3+} is not completely similar, a much weaker pre-edge peak was expected for $\alpha\text{-Fe}_2\text{O}_3$.

The shift in edge energy of around 1 eV between Fe_3O_4 and $\alpha\text{-Fe}_2\text{O}_3$ results from different iron oxidation states. Fe^{2+} iron oxides were reported to show pre-edges at 7118 eV, whereas purely Fe^{3+} compounds exhibit 7122 eV.^[300] The latter value is in excellent agreement with the analyzed $\alpha\text{-Fe}_2\text{O}_3$ sample. As magnetite has one-third Fe^{2+} ions, not the full shift of 4 eV can be expected but around one third of this value. This is in the range of the measured edge shift. The position of the pre-edge peaks, determined by the Fe^{3+} character of both samples, are at similar positions. The satellite peak can be attributed to charge transfer interactions within the material.^[300]

Furthermore, site-selective XES spectra of $K\alpha$ emission lines were collected for both reference compounds, which are shown in Figure 5.20.

Figure 5.20: XES spectra of a) Fe_3O_4 and b) $\alpha\text{-Fe}_2\text{O}_3$.

Here, large differences in peak intensity were found. The spectra were fitted with *PyMca* software using a Split Pseudo-Voigt function. The fit results are listed in Table 5.2.

Table 5.2: XES fits of reference compounds.

Sample	$E_{\text{ex}} / \text{eV}$	$E_{\text{em}} / \text{eV}$	$FWHM / \text{eV}$	A	$E_{\text{trans}} / \text{eV}$
Fe_3O_4	7113	6405.4	3.94	0.000722	707.6
	7114	6405.8	3.78	0.001195	708.2
	7118	6405.5	5.32	0.000516	712.5
$\alpha\text{-Fe}_2\text{O}_3$	7113	6405.4	3.96	0.000270	707.6
	7114	6405.8	3.64	0.000522	708.2
	7118	6405.6	4.63	0.000190	712.4

E_{ex} – excitation energy / E_{em} – emission energy / $FWHM$ – full width at half maximum / A – peak area / E_{trans} – energy transfer

The tabulated values show very similar emission behavior of both samples. When they are excited with the same energy, the emitted photons have identical energy. This was expectable, as both samples purely consist of iron ions in an oxygen lattice with mostly similar coordination and metal-to-ligand distance, the peak emission energy should not differ drastically. This leads to identical energy transfer values. The largest difference was found for the peak areas, where magnetite exhibits larger values for all excitation energies. As discussed in chapter 4.1.5, the intensity of the XES signal is sensitive to the metal-to-ligand distance. With Fe^{3+} found also in tetrahedral sites in the case of Fe_3O_4 , the oxygen ligands are closer to the absorbing atom, leading to higher XES intensity. The emission can be attributed to excitation into t_{2g} and e_g orbitals according to reports of Caliebe *et al.*^[303] However, the narrow line width and resolution of weak satellite features was not achieved due to lower spectral resolution of the applied Si (111) monochromator crystal.

As magnetite exhibits the highest values, the peak area of all following samples was calculated relative to the values of magnetite. The absolute values can be found in Table 9.4. The general difference in emission energy, peak width and area are relatively small, though. These shifts should not be over-interpreted.

Finally, RIXS 2D counter plots of both reference compounds are shown in Figure 5.21. The vertical lines mark the course of resonant XES, also showing the shift in maximum energy transfer. The maxima at these cross-sections match well with the calculated energy transfer values from site-selective XES (Table 5.2). A much higher pre-edge intensity was found for the magnetite sample (Figure 5.21a). The same trend was actually expected during XANES measurements, but was not observed. However, the higher pre-edge intensity due to iron ions in both, octahedral and tetrahedral coordination, matches literature reports.^[354] Both samples show a diagonal trend, because of iron ions in octahedral

coordination. The broader energy transfer region in the magnetite sample at 7118 eV emission energy fits the larger FWHM value found in XES (Figure 5.20a).

For α - Fe_2O_3 (Figure 5.21a), a clear diagonal structure was found due to only one allowed final state, with maximum in excitation energy and energy transfer was found at 7114 eV and 708 eV matching literature reports.^[300] A smaller peak at 7117 eV excitation energy and 711 eV energy transfer was slightly shifted to lower energy values compared with the literature reference^[300] and can be attributed to a small amount of 3d orbital mixing. Fe_3O_4 shows additional features in the horizontal direction (Figure 5.21b). This indicates different energy transfers at the same excitation energy, *i.e.* more than one final state.^[300] This has been reported for Fe^{3+} in tetrahedral sites due to additionally allowed dipole interactions. Furthermore, Fe^{2+} with crystal field splitting can lead to multiple final states close in energy (compare Figure 2.20). The observed patterns were expected from literature reports.^[355] The maximum of excitation energy and energy transfer was found at 7113.5 eV and 708.4 eV, matching literature-known values.^[313]

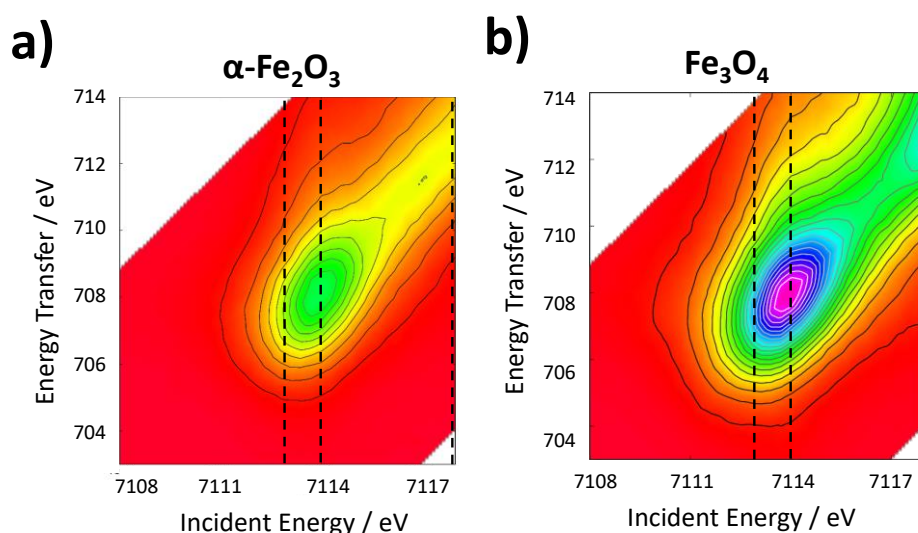


Figure 5.21: RIXS counter plots of a) Fe_3O_4 and b) α - Fe_2O_3 .

5.2.2.2 XAS Investigation of ZnFe_2O_4 Nanoparticles

Different samples of as-synthesized and post-synthetically calcined ZnFe_2O_4 nanoparticles were chosen for detailed investigation using synchrotron radiation based methods. At first, X-ray absorption near edge spectra (XANES) were recorded, as shown in Figure 5.22. Full spectra of as-synthesized nanoparticles derived from batch (ZnFe_2O_4 Batch) and microwave-assisted synthesis in the absence (ZnFe_2O_4 MW as-syn) and presence of PVP (ZnFe_2O_4 PVP) are compared in Figure 5.22a. A difference in post-edge absorption can be found between batch and microwave samples. The batch sample

shown higher absorption around 7130 eV. In contrast, the post-edge fine structure of microwave-derived samples is more defined. This is due to multiple electron scattering in a periodic crystal lattice and hints to higher crystal lattice ordering. The pre-edge absorption of all as-synthesized ZnFe_2O_4 nanoparticle samples is identical (see Figure 5.22b), indicating no major differences in the occupation of octahedral and tetrahedral positions by Fe^{3+} . Therefore, the degree of inversion in all three samples is believed to be identical.

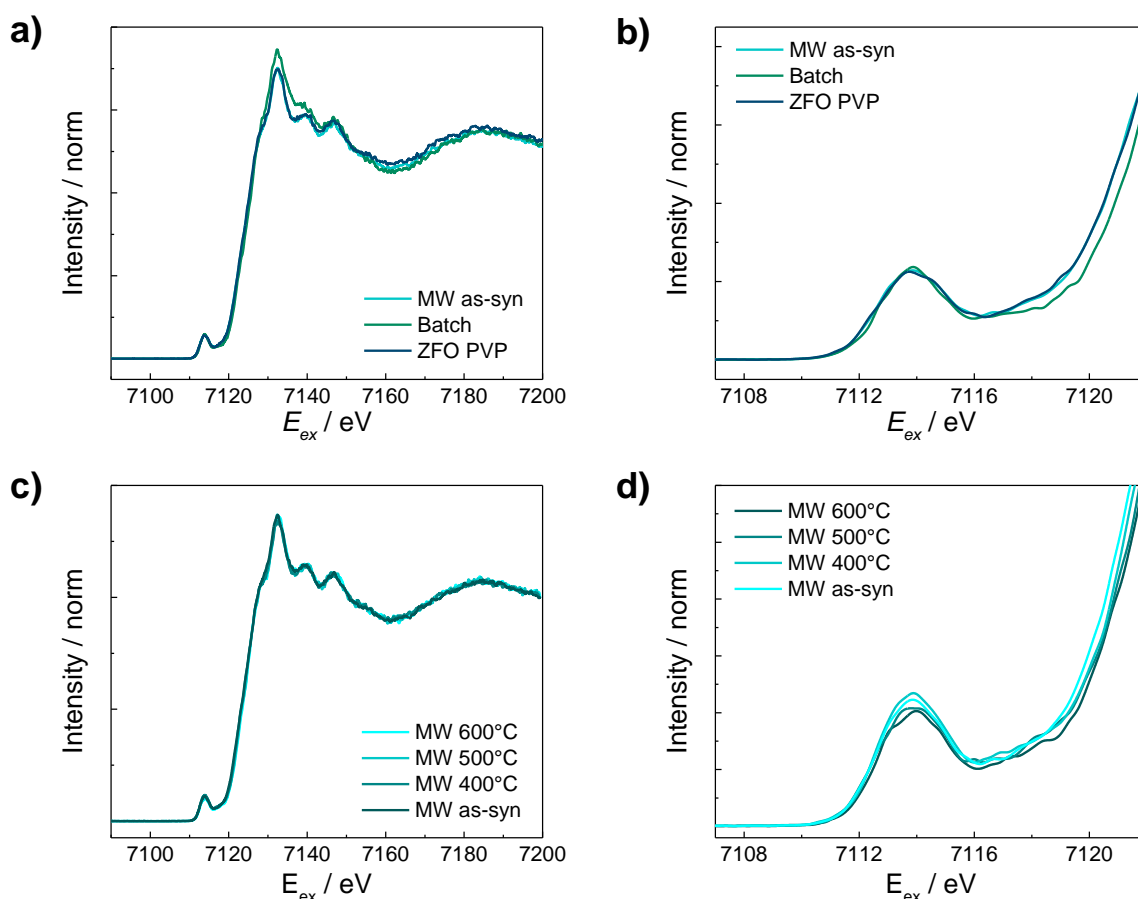


Figure 5.22: Full and pre-edge XANES spectra of a-b) freshly synthesized and c-d) calcined, microwave-derived ZnFe_2O_4 nanoparticles.

The absorption edge is slightly shifted for the batch-derived sample, but as the shift of 0.65 eV is in the range of measuring inaccuracy, this should not be over-interpreted. For microwave-derived ZnFe_2O_4 nanoparticles, which were calcined after synthesis, the absorption fine structure is nearly identical (see Figure 5.22c). The pre-edge absorption of these samples, depicted in Figure 5.22d, shows a slight decrease of absorption intensity with increasing calcination temperature. This might result from less octahedral distortion leading to less orbital hybridization.^[297] The absorption edge of these samples is almost constant (shift ≈ 0.5 eV). The post-edge region shows clear multiple scattering patterns, which are congruent. Comparing all ZnFe_2O_4 nanoparticle samples, there are only minor changes in the XANES spectra. This leads to the conclusion, that the normal spinel structure of ZnFe_2O_4

cannot be influenced by either choice of synthesis method nor post-synthetic calcination, underlining the stability of this crystal structure for ZnFe_2O_4 .

The characteristics obtained from fitting of the XANES pre-edge region are listed in Table 5.3.

Table 5.3: XANES fits of ZnFe_2O_4 nanoparticles.

Sample	x_1 / eV	$FWHM_1 / \text{eV}$	A_1	x_2 / eV	$FWHM_2 / \text{eV}$	A_2	E_0 / eV
ZnFe_2O_4 Batch	7113.74	1.08	0.30	7116.61	1.19	0.12	7123.02
ZnFe_2O_4 MW as-syn	7113.68	1.11	0.29	7116.74	1.76	0.19	7122.37
ZnFe_2O_4 MW 400 °C	7113.72	1.10	0.29	7116.70	1.71	0.19	7122.74
ZnFe_2O_4 MW 500 °C	7113.68	1.17	0.28	7116.78	1.79	0.19	7122.93
ZnFe_2O_4 MW 600 °C	7113.70	1.08	0.24	7116.60	1.84	0.19	7122.91
ZnFe_2O_4 PVP	7113.76	1.11	0.29	7116.61	1.19	0.12	7122.91

x – peak position / $FWHM$ – full width at half maximum / A – peak area / E_0 – edge energy

Here, the qualitative impression of similar absorption behavior is confirmed, as the fitted values for two peaks detectable within the pre-edge structure show almost identical values for all ZnFe_2O_4 samples. The calculated values are slightly lower than reported for ZnFe_2O_4 .^[356] As in the reference, the edge position is shifted by ≈ 1.5 eV, too, this was attributed to differences in the energy calibration procedure. The area of pre-edge peaks is only about one-third or less compared to the area of Fe_3O_4 reference compound, which was expected due to a low amount of Fe^{3+} in tetrahedral sites.

Site-selective XES analysis was performed of as-synthesized and heat-treated samples, respectively. The resulting XES spectra of selected samples are depicted in Figure 5.23. The results of XES fits of all analyzed samples are listed in Table 5.4.

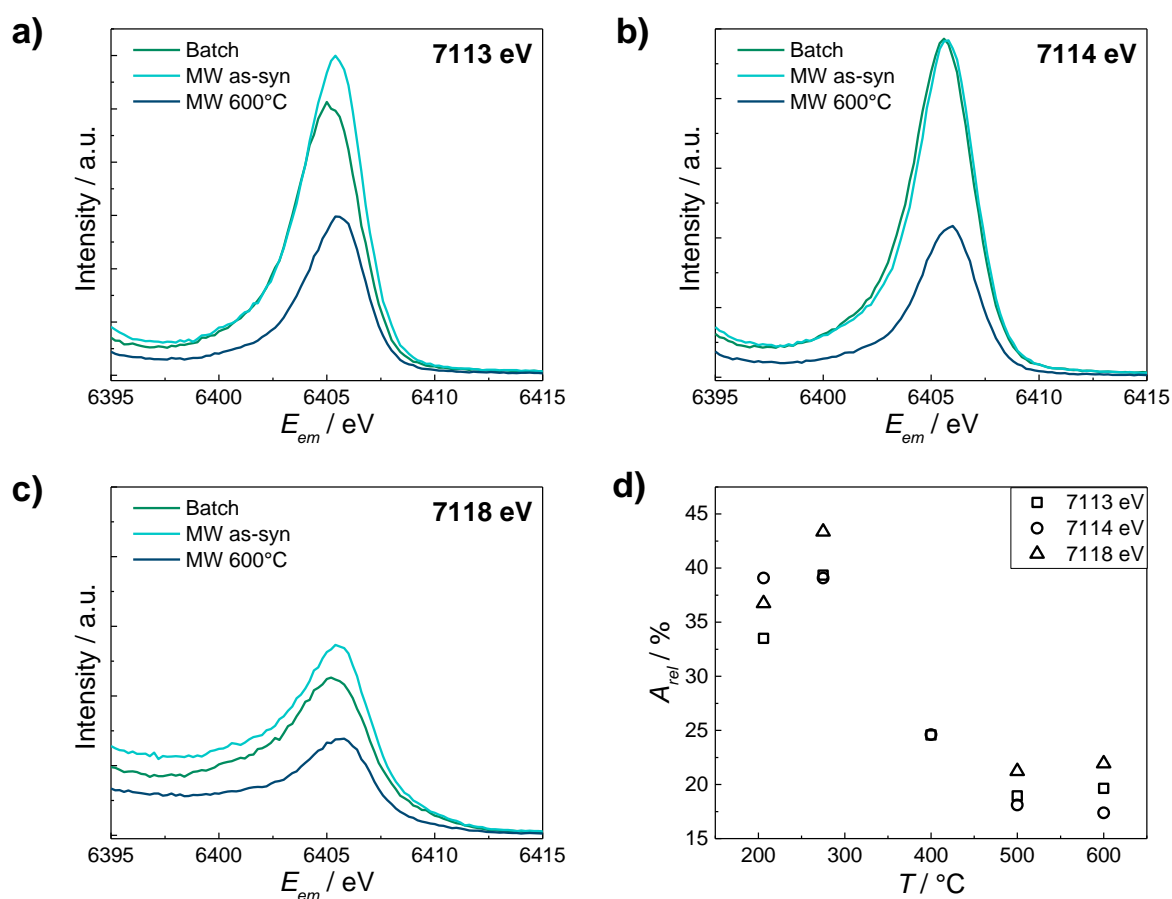


Figure 5.23: a-c) XES spectra of ZnFe₂O₄ nanoparticles and d) relative peak areas A_{rel} obtained by spectra fitting.

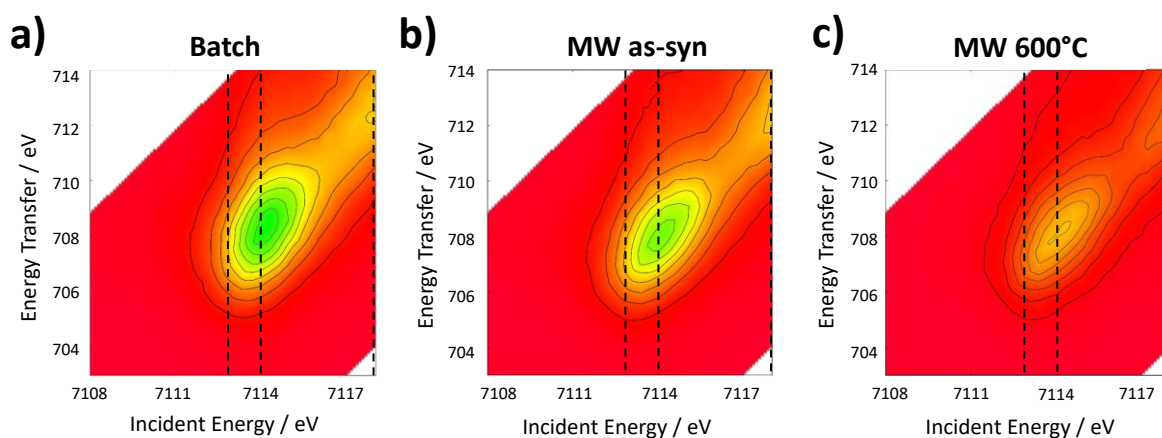
In site-selective XES, a shift between the as-synthesized samples prepared under batch and microwave conditions and the sample calcined at 600 °C was found. However, this shift of ≈ 0.5 eV is in the area of analysis step width. Therefore, this might have been caused by the measurement conditions. The difference in peak intensity is quite prominent. Here, microwave-derived as-synthesized nanoparticles show the highest intensity and the calcined sample shows the lowest intensity. This can be assigned to intrinsic defects, which were thermally healed in case of the calcined sample. Therefore less distorted octahedral are found, resulting in a lower amount of hybrid orbitals with allowed quadrupole transitions.

Table 5.4: XES fits of ZnFe₂O₄ nanoparticles.

Sample	E_{ex} / eV	E_{em} / eV	$FWHM$ / eV	A	E_{trans} / eV
7113	ZnFe ₂ O ₄ Batch	6405.3	4.37	0.000242	707.7
	ZnFe ₂ O ₄ MW as-syn	6405.6	4.20	0.000284	707.4
	ZnFe ₂ O ₄ MW 400 °C	6405.5	4.33	0.000177	707.5
	ZnFe ₂ O ₄ MW 500 °C	6405.7	4.22	0.000137	707.3
	ZnFe ₂ O ₄ MW 600 °C	6405.8	4.20	0.000142	707.2
7114	ZnFe ₂ O ₄ Batch	6405.8	4.07	0.000467	708.2
	ZnFe ₂ O ₄ MW as-syn	6405.9	3.85	0.000467	708.1
	ZnFe ₂ O ₄ MW 400 °C	6405.5	3.86	0.000294	708.5
	ZnFe ₂ O ₄ MW 500 °C	6406.0	3.80	0.000216	708.0
	ZnFe ₂ O ₄ MW 600 °C	6406.0	3.90	0.000208	708.0
7118	ZnFe ₂ O ₄ Batch	6405.7	6.04	0.000190	712.3
	ZnFe ₂ O ₄ MW as-syn	6405.9	5.75	0.000224	712.1
	ZnFe ₂ O ₄ MW 400 °C	/	/	/	/
	ZnFe ₂ O ₄ MW 500 °C	6405.9	5.12	0.000110	712.2
	ZnFe ₂ O ₄ MW 600 °C	6406.0	5.36	0.000113	712.0

E_{ex} – excitation energy / E_{em} – emission energy / $FWHM$ – full width at half maximum / A – peak area / E_{trans} – energy transfer

Finally, RIXS planes were constructed from analysis data of batch-synthesized, as-synthesized microwave-derived and post-synthetically calcined (600 °C) ZnFe₂O₄ nanoparticles. As shown in Figure 5.24, the excitation energies for site-selective XES are marked in the 2D counterplots.

Figure 5.24: RIXS planes of a) batch-synthesized, b) microwave-derived and c) calcined ZnFe₂O₄ nanoparticles.

All samples show a diagonal trend, which was also found for α - Fe_2O_3 reference sample (compare Figure 5.21a). As reported in literature^[298], this shape is assigned to only one final state allowed in ZnFe_2O_4 . The intensity maxima, which are obviously different, are found at 7114.1 eV and 708.1 eV for all samples., which matches the values reported^[300] and found (compare Figure 5.21a) for α - Fe_2O_3 with an identical coordination geometry. The difference in intensity results from different emission intensities already discussed previously (compare Figure 5.23).

XANES spectra of PVP-coated nanoparticles of MgFe_2O_4 and ZnFe_2O_4 , which have been reported in chapter 5.2.1.2, are compared in Figure 5.25. Here, the contrary tendency for spinel inversion becomes evident.

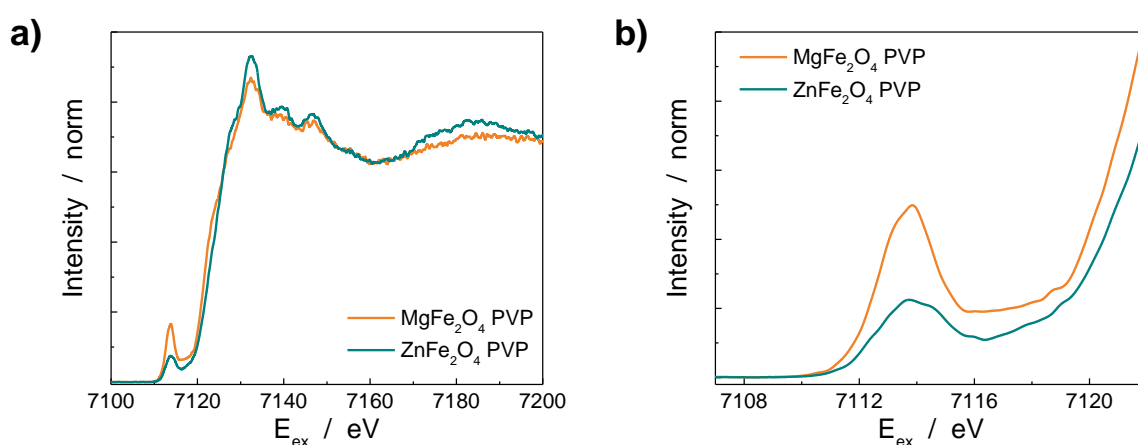


Figure 5.25: a) Full and b) pre-edge XANES spectra of PVP-coated MgFe_2O_4 and ZnFe_2O_4 nanoparticles.

The partly inverted spinel structure of MgFe_2O_4 with Fe^{3+} also present in tetrahedral sites causes a much higher pre-edge intensity resulting from dipole transition contribution. In contrast, the pre-edge spectrum of PVP-encapsulated ZnFe_2O_4 nanoparticles matches well with those of bare and post-synthetically heat-treated samples (compare Figure 5.22a-b). The pre-edge position at 7113.7 eV matches the literature value of 7114.0 eV.^[356] The difference is in the range of measuring step size of 0.2 eV (compare 4.1.5). There, an intensity ratio of the pre-edge peak of 1:2.5 for ZnFe_2O_4 : MgFe_2O_4 was stated, which is close to the detected ratio (1:2.2).^[356] The edge shift between the MgFe_2O_4 and ZnFe_2O_4 sample is clearly visible. The resulting edge step at 7121.9 eV (see Table 5.5) still matches the values reported for purely Fe^{3+} materials.^[300]

Therefore, it was assumed that the shift was not caused by Fe^{2+} impurities but due to the higher degree of inversion influencing the occupied and unoccupied states within the semiconductor. In the post-edge region, the multiple scattering pattern is less prominent within PVP-coated MgFe_2O_4 . This indicates a lower periodicity of the crystal lattice owing to the much smaller crystallite size of these nanoparticles (compare Table 9.1).

5.2 Results and Discussion – Surface Functionalization

Table 5.5: XANES fits of PVP-coated ferrite nanoparticles.

Sample	x_1 / eV	$FWHM_1$ / eV	A_1	x_2 / eV	$FWHM_2$ / eV	A_2	E_0 / eV
ZnFe ₂ O ₄ PVP	7113.76	1.11	0.29	7116.61	1.19	0.12	7122.91
MgFe ₂ O ₄ PVP	7113.73	1.11	0.64	7117.24	1.18	0.21	7121.91

x – peak position / $FWHM$ – full width at half maximum / A – peak area / E_0 – edge energy

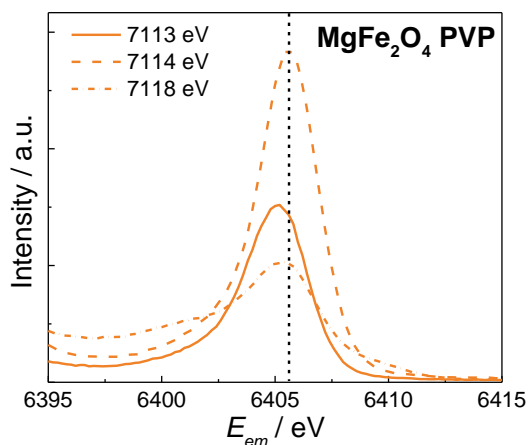


Figure 5.26: Site-selective XES spectra of PVP-coated MgFe₂O₄ nanoparticles.

In Figure 5.26, the obtained spectra for site-selective XES measurements are shown. The highest emission was detected at 7114 eV excitation energy, which is the position of the pre-edge maximum. This is consistent with the analysis results of ZnFe₂O₄ and the chosen reference compounds. For the PVP-coated MgFe₂O₄ sample, the maximum of the second peak is slightly shifted, also having a larger peak area in comparison the ZnFe₂O₄ nanoparticles (compare Table 5.4). However,

maxima of emission energy coincide with those found for ZnFe₂O₄. The results from XES peak fitting are listed in Table 5.6 (compare Table 5.4 and Table 9.4).

Table 5.6: XES fits of MgFe₂O₄ nanoparticles.

E_{ex} / eV	E_{em} / eV	$FWHM$ / eV	A	E_{trans} / eV
7113	6405.3	4.05	0.000439	707.7
7114	6405.8	3.71	0.000837	708.2
7118	6405.7	6.20	0.000269	712.3

E_{ex} – excitation energy / E_{em} – emission energy / $FWHM$ – full width at half maximum / A – peak area / E_{trans} - energy transfer

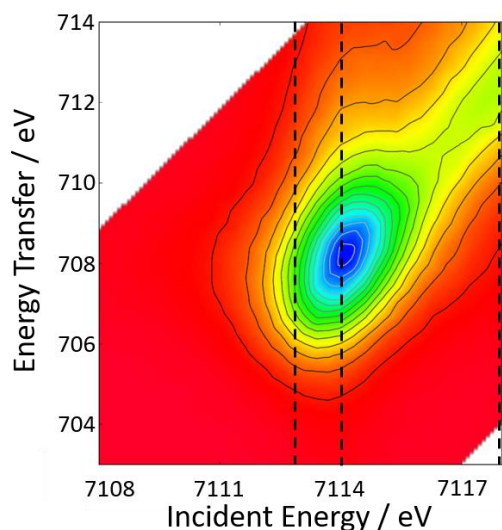


Figure 5.27: RIXS plane of PVP-coated MgFe_2O_4 nanoparticles.

Finally, the RIXS plane obtained for PVP-coated MgFe_2O_4 nanoparticles is shown in Figure 5.27. A much higher intensity compared to hematite and the analyzed ZnFe_2O_4 samples (compare Figure 5.21a and Figure 5.24). This is attributable to the higher amount of Fe^{3+} in tetrahedral sites, which also caused a higher XANES pre-edge intensity and higher XES emission intensity. Therefore, the RIXS plane intensity, which combines both processes, should be larger, too. The feature is still lower than the one found in magnetite (compare Figure 5.21b), which indicates that no completely inverted spinel structure is found in MgFe_2O_4 . The maximum in absorption energy and

energy transfer was determined at 7114.1 eV and 708.1 eV. The position matches the findings for octahedrally coordinated $\alpha\text{-Fe}_2\text{O}_3$.

5.2.3 Photocatalytic Degradation of Model Compounds

To evaluate the photocatalytic activity of ZnFe_2O_4 and MgFe_2O_4 nanoparticles, photocatalytic degradation of different pollutants were performed in aqueous solution under simulated sunlight irradiation. As model compounds, rhodamine B and tetracycline were chosen to cover the field of dye removal and antibiotic degradation via visible light driven photocatalysis.

At first, the stability of the chosen model compounds in the absence of a photocatalyst was analyzed. For this purpose, an aqueous solution of rhodamine B or tetracycline, respectively, was illuminated using a sunlight simulator equipped with an AM1.5G filter. UV-Vis spectra of the freshly-prepared aqueous solutions were recorded prior to the illumination and after 2 hours. The resulting spectra shown in Figure 9.5a underline, that rhodamine B does not decompose under sunlight illumination if there is no photocatalyst present. Therefore, the process was repeated in the presence of ZnFe_2O_4 and MgFe_2O_4 nanoparticles according to the procedure reported in chapter 4.7.

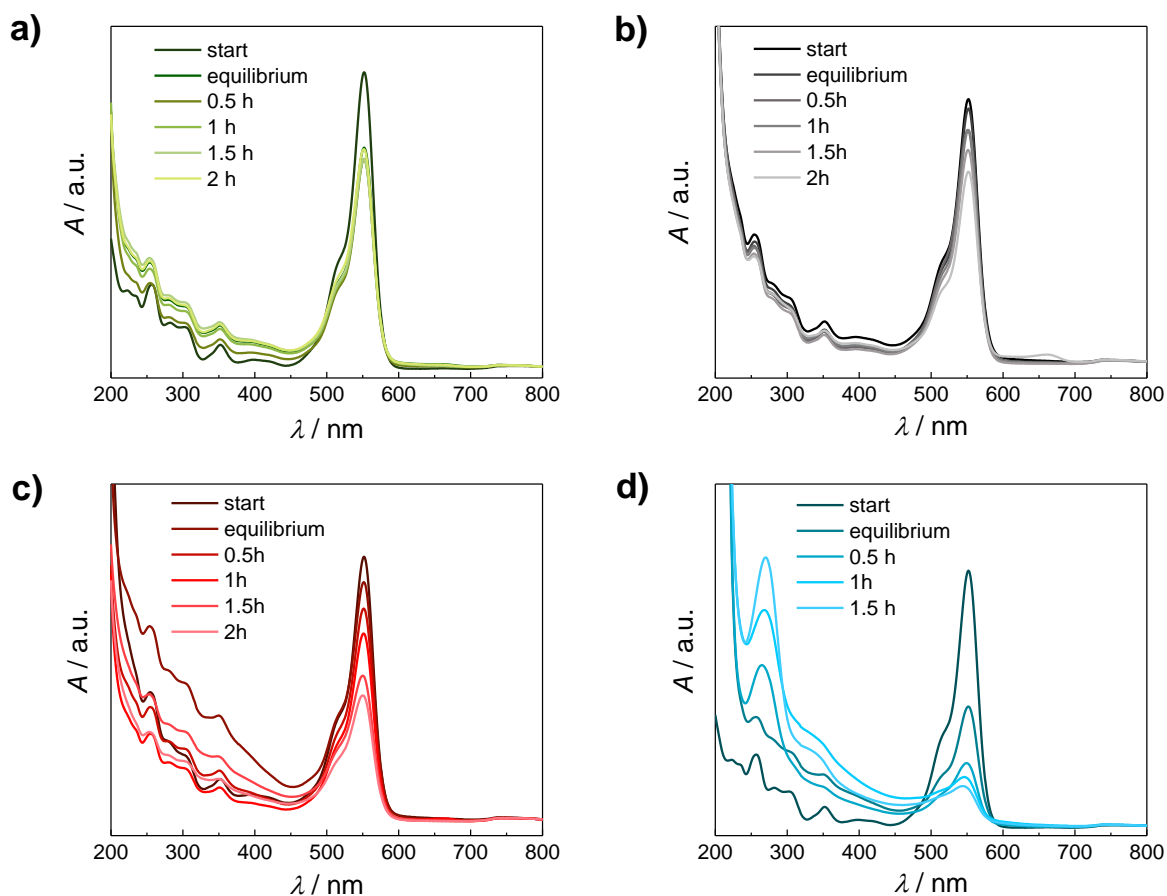


Figure 5.28: UV-Vis spectra collected during rhodamine B degradation experiments under simulated sunlight (AM1.5G) using a) non-functionalized ZnFe_2O_4 nanoparticles, b) non-functionalized MgFe_2O_4 nanoparticles, c) betaine-capped MgFe_2O_4 nanoparticles, and d) citrate-capped MgFe_2O_4 nanoparticles (adapted from literature).^[1,350]

As shown in Figure 5.28a, a change in the absorption spectra of the starting point and the equilibrium states indicates a strong adsorption of the colorant onto the ZnFe_2O_4 nanoparticles surface. After reaching an adsorption-desorption equilibrium in the dark, there is hardly any decrease of the main absorption band of rhodamine B at 552 nm in the presence of ZnFe_2O_4 nanoparticles. After 2 hours, the degradation is only 5 % compared to the equilibrium state. In contrast, in the presence of non-functionalized MgFe_2O_4 nanoparticles (Figure 5.28b), a clear decrease of the absorption maximum over time is visible reaching a degradation of 24 % compared to the equilibrium state. This indicates that MgFe_2O_4 nanoparticles have a higher photocatalytic activity towards the degradation of rhodamine B under solar light irradiation. Therefore, only MgFe_2O_4 nanoparticles were further pursued.

To identify the impact of deagglomeration and colloidal stability, the degradation of rhodamine B under simulated solar light was performed in the presence of betaine-capped Figure 5.28c) and citrate-capped (Figure 5.28d) MgFe_2O_4 nanoparticles, too. In case of betaine surface functionalization, a larger decrease of the absorption maximum was achieved, indicating a higher degree of degradation compared to non-functionalized MgFe_2O_4 nanoparticles. With citrate-capped MgFe_2O_4 nanoparticles,

a strong adsorption of rhodamine B during stirring in the dark was observed. The improved absorption of cations in the presence of surface-bond citrate ions has already been reported by Redden *et al.* and might be attributed to the negative zeta potential of this colloidal solution.^[357] In Figure 5.29, the decrease of rhodamine B over time is displayed. The relative concentrations c_{rel} were calculated from the absorption maximum at 552 nm concerning the starting value in equilibrium state (see chapter 4.7). From Figure 5.29a, the impact of surface functionalization on the rhodamine B degradation over time becomes apparent. With non-functionalized $MgFe_2O_4$ nanoparticles 24 % of the model compound were decomposed after 2 hours. With betaine-capped $MgFe_2O_4$ nanoparticles, having a positive zeta potential, the amount of decomposed rhodamine B is almost twice as high (45 % after 2 hours). The highest degradation of 62 % after 1.5 h was achieved in the presence of citrate-capped $MgFe_2O_4$ nanoparticles, which is approximately three times as high as for non-functionalized $MgFe_2O_4$ nanoparticles. For all samples, a linear decay was found (see Figure 5.29b) indicating first-order reaction kinetics. The calculated kinetic constants of non-functionalized ($k = 0.123 \pm 0.014$), betaine-capped ($k = 0.311 \pm 0.025$) and citrate-capped ($k = 0.638 \pm 0.103$) $MgFe_2O_4$ nanoparticles are in agreement with the previously reported trends.

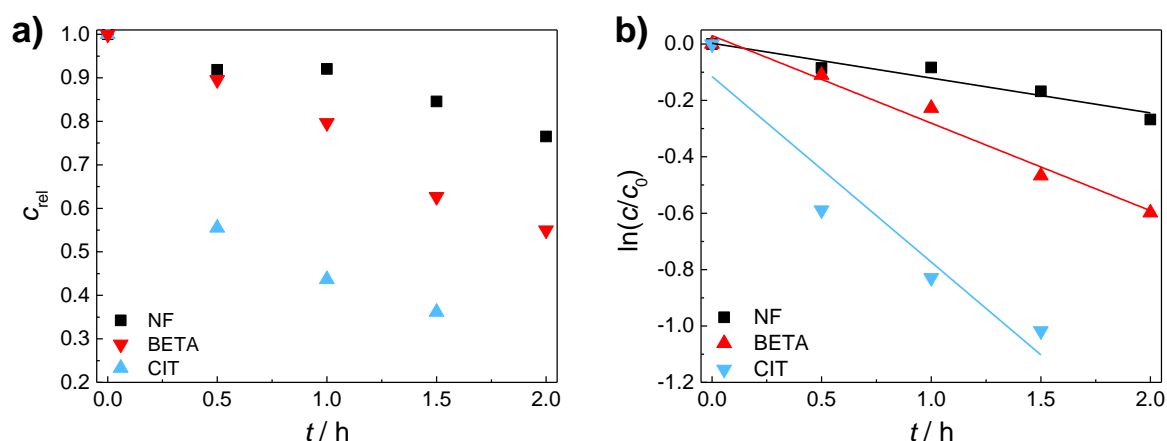


Figure 5.29: a) Calculated relative concentrations c_{rel} and b) kinetic evaluation of rhodamine B in the presence of non-functionalized (NF, black), betaine-capped (BETA, red) and citrate-capped (CIT, blue) $MgFe_2O_4$ nanoparticles (adapted from literature).^[1]

A clear correlation between deagglomeration and photocatalytic activity can be concluded from these results. With stable colloidal $MgFe_2O_4$ nanoparticles, a higher degradation rate can be achieved compared to non-stabilized $MgFe_2O_4$ nanoparticles. Furthermore, the zeta potential shows a strong impact on the absorption of the model compound onto the photocatalyst surface. With a negative zeta potential, rhodamine B adsorption is highly promoted, resulting in the highest degree of degradation and the largest kinetic constant for the decomposition reaction.

As already discussed in chapter 2.2.4, rhodamine B as a colorant is a non-ideal model system, as it absorbs a large part of the incident light, which is then non available for generation of photo-excited

electrons in the photocatalyst. Furthermore, detection of the degradation rate solely by UV-Vis does not allow insights into the degree of mineralization. Therefore, the colorless antibiotic compound tetracycline was chosen as a second model compound for photocatalytic degradation experiments. As shown in Figure 5.30, slight shifts of the absorption maxima were observed, but as the maximum intensity did not change, this shift was attributed to the formation of tetracycline dimers in solution. It was assumed, that no degradation of the model compound occurs under simulated solar light when the photocatalyst material was absent. Therefore, photocatalytic degradation experiments in the presence of ZnFe_2O_4 and MgFe_2O_4 nanoparticles were performed.

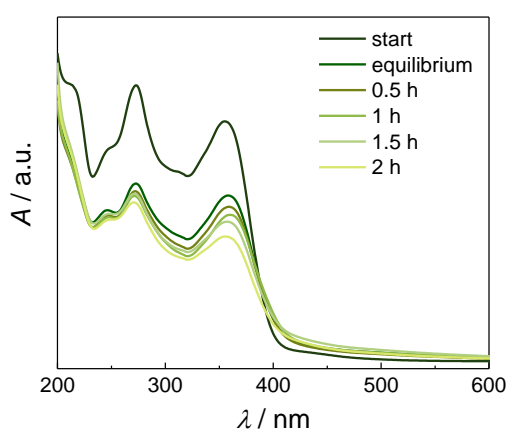


Figure 5.30: UV-Vis spectra of tetracycline degradation experiments under simulated sunlight (AM1.5G) using non-functionalized ZnFe_2O_4 nanoparticles (adapted from A. Becker).^[350]

Again, non-functionalized ZnFe_2O_4 nanoparticles show only a modest photocatalytic activity indicated by a small decrease of the absorption maximum at 356 nm shown in Figure 5.30. The second maximum at 273 nm stays nearly constant, which might be due to the removal of functional groups instead of a complete mineralization.

In comparison, non-functionalized MgFe_2O_4 nanoparticles (Figure 5.31a) show a shift of the absorption maximum comparing the freshly-mixed solution and the equilibrium state. This is a first indication for adsorption of tetracycline to the nanoparticle surface. A high adsorption of tetracycline onto the surface of ferrite nanoparticles was also reported by Shao *et al.* for MnFe_2O_4 /activated carbon composites.^[358] During irradiation, a strong decrease of the absorption maximum is visible. For quantification, the decrease of the absorption band at 374 nm was chosen indicating 76 % degradation. For betaine-capped MgFe_2O_4 nanoparticles, a strong decrease of the absorption was detected already at the equilibrium state, which is why no quantification of the degradation was possible, although a decrease over time is shown in Figure 5.31b. The strong decrease indicates a high degree of adsorption of tetracycline molecules onto the nanoparticle surface, which seems to be enhanced due to the positive zeta potential found for betaine-capped MgFe_2O_4 nanoparticles.

Additionally, TOC analysis of the aliquot solutions obtained for MgFe_2O_4 experiments was performed (see chapter 4.8) with the corresponding results shown in Figure 5.31c and Figure 5.31d. For both samples, comparable starting values of 22 – 22.8 mg L^{-1} were detected. Considering the non-functionalized sample, a strong decrease in TOC value was detected already after the equilibrium phase (second point in Figure 5.31c). When the illumination is started, the TOC value slightly decreases before an increase over time is detected.

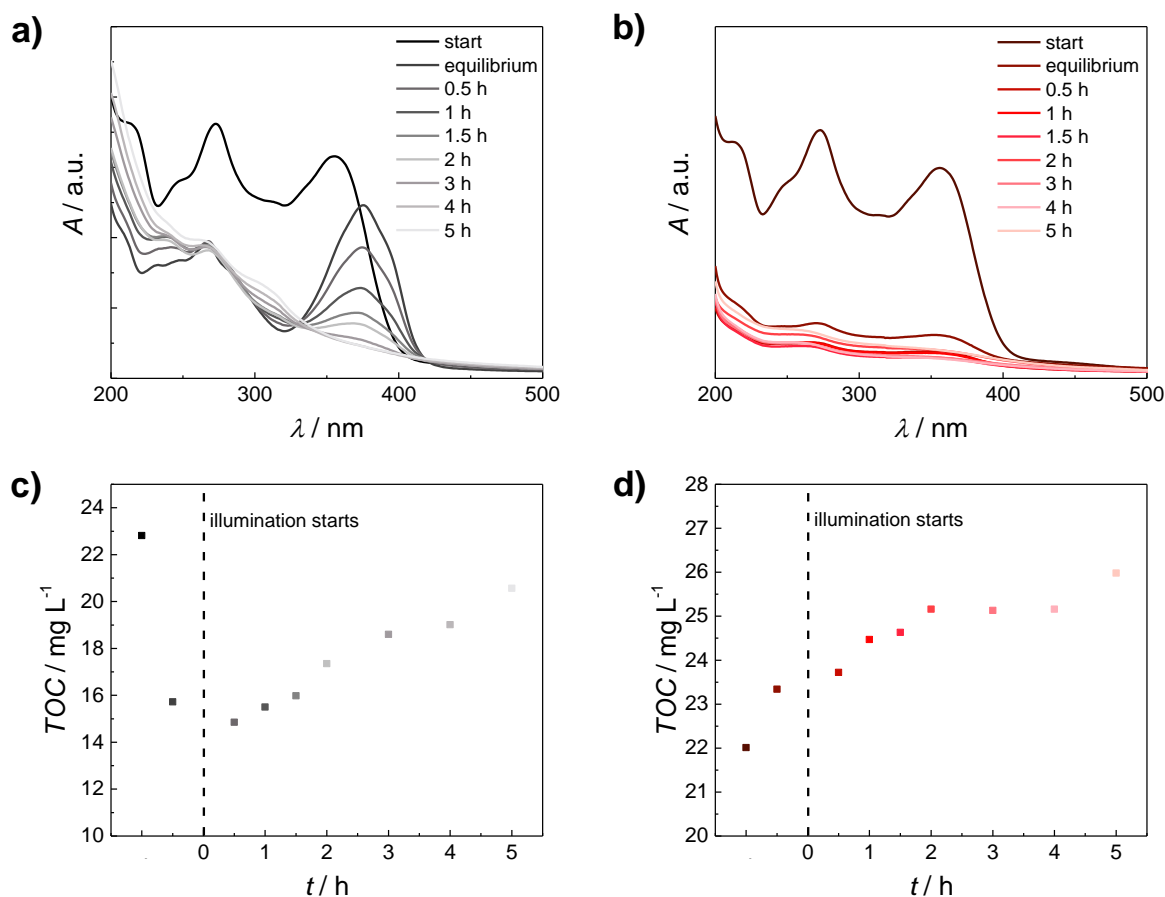


Figure 5.31: UV-Vis spectra collected during tetracycline degradation experiments under simulated sunlight (AM1.5G) using a) non-functionalized MgFe_2O_4 nanoparticles, b) betaine-capped MgFe_2O_4 nanoparticles, and TOC measurements of tetracycline degradation in the presence of c) non-functionalized MgFe_2O_4 nanoparticles and d) betaine-capped MgFe_2O_4 nanoparticles (adapted from A. Becker).^[350]

This unusual progression can be explained with the strong adsorption of tetracycline at the nanoparticle surface, which also caused the shift of the absorption maximum. As the nanoparticles were removed prior to TOC analysis, the adsorbed tetracycline is not detected.

When the irradiation is started, the photocatalytic degradation of the model compound begins, leading to the incremental decomposition of the complex molecular structure. Therefore, certain functional groups, which promoted the adsorption of tetracycline, are removed and the resulting intermediate cannot adsorb as effectively as the original compound. Therefore, the intermediates are not removed with the solid photocatalyst and can be detected during TOC analysis, resulting in higher TOC values. With betaine-capped MgFe_2O_4 nanoparticles, there is a constant increase in TOC value, which indicates different interactions between the photocatalyst and the model compound. Due to the ionic surfactant, a permanent adsorption of tetracycline onto the surface of betaine-capped MgFe_2O_4 nanoparticles is not possible. Therefore, no decrease in TOC concentration was detected. Instead, a constant increase in TOC concentration over time indicates the partial decomposition of tetracycline. This suggests, that betaine-capped MgFe_2O_4 nanoparticles show photocatalytic activity

for tetracycline degradation. However, a complete mineralization to CO_2 , which would have been removed prior to the actual analysis, was not fully achieved. Instead, the organic decomposition products desorbed from the nanoparticle surface and therefore increased the TOC concentration of the solution.

5.3 Sol-Gel Derived Mesoporous Ferrite Thin Films

A synthesis for mesoporous ferrite thin films, which was reported by Haetge *et al.*^[5], was selected as fundament for synthesis of ZnFe_2O_4 , MgFe_2O_4 and CaFe_2O_4 mesoporous thin films. As soft templates, different block-copolymers were selected. On the one hand, commercially available block-copolymer poly(ethylene oxide)-*b*-poly(propylene oxide)-*b*-poly(ethylene oxide) (Pluronic® F127, abbr. PLU) was used. This polymer is reported to form micelles with hydrodynamic radii of 10.2 nm.^[126] On the other hand, tailor-made block-copolymer poly(isobutylene)-*b*-poly(ethylene oxide) in three molecular weights of the polyisobutylene unit ($\text{MW}_{\text{PIB}} = 3000$, $\text{MW}_{\text{PIB}} = 6000$ or $\text{MW}_{\text{PIB}} = 10000$, BASF SE, abbr. either PIB3000, PIB6000 or PIB10000) was utilized. The complete synthesis procedure is described in chapter 3.2.3.1.

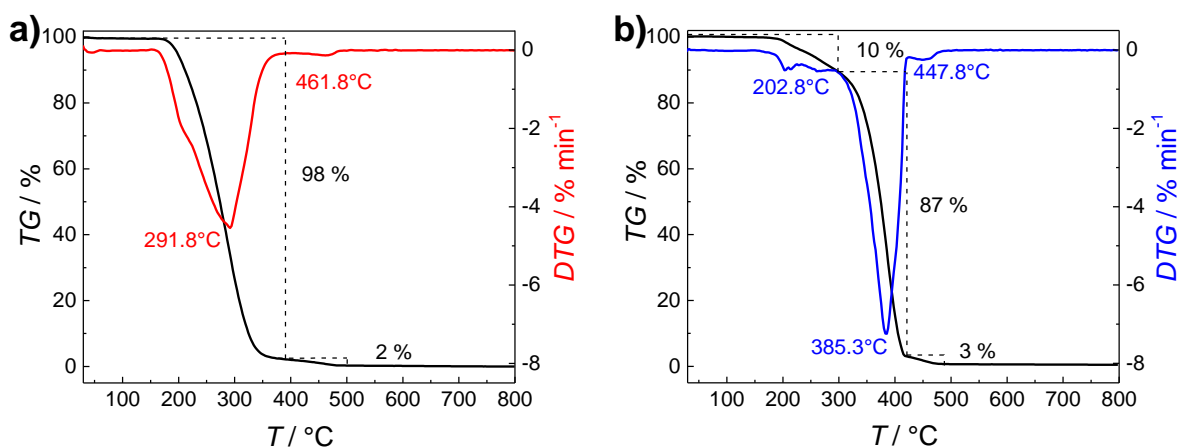


Figure 5.32: TG-MS measurements of a) Pluronic® F127 and b) PIB3000 polymer.^[34]

The two sorts of polymers show different thermal stability due to different polymer block units within the macromolecules. As shown in Figure 5.32, PLU decomposes in a wide temperature range with the main decomposition temperature at 291.8 °C accompanied by a weightless of 98 %. This points to almost complete decomposition below 300 °C. In contrast, PIB polymer ($M_w = 3000$) starts to decompose with 10 % weightless around 200 °C, which might be due to interconnecting polymer units. In the following, PIB shows a very sharp DTG signal at 385.3 °C with the main weightless of 87 %, which indicates a much higher thermal stability and a very concerted polymer decomposition. As the

synthesis route is based on a sol-gel mechanism, where the gelation occurs at 300 °C, in one case (PIB) the soft template is still present, while in the other case (PLU) the decomposition of the polymer is almost completed. Therefore, different pore morphologies due to the different thermal stability of the porogens can be expected.

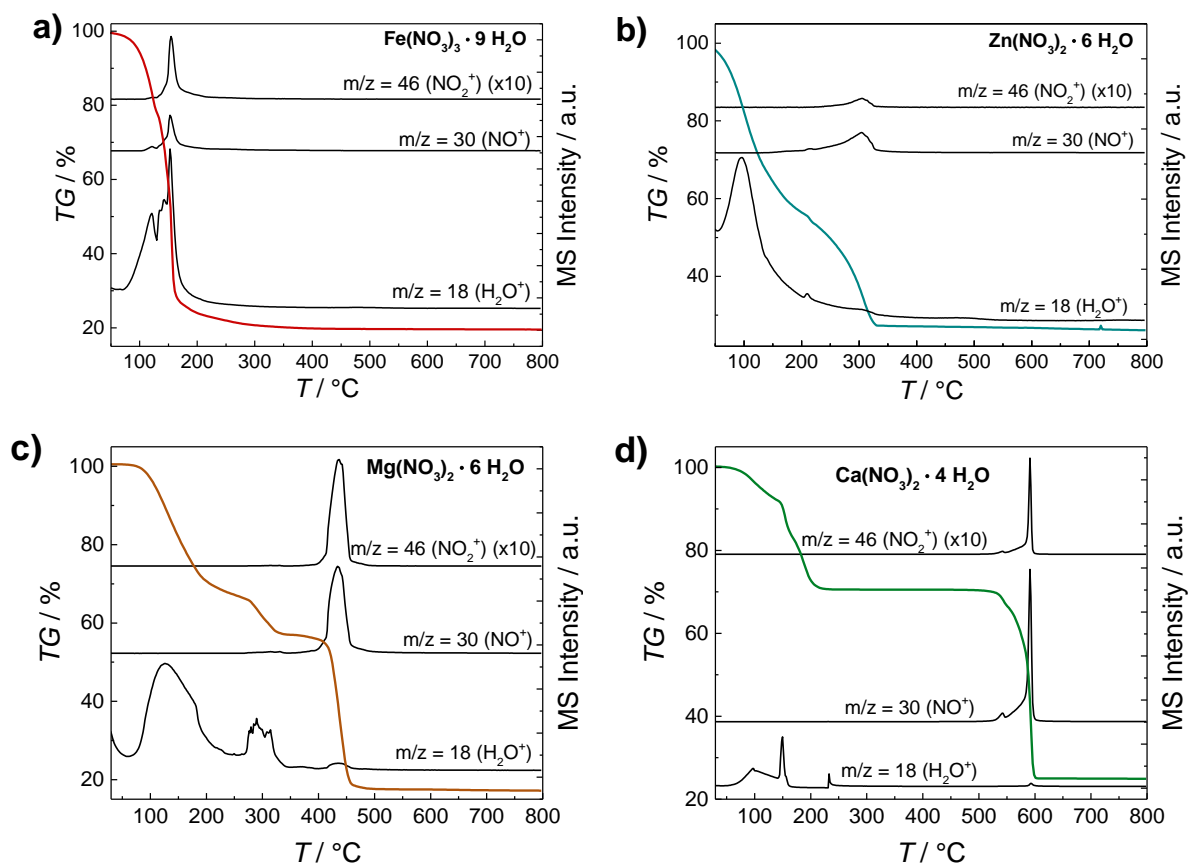


Figure 5.33: TG-MS data of the used metal nitrate precursors (Figures a) and b) also presented elsewhere)^[34].

Metal nitrates were used as metal ion source for the sol-gel process. Their thermal decomposition behavior was analyzed using TG-MS, too. The graphs in Figure 5.33 already show that thermal decomposition occurs at very different temperatures for iron(III) nitrate nonahydrate, zinc nitrate hexahydrate, magnesium nitrate hexahydrate and calcium nitrate tetrahydrate. The iron precursor decomposes already below 200 °C, while zinc nitrate decomposition is finished at 350 °C (see Figure 5.33a-b). These are still rather low temperatures, which portend possibly low synthesis temperatures for the formation of ZnFe_2O_4 . For full decomposition of magnesium nitrate, at least 450 °C are necessary (Figure 5.33c), which is already much higher than the values found for Fe and Zn precursors. Besides, a multistep decomposition behavior became evident from TG analysis, which was also found for calcium nitrate, having the highest decomposition temperature of 600 °C (Figure 5.33d). Multistep decomposition indicates a more complex mechanism, where also intermediates can be formed. In the case of Mg and Ca, the respective carbonates might be formed during decomposition

in air, as these elements strongly tend to form carbonates because of very low enthalpy of formation ($\Delta_f H^\circ(\text{MgCO}_3) = -1095.8 \text{ kJ mol}^{-1}$, $\Delta_f H^\circ(\text{CaCO}_3) = -1206.9 \text{ kJ mol}^{-1}$).^[359] From these results, different synthesis temperatures for formation of crystalline ferrite compounds can be expected. Of course, within a synthesis mixture the decomposition pathway can be different, which is why the precursor mixtures of all ferrite thin films will be analyzed in detail in the respective chapters.

5.3.1 Mesoporous Zinc Ferrite Thin Films

Reports discussed in chapter 2.2.3 revealed, that many factors influence the photoelectrochemical performance of ZnFe_2O_4 thin films, namely crystallinity, phase composition, and film thickness, porosity, surface defect states and surface kinetics. Within this thesis, systematic studies on interacting key factors for high PEC performance of sol-gel-derived ZnFe_2O_4 thin film photoelectrodes shall be provided with special focus on the synergistic effects of crystallinity and porosity.

5.3.1.1 Polymer-Templated Zinc Ferrite Synthesis

At first, closer look into the synthesis procedure of mesoporous ZnFe_2O_4 was gained by TGA analysis jointly with MS detection of pre-dried precursor sols containing the two aforementioned porogens (see Figure 5.34). The first weight loss in both precursor mixtures around 150 °C can be attributed to loss of crystal water and nitrate decomposition as identified via MS signals $m/z = 18$, $m/z = 30$ and $m/z = 46$. In PLU-containing sample, a clear signal for CO_2 loss ($m/z = 40$) starting at 234 °C and finishing around 300 °C can be seen. This indicates the decomposition of the polymer template. A tailing of the CO_2 signal with a peak 349 °C can be assigned to the minor weightless already observed in Figure 5.34a. For the PIB-derived sample, this signal appears at 251 °C and shows a broad plateau until 366 °C, which matches the higher thermal stability of PIB. A small CO_2 signal at 209 °C matches the first decomposition step of PIB already identified in Figure 5.34b. Overall, the precursor decomposition and transition from the nitrate-containing precursor sol into the solid, nitrate-free gel appears to be finished at 300 °C according to the corresponding MS signals.

Comparing IR spectra of the precursor gels, many similarities are found due to PEO building blocks present in both molecules. As evident from Figure 5.32c-d, aliphatic stretching vibrations of CH_3 , C-O-C and C=C are found in both samples, whereas the first mentioned is better resolved in PIB3000 due to CH_3 signals from both, PEO and PIB units.^[314] Furthermore, clear evidence of doublet caused by asymmetric stretching vibrations of NO_3^- (1390 cm^{-1} and 1354 cm^{-1}) and a deformation vibration for

NO_3^- at 831 cm^{-1} from nitrate precursor units were found.^[360] The typical broad stretching vibration of OH groups around 3435 cm^{-1} as well as deformation vibration water at 1625 cm^{-1} were detected, too. In both samples, stretching vibrations of metal-oxygen bonds were detected. In the PIB-derived sample, these are more distinct, which might indicate larger change in dipole moment due to a less rigid structure within the prepared gel.

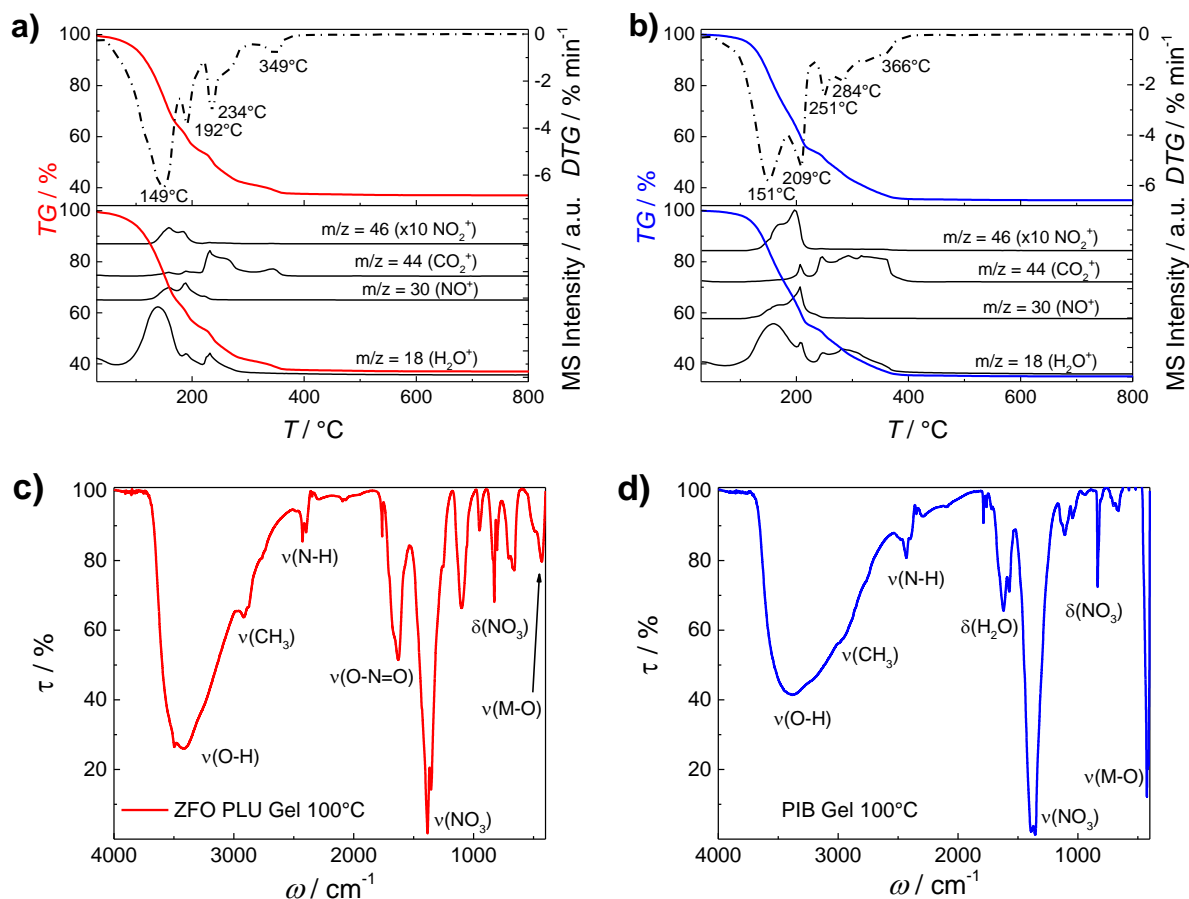


Figure 5.34: TG-MS measurements and IR patterns of a+c) PLU-derived and b+d) PIB-derived ZnFe_2O_4 precursor gels pre-dried at $100\text{ }^\circ\text{C}$.^[34]

GIXRD measurements during *in situ* calcination in a domed hot stage were performed to find the minimum crystallization temperature for synthesis of ZnFe_2O_4 thin films. For this purpose, thin films prepared with both polymer templates were pre-heated to $300\text{ }^\circ\text{C}$ according to the standard synthesis route for full gelation of the precursor sols. These gelled films were mounted inside the heating dome and heated to the desired temperature (either $300\text{ }^\circ\text{C}$, $400\text{ }^\circ\text{C}$, $500\text{ }^\circ\text{C}$ or $600\text{ }^\circ\text{C}$). GIXRD measurements in the range of 27° to 40° were performed, as here the most intense reflections of ZnFe_2O_4 were expected to appear. The resulting patterns can be seen in Figure 5.35.

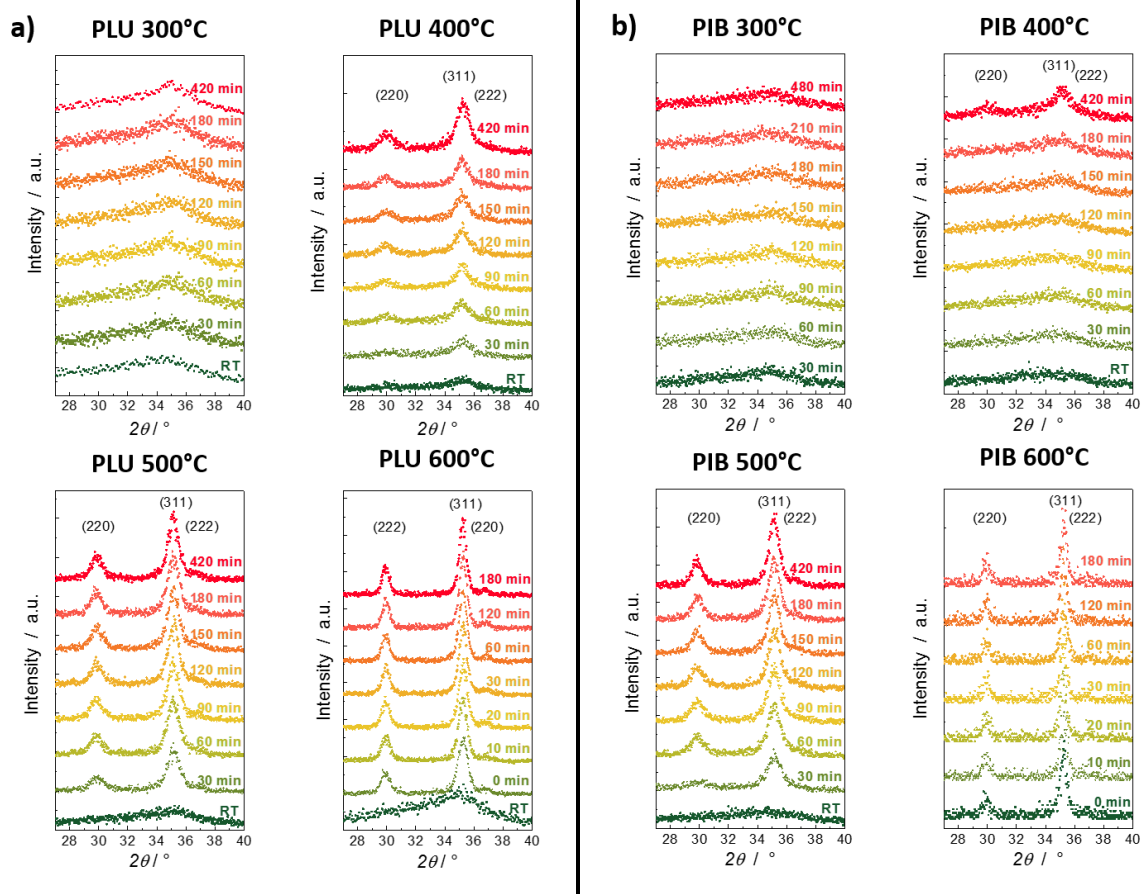


Figure 5.35: GIXRD measurements during *in situ* heating of a) PLU-derived and b) PIB-derived mesoporous ZnFe_2O_4 thin films.^[34]

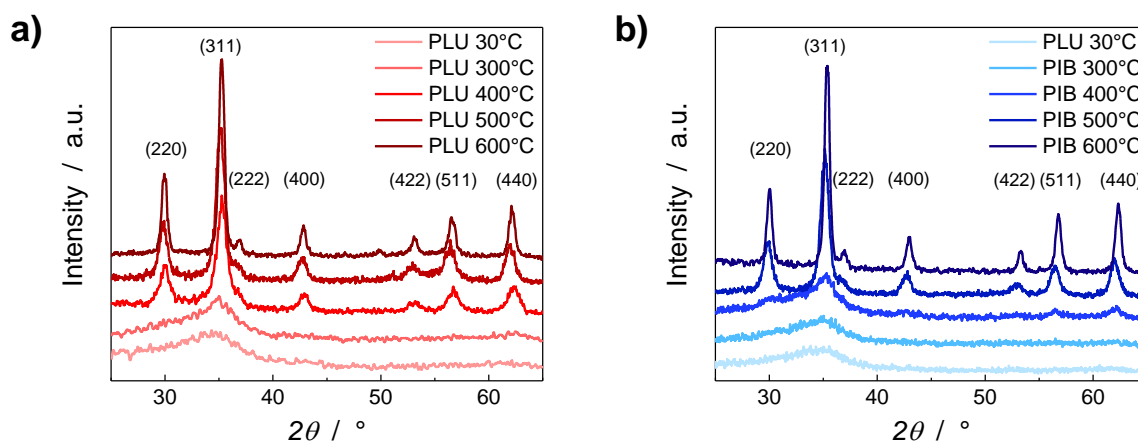


Figure 5.36: GIXRD patterns of a) PLU-derived and b) PIB-derived obtained after *in situ* calcination of ZnFe_2O_4 gel films.^[34]

The data show very similar behavior of thin films containing either one polymer precursor, underlining the formation of large ZnFe_2O_4 crystallites is not heavily dependent on the soft template. For both samples, significant crystallization can be observed at temperatures of 500 °C and above. Below this temperature, even after extended calcination periods hardly any reflections were detected (see Figure 5.36), which indicating a mainly X-ray amorphous material. This matches findings from

ZnFe₂O₄ nanoparticles, which did not show an increase in crystallite size due to missing sintering during calcination at 400 °C, but a rising value for higher calcination temperatures (compare Figure 5.7). At 500 °C and 600 °C, typical reflections of ZnFe₂O₄ appear already after 30 min, which suggests that already short calcination periods are sufficient for ZnFe₂O₄ formation.

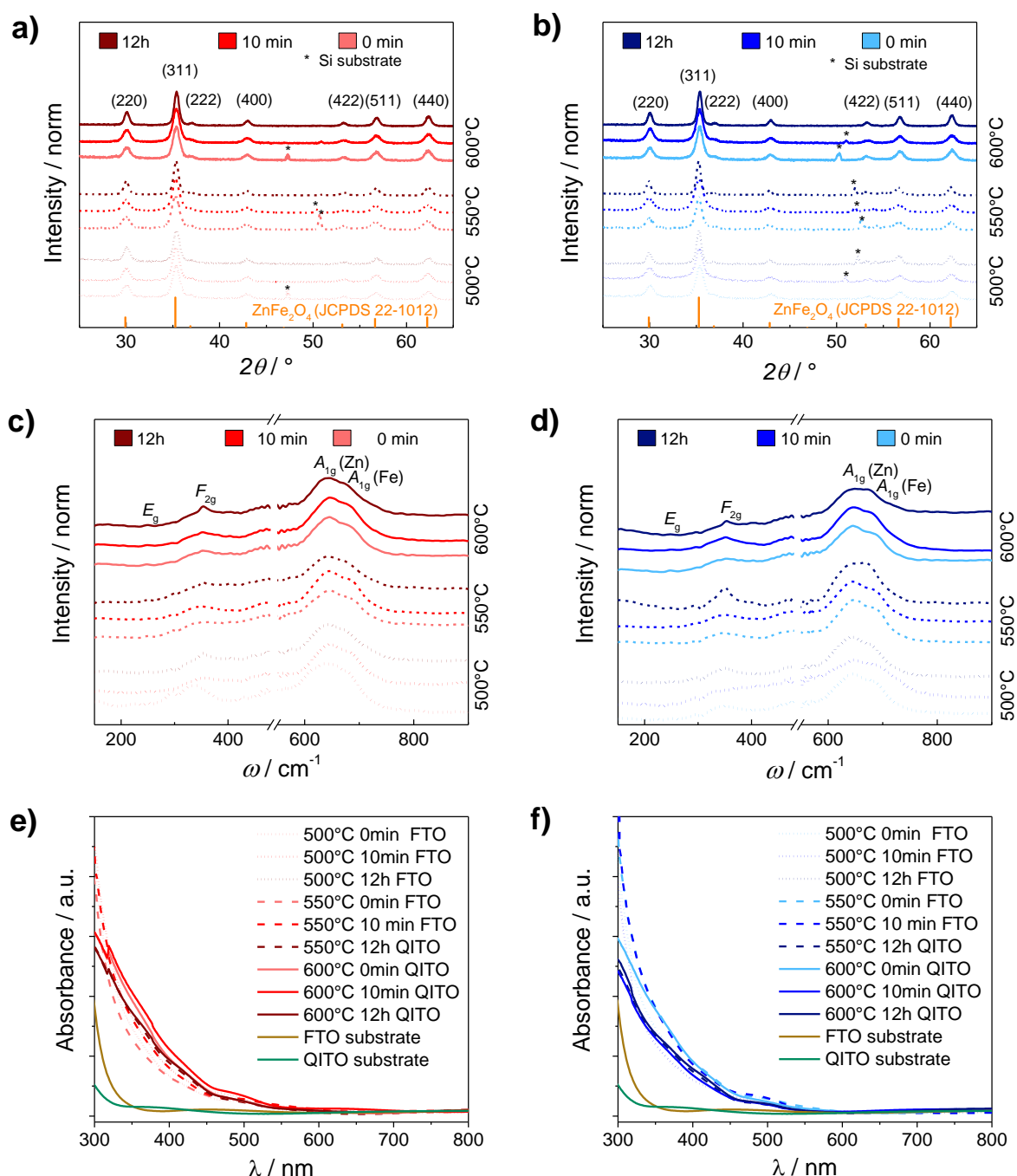


Figure 5.37: GIXRD measurements of a) PLU-derived and b) PIB-derived as well as Raman spectra of c) PLU-derived and d) PIB-derived and UV-Vis spectra of e) PLU-derived and f) PIB-derived mesoporous ZnFe₂O₄ thin films.^[34]

From these results, a temperature study of calcination between 500 °C to 600 °C with variation of the calcination period was performed. The temperature range was chosen to avoid appearance of

α -Fe₂O₃ impurities at very high temperatures, because the formation of α -Fe₂O₃ is thermodynamically favored. As shown in Figure 9.6, calcination at very high temperatures leads to a transformation of ZnFe₂O₄ into α -Fe₂O₃, which was already presented elsewhere.^[34] Furthermore, a lower temperature leads to a more cost-efficient process, which is highly desirable. Finally, it is easier to maintain the desired mesoporosity at lower calcination temperatures due to limited sintering. GIXRD patterns, Raman and transmission UV-Vis spectra (see Figure 5.37) were collected of PLU- and PIB-templated thin films, which were calcined at either 500 °C, 550 °C or 600 °C with 0 min, 10 min or 12 hours holding time, respectively.

The expected reflections of ZnFe₂O₄ were found in all prepared thin films. An extra reflection of the Si wafer (marked with *) can be seen in some samples. This reflection is moving due to differences in the omega angle, which is specific for each sample and necessary for measurement optimization. Raman spectra, which were Si background corrected, also proof the high phase purity of the prepared ZnFe₂O₄ films. Transmission UV-Vis spectra (Figure 5.37e-f) of PLU- and PIB-templated samples on FTO and quartz ITO substrates show comparable absorption behavior. With similar solar light absorption, differences in PEC performance would not derive from absorption phenomena, but rather from intrinsic differences, *e.g.* different crystallite sizes, microstrain or donor densities (see 5.3.1.2).

From GIXRD data presented in Figure 5.37a-b, Rietveld refinement was performed to gain deeper insight into the crystallization process (for details see Table 9.1). The average crystallite size obtained from the refinements in dependence of the calcination temperature is shown in Figure 5.38a.

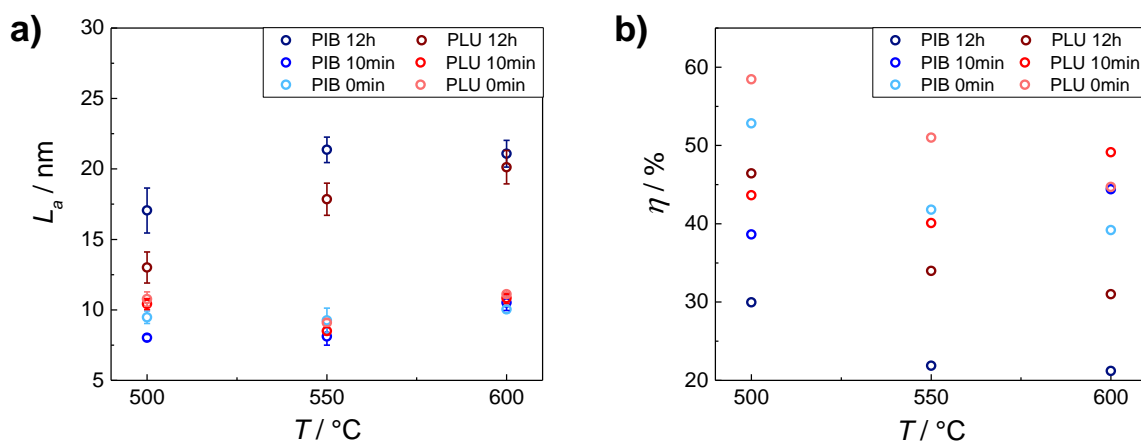


Figure 5.38: a) Average crystallite sizes and b) average microstrain of mesoporous ZnFe₂O₄ thin films calcined at 600 °C.^[34]

As can be seen, shorter calcination periods applied to PLU- and PIB-derived samples leads to small crystallite sizes in all samples. With increasing calcination temperature, a slight increase in crystallite size is observable, which matches the crystallization theory. Samples calcined for 12 hours show significantly larger average crystallite size already at 500 °C. Again, with higher calcination temperature, the average crystallite size obtained from refinement increases. At 600 °C, for both PIB-

and PLU-derived samples calcined for 12 hours reach identical values, indicating that with this calcination approach, the nature of the porogen does not influence the crystallite size anymore. Figure 5.38b shows the evolution of microstrain depending on the calcination approach. As microstrain is a very important parameter in porous materials, as it not only reflects the amount of intrinsic defects but the crystal distortion due to pore formation. Although both polymer templates cause a similar pore morphology after long-term calcination, a significant difference in microstrain is observable. With a similar pore structure, this is probably caused by a higher number of intrinsic defects.

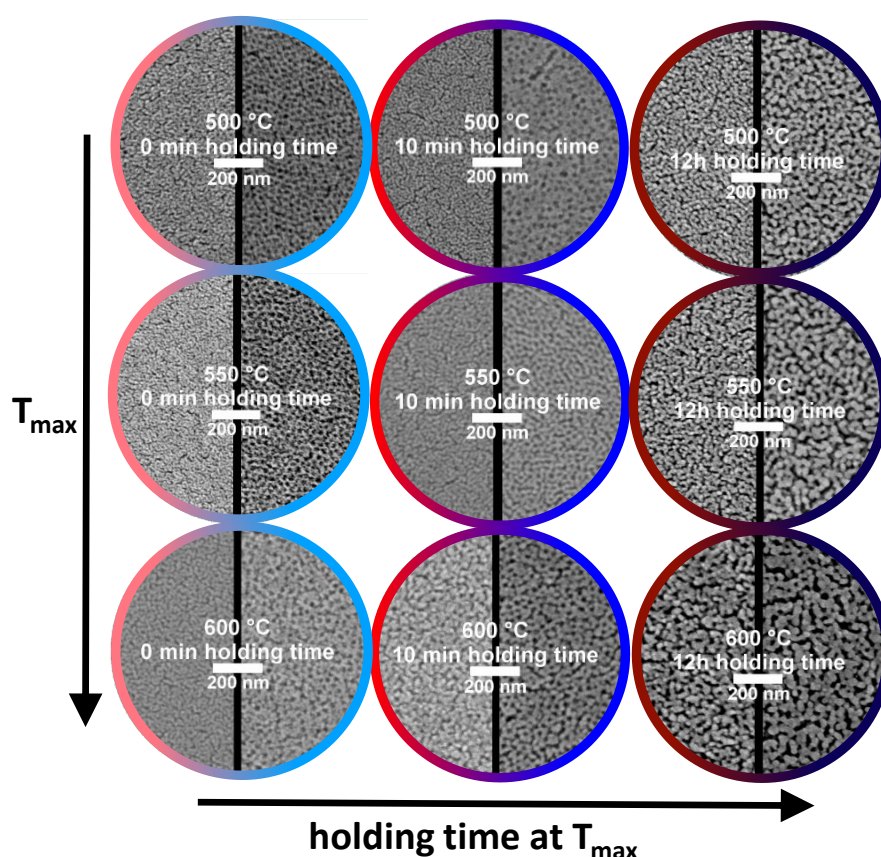


Figure 5.39: SEM images of PLU-templated (left, red half-circle) and PIB-templated (right, blue half-circle) samples obtained after different calcination procedures.^[34]

The induced crystallite growth can also be followed using SEM (see Figure 5.39). Samples synthesized at 500 °C without holding time show completely different pore morphologies. For PLU-derived samples, an irregular pore structure with very fine grains was found, while PIB-templating results in spherical mesopores. This was assigned to the difference in polymer template stability under thermal conditions as discussed earlier (compare Figure 5.32). During calcination at different temperatures without holding time, the original morphology is changed slightly, as crystallization is a

time dependent process. This matches the findings from *in situ* GIXRD measurements (compare Figure 5.35 and Figure 5.36).

With extended calcination period, crystallite growth leads to an enlargement of the grains, which is also visible in SEM (see Figure 5.39). At 500 °C, where only minor crystallite growth was observed from *in situ* GIXRD experiments (compare Figure 5.35 and Figure 5.36), the change in morphology is still moderate. A minor increase in feature size was found for PLU-templated samples, while PIB-derived samples still show some spherical pores. By increasing the calcination temperature, the formation of crystalline ZnFe_2O_4 domains is promoted, which is why a strong restructuring takes place. PIB-templated samples lose their spherical pore shape due to sintering, which increases the size of the solid features in both sample types. After calcination at 600 °C for 12 hours, no difference in pore morphology or feature size is detectable anymore.

The changes in pore morphology due to sintering go along with a loss of surface area. This can be followed by Kr physisorption, which was used to determine the surface area of as-prepared thin films. For both polymer templates, similar trends in change of BET surface area were found, which are depicted in Figure 5.40. A rise in surface area was found, when the calcination period was extended from 0 min to 10 min at 600 °C (Figure 5.40a). This was assigned to improved removal of polymer template residues, leading to a better pore accessibility. With an increase in calcination period to 12 hours, a conspicuous loss in surface area was found. This was attributed to pore collapsing due to sintering effect in the pore walls, which was already observed in XRD and SEM analysis (compare Figure 5.35 and Figure 5.39). Concerning the influence of the maximum temperature during 12 hours of calcination (Figure 5.40b), a linear decrease in surface area was found with rising temperature. This is in agreement with findings from SEM analysis (compare Figure 5.39). Generally, the BET surface area of both polymer templates is comparable at long calcination periods.

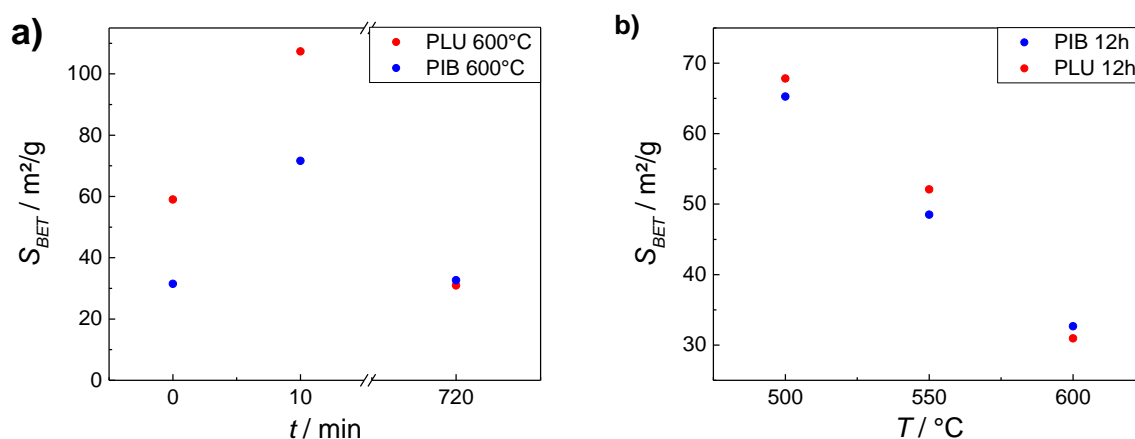


Figure 5.40: Kr BET measurements of PIB- and PLU-derived ZnFe_2O_4 thin films.^[34]

5.3.1.2 PEC Performance of Sol-Gel Derived Mesoporous Zinc Ferrite Thin Films

By photocurrent measurements in the dark and under simulated sunlight irradiation (AM 1.5G), the output in photocurrent density of the previously described mesoporous ZnFe_2O_4 thin films were investigated. The resulting photocurrent densities at $1.23 V_{\text{RHE}}$ are displayed in Figure 5.41. The high photocurrent values of samples calcined at 500°C for short time (0 min or 10 min) have to be evaluated very carefully, as these samples were not stable under measurement conditions and depleted from the substrate. The lower chemical stability probably arises from a high amount of precursor gel still present in those samples, as it was found from *in situ* GIXRD measurements (compare Figure 5.35).

Nevertheless, the samples prepared calcining for 12 hours at 500°C were stable during and after the PEC measurements.

A clear dependence of the photocurrent density on the calcination temperature and calcination period was found for both sample types. Mesoporous thin films calcined at the same temperature show rising photocurrent densities, when the calcination period is extended. With increasing calcination temperature is increased, higher photocurrent densities were detected although the active surface area decreased. This was assigned to average crystallite sizes and microstrain values of the samples. The crystallite size increases

with higher calcination temperature and longer calcination period, while the microstrain decreases at the same time (compare Figure 5.38). This leads to improved charge carrier transport to the thin nanostructured surface, which improves the measured photocurrent. Furthermore, long-term calcined PLU-derived samples show higher photocurrent densities in comparison to their PIB-derived analogues. Although similar average crystallite sizes were obtained, the interconnection of these crystallites might vary due to the strong restructuring during pore wall sintering. As the crystallite sizes calculated from Rietveld refinement represent only average values, it is possible, that higher differences in actual crystallite size could be present in the PIB-templated samples, which might lead to a higher number of grain boundaries in the PIB-templated samples. These would react as recombination centers and therefore suppress the maximum achievable photocurrent density. The results show, that improving the crystallinity of the mesoporous thin films outlines the influence of accessible surface area in terms of overall PEC performance.

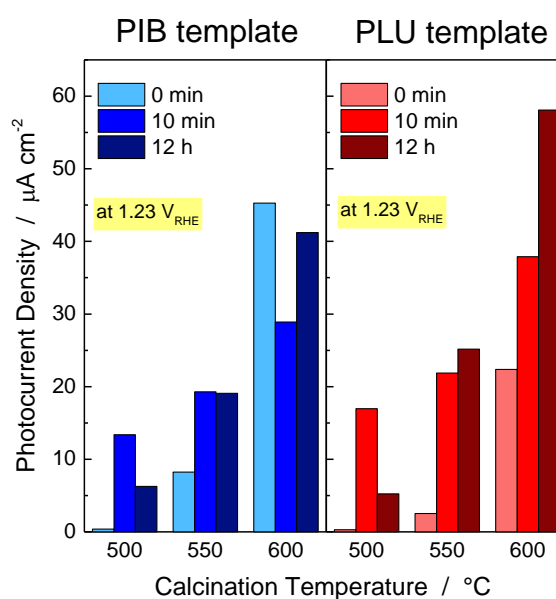


Figure 5.41: Photocurrent values at $1.23 V_{\text{RHE}}$ of PLU- and PIB-derived mesoporous ZnFe_2O_4 photoanodes measured in $1\text{M NaOH}/1\text{M Na}_2\text{SO}_3$ electrolyte.^[34]

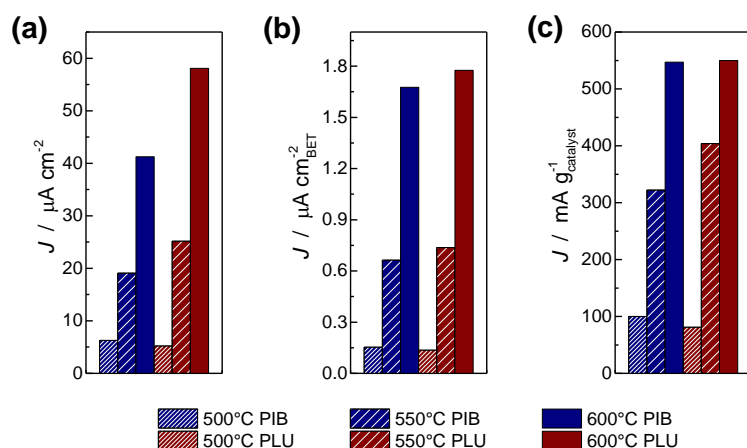


Figure 5.42: PEC densities at 1.23 V_{RHE} PIB- and PLU-derived samples calcined for 12 hours calculated in respect to different photoelectrode features.^[34]

As already shown during previous analysis (see Figure 5.40, the highly porous thin films exhibit a higher surface area than a dense photoelectrode. The standard procedure for photocurrent density calculation is the normalization on the irradiated geometric area (1 cm^2 in this case). As the irradiated area is not the active area when it comes to porous systems, photocurrent density values at 1.23 V_{RHE} obtained of both polymer templates were re-evaluated with regard to the thin films properties. This is shown in Figure 5.42, where the photocurrent density normalized on the diameter of irradiated area (a) is compared to the values considering the actually irradiated surface area obtained from Kr physisorption (b) and the catalyst loading per irradiated area (c). By comparing these photocurrent density values, the problem of evaluation of the PEC performance becomes evident. The standard method applied today (case (a)) might not be suitable for porous photoelectrodes, as it neglects the exposed surface to the electrolyte. Furthermore, in nanostructured electrodes, less bulk recombination might occur, as the diffusion pathways from to the nanostructured surface are much shorter than in bulk materials, leading to less inactive zones within the photoelectrode. Therefore, the same amount of absorber could generate a higher photocurrent, when it is nanostructured, which is why the absorber loading is not neglectable. Depending on the considered assumptions, the assessment of a “good” absorber can be very different. Therefore, this assessment should be stated very carefully.

In Figure 5.43, the photocurrent responses under front side and backside illumination with simulated solar light of long-term calcined (12 hours) photoelectrodes and their calculated donor densities are shown. There is no major difference in photocurrent density between foreside and backside illumination of photoelectrodes, which suggests a similar transport behavior for photo-generated electrons and holes. This was not expected, as the transport of holes (in this case minority carriers) in the oxide is usually quite limited. The equally good transport behavior was accounted to the thin film thickness the approx. 240 nm, which allows charge carrier generation across the whole thin film, and the nanostructuring, which shortens the diffusion pathway for the minority carriers towards the semiconductor surface and was already reported to improve the performance of $\alpha\text{-Fe}_2\text{O}_3$ photoanodes.^[89,91] The donor densities are all in the same range, showing a minor decline with higher

calcination temperature. As these samples showed the highest PEC performance in their groups, the slight decrease is not expected to have a negative influence on the overall PEC performance.

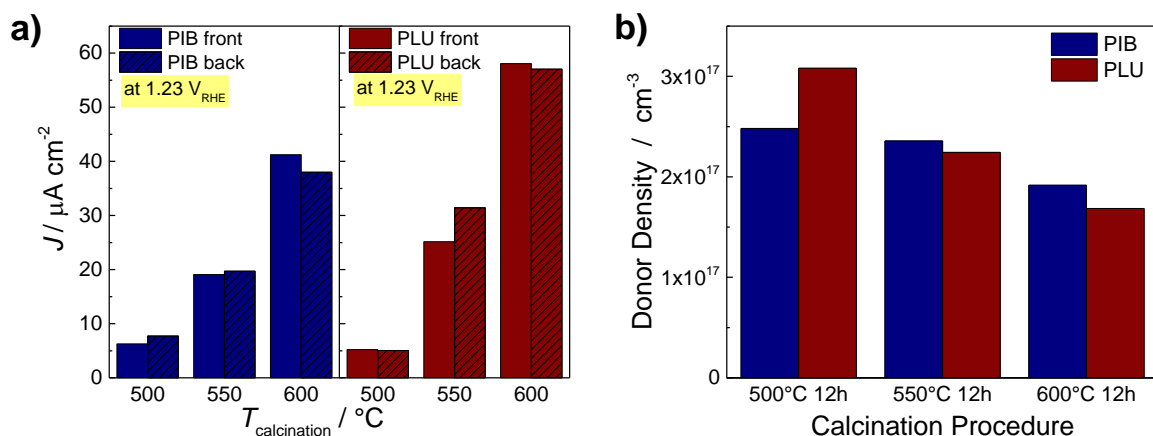


Figure 5.43: Photocurrent densities under front side and back side solar irradiation and b) calculated donor densities of PIB-templated (blue) and PLU-templated (red) mesoporous ZnFe_2O_4 thin films calcined for 12 hours.^[34]

As the samples calcined at 600°C for 12 hours showed the highest photocurrent densities, they were investigated in more detail. Mott Schottky plots (Figure 5.44) show an identical shape identifying ZnFe_2O_4 as n-type semiconductor with a flat band potential of $0.84 \text{ V}_{\text{RHE}}$ for both samples. This is in the dimension of values reported for non-porous ZnFe_2O_4 thin films prepared by ALD^[30] or ZnFe_2O_4 films prepared by CVD^[31], but slightly shifted to higher potential values, which might be attributed to the very small grain size of the mesostructure increasing the impedance of the thin film.

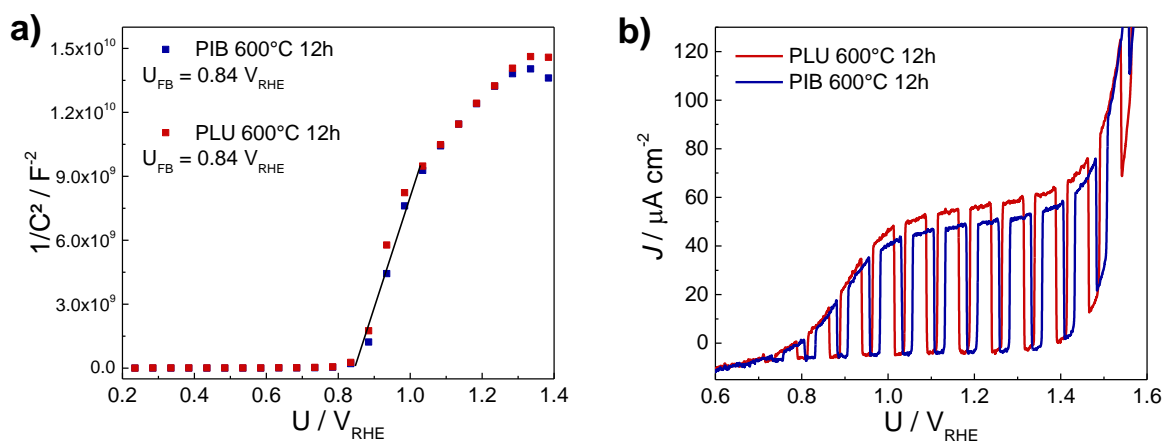


Figure 5.44: a) Mott-Schottky plots and b) photocurrent measurements with intermittent irradiation with simulated solar light of PLU- and PIB-derived mesoporous ZnFe_2O_4 thin films calcined at 600°C with 12 hours holding time.^[34]

Under intermittent illumination with simulated solar light, both samples show clear photocurrent responses. No transients were detected, which is assigned to the presence of Na_2SO_3 hole scavenger.

Again, the PLU-derived sample shows higher photocurrent densities over a wide potential range compared to its PIB-derived analogue. The detected photocurrent onset potential of 0.62 V_{RHE} under intermittent irradiation matches with the flat-band potentials reported in literature.^[30,31] In general, measured and literature values locate the valence band of n-type ZnFe₂O₄ above the redox potential for HER indicating that ZnFe₂O₄ thin films are suitable to be used as photoanodes for OER in PEC water splitting, however not for HER without any bias.

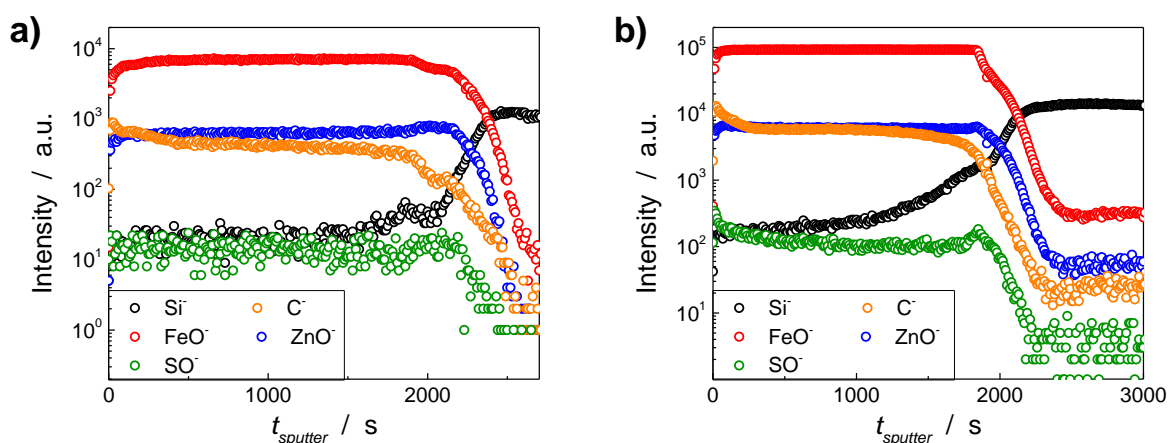


Figure 5.45: ToF-SIMS depth profile of mesoporous ZnFe₂O₄ thin films derived from a) PLU and b) PIB template.

Using Time of Flight Secondary Ion Mass Spectrometry (ToF-SIMS), a depth profile containing information on the elemental distribution across the thin film depth can be obtained. To locate the beginning of the Si substrate, the Si⁻ fragment was detected ($m/z = 27.98$). As shown in Figure 5.45, mesoporous thin films, obtained by calcination at 600 °C for 12h, show similar elemental distribution for both polymer templates. Across the complete ZnFe₂O₄ thin film depth, constant amounts of Zn (detected by ZnO⁻ fragment, $m/z = 79.95$) and Fe (detected by FeO⁻ fragment, $m/z = 71.95$) were found. Detection of the C⁻ fragment ($m/z = 12.00$) implies the presence of carbon residues inside the mesoporous films. Analysis of the thin films after PEC measurement revealed a mass signal at $m/z = 47.98$, which belongs to SO⁻ residues from SO₃²⁻ hole scavenger. The signal course proves that SO₃²⁻ containing electrolyte infiltrated the mesoporous samples over their complete film thickness suggesting that the interconnected pore network is fully accessible.

Because the PLU-templated sample obtained after calcination at 600 °C for 12h was most promising concerning its PEC performance, this sample was further investigated. Using intermittent illumination with a white light LED ($\lambda \geq 400$ nm), the photocurrent density under visible light excitation in the presence and in the absence of SO₃²⁻ hole scavenger was analyzed (see Figure 5.46a).

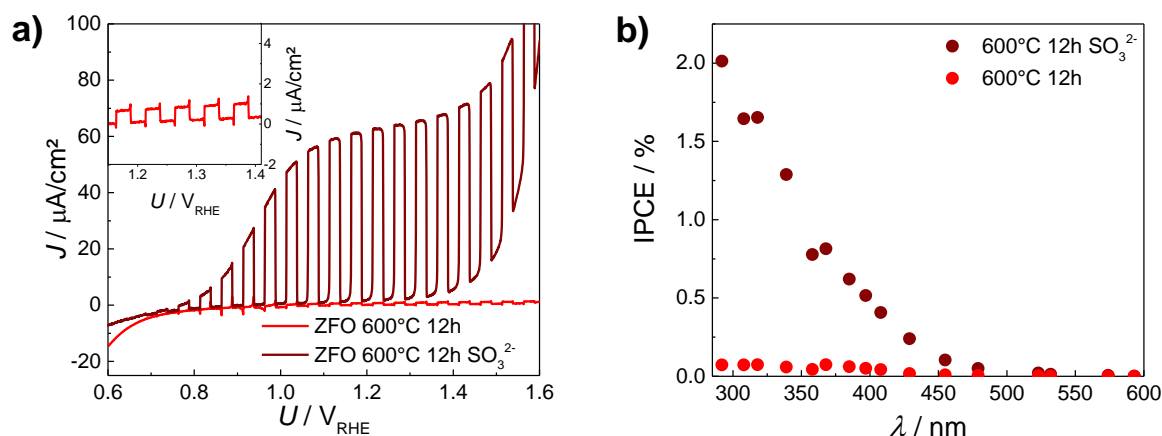


Figure 5.46: a) Photocurrent density and b) IPCE measurements of a mesoporous PLU-derived ZnFe_2O_4 photoelectrode calcined at 600 °C for 12 hours in 1 M NaOH (bright red) and in 1 M NaOH with 1 M Na_2SO_3 (dark red).

In the absence of the sacrificial agent, only a minor photocurrent response was detected with transient responses indicating charge carrier accumulation (see Figure 5.46a inset). Whereas, a clear distinction between dark current and photocurrent is possible, when SO_3^{2-} is present. The photocurrent onset was found to be 0.69 V_{RHE} for both samples. Resulting from this behavior, no self-corrosion during the photocatalytic process is expected. In addition, slow charge transfer kinetics to fill the photogenerated holes were identified. This leads to a high recombination rate, which significantly lowers the resulting photocurrent.

By IPCE measurements, determination of the quantum efficiency of the photoelectrode in dependence of the illumination wavelength is possible (compare equation (2.29)). As shown in Figure 5.46b, very low IPCE was found in the absence of SO_3^{2-} . In contrast, a drastic increase in IPCE with the hole scavenger was detected. This matches with the findings from Figure 5.46a. With decreasing photon energy, lower IPCE was found. At 397 nm, an IPCE of 0.05 % is found in the absence of Na_2SO_3 and an IPCE of 0.52 % in the presence of Na_2SO_3 . With a maximum value of 2.01 % at 292 nm, the overall IPCE is still quite low. Here, optimization of the photoelectrode by co-catalyst loading^[152,246], electrochemical treatment^[361,362] or combination with other semiconductors to form hetero-nanostructures^[25,196] might help to improve the PEC performance.

5.3.1.3 Morphology Conservation via SiO_2 Infiltration

In literature, hard-templating is reported to preserve smaller pore sizes during high temperature treatment.^[138] To see, if this is also applicable for PLU- and PIB-templated ZnFe_2O_4 thin films, two films previously calcined at 600 °C without holding time were infiltrated with SiO_2 according to 0. Subsequently, they were heat-treated at 600 °C for 12 hours in air. Afterwards, the SiO_2 scaffold was

etched resulting in pure ZnFe_2O_4 thin films again. The obtained films were compared to films, which were calcined identically but without the SiO_2 scaffold. Using XPS analysis, incorporation and removal of the scaffold was monitored (Figure 5.47).

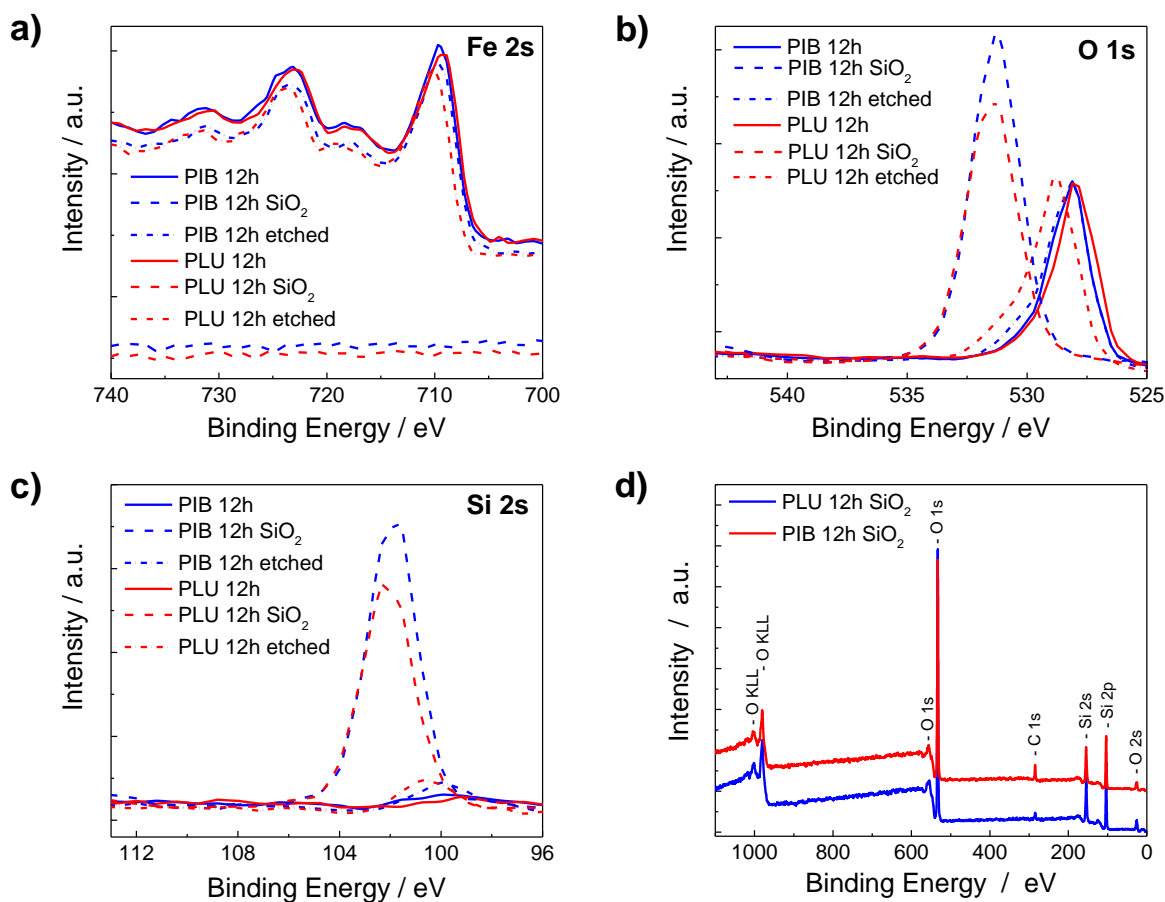


Figure 5.47: XPS measurements of ZnFe_2O_4 thin films with and without SiO_2 scaffold.^[34]

As shown in Figure 5.47d, there are no signals from Fe 2p or Zn 3s detectable in the samples with SiO_2 still present. This proves the complete encapsulation of the mesoporous ZnFe_2O_4 with SiO_2 . Instead, in the scaffold samples an intense Si 2p signal at 102.3 eV and an O 1s signal at 533.1 eV were detected, which is typical for SiO_2 .^[363] In the samples calcined without scaffold and those after SiO_2 removal, XPS signals were found at 137.5 eV and 138.0 eV, which belong to Zn 3s binding energy. The Fe 2p signals were detected at 711.3 eV and 711.2 eV, respectively, and match literature values reported for ZnFe_2O_4 .^[31,240,246] Additionally, the O 1s signals can be seen at 530.1 eV in both sample types. A minor Si 2p signal at 99.8 eV can be attributed to Si from the Si wafer substrates.^[364] The results from XPS analysis match those reported for hematite films with SiO_2 scaffold by Brillat *et al.*^[138]

SEM images of infiltrated samples (Figure 5.48) proof the full encapsulation on the original pore structure. Only a smooth surface of SiO_2 is visible. After etching, the mesoporous morphology is revealed again. Comparing the resulting films with those calcined without SiO_2 scaffold (see

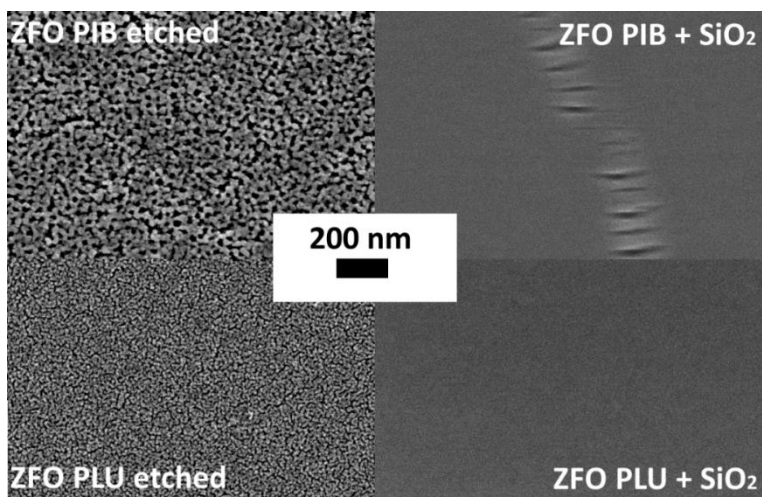


Figure 5.48: SEM images of PIB-derived (upper) and PLU-derived (lower) ZnFe_2O_4 samples with and without SiO_2 scaffold.^[34]

Figure 5.39), the successful conservation of the fine pore morphology of the PLU-templated sample becomes evident.

In contrast, the PIB-derived sample shows some pore collapsing, although the original spherical pores can still be estimated. As the spherical pore network caused by PIB soft template is already highly

interconnected, SiO_2 hard-templating cannot fully prevent sintering of the pores during heat treatment. With the well-separated grains of PLU-derived sample, the full encapsulation with SiO_2 is possible enabling complete retaining of the original pore morphology. As a result, the PEC performance of PLU sample after etching is only slightly increased due to defect healing during long-term high temperature treatment (Figure 5.49a). The higher sintering within the PIB-derived sample leads to larger crystallites and less intrinsic defects, which improves the PEC performance (Figure 5.49b). This is in agreement with the previous results (compare 5.3.1.2).

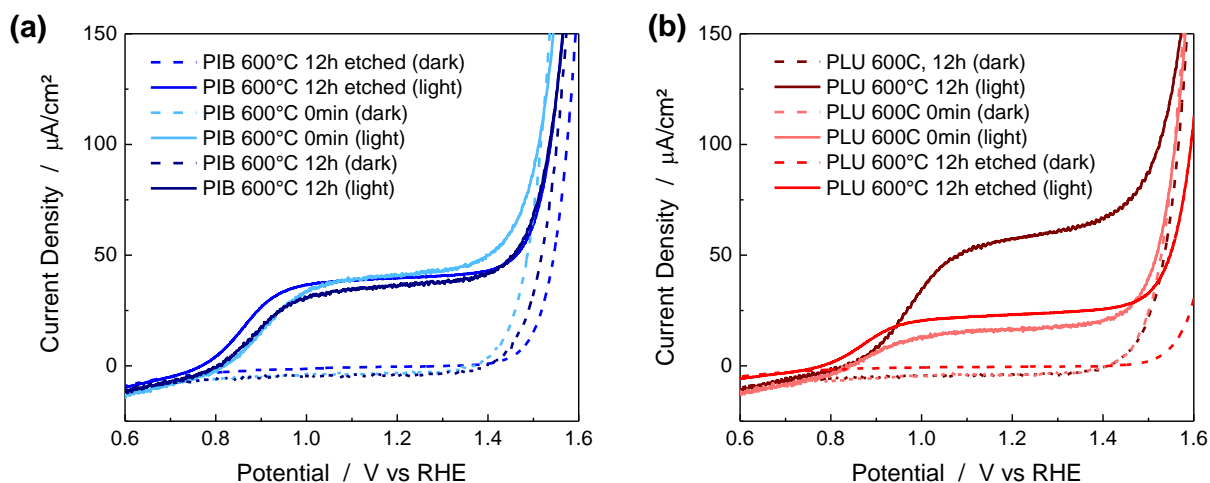


Figure 5.49: PEC performance of (a) PIB-derived and (b) PLU-derived samples with and without SiO_2 hard templating.^[34]

5.3.2 Mesoporous Magnesium Ferrite Thin Films

5.3.2.1 Polymer-Templated Magnesium Ferrite Thin Film Synthesis

As preparation of mesoporous ZnFe_2O_4 was very successful, the synthesis approach was transferred to MgFe_2O_4 . Again, metal nitrates were chosen as metal precursors. Because spherical pore shape was not improving the PEC performance compared to irregular pore shapes, Pluronic® F127 was chosen as soft template. The calcination procedure was adapted according to chapter 5.3.1, and a maximum temperature of 600 °C was chosen.

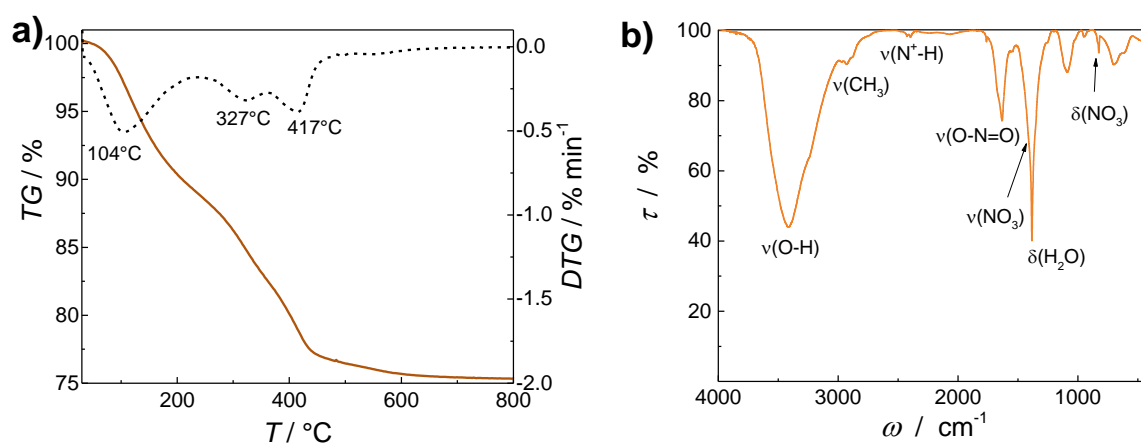


Figure 5.50: TG-MS data and b) IR pattern of precursor gel.

At first, a characterization of the precursor gels obtained after heat treatment at 300 °C was performed. As can be seen in Figure 5.50a, TG analysis revealed three weight loss steps during thermal decomposition of the MgFe_2O_4 precursor gel (104 °C, 327 °C, 417 °C). The first decomposition step is probably due to loss of water. By comparison with the TG data of PLU polymer (see Figure 5.32a), the second weight loss at 327 °C can be assigned to the removal of the soft template. This was also the case for ZnFe_2O_4 (compare Figure 5.34a). The last weight loss probably marks the final decomposition of the nitrate components within the precursor gel, as these appeared in a similar temperature range for $\text{Mg}(\text{NO}_3)_2$ precursor (compare Figure 5.33c). The thermal decomposition steps are higher than those found for ZnFe_2O_4 precursor gels. As this was also the case for the nitrate salts of Mg and Zn (compare Figure 5.33b-c), the temperature difference can be assigned to a difference in the decomposition behavior of the latter. This leads to a higher minimum temperature for the sol-gel transition in the MgFe_2O_4 precursor mixture.

In the IR spectrum of the 300 °C precursor gel (Figure 5.50b), all expected vibrational bands for the precursor gel were detectable. Only a weak signal at 2925 cm^{-1} indicates residues of PLU, as the polymer already decomposes at 300 °C. Therefore, characteristic features of the nitrate components become more prominent. Furthermore, very distinct vibrations for OH stretching (3400 cm^{-1}) and

OH deformation (1385 cm^{-1}) were found. The pattern looks very similar to the one measured for ZnFe_2O_4 -PLU precursor gel (compare Figure 5.34c), which was expected.

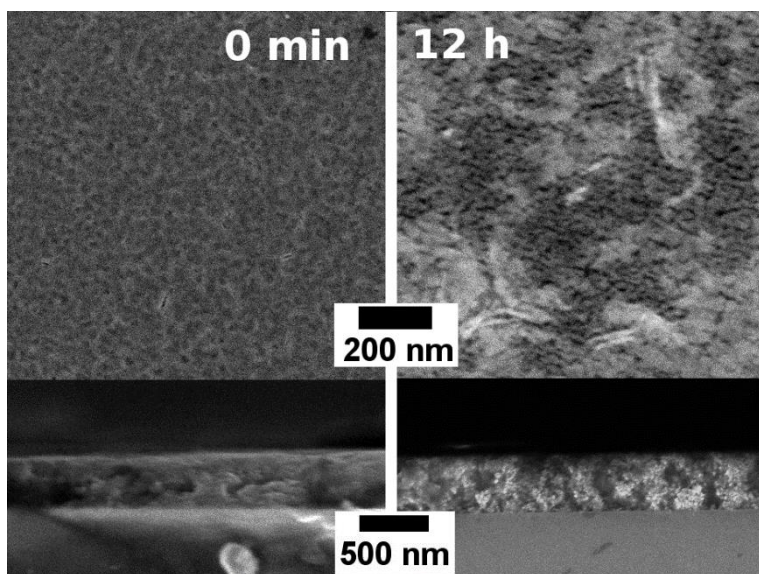


Figure 5.51: SEM top view (above) and cross section (below) images of MgFe_2O_4 thin films calcined at $600\text{ }^\circ\text{C}$ for 0 min (left) and 12 hours (right).

Nevertheless, the surface is partly covered, which might be due to the formation of MgCO_3 surface layers. With a short holding time, a fine pore structure with small grain sizes was observed, while enhancing the calcination period up to 12 hours led to larger pore sizes and MgFe_2O_4 grains. These results match observations made for PLU-derived ZnFe_2O_4 thin films (compare Figure 5.39). Kr physisorption measurement revealed a BET surface area of $70\text{ m}^2\text{ g}^{-1}$ for the sample calcined for 12 hours, which is larger than the value of the PLU-derived ZnFe_2O_4 analogue ($38\text{ m}^2\text{ g}^{-1}$). This is in agreement with SEM images, where the MgFe_2O_4 thin film shows smaller pores.

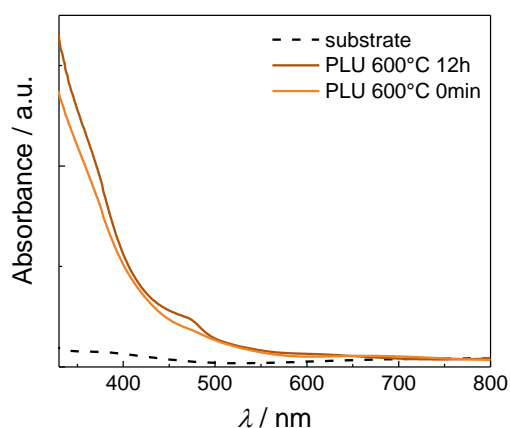


Figure 5.52: Transmission UV-Vis spectra of MgFe_2O_4 thin films.

To compare the UV-Vis absorbance of the prepared thin films, transmission UV-Vis measurements were performed (Figure 5.52), showing a similar light absorption. After GIXRD and Raman measurements (Figure 5.53), the morphological difference was linked to the phase composition of the prepared thin films. Using GIXRD and Raman analysis, phase purity of the prepared thin films was checked. In the GIXRD patterns shown in Figure 5.53a, only an amorphous phase was found for the short calcination period. Furthermore, no clear signals

can be seen in the Raman spectrum (Figure 5.53b), which results from non-ordered amorphous structure. In contrast, a prolonged calcination period at 600 °C leads to fully crystalline MgFe_2O_4 . All reflections match the reference pattern (JCPDS card no. 36-0398) and no additional reflections or phase impurities were found. From Rietveld refinement, an average crystallite size of 4.3 ± 0.8 nm and an average microstrain of 33.7 % were found (see Table 9.1). The microstrain is in the order of magnitude as are the values found for mesoporous ZnFe_2O_4 , but the crystallite size is quite low compared to ZnFe_2O_4 thin films. The Raman spectrum shows all expected vibrational modes of spinel-type MgFe_2O_4 . They match well with those found for MgFe_2O_4 nanoparticles (compare Figure 5.1) and literature values.^[365] The results indicate that short time calcination at 600 °C is not sufficient for synthesis of phase pure MgFe_2O_4 thin films from sol-gel approach.

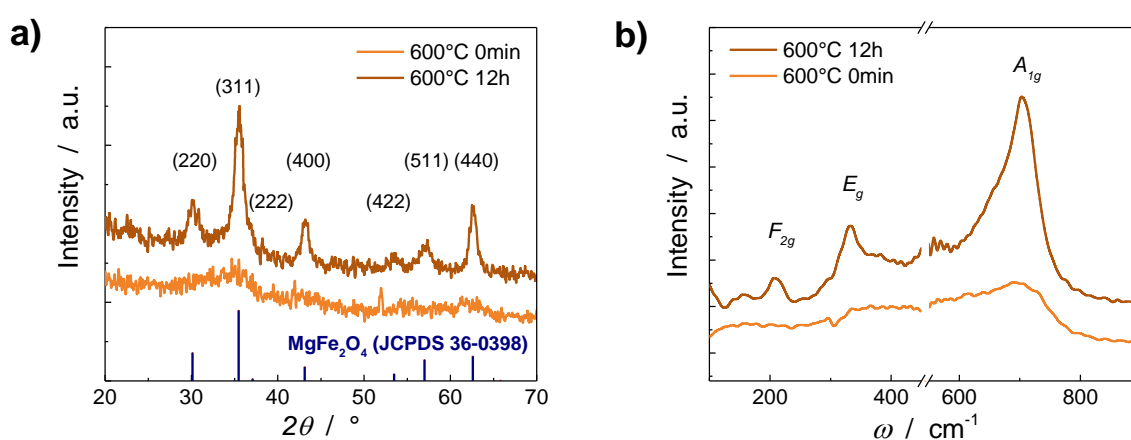


Figure 5.53: a) GIXRD patterns and b) Raman spectra of mesoporous MgFe_2O_4 thin films calcined at 600 °C.

5.3.2.2 PEC Performance of Sol-Gel Derived Magnesium Ferrite Thin Films

After full phase characterization, the photoelectrochemical (PEC) performance of the prepared mesoporous thin films was elucidated. The experimental settings are described in chapter 4.9. At first, photocurrent density of both samples was detected during intermittent irradiation with a white light LED in the presence of Na_2SO_3 acting as hole scavenger.

As displayed in Figure 5.54a, only a minor photocurrent response was detected for the sample produced with short calcination period. Furthermore, across a broad range of excitation wavelengths, the non-calcined sample shows only very small IPCE values in the presence of Na_2SO_3 hole scavenger, which means only very low photocurrent responses in this range. The IPCE performance at 397 nm is < 0.01 %. This poor performance can be attributed to the non-crystalline phase composition. As charge carrier separation and transport demand a high crystallinity with few crystal defects. An amorphous material exhibits no long-range order, which might lead to a higher recombination rate if the

amorphous semiconductor is undoped.^[366] In addition, the precursor gel is more an ionic compound than a semiconductor, which affects the ability to generate and separate photo-excited charge carriers. Although the flat band potential of 0.48 V_{RHE} obtained from Mott Schottky measurement would allow OER, the insufficient crystallinity lead to minor PEC performance of this sample, discarding it as potential photoelectrode.

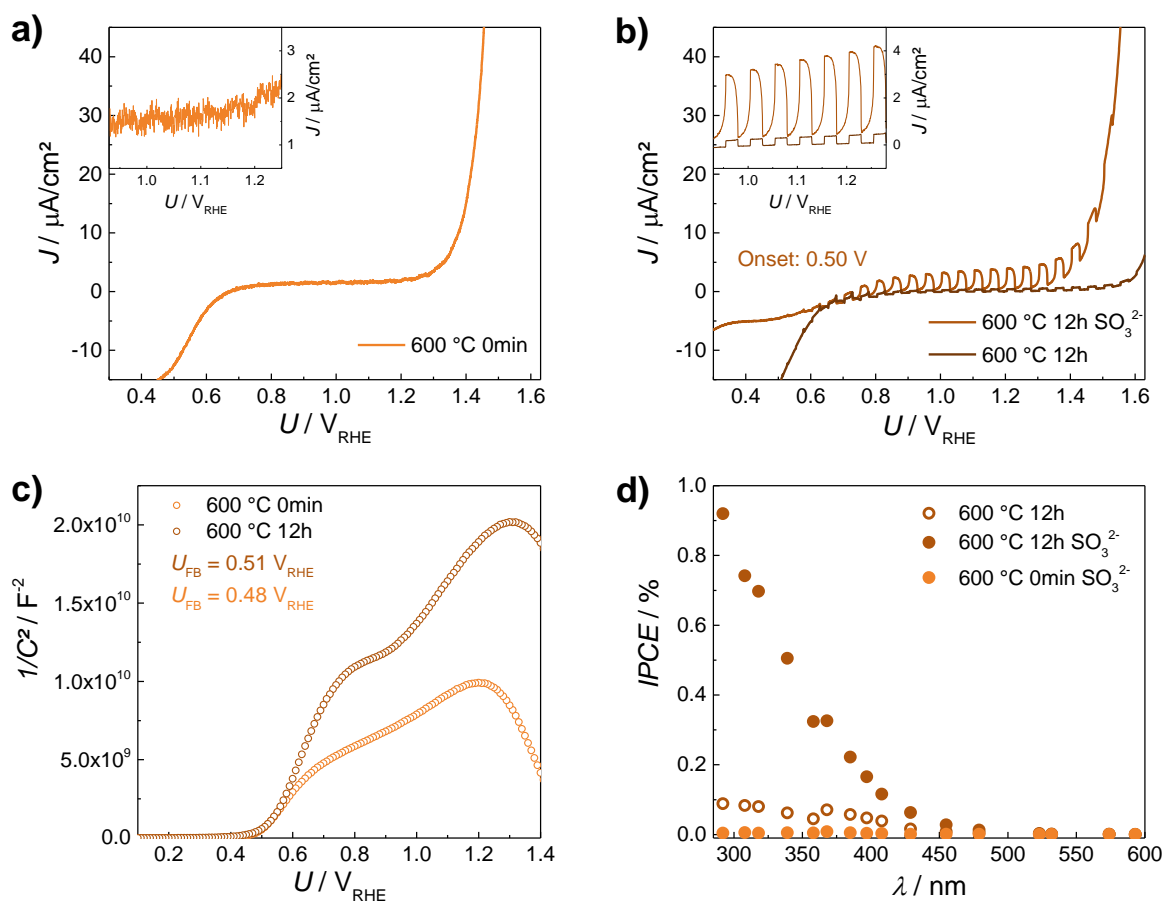


Figure 5.54: Photocurrent density measurements of mesoporous MgFe₂O₄ thin films calcined at 600 °C with a holding time at T_{max} of a) 0 min and b) 12 h as well as c) Mott Schottky plots and d) IPCE measurements.

In contrast, the sample calcined for 12 hours shows a clear photocurrent response under intermittent illumination in the presence of Na₂SO₃ (Figure 5.54b). The shape of the photocurrent response is not well defined but increases before the light is turned off again, indicating that steady state was not reached directly after light exposure. This delayed behavior indicates surface passivation, which might be due to carbonate species on the semiconductor surface. As expected, without hole scavenger, the observed photocurrent density is significantly lower. This indicates that the photocurrent under illumination is not generated by material degradation, but due to charge carrier exchange with the electrolyte. With a scavenger in the electrolyte, hole transfer is increased, leading to higher photocurrent density. The onset potential was detected at 0.5 V_{RHE}. The IPCE measurements match with the photocurrent measurements, revealing significantly higher efficiencies in the presence

of the sacrificial agent. At 397 nm, an IPCE of 0.05 % is found in the absence of Na_2SO_3 , which matches the value found for ZnFe_2O_4 (compare Figure 5.46b). This is already higher as the value reported for the previously discussed sample, indicating a better charge separation and charge transfer efficiency inside the crystalline MgFe_2O_4 material already without hole scavenger. When Na_2SO_3 is present, the IPCE value increases up to 0.17 % at 397 nm, which is only one third of the IPCE reported for mesoporous ZnFe_2O_4 calcined under identical conditions (compare Figure 5.46b). From Mott Schottky measurement (Figure 5.54d), a flat band potential of $0.51 \text{ V}_{\text{RHE}}$, matching the onset potential was obtained. The donor density of $1.01 \cdot 10^{20} \text{ cm}^{-3}$ is slightly lower than the value of $1.89 \cdot 10^{20} \text{ cm}^{-3}$ calculated for the sample, which was calcined without holding time. This indicates a thermal healing of intrinsic defects during extended calcination period.^[88]

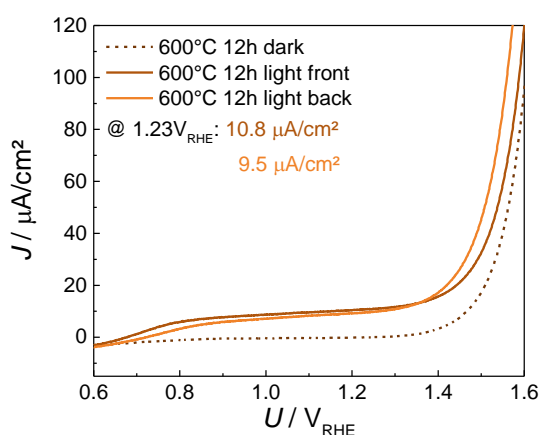


Figure 5.55: Photocurrent measurement of mesoporous MgFe_2O_4 during front and backside illumination with simulated solar light.

Consequently, the PEC performance under simulated sunlight was evaluated. As shown in Figure 5.55, no difference was observed between front and backside illumination. Due to the similarity of MgFe_2O_4 and ZnFe_2O_4 concerning their crystal structure and film thickness (approx. 350 nm for mesoporous MgFe_2O_4 thin films), this behavior was expected as it was already observed for mesoporous ZnFe_2O_4 thin films. This underlines that charge transport exhibits the same efficiency for both illumination sides in the mesoporous MgFe_2O_4

thin film, *i.e.* electrons and holes are transported equally well. Nevertheless, due to the limited current density, problems in charge carrier transport and injection are assumed. Photocurrent density values at $1.23 \text{ V}_{\text{RHE}}$ obtained from both illumination sides are then re-evaluated in regard of the thin films features. This is shown in Figure 5.56, where the photocurrent density calculated on irradiated area (1) is compared to the values considering the BET surface area per irradiated area (2) and the photocatalyst loading per irradiated area (3). When combining both, the actual accessible surface area and photocatalyst loading, this results in Figure 5.56(4). Comparison of these values underlines the problem of evaluation of the PEC performance, which has already been discussed for mesoporous ZnFe_2O_4 photoanodes. The assessment of a “good” absorber can be very difficult, if not all photoelectrode characteristics are considered, which is why this assessment should be stated very carefully.

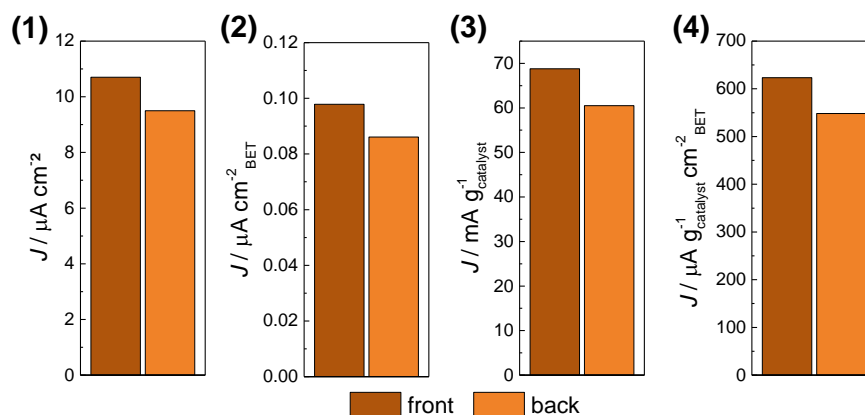


Figure 5.56: Photocurrent densities at 1.23 V_{RHE} normalized to (1) 1 cm² irradiated area (2) irradiated surface area (3) irradiated absorber loading (4) irradiated area and absorber loading.

The low performance and conspicuous transient signals shapes from photocurrent measurements under intermittent illumination lead to the suspicion of a blocking surface layer covering the photoelectrode. Due to this, XPS measurements were performed of the sample obtained after 12 hours of calcination.

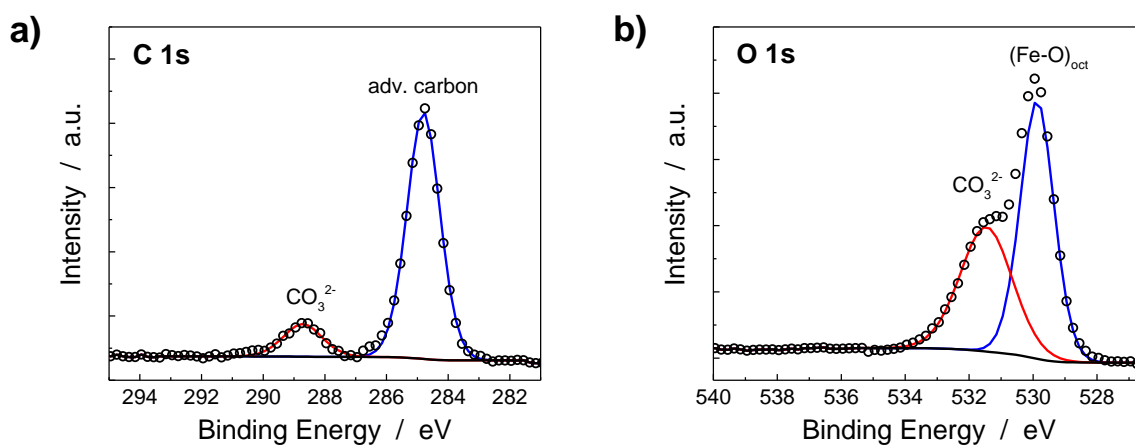


Figure 5.57: XPS spectra for the a) C 1s and b) O 1s emission line of MgFe₂O₄ photoelectrode calcined for 12 hours.

In Figure 5.57, the obtained, carbon-corrected C 1s and O 1s XPS spectra are shown. As expected, signals for Fe 2p and Mg 1s were found matching the values for Mg-O and Fe-O.^[367,368] Furthermore, the O 1s and C 1s signal were analyzed. These show the peak of adventitious carbon at 284.8 eV from common carbon impurities accompanied by a signal at 288.6 eV. This was assigned to CO₃²⁻, indicating the presence of MgCO₃.^[286] The same indication was obtained from the O 1s spectrum, which shows a main peak at 530.0 eV for the iron-oxygen bond with Fe³⁺ in octahedral coordination and a smaller peak at 531.5 eV, which is characteristic for carbonate ions.^[368,369] As already mentioned, Mg has a high

tendency for carbonate formation ($\Delta_f H^\circ(\text{MgCO}_3) = -1095.8 \text{ kJ mol}^{-1}$).^[359] A MgCO_3 layer on the electrode would act as a blocking layer for charge carrier transfer into the solution. Thus, the recombination rate is higher and the photocurrent density is lowered. This matches the findings from previous experiments (compare Figure 5.54b).

In summary, phase-pure mesoporous MgFe_2O_4 photoanodes were prepared already at 600°C . With a flat band potential of $0.51 V_{\text{RHE}}$ according to Mott Schottky measurements and a detectable, when moderate photocurrent response, mesoporous MgFe_2O_4 would be a potential material for OER in PEC cells. Nevertheless, optimization of the anode material is necessary in order to remove the inactive MgCO_3 surface layer and improve the photocurrent density. For this, also the influence of the variation of thin films thickness should be analyzed. Besides, the introduction of co-catalysts or protection layers as well as electrochemical activation has been reported to improve the PEC performance of other photocatalyst.^[152,200,202] This would allow photoelectrode optimization in the future.

5.3.3 Mesoporous Calcium Ferrite Thin Films

5.3.3.1 Polymer-Templated Calcium Ferrite Thin Film Synthesis

As the preparation of spinel type ferrites ZnFe_2O_4 and MgFe_2O_4 via sol-gel method was successfully realized, this approach was desired to be transferred to orthorhombic CaFe_2O_4 . In a first attempt, metal nitrate precursors and PIB 3000 as soft template were chosen. The gelation procedure was adapted as previously mentioned.

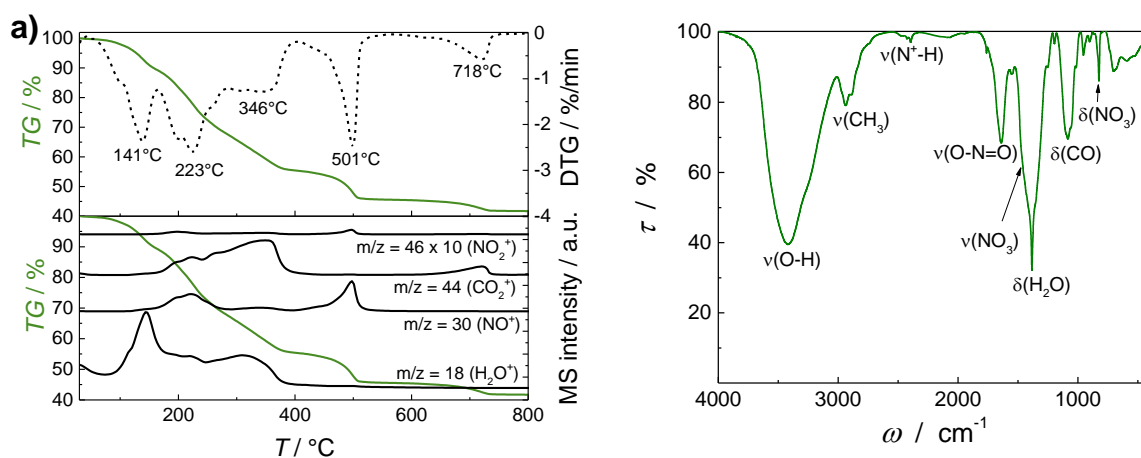


Figure 5.58: a) TG-MS data and b) IR patterns of precursor gels (adapted from Ref. 370 with permission from The Royal Society of Chemistry).^[370]

In Figure 5.58, TG-MS data and IR pattern of the precursor mixture pre-dried at 100 °C are shown. Already from DTG data (Figure 5.58a), a multistep decomposition up to very high temperatures is visible. The main transformation of the precursor sol into the gel, marked by loss of H₂O ($m/z = 18$) takes place until 380 °C. The decomposition of the polymer template, indicated by CO₂ evolution ($m/z = 44$) finishes at 400 °C. At 501 °C, distinct signals for loss of NO and NO₂ from the nitrate precursors appear. This suggests a higher thermal stability of the preformed gel compared to ZnFe₂O₄ and MgFe₂O₄ (compare Figure 5.34 and Figure 5.50). These differences in thermal decomposition probably derive from the calcium nitrate precursor, which showed decomposition steps at very high temperatures in contrast to nitrate precursors of iron, zinc and magnesium (compare Figure 5.33). A final decomposition step at 718 °C accompanied by a CO₂ mass signal gives evidence to the decomposition of CaCO₃, which had formed during the synthesis. In the IR pattern of the precursor gel, typical vibrations caused by NO₃⁻ are visible at 1642 cm⁻¹, 1460 cm⁻¹ and 824 cm⁻¹. Furthermore, also signals caused by the polymer template were detected at 2929 cm⁻¹ attributed to aliphatic C-H groups and 1086 cm⁻¹ due to C=O deformation vibration. In the fingerprint region, no sharp band for Fe-O was found. Instead, a broad signal between 690 cm⁻¹ and 423 cm⁻¹ indicates first weak metal-oxygen bonds with no defined coordination.

In a first approach, thin films were coated on Si substrates and calcination was performed without holding time at 700 °C to follow the pore evolution. Tailor-made polymers with extended polyisobutylene unit were chosen as soft templates. The molecular weight of the polymers was varied *via* the length of the polyisobutylene unit (PIB3000, PIB6000 or PIB10000) to create different pore sizes. In Figure 5.59a, thin films prepared with different pore templates (PIB3000 and PIB6000 and PIB10000) after calcination at 700 °C without holding time are shown.

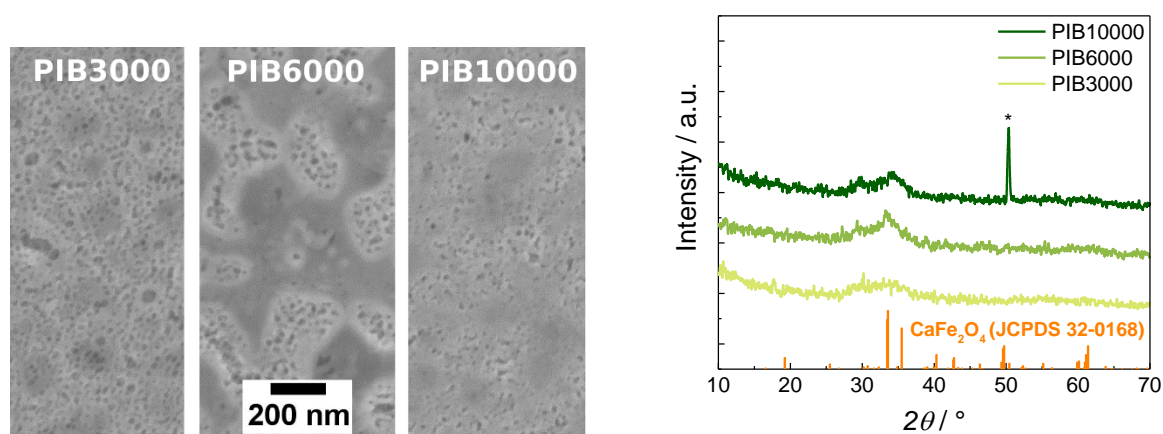


Figure 5.59: a) SEM images and b) GIXRD patterns of CaFe₂O₄ films produced with soft templates of different molecular weight (* marks artefact of sample holder).

As can be seen, pore size varies depending on the pore template, as these form micelles of different sizes. GIXRD patterns of these samples (see Figure 5.59b) revealed, that no crystalline phase of CaFe₂O₄

was obtained at the chosen calcination temperature. Therefore, optimization of the calcination procedure became necessary. As PIB polymers of higher molecular weight showed difficulties concerning their solubility and did not lead to a homogeneous pore distribution, PIB 3000 was chosen as soft template for following experiments.

To achieve crystalline samples, the calcination temperature for polymer removal was varied while there was no holding at T_{\max} applied to the samples. In Figure 5.60a, SEM images of samples produced with PIB3000 template and calcined at different temperatures without holding time are presented.

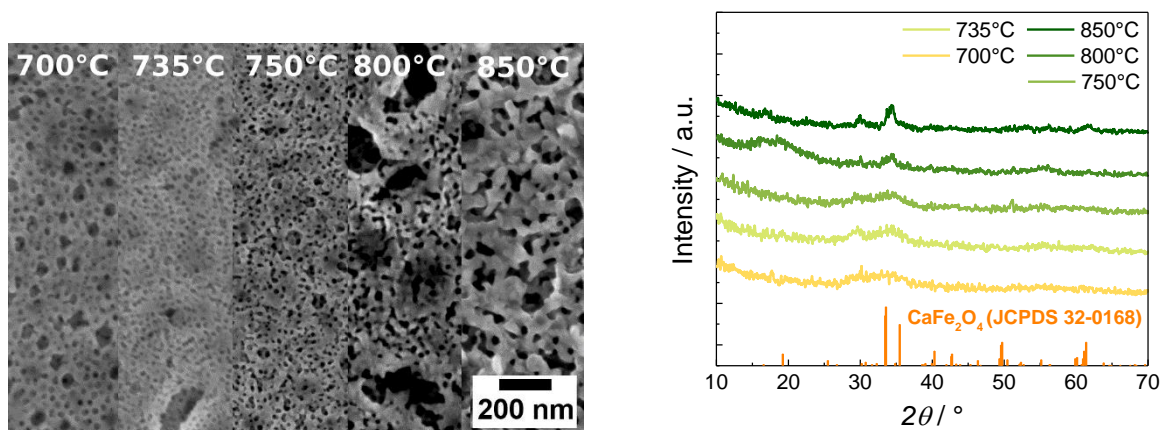


Figure 5.60: Left: SEM images of CaFe_2O_4 thin films calcined at different temperatures without holding time; right: respective GIXRD patterns.

The original spherical pore structure changes to an interconnected network with various grain sizes. This was attributed to crystallization of CaFe_2O_4 , leading to average crystal sizes exceeding the pore wall thickness. Therefore, the original structure breaks down. Here, the highest temperature shows the highest pore restructuring, which would indicate the highest amount of crystalline CaFe_2O_4 . Again, no reflections were found in GIXRD patterns of most of the samples (Figure 5.60b). Instead, an amorphous background was detectable resulting from the precursor gel. This indicates that the crystallite formation observed in SEM images probably only occurred at the thin film surface or in minor amounts, still yielding a mostly amorphous sample.

Only the sample calcined at 850 °C showed small reflections indicating the formation of crystalline material. Although the reflections were still very broad indicating only very small crystallites and excess amorphous components, this sample was chosen for first PEC characterization, which is discussed in chapter 5.3.3.2. As a brief outlook, *p*-type behavior of CaFe_2O_4 was found, but only limited PEC performance was detected.

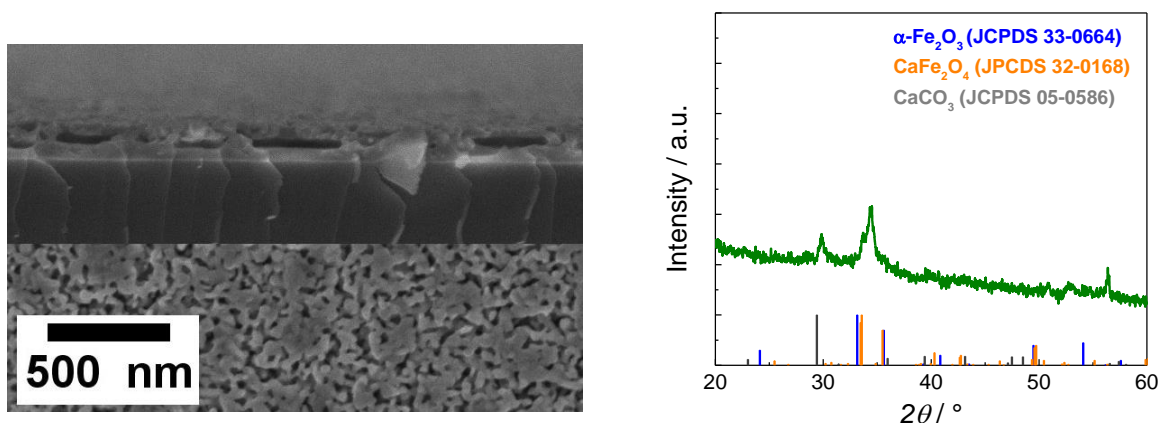


Figure 5.61: Left: top view and cross section SEM images of CaFe_2O_4 thin film calcined at 850 °C without holding time; right: respective GIXRD pattern.

Cross sectional SEM images (Figure 5.61a) show, that large parts of the prepared thin film are not connected to the substrate leading to holes inside the mesoporous thin film, which were not visible in top view images. Furthermore, the detailed analysis of the GIXRD pattern (Figure 5.61) revealed not only the presence of small CaFe_2O_4 crystallites, but also CaCO_3 was formed during synthesis. This can react as a passivation layer leading to low photocurrents. With the poor PEC performance, optimization of the electrode preparation was necessary.

As it was already shown for ZnFe_2O_4 and MgFe_2O_4 , extended calcination periods can lead to sufficiently crystalline, mesoporous thin film samples (compare Figure 5.36 and Figure 5.53). This is why the prolongation of the holding time was the next step in the calcination optimization. Low calcination temperatures were still desired to develop a competitive synthesis alternative to high temperature solid state reactions known for CaFe_2O_4 . Therefore, a maximum calcination temperature of 800 °C was chosen. The calcination period was extended to 4 hours.

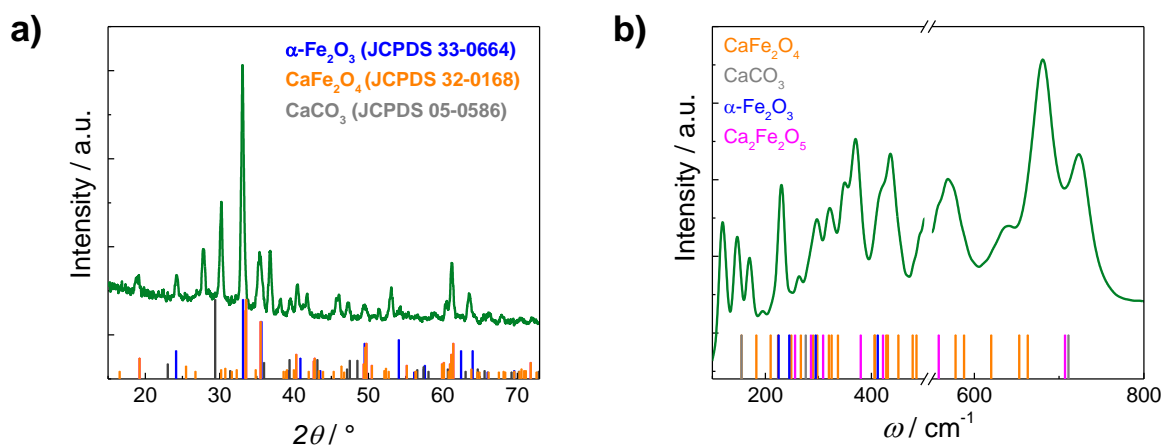


Figure 5.62: GIXRD pattern and Raman spectrum of PIB-templated CaFe_2O_4 thin film calcined at 800 °C in air for 4h.

With the chosen calcination procedure, crystalline thin films with a porous structure were obtained. GIXRD and Raman measurements (see Figure 5.62) revealed a large number of by-phases, especially α - Fe_2O_3 and $\text{Ca}_2\text{Fe}_2\text{O}_5$ as thermodynamically favored phases due to their low Gibbs free formation enthalpies.^{[359],[371]} Further investigations using EDX technique revealed a non-ideal Ca:Fe ratio of 1:4.74:1 already in the precursor gel (compare Figure 9.8). Although stoichiometric amounts of metal nitrates were used, this did not result in stoichiometric metal cation ratio in the gel. It is widely reported in literature, that calcium nitrate is highly hygroscopic.^[372] With an undefined water uptake of the calcium precursor under ambient conditions, the calculated masses would not correspond to the desired Ca amounts. This was presumed to be the reason for underrepresented Ca. Therefore, fresh calcium nitrate precursor was stored and handled inside a glovebox to suppress water uptake from the surrounding.

To check, whether the desired Ca:Fe was achieved, a precursor gel film (300 °C) was analyzed using EDX. This revealed an almost ideal ratio (Ca:Fe 1:1.91) in the precursor gel (compare Figure 9.9). Furthermore, because enhanced crystallite growth leads to full breakdown of the original pore morphology (compare Figure 5.39), the use of expensive tailor-made soft template PIB3000 was not necessary because the original pore structure was not maintained during calcination. This is why all further samples were produced with Pluronic® F127 (PLU) as porogen.

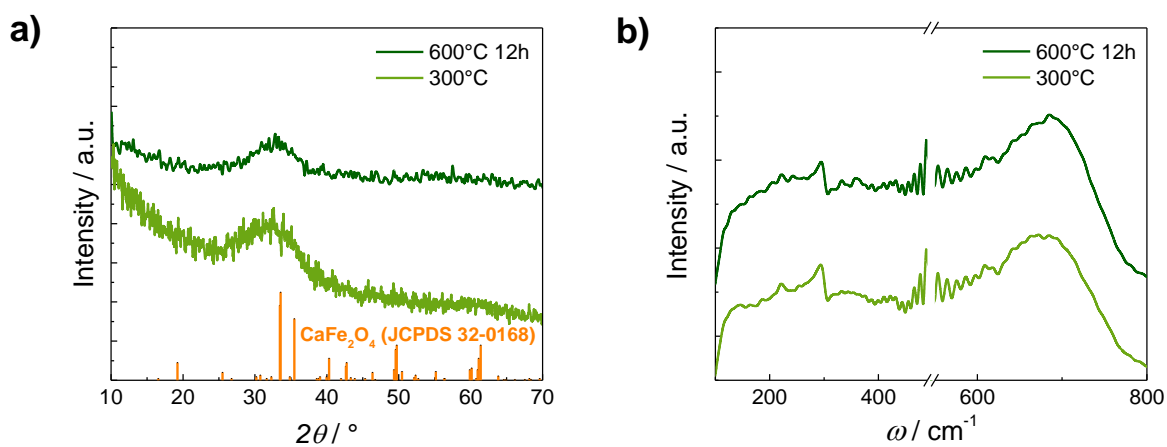


Figure 5.63: a) GIXRD patterns and b) Raman spectra of CaFe_2O_4 precursor gel and obtained after calcination at 600 °C (adapted from Ref. 370 with permission from The Royal Society of Chemistry).^[370]

With the optimized precursors and new polymer template, the minimum temperature for formation of crystalline CaFe_2O_4 was investigated. Calcination at 600 °C, even after 12 hours, did not yield the ferrite phase, as evident from GIXRD and Raman measurements (Figure 5.63), in contrast to cubic spinel type ZnFe_2O_4 and MgFe_2O_4 , which were successfully prepared under these calcination conditions. This is due to the complex, multistep decomposition of the precursor gel as shown in Figure 5.58 (compare also Figure 5.33), and the necessary Gibbs free formation energy for CaFe_2O_4 ($\Delta_f H^\circ(\text{CaFe}_2\text{O}_4) = -37.48 + 1.16 \cdot T \text{ kJ mol}^{-1}$).

As already used for investigation of ZnFe_2O_4 formation from precursor gels, GIXRD in combination with an *in situ* heating stage was used to perform calcination experiments in synthetic air. The results displayed in Figure 5.64 show, that no reflections appear for the samples calcined at 600 °C, which is in agreement with Figure 5.63. This indicates that this temperature is not sufficient to induce crystallization of CaFe_2O_4 . The successful transformation of amorphous precursor gel into crystalline compound was achieved during *in situ* experiments at 700 °C. The increase of the (320) reflection of CaFe_2O_4 between 0 min and 120 min can be seen. After 120 min of calcination, a shift in the maximum alongside reflex broadening appears. Comparison of the Gibbs free enthalpy of formation for CaFe_2O_4 ($\Delta_f H^\circ(\text{CaFe}_2\text{O}_4) = -37.48 + 1.16 \cdot T \text{ kJ mol}^{-1}$) and $\text{Ca}_2\text{Fe}_2\text{O}_5$ ($\Delta_f H^\circ(\text{Ca}_2\text{Fe}_2\text{O}_5) = -45.28 - 13.51 \cdot T \text{ kJ mol}^{-1}$) also shows that the formation of CaFe_2O_5 is thermodynamically favored, especially at high temperatures.^[371]

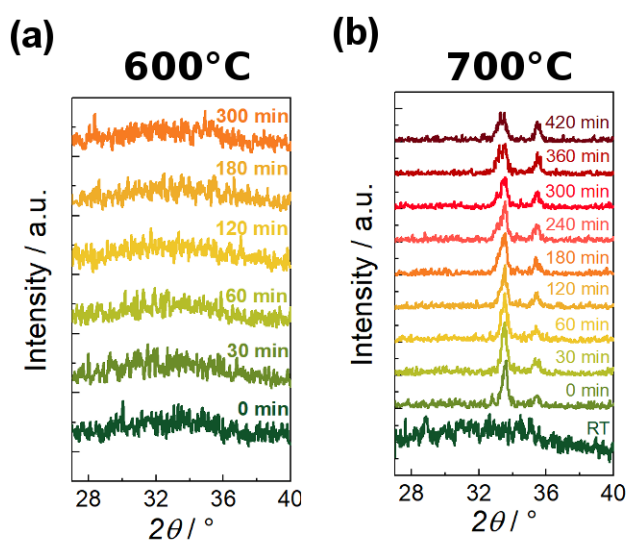


Figure 5.64: GIXRD measurements during *in situ* heating of mesoporous CaFe_2O_4 thin films at (a) 600 °C and (b) 700 °C (adapted from Ref. 370 with permission from The Royal Society of Chemistry).^[370]

Therefore, the shift of the (320) reflection is a first hint of transformation of CaFe_2O_4 into $\text{Ca}_2\text{Fe}_2\text{O}_5$.^[371] With a constant holding time of 4 hours, the maximum temperature during calcination was varied to influence the pore morphology. In Figure 5.65, SEM top view images of films obtained after calcination at 600 °C, 700 °C, 750 °C and 800 °C are shown. The originally pore structure of small mesopores combined with larger macropores, which can be found in the 600 °C sample, is only present in the precursor gel. When CaFe_2O_4 crystallization starts, the pore walls of the

mesopores break down and a restructuring takes place.

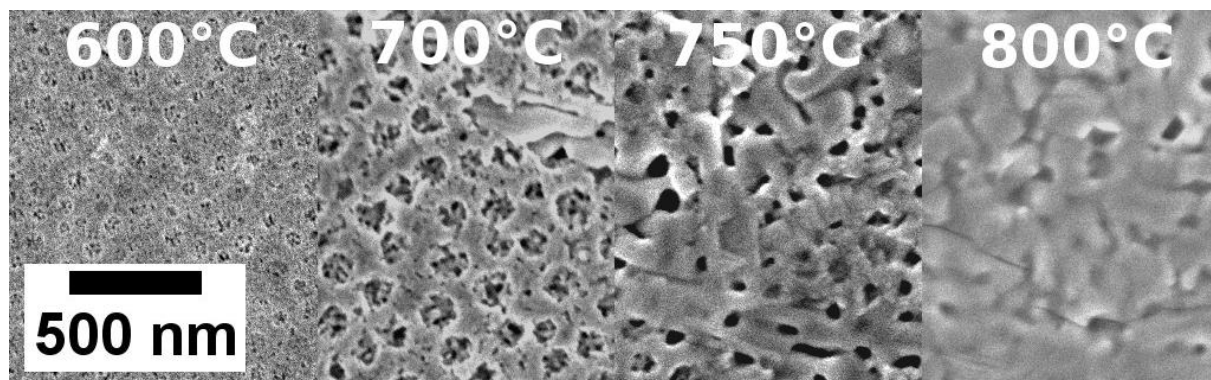


Figure 5.65: SEM images of CaFe_2O_4 thin films calcined in air at different temperatures with 4 hours holding time.

After calcination at 800 °C most of the pores have been lost due to strong sintering of the pore walls, which is why 800 °C should not be exceeded when porous CaFe_2O_4 thin films are desired. XRD and Raman analysis of these samples is displayed in Figure 5.66. When samples were calcined at 750 °C and 800 °C, high amounts of by-phases ($\alpha\text{-Fe}_2\text{O}_3$ and $\text{Ca}_2\text{Fe}_2\text{O}_5$) were detected in GIXRD patterns (Figure 5.66a). The same trend was found in the Raman spectra (Figure 5.66b). Here, the development of the second prominent by-phase $\text{Ca}_2\text{Fe}_2\text{O}_5$ can be followed *via* the increase of the Raman mode above 700 cm^{-1} . The lower calcium amount available for formation of CaFe_2O_4 supported its thermal decomposition into thermodynamically more stable phases.

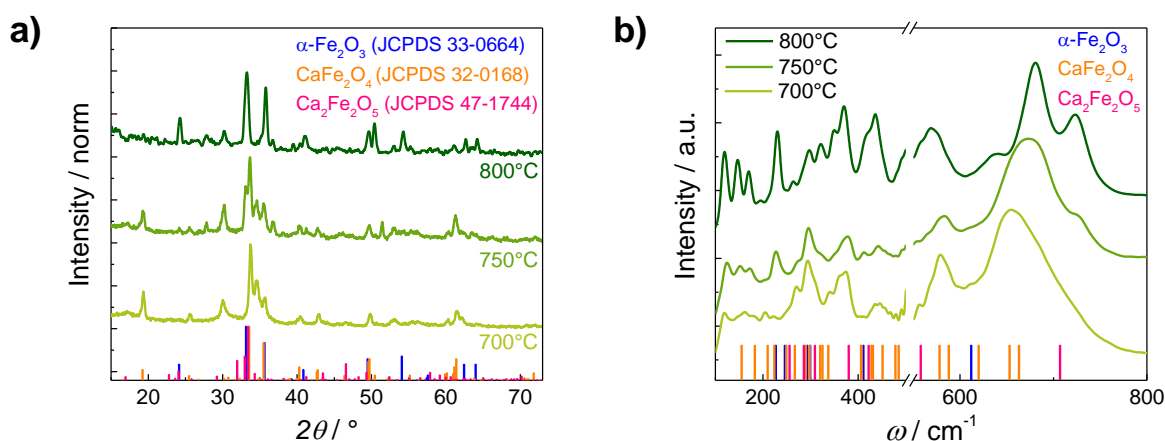


Figure 5.66: a) GIXRD patterns and b) Raman spectra of CaFe_2O_4 thin films calcined in air at different temperatures with 4 hours holding time.

As calcium precursors highly tend to form calcium carbonate under temperature treatment in air, this was assumed to cause a lowering in the overall calcium content, leading to non-stoichiometric metal amounts. With calcination in air, a certain amount of CO_2 is always present, which would expedite carbonate formation. Furthermore, no gas flow was used during the calcination so far, which is why CO_2 evolved during porogen decomposition was not flushed away. Therefore, calcination with constant gas flow in different gas atmospheres was investigated in order to achieve phase pure CaFe_2O_4 .

Measuring GIXRD and Raman spectra (Figure 5.67) revealed that calcination under O_2 exclusion leads to even higher amounts of $\alpha\text{-Fe}_2\text{O}_3$ by-phase. As $\alpha\text{-Fe}_2\text{O}_3$ is a thermodynamically very favored structure ($\Delta_f H^\circ(\alpha\text{-Fe}_2\text{O}_3) = -824.2 \text{ kJ mol}^{-1}$)^[359], oxygen-free conditions only lead to this stable form, while CaFe_2O_4 with a more complex structure needs longer time and sufficient oxygen supply, obviously. Comparison of the Gibbs free enthalpy of formation for CaFe_2O_4 and $\text{Ca}_2\text{Fe}_2\text{O}_5$ ($(\Delta_f H^\circ(\text{CaFe}_2\text{O}_4) = -37.48 + 1.16 \cdot T \text{ kJmol}^{-1})$, $(\Delta_f H^\circ(\text{Ca}_2\text{Fe}_2\text{O}_5) = -45.28 - 13.51 \cdot T \text{ kJmol}^{-1})$)^[371] also shows, that the formation of CaFe_2O_5 is thermodynamically favored, especially at high temperatures.

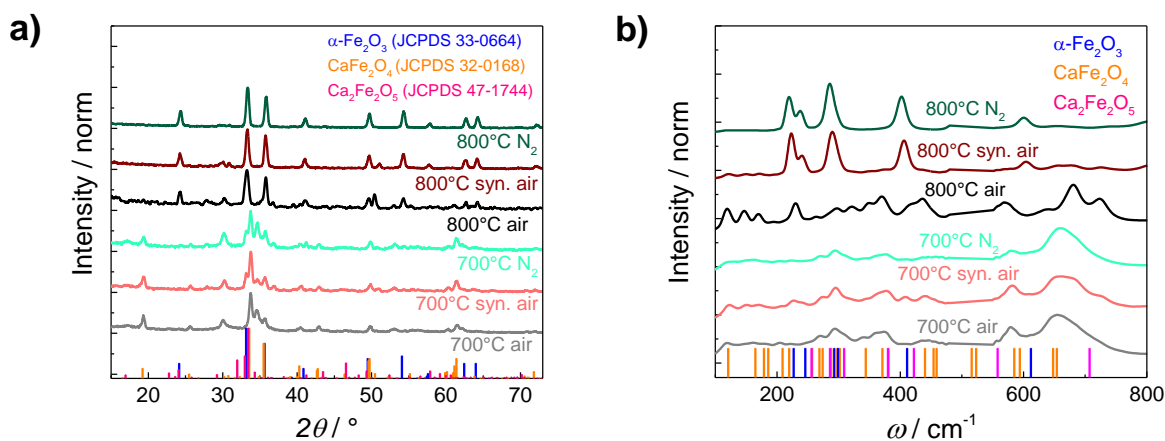


Figure 5.67: a) GIXRD patterns and b) Raman spectra of CaFe₂O₄ thin films calcined in different gas atmospheres for 4 hours.

This matches the results of *in situ* GIXRD measurements, where a formation of CaFe₂O₅ over time was observable (compare Figure 5.64b). These results suggest lower calcination temperatures and shorter calcination periods for synthesis of phase-pure CaFe₂O₄ thin films. Furthermore, no improvement was found when CO₂-free synthetic air (20 % O₂, 80 % N₂) was used during calcination. From this, the conclusion was drawn that carbonate formation was not the main problem leading to by-phase formation. EDX analysis revealed an almost ideal ratio (Ca:Fe 1:1.91, Figure 9.9) in the precursor gel, but a decreased Ca amount in the calcined sample (Ca:Fe 1:4.10, Figure 9.10). The decreased amount of Ca in calcined samples could not be explained. To overcome this, 30 % excess of Ca precursor was used to overcome the shortfall observed for the previous samples, leading to molar ratio of 1:1.99 (compare Figure 9.11) in the precursor mixture. This led to phase pure mesoporous CaFe₂O₄ samples according to GIXRD and Raman analysis (Figure 5.68).

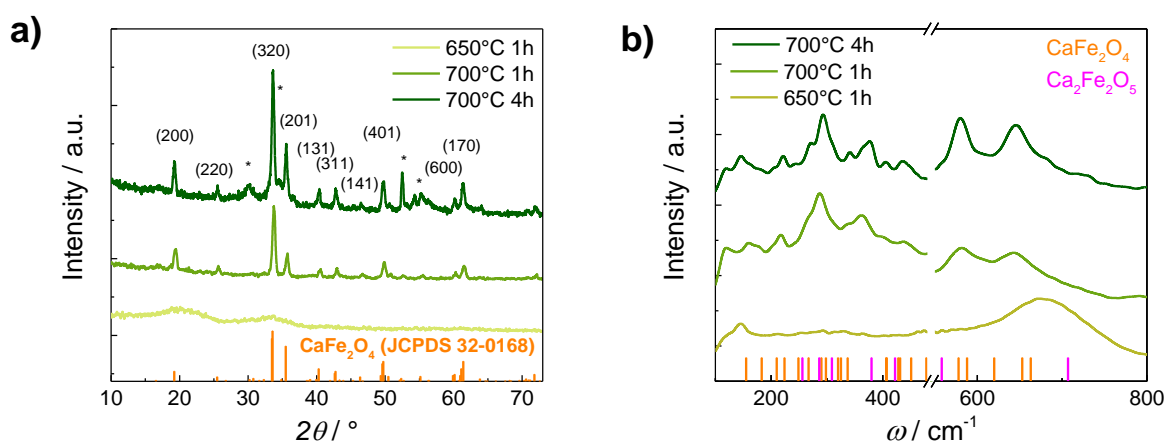


Figure 5.68: a) GIXRD patterns (* marks artefacts of CaFe₂O₅) b) Raman spectra of CaFe₂O₄ thin films synthesized with 30 % Ca precursor excess (adapted from Ref. 370 with permission from The Royal Society of Chemistry).^[370]

The GIXRD patterns (Figure 5.68a) of samples calcined at 650 °C and 700 °C reveal a mainly amorphous phase produced at 650 °C, while calcination at 700 °C for either 1 hour or 4 hours leads to phase pure CaFe_2O_4 when comparing the measured data to the JCPDS reference pattern (JCPDS card no. 32-0168). Using the Scherrer equation (equation (4.1)), a rough estimation of the crystallite size was made for the thin films calcined at 700 °C. For this purpose, three reflections ((200), (311), and (220)) were fitted with a Gaussian curve and the average of the obtained crystallite sizes was taken. For the sample calcined for one hour, an average crystallite size of 24.9 nm was calculated, while 25.5 nm is a slightly higher value found for the sample obtained after longer calcination period. The same trend was found for mesoporous ZnFe_2O_4 thin film samples (compare Table 9.1). For the two crystalline films, Ca:Fe ratios of 1:1.92 and 1:2.31 (compare Figure 9.12) were found after calcination at one hour or 4 hours, respectively. Some weak reflections were found for the sample calcined for 4 hours, which were attributed by comparison with the COD spectral database suggested very small crystallites of $\text{Ca}_2\text{Fe}_2\text{O}_5$ (JCPDS card no. 47-1744). Raman spectra (Figure 5.68b) were recorded to exclude minimum amounts of $\alpha\text{-Fe}_2\text{O}_3$ impurities. According to group theory, orthorhombic $Pnma$ structure of CaFe_2O_4 has 42 Raman active modes (14 A_g , 14 B_{2g} , 7 B_{1g} , 7 B_{3g}), which should be triggered by polarized Raman scattering.^[373] In the recorded spectra, 13 and 18 respective Raman modes were detected. As non-polarized light was used for Raman excitation, the lower number of modes can be explained by superimposition of Raman modes. The detected values were compared to literature reports (Table 9.5), matching well with the theoretical band positions.^[373] No additional bands indicating $\alpha\text{-Fe}_2\text{O}_3$ or other impurities were found.^[33] With a closer look into the low frequency region of the sample calcined for 4 hours, a weak signal above 700 cm^{-1} is visible, which was attributed to minor amounts of $\text{Ca}_2\text{Fe}_2\text{O}_5$ appearing after long-term calcination.^[374] The uncontrolled evolution of a secondary phase means the formation of internal junctions, which can influence the photoactivity of the material.

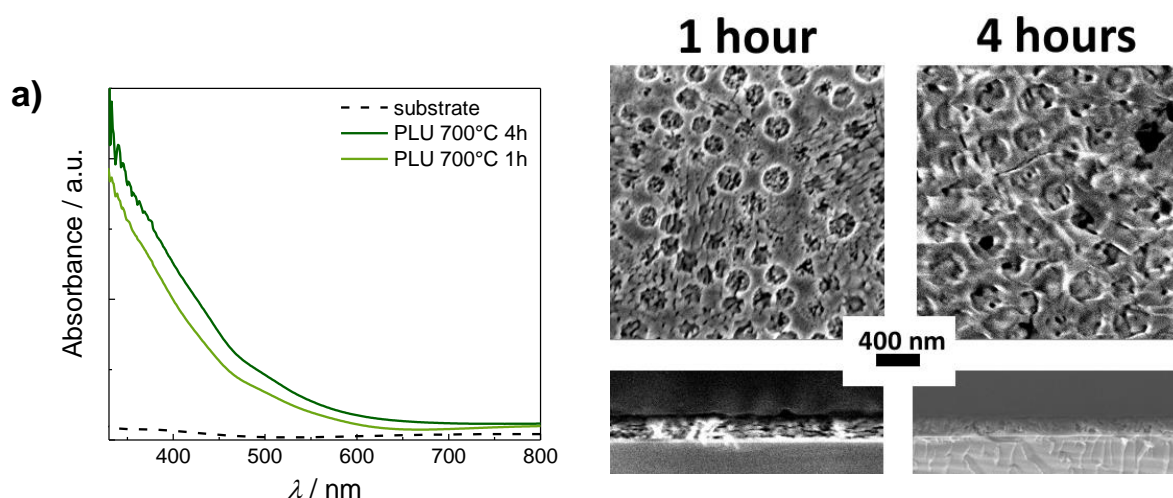


Figure 5.69: a) UV-Vis spectra, b) SEM top view (above) and cross section (below) images of CaFe_2O_4 thin films calcined at 700 °C (adapted from Ref. 370 with permission from The Royal Society of Chemistry).^[370]

Besides, both samples show comparable absorbance according to UV-Vis analysis (Figure 5.69a). Furthermore, a rather homogenous pore size distribution in the mesopore range was found from SEM analysis (Figure 5.69b). Furthermore, macropores developed during the sintering process. This lead to a hierarchical pore structure, which can be very beneficial for photocatalytic applications as reported in literature.^[42]

From these results, it can be assumed that CaFe_2O_4 with hierarchical pore structure was synthesized at rather low temperatures using a sol-gel based dip coating approach. Sufficient phase purity was observed after short calcination periods, while Raman spectroscopy revealed minor amount of $\text{Ca}_2\text{Fe}_2\text{O}_5$ by-phase after calcination at extended periods. As already discussed earlier, CaFe_2O_4 is an interesting material for photocatalytic and photoelectrochemical applications. Therefore, photoelectrochemical characterization of macro-mesoporous CaFe_2O_4 thin films produced at $700\text{ }^\circ\text{C}$ with different holding periods were performed.

5.3.3.2 PEC Performance of Sol-Gel Derived Calcium Ferrite Thin Films

In Figure 5.70, Mott Schottky plot and photocurrent measurement during intermittent light irradiation are shown. The Mott Schottky plot (Figure 5.70a) shows a negative slope suggesting *p*-type semiconducting behavior of CaFe_2O_4 . This is remarkable as there are only few reports about oxide-based semiconductors with *p*-type behavior.^[54,204] The flat band potential was estimated to be $1.29\text{ V}_{\text{RHE}}$, which would locate the Fermi level. In *p*-type semiconductors, the Fermi level is close to the valence band level. Regarding in the reported band gap for CaFe_2O_4 of $1.9\text{ eV}^{[3]}$, the conduction band potential of the fabricated CaFe_2O_4 electrode would be around $-0.6\text{ V}_{\text{RHE}}$, which is suitable for hydrogen evolution reaction.

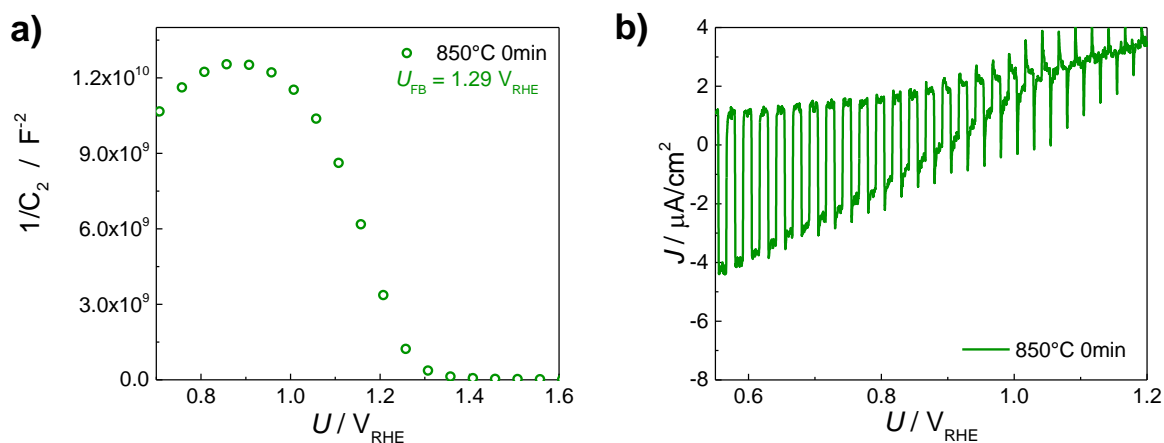


Figure 5.70: a) Mott Schottky plot and b) photocurrent measurement in Ar-purged $0.1\text{ M Na}_2\text{SO}_4$ during intermittent irradiation of CaFe_2O_4 photoelectrode calcined at $850\text{ }^\circ\text{C}$ with 0 min holding time.

Moreover, *p*-type semiconductors show downwards band bending, which is beneficial for H₂ evolution reaction (HER) as already discussed in 2.2.2. This means that porous CaFe₂O₄ are promising candidates as photocathodes in HER due to their earth-abundant elements, low cost precursor materials, cheap synthesis approach and cathodic photoelectrochemical behavior. The photocurrent measurements (Figure 5.70b) underline the *p*-type behavior of the prepared photoelectrode, but show only limited photocurrent densities in the analyzed range. It was assumed that low crystallinity of the prepared sample leads to insufficient charge carrier separation and transport. This was already found for MgFe₂O₄ photoelectrodes (compare Figure 5.54). Therefore, further optimization of the synthesis and calcination procedure was necessary, which was discussed in chapter 5.3.3.

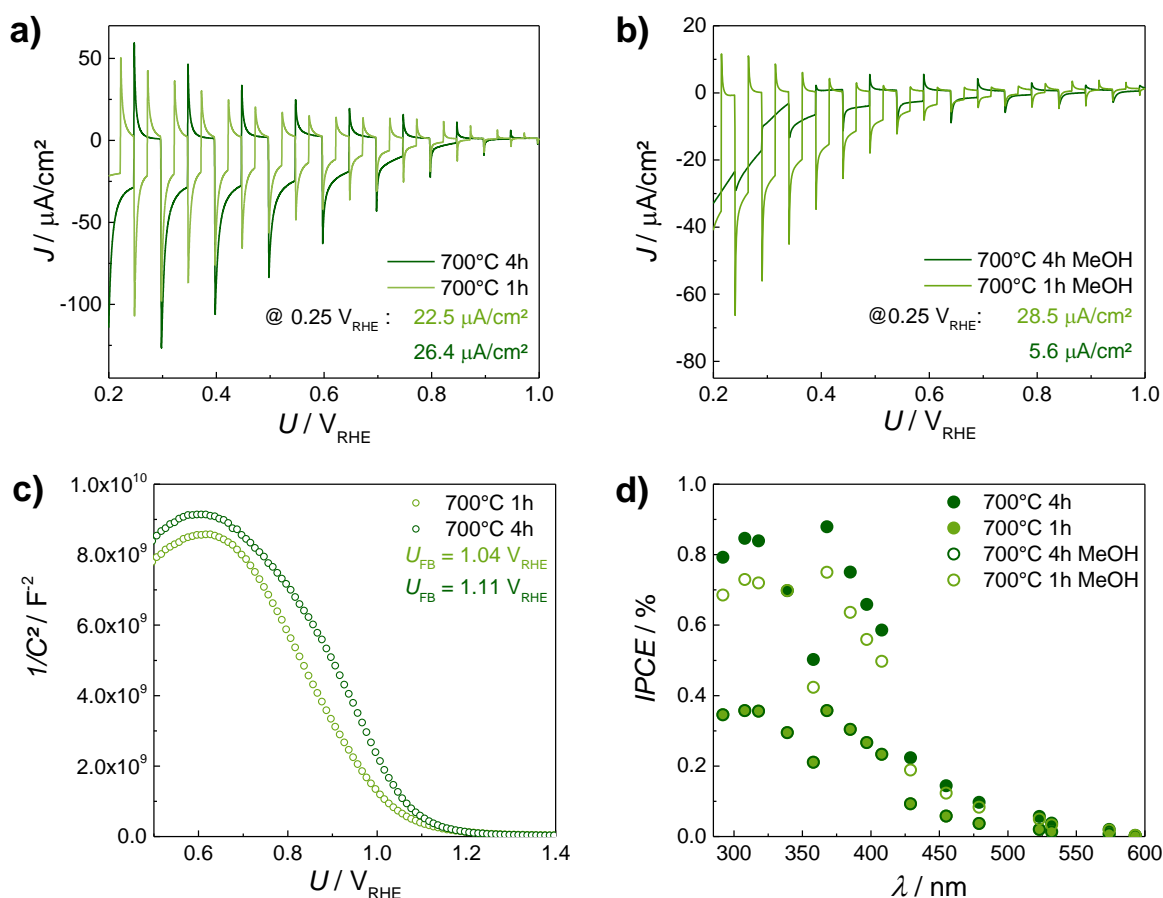


Figure 5.71: Photocurrent measurements under intermittent illumination a) in the absence of sacrificial agents and b) with methanol, as well as c) Mott Schottky and d) IPCE measurements of porous CaFe₂O₄ thin films calcined at 700 °C; measurements conducted in a+c) Ar-purged 0.1 M Na₂SO₄, b+d) Ar-purged 0.1 M Na₂SO₄ with 10 % MeOH (adapted from Ref. 370 with permission from The Royal Society of Chemistry).^[370]

PEC characterization of the optimized photoelectrodes calcined at 700 °C in air for 1 hour and 4 hours, respectively, is shown in Figure 5.71. Photocurrent measurements with intermittent irradiation as well as Mott Schottky plots indicate a *p*-type semiconductor. Both samples show comparable flat band potentials of 1.04 V_{RHE} and 1.11 V_{RHE} . With a reported band gap of 1.9 eV^[3], the valence band potentials of the fabricated CaFe₂O₄ electrodes would be around -0.8 V_{RHE} , which is

suitable for HER. The calculated band positions are in the range of values reported by Kim *et al.*^[3], but shifted to lower potentials by approx. 0.1 V. This discrepancy can be explained by the different analysis methods used to determine the band positions.

The photocurrent densities are in the same range, too. 22.5 $\mu\text{A cm}^{-2}$ were found for the sample calcined for 1 hour and 26.4 $\mu\text{A cm}^{-2}$ were found for the sample calcined for 4 hours. This indicates that prolonged calcination at 700 °C does not increase the photoactivity for CaFe_2O_4 prepared according to 3.2.3.1. Therefore, one hour of calcination period at 700 °C is already sufficient to gain photoactive, porous CaFe_2O_4 photoelectrodes. With SO_3^{2-} hole scavenger both samples did not show any photocurrent activity, indicating that SO_3^{2-} is not matching the system. This is why methanol (MeOH) was chosen as alternative sacrificial agent. In the presence of MeOH the sample calcined for one hour shows better photocurrent response, while the photocurrent density is drastically decreased for the sample calcined at 4 hours when MeOH is present. This indicates disturbed hole transfer to the scavenger leading to higher recombination rates, which lowers the measured photocurrent. Although the photocurrent improved for the other sample, it did not double compared to scavenger-free experiments, which had been expected due to photocurrent doubling effect caused by MeOH. The same phenomenon was observed for IPCE measurements of both samples in the absence and presence of MeOH hole scavenger (see Figure 5.71d). The IPCE of samples without scavenger match the observations from photocurrent density and UV-Vis with a higher efficiency found for the sample with longer calcination period. At 400 nm, an IPCE of 0.59 % was recorded. In the presence of MeOH, the IPCE of this sample drops to 0.23 % at 397 nm. Again, this suggests hindered hole transfer in the presence of MeOH. The IPCE value of the sample with shorter calcination period rises, when MeOH is present. The value detected at 397 nm being 0.5 % with MeOH is more than twice as high compared to scavenger-free experiments with 0.23 %. This can be attributed to a slightly better hole transfer and of course photocurrent doubling caused by MeOH.

The intense spikes indicate very slow hole transfer reaction at the solid-liquid interface. Even though typical hole scavengers were used, the overshoots improved only slightly. This leads to the assumption, that not only hole transfer is problematic within the system. As reports already states strong Fermi level pinning in CaFe_2O_4 ^[241], the rate-determining step occurs within the Helmholtz layer.

For further insights, the phase-pure CaFe_2O_4 photoelectrode obtained after 1-hour calcination was studied in 0.1 M Na_2SO_4 with the presence of hydrogen peroxide (H_2O_2). At first, the photocurrent output during linear potential sweeping under front and backside solar light illumination was investigated. In Figure 5.72, the results are shown in comparison to the PEC response in the absence of sacrificial agents. A clear improvement in photocurrent density is visible, which is attributed to H_2O_2 , which has a much higher reaction rate for oxidation compared to water.^[375] Furthermore, no significant difference was found for illumination from the front or the back, which indicates that the bulk recombination is comparable under both conditions (Figure 5.72a). Under intermittent front side

illumination (Figure 5.72b), an improved charge carrier transfer was found in the presence of H_2O_2 , as the large overshoots discussed earlier completely disappear.

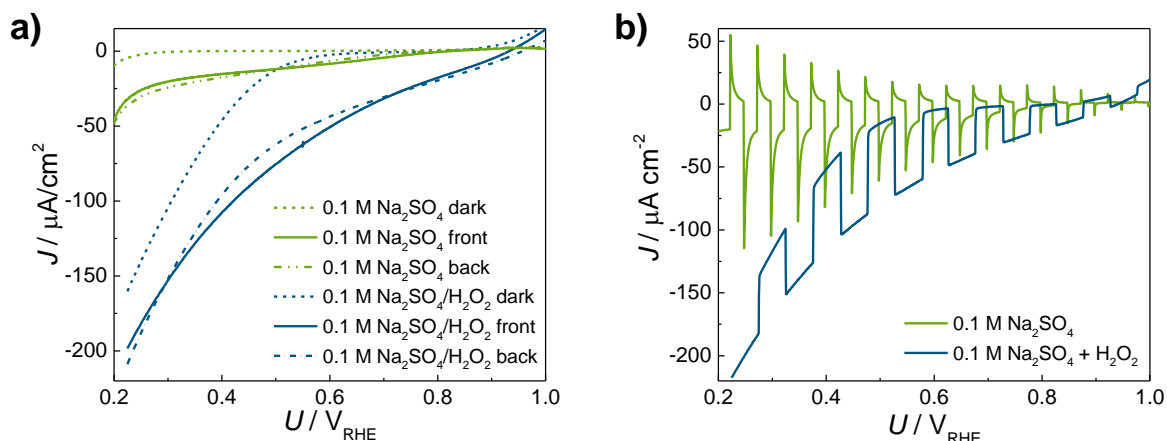


Figure 5.72: Photocurrent measurements in 0.1 M Na_2SO_4 under simulated solar light (AM 1.5G) in the absence (green) and presence (blue) of H_2O_2 under a) dark conditions and illumination from the front and backside, and b) under intermittent front side illumination (adapted from Ref. 370 with permission from The Royal Society of Chemistry).^[370]

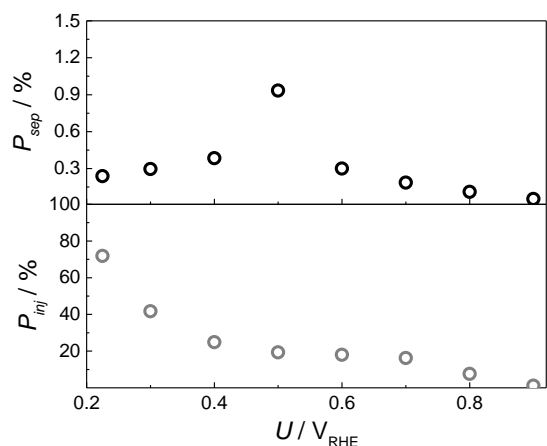


Figure 5.73: Charge separation efficiency (upper, black) and charge injection efficiency (lower, grey) calculated according to a procedure reported by Dotan *et al.*^[375] (adapted from Ref. 370 with permission from The Royal Society of Chemistry).^[370]

According to these measurements, the charge injection and charge recombination rates were calculated according to a procedure proposed by Dotan *et al.*^[375] With the charge separation efficiency (upper part of Figure 5.73), the amount of photogenerated holes, which successfully diffused to the electrode's surface without recombination within the bulk material can be determined.^[375] A maximum value of

0.9 % was reached at $0.5 V_{\text{RHE}}$, which suggests that at this potential vs RHE, the recombination rate within the bulk material is the lowest.

Nevertheless, all calculated charge separation

efficiencies are very low. This can be attributed to a very short diffusion length of the minority charge carriers, which promotes fast recombination before the charge carriers reach the electrode surface. Here, either doping with suitable elements could lead to larger charge carrier diffusion length, or even thinner pore walls could shorten the diffusion pathway towards the electrode surface. For non-porous $\alpha\text{-Fe}_2\text{O}_3$ photoelectrodes, Dotan and co-workers reported a maximum charge separation efficiency of 18.6 %, which is a desirable value for the produced electrodes to improve their PEC performance.^[375]

The charge injection efficiency, depicted in the lower part of Figure 5.73, describes the yield of holes reaching the photoelectrode surface and being injected into the electrolyte to perform oxidation

processes.^[375] Here, a maximum value of 72 % was found at 0.2 V_{RHE}, which is equal to an external bias of -0.2 V in 0.1 M Na₂SO₄. This is a quite promising value for charge carrier injection, but there is room for improvement compared to the maximum value of over 90 % reported for non-porous α -Fe₂O₃ photoelectrodes.^[375] A larger external bias or a suitable protection layer could drive the charge injection to higher efficiency. The charge injection efficiency decreases with higher potential, but stays around 20 % over a wide range before almost complete decline at the photocurrent onset potential.

From these results, issues in charge carrier transport within the solid material as well as an optimizable charge carrier transfer become apparent. Both aspects need to be addressed for overall PEC performance improvement.

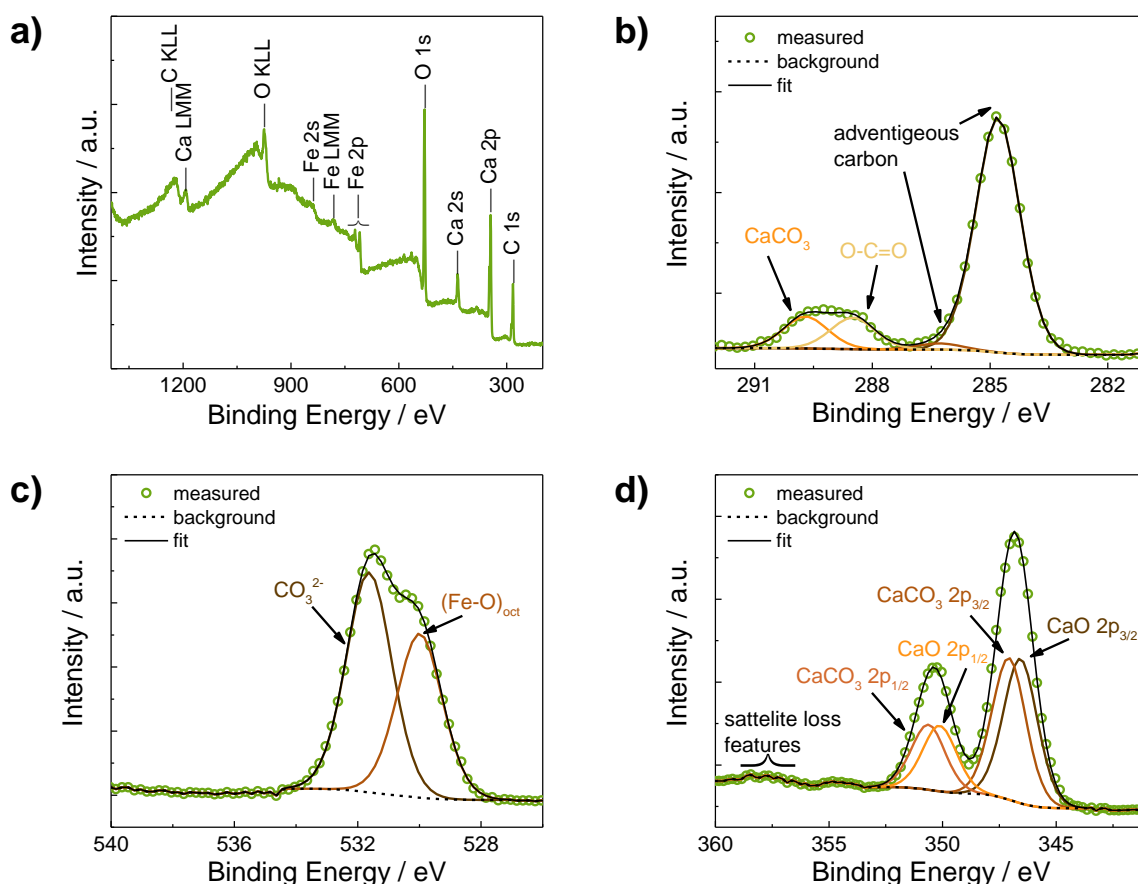


Figure 5.74: XPS spectra of the CaFe₂O₄ thin film calcined for 1 hour at 700 °C: a) survey spectrum, b) C 1s spectrum, c) O 1s spectrum and d) Ca 2p spectrum (adapted from Ref. 370 with permission from The Royal Society of Chemistry).^[370]

One reason for the limited PEC performance could be the presence of CaCO₃ at the thin film surface. From XPS measurements, which are sensitive to species at the surface of the sample, the presence of CaCO₃ was identified.

The survey spectrum (Figure 5.74a) shows signals for calcium, oxygen, iron and carbon. No additional elements were detectable. In the C 1s spectrum (Figure 5.74b) calcium carbonate (289.7 eV) and carbonate-like (288.5 eV) species were detected.^[376] Further evidences for CaCO₃ were found in

the O 1s spectrum (Figure 5.74c), which revealed a peak at 531.3 eV in addition to the typical Fe-O signal at 529.5 eV reported for octahedrally-coordinated iron oxides.^[368,377] The Ca 2p spectrum (Figure 5.74d) shows the most complex structure with signals for Ca-O bonding at 350.1 eV ($2p_{1/2}$) and 346.6 eV ($2p_{3/2}$) in addition to signals at 350.6 eV ($2p_{1/2}$) and 347.1 eV ($2p_{3/2}$) typical for CaCO_3 .^[378] The spin-orbit splitting of 3.5 eV matches calcium with an oxidation state of +2. With the very low formation enthalpy of CaCO_3 ($\Delta_f H^\circ(\text{CaCO}_3) = -1206.9 \text{ kJ mol}^{-1}$)^[359], which was already discussed previously, the appearance of CaCO_3 during calcination in air seems to be unavoidable.

5.4 Nanoparticle-Derived Zinc Ferrite Thin Films

In a report from 2011, the production of mesoporous $\alpha\text{-Fe}_2\text{O}_3$ thin films by deposition of a Fe_3O_4 colloidal solution and consecutive heat treatment.^[127] As a monocrystalline precursor for thin film preparation might be advantageous for charge carrier transport within mesoporous films, a synthesis procedure for mesoporous ZnFe_2O_4 thin films from colloidal ZnFe_2O_4 solution was developed.

In a first approach, PVP-coated ZnFe_2O_4 nanoparticles in polar solvents were used in order to produce porous thin films directly created from crystalline nanoparticles (see chapter 3.2.2.1). The complete analysis of PVP-encapsulated ZnFe_2O_4 nanoparticles was presented in chapter 5.2.1.2.

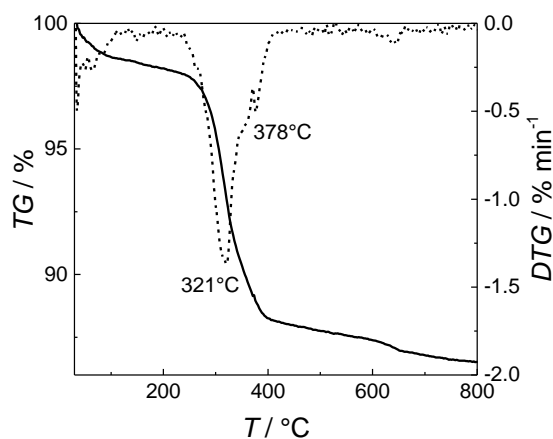


Figure 5.75: TG-DTG of PVP-coated ZnFe_2O_4 nanoparticles.

At first, TGA was used to follow the polymer removal. The thermal decomposition of PVP-encapsulated ZnFe_2O_4 nanoparticles, which is displayed in Figure 5.75, shows a first weight loss of 5 % at 70 °C. This can be attributed to residue of ethanol solvent. The main decomposition between 300 °C and 400 °C is due to removal of the polymer shell. After this weight loss of 12 %, no change in sample mass was observed up to 800 °C. This indicates that all organic compounds can be completely removed by thermal treatment at 400 °C. Also, after heat treatment

at 300 °C, complete polymer removal cannot be achieved and a certain amount of PVP will still be left within the thin films. To see if the morphology and crystallinity of ZnFe_2O_4 nanoparticle derived thin films can be influenced by thermal treatment, calcination of as-prepared thin films in air was performed. Then, GIXRD data were collected to validate the phase purity of the samples. No impurities of hematite or zinc oxide were detectable. All XRD reflections were attributed to phase pure ZnFe_2O_4 .

In Figure 5.76, Rietveld refinements of the GIXRD patterns are shown. By calcination at different temperatures, the average crystallite size and microstrain of the thin films was tunable. At calcination temperatures of 500 °C and below, crystalline materials of around 16 nm with microstrain values of 36 % to 42 % were obtained (see Figure 5.76a-b and Table 9.1). This suggests, that no sintering appears at these temperatures, matching the findings from *in situ* GIXRD measurements of sol-gel derived mesoporous thin films (compare Figure 5.35). With calcination temperatures above 500 °C, sintering of the nanoparticles together with crystallite growth is induced (Figure 5.76c-d). This is in agreement with observations made for sol-gel derived thin films (compare Figure 5.35 and Figure 5.38).

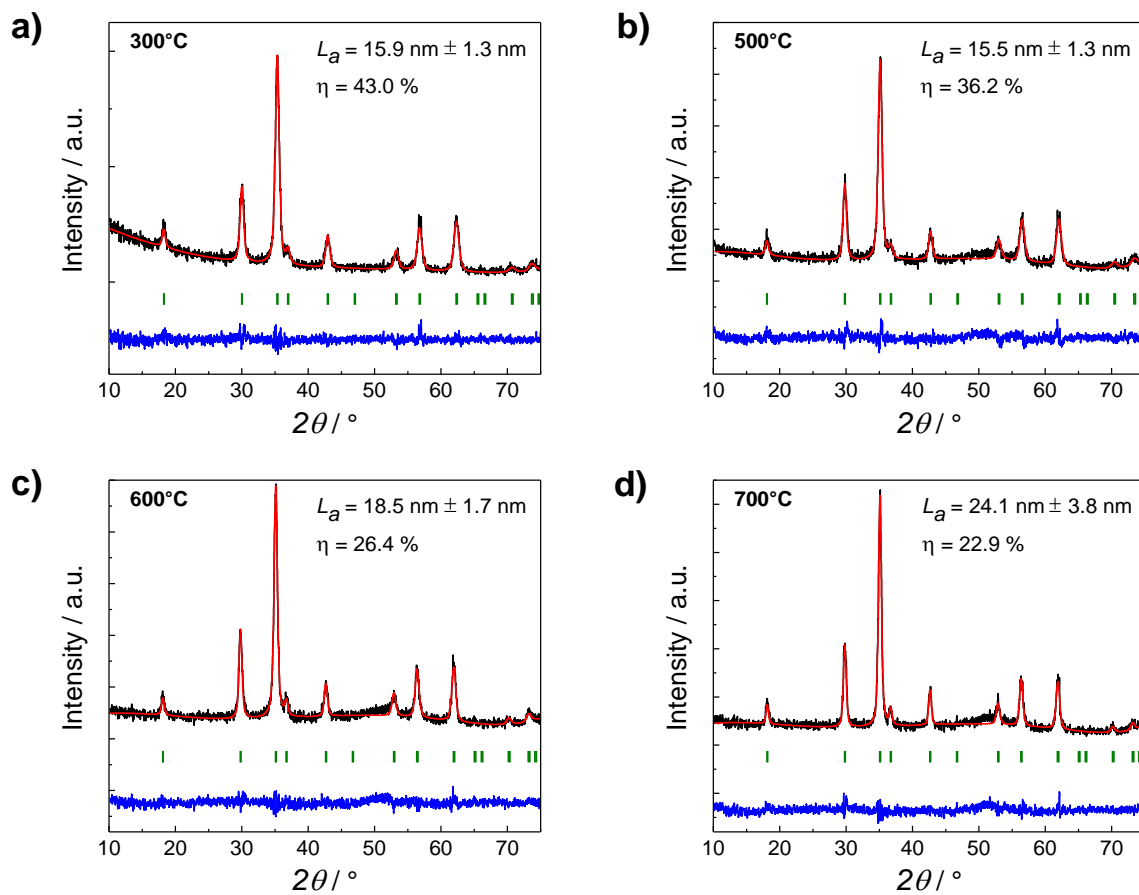


Figure 5.76: Rietveld refinement of XRD patterns obtained for nanoparticle-derived ZnFe_2O_4 thin films.

SEM images (Figure 5.77) of the calcined films underline the suggested sintering. The sample prepared at 300 °C clearly consists of single nanoparticles matching the average crystallite size obtained from Rietveld refinement (compare Figure 5.13a).

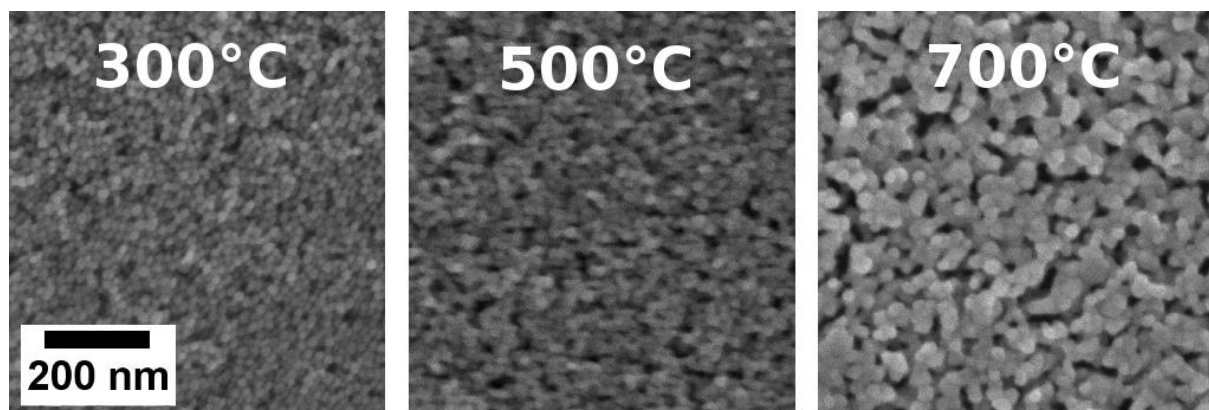


Figure 5.77: SEM images of heat-treated mesoporous thin films prepared from PVP-coated ZnFe_2O_4 nanoparticles.

These single nanoparticles grow to larger grains already at 500 °C due to particle sintering. After calcination at 700 °C, drastically increased grain sizes around 30 nm are visible. Interestingly, the typical worm-like pore morphology of mesoporous ZnFe_2O_4 appears, which was also obtained after long-term thermal treatment of sol-gel derived, polymer templated thin films. This implies that the obtained pore morphology represents an equilibrium in mesopores evolution of ZnFe_2O_4 .

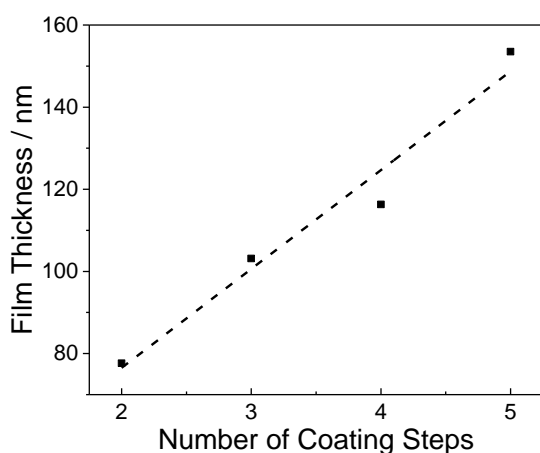


Figure 5.78: Dependence of the film thickness on the number of coating steps.

Film thickness was tailored by multiple coating with linear coherence of the thickness and the number of coating steps. In Figure 5.78, this is depicted for film thicknesses obtained from SEM cross-section analysis of a film prepared at 300 °C. The thickness of monolayer samples was not measurable due to very small extension of the layer.

For first evaluation of the PEC performance, a thin film of 239 nm thickness prepared by five times coating was calcined at 600 °C for 12 hours exhibiting a relative surface area of $31.2 \text{ m}^2 \text{ g}^{-1}$. This is comparable to the film thickness and calcination procedure of the best-performing ZnFe_2O_4 thin film produced by soft template sol-gel approach. The measurement was performed in 1 M NaOH/1 M Na_2SO_3 electrolyte in the dark, under simulated solar light and with LEDs of selected wavelength. The results of PEC analysis are displayed in Figure 5.79.

The photocurrent response under intermittent illumination with simulated solar light (Figure 5.79a) does not show any transients, which proves the suitability of the chosen sacrificial agent. The onset potential ($0.74 V_{\text{RHE}}$) and the flat band potential ($0.73 V_{\text{RHE}}$) are in good agreement. Furthermore, the flat band potential obtained from Mott Schottky plot (Figure 5.79c) is lower than for sol-gel derived thin films (compare Figure 5.44a) and matches well with literature reports.^[30,31] The

donor density N_D is two orders of magnitude higher than the values found for different sol-gel derived ZnFe_2O_4 thin films (compare Figure 5.43b). This can result from more intrinsic defects, such as grain boundaries, which develop during particle sintering.

Additionally, there is a significant difference in the photocurrent density under foreside and back side illumination with simulated solar light as shown in Figure 5.79b (compare Figure 5.43a). Although the thin films shows a similar film thickness, the charge carrier transport inside the thin film is significantly different from the behavior found for sol-gel-derived mesoporous ZnFe_2O_4 thin films. The foreside photocurrent density matches with the value reported for the PLU-derived sample calcined after an identical procedure. In contrast, the backside illumination results in a 95 % higher value ($122 \mu\text{A cm}^{-2}$). The dependence of the photocurrent from the illumination side unveils difficulties in charge carrier transport across the ZnFe_2O_4 layer.

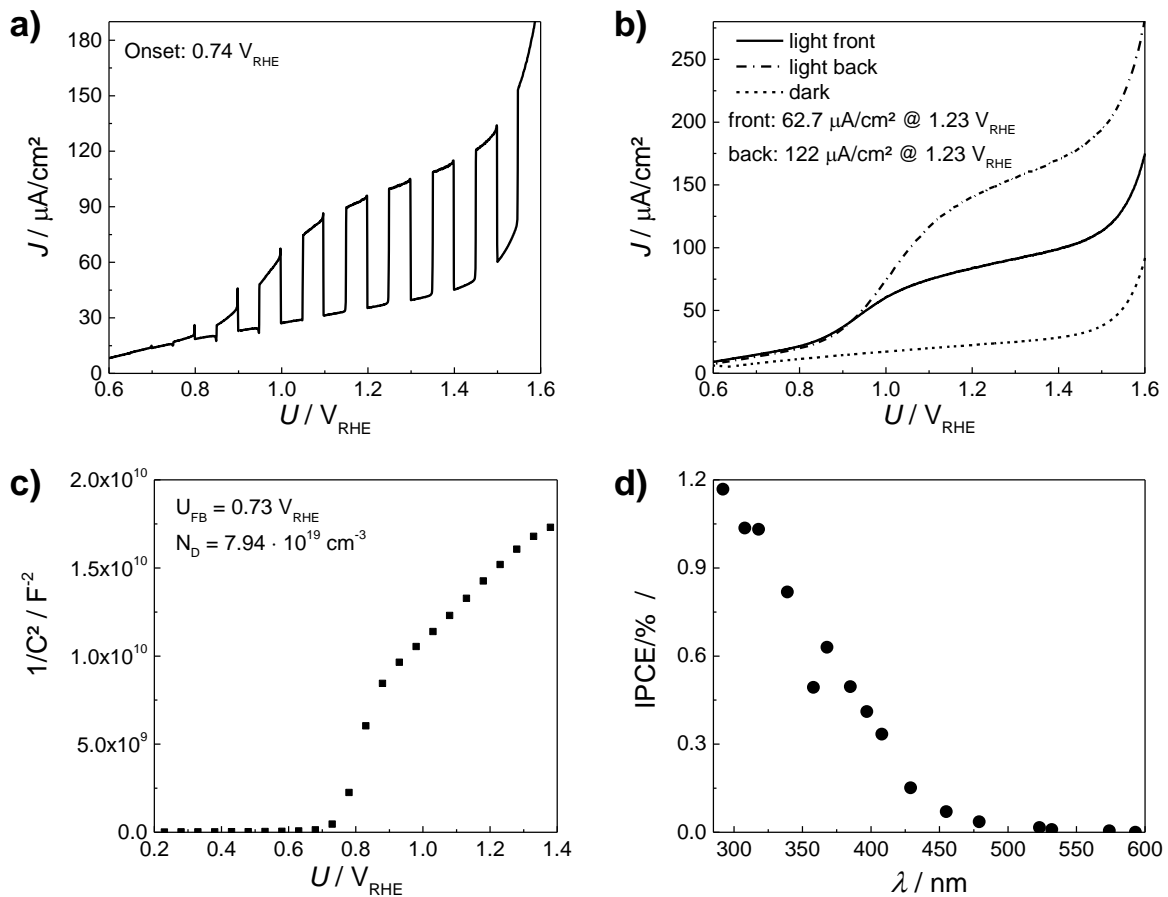


Figure 5.79: PEC performance under a) intermittent illumination, b) front and backside illumination, c) Mott Schottky plot and d) IPCE of the nanoparticle-derived ZnFe_2O_4 thin film.

As the light penetration depth is limited and decreases over the thickness of the thin film, the side of illumination determines where a larger number of charge carriers are generated. For front side illumination, the majority of charge carriers are created close to the electrode-electrolyte interface, while under backside illumination, more charge carriers are generated close to the ohmic contact with

the conductive layer. For ZnFe_2O_4 , being an n-type semiconductor, the holes generated during illumination are supposed to be transported to the electrode-electrolyte interface, where they can perform oxidation reaction. Therefore, under front side illumination the diffusion path for holes is less critical, as they are already generated close to the surface. In contrast, the diffusion path for electrons created close to the surface is significantly longer, as they need to travel to the back contact to be extracted. Under backside illumination, this principle is reversed. Therefore, an increased photocurrent under backside illumination indicates difficulties in the electron transport process to the back-contact for nanoparticle-derived ZnFe_2O_4 thin films. The electrons generated close to the electrode-electrolyte interface are not efficiently transported through the layer to be collected at the backside of the electrode, which reduces the overall photocurrent. Instead, charge carrier recombination occurs during charge carrier transport. This implies a short diffusion length for electrons possible in the material, which would match reports of only few nanometers diffusion length in α - and γ - Fe_2O_3 .^[212] Furthermore, the grain boundaries formed during particle sintering can act as electron recombination sites. The hindered electron transport is also the reason for lower IPCE values compared to the best-performing sol-gel derived mesoporous ZnFe_2O_4 electrode (compare Figure 5.46b).

5.5 Mesoporous Zinc Ferrite Powders

Bridging the gap between single ferrite nanoparticles and mesoporous ferrite thin films, an additional class of solid materials was investigated. For this purpose, porous ferrite powders were synthesized according to chapter 3.2.5. A class of PLU-templated ZnFe_2O_4 powders were heat-treated identically to the mesoporous thin films. For comparison, also PIB-derived powders were synthesized. The samples were found to be phase pure according to XRD and Raman analysis as shown in Figure 5.80. PLU and PIB-derived precursor gels obtained after heat treatment at 300 °C do not show any reflections in their XRD patterns. This is in agreement with mesoporous thin films prepared under identical conditions. For calcined samples, all reflections match the reference pattern (JCPDS reference card no. 22-1012). Furthermore, all expected Raman resonance vibrations were detectable in these samples. No further signals were found, proving the absence of impurity phases in the prepared materials. To evaluate the crystallinity of mesoporous ZnFe_2O_4 powder Rietveld refinements of their XRD patterns were created (see Table 5.7). Furthermore, N_2 physisorption data were recorded to evaluate if the synthesis approach yielded mesoporous powders.

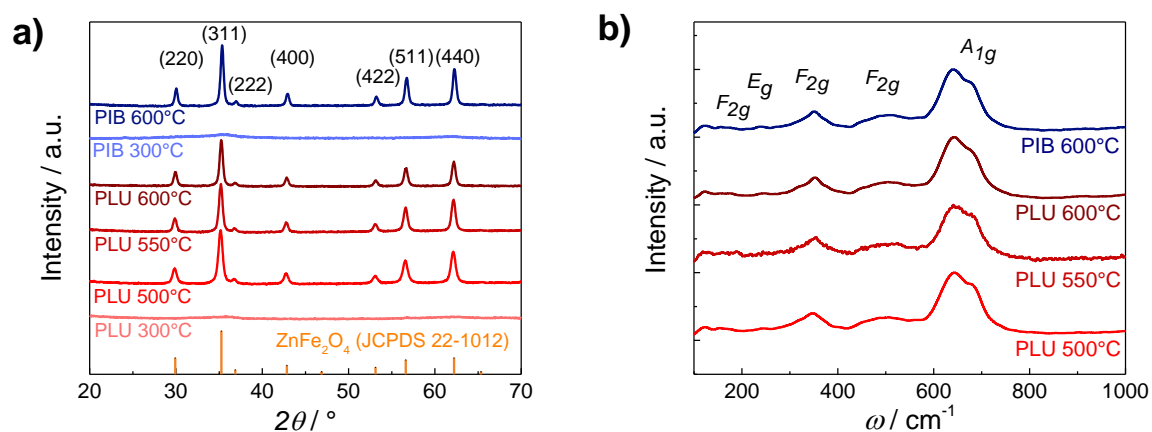


Figure 5.80: XRD data and b) Raman spectra of mesoporous ZnFe_2O_4 powders.

The N_2 physisorption isotherms and pore size distributions of PLU- and PIB-templated samples are shown in Figure 5.81. N_2 physisorption of the calcined powders revealed a type IV(a) isotherm, which is typical for mesoporous materials, with a H3 hysteresis loop indicating slit pores in a mesoporous solid compound. The precursor gels only show a H2(b) hysteresis, which is typical for pore blocking in wider pore necks, and inter-particle porosity because of incomplete porogen removal (compare Figure 5.32 and Figure 5.34). Here, a strong decrease in cumulative pore volume in combination with increasing pore diameters was found for calcined samples in comparison to their precursor gels (Figure 5.81c-d). The gels obtained after heat treatment at 300 °C of both polymer templates show a comparable pore radius, while the PLU-templated sample has a higher pore volume indicating a higher mesopore content. Calcination at elevated temperatures for 12 hours leads to a significant loss of pore volume accompanied by decreasing surface area and larger pore diameters, which is indicative for a strong sintering of the nanostructured solid. The pore sizes obtained after calcination are around the same size, which matches observations made for mesoporous ZnFe_2O_4 thin films (compare Figure 5.39). With higher temperature, stronger sintering occurs resulting in the lowest surface area and smallest pore volume for the PLU-templated sample calcined at 600 °C for 12 hours.

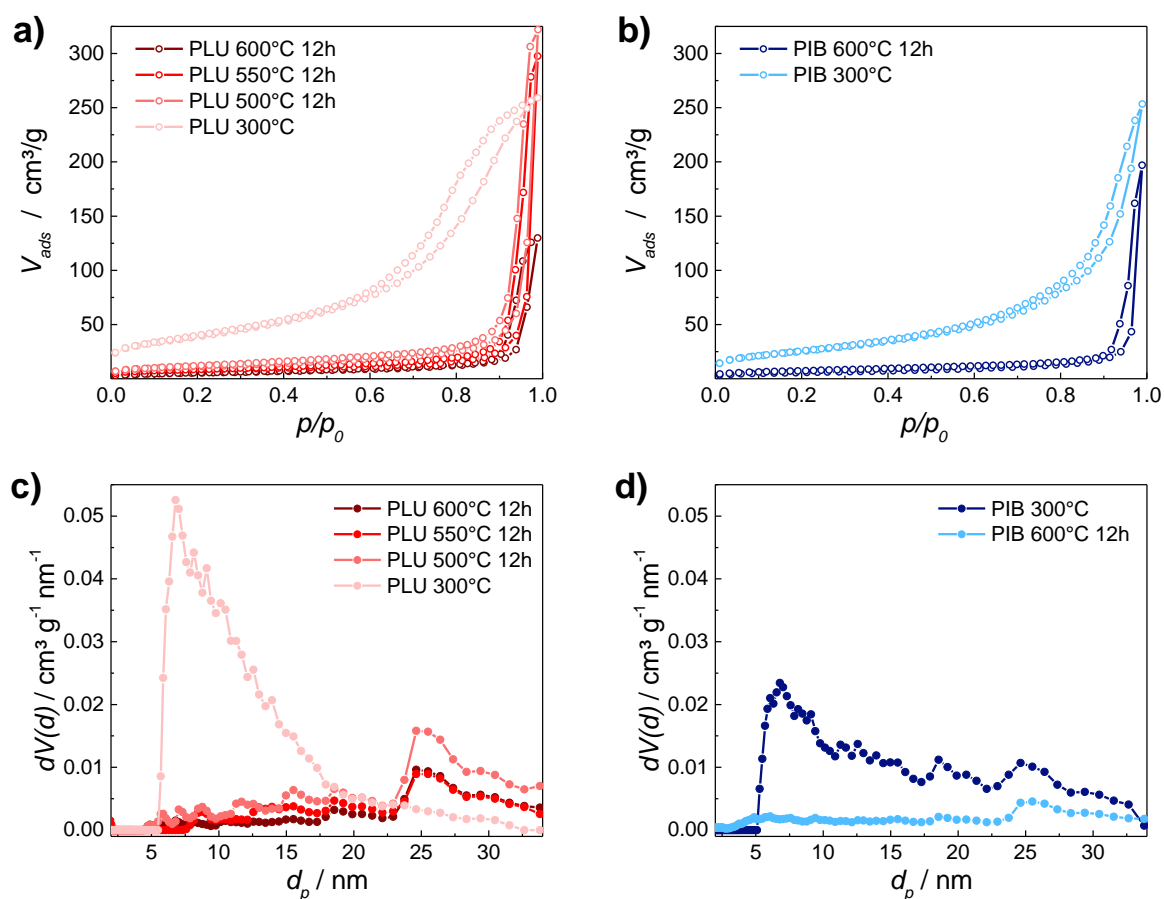


Figure 5.81: N_2 physisorption isotherms of $ZnFe_2O_4$ powders synthesized with a) Pluronic® F127 and b) PIB3000 soft template.

When comparing an equally treated PIB-templated sample (600 °C, 12 hours), pore size and surface area are in good agreement with the values of the PLU-templated sample, while the pore volume is slightly lower. As the uncalcined PIB gel already showed lower pore volume compared to the PLU-derived gel, a lower final pore volume after sample sintering was expectable. The results of N_2 physisorption and Rietveld refinement are listed in Table 5.7.

Table 5.7: Parameters obtained from Rietveld refinement of XRD data from $ZnFe_2O_4$ powders.

Sample	L_a / nm	η / %	d_p (NLDFT _{ads}) / nm	V_p / cm ³ g ⁻¹	S_L / m ² g ⁻¹
ZFO PLU 300 °C	-	-	6.8	0.374	252.0
ZFO PIB 300 °C	-	-	6.8	0.286	168.1
ZFO PLU 500 °C 12h	16.1 ± 1.2	22.9	24.6	0.180	66.0
ZFO PLU 550 °C 12h	19.7 ± 1.7	20.9	25.5	0.109	44.2
ZFO PLU 600 °C 12h	21.4 ± 1.5	17.1	24.6	0.094	32.0
ZFO PIB 600 °C 12h	21.3 ± 1.0	7.8	25.5	0.063	34.0

L_a = average crystallite size / η = average microstrain / V_p = pore volume / d_p = pore diameter / S_L = Langmuir surface area

The increasing crystallite size with increasing calcination temperature supports the theory of sintering, which leads to crystallite growth in solid materials. Alongside this, the microstrain decreases at higher calcination temperatures. This indicates a loss in surface area, because microstrain depicts crystal defects including surface area being the largest defect in a highly mesoporous material.^[379]

Similar trends and crystallite sizes were obtained from Rietveld refinement of mesoporous ZnFe_2O_4 thin films (compare Figure 5.38). Besides, the results match well with those from N_2 physisorption measurements. Overall, the trend of increased sintering alongside with loss of surface area during calcination at higher temperatures is in good agreement with the findings from Kr physisorption measurements of mesoporous ZnFe_2O_4 thin films mentioned in chapter 5.3.1 (compare Figure 5.40). Physisorption results prove that mesoporous powders were obtained from the synthesis as desired.

The IR patterns depicted in Figure 5.82 show the transformation of the precursor gels obtained from calcination of polymer template containing synthesis mixtures. In the region between 1500 cm^{-1} and 1200 cm^{-1} , distinct vibration signals can be found in the gels. These originate from the organic building blocks of the soft templates. Instead of two sharp bands at 552 cm^{-1} and 439 cm^{-1} , which are typical for solid ZnFe_2O_4 , only a very broad vibration band can be seen. This indicates a preformed connection with non-uniform bond length in the precursor gel.

The calcined samples show the expected, well-separated vibrational bands of the solid compound. Besides, the signals originated from the polymer decline. Only a weak, sharp signal at 1348 cm^{-1} for OH deformation vibration is detectable. Furthermore, the broad band around 3400 cm^{-1} is narrowing, which indicates less dipole-dipole interactions from hydroxide species in the material. Instead, the signal develops due to adsorbed water molecules in the porous compound. Some organic residues due to polymer removal show stretching vibrations at 2916 cm^{-1} .

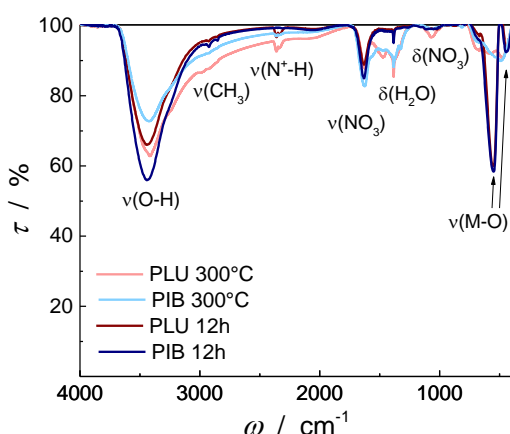


Figure 5.82: IR patterns of mesoporous ZnFe_2O_4 powders.

The IR patterns depicted in Figure 5.82 show the transformation of the precursor gels obtained from calcination of polymer template containing synthesis mixtures. In the region between 1500 cm^{-1} and 1200 cm^{-1} , distinct vibration signals can be found in the gels. These originate from the organic building blocks of the soft templates. Instead of two sharp bands at 552 cm^{-1} and 439 cm^{-1} , which are typical for solid ZnFe_2O_4 , only a very broad vibration band can be seen. This indicates a preformed connection with non-uniform bond length in the precursor gel.

The calcined samples show the expected, well-separated vibrational bands of the solid compound. Besides, the signals originated from the polymer decline. Only a weak, sharp signal at 1348 cm^{-1} for OH

deformation vibration is detectable. Furthermore, the broad band around 3400 cm^{-1} is narrowing, which indicates less dipole-dipole interactions from hydroxide species in the material. Instead, the signal develops due to adsorbed water molecules in the porous compound. Some organic residues due to polymer removal show stretching vibrations at 2916 cm^{-1} .

In Figure 5.83, TEM images of the calcined samples are shown. There, a connected network of ZnFe_2O_4 particles forming pores of different size and shape are visible. This matches N_2 physisorption analysis (compare Table 5.7 and Figure 5.81), where a broad pore size distribution with an average pore size round 25 nm was found. HRTEM images show the single crystal domains grew larger for the highest calcination temperature, which is consistent with results from Rietveld refinement (compare Table 5.7).

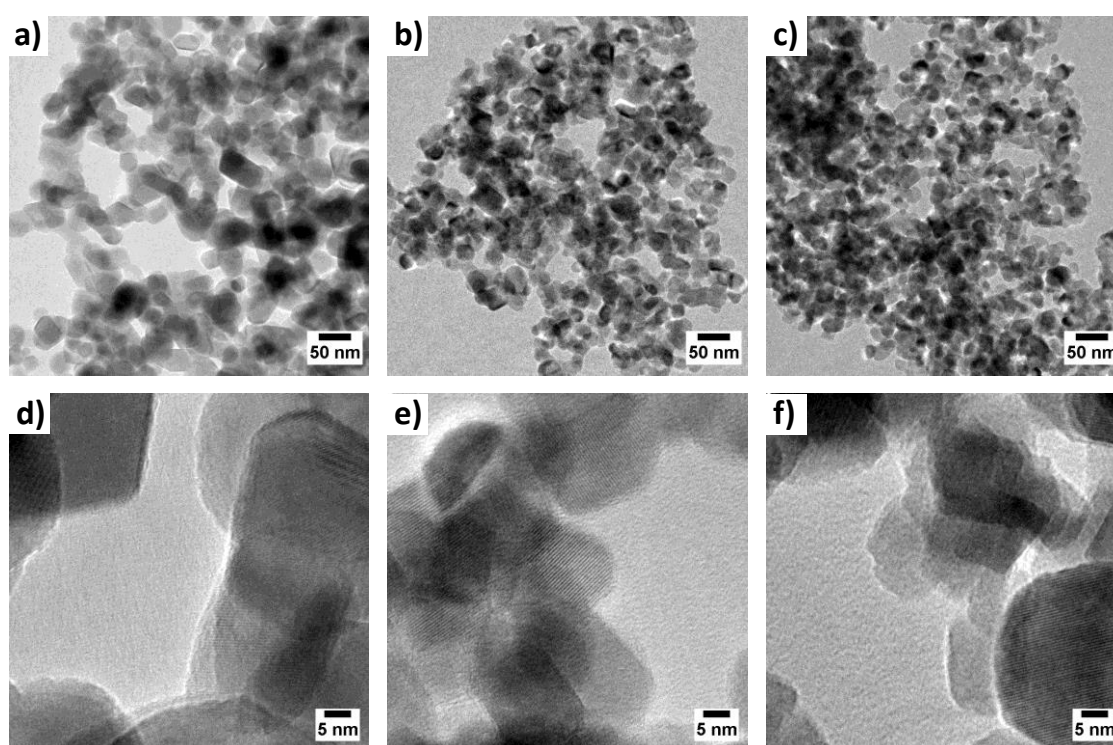


Figure 5.83: TEM images of PLU-derived ZnFe_2O_4 powders calcined at a+d) $600\text{ }^\circ\text{C}$, b+e) $550\text{ }^\circ\text{C}$ and c+f) $500\text{ }^\circ\text{C}$.

5.5.1 XAS Investigation of Mesoporous Zinc Ferrite Powders

Because mesoporous ZnFe_2O_4 powders and thin films are very similar in terms of crystallinity, porosity and phase purity, further structural analysis using synchrotron irradiation was only performed on the powder samples to draw conclusions about thin films samples, too. First, XANES measurements of the Fe K-edge of PLU-templated samples were performed to gain deeper insight into the coordination geometry around the Fe^{3+} ions within the samples.

The obtained spectra (Figure 5.84) reveal significant structural difference between the precursor gel and the calcined samples. Especially in the post-edge region, the multiple scattering is much more distinct in the calcined samples, indicating higher crystal ordering. In the pre-edge region, a clear feature around 7113.6 eV was found for all samples, which fits the literature value of 714.0 eV.^[356] Again, the precursor gel differs from the calcined samples, showing a much higher pre-edge intensity. The pre-edges were fitted using *Athena* software^[304] to allow a detailed comparison of the samples. All fits can be seen in Figure 4.4 and the parameters obtained from pre-edge fitting are listed in Table 5.8.

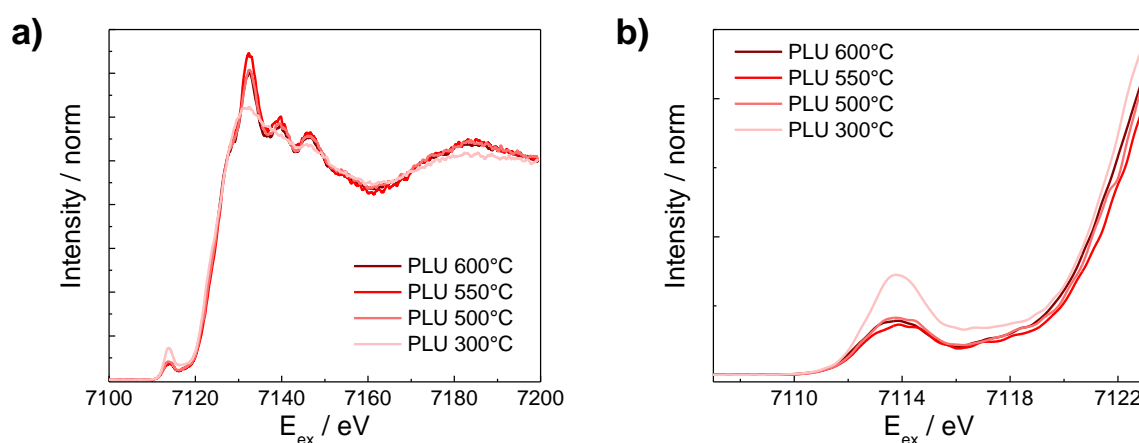


Figure 5.84: a) Full XANES spectra and b) XANES pre-edge features of PLU-derived mesoporous ZnFe_2O_4 powders.

Table 5.8: XANES fits of mesoporous ZnFe_2O_4 powders.

Sample	x_1 / eV	$FWHM_1$ / eV	A_1	x_2 / eV	$FWHM_2$ / eV	A_2	E_0 / eV
ZFO PLU 300 °C	7113.64	0.99	0.32	7116.07	1.51	0.20	7122.90
ZFO PLU 500 °C 12h	7113.56	0.83	0.10	7115.87	2.60	0.34	7123.05
ZFO PLU 550 °C 12h	7113.59	1.05	0.13	7116.23	2.42	0.26	7123.05
ZFO PLU 600 °C 12h	7113.60	1.02	0.16	7116.32	2.53	0.25	7122.84

x – peak position / $FWHM$ – full width at half maximum / A – peak area / E_0 – edge energy

For all samples, reasonably good fits of the pre-edge structure were obtained. These fits revealed a pre-edge position at 7113.6 eV with a satellite around 7116 eV found for all samples. The pre-edge position is sensitive to the oxidation state of the metal ion and the calculated values match well with those reported for Fe^{3+} containing iron oxide compounds.^[298] Whereas, the pre-edge intensive is sensitive to the coordination around the metal ions, which is why conclusions on tetrahedral or octahedral oxygen coordination can be drawn. For ZnFe_2O_4 being considered a normal spinel, Fe^{3+} are expected to be in octahedral positions, while Zn^{2+} occupy tetrahedral sites. With a relative intensity

around 0.15, all calcined samples indicate iron ions mainly in octahedral positions, which agrees with reports on low degree of inversion in ZnFe_2O_4 . The absorption edge of XANES is determined by the valence state and also by the metal-oxygen distance as shown by De Vries *et al.*^[291] For Fe^{3+} , an absorption edge energy of 7122 eV has been reported,^[298] which matches well with the observed values of around 7123 eV. If Fe^{2+} was present, the edge energies would be shifted to lower energies by around 1.5 eV.^[298] Splitting of the pre-edge feature by around 1.5 eV for octahedral Fe^{3+} complexes has been reported by Westre *et al.*^[290] With oxygen ligands in the mesoporous ZnFe_2O_4 powders, a slightly larger splitting of around 2 eV was observed. Comparing the samples prepared at 300 °C, 500 °C and 600 °C, respectively, slight differences were found. Especially when comparing the precursor gel and the calcined samples, a minor shift to larger emission energies was found for excitation at 7114 eV (see Figure 5.85c), which is equal to the position of the pre-edge maximum (compare Figure 4.4 and Table 5.8).

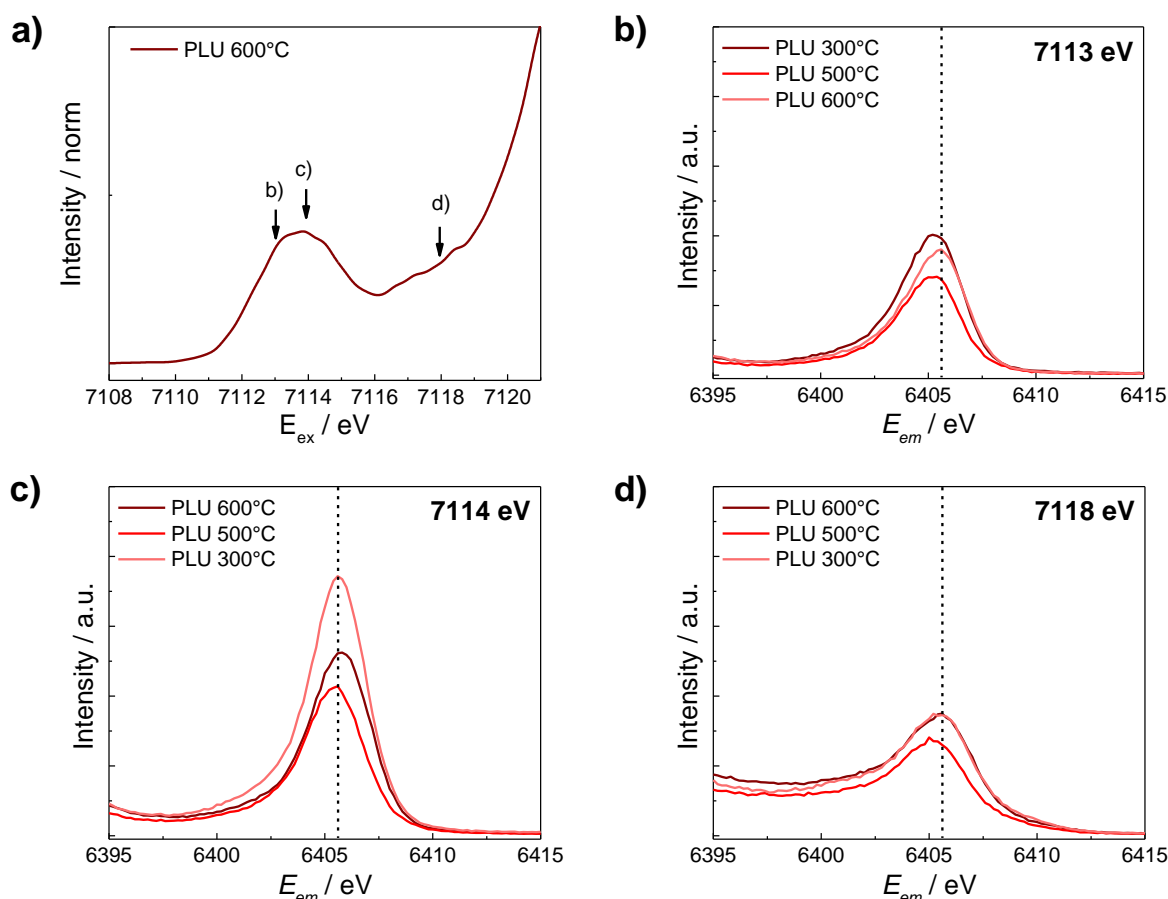


Figure 5.85: K-edge absorption spectrum of PLU with corresponding excitation energies for b-d) the corresponding X-ray emission spectra of mesoporous ZnFe_2O_4 powders.

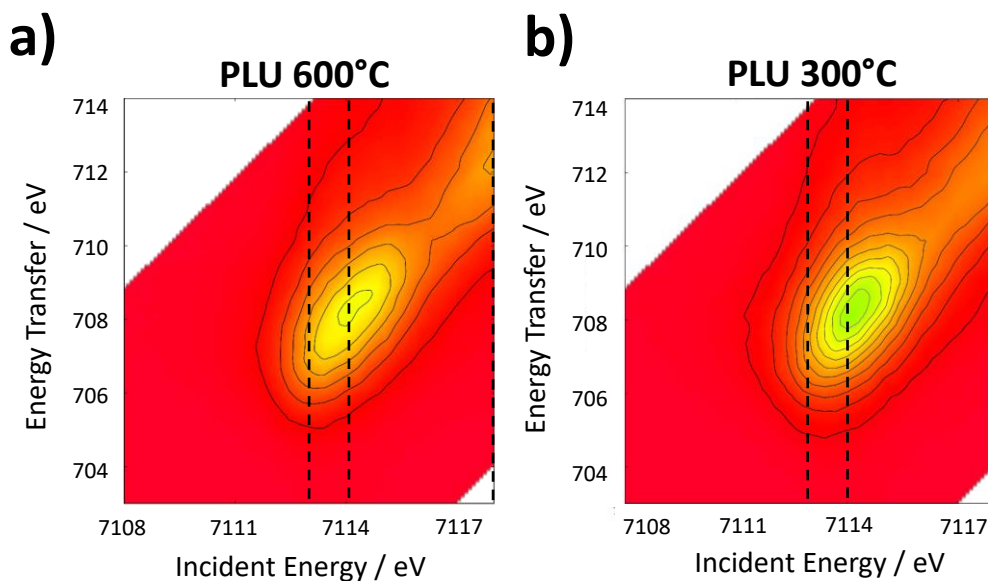
When the samples were excited with 7113 eV (Figure 5.85b), both crystalline samples show a lower emission energy. With an excitation energy close to the edge (7118 eV), all samples show identical emission energies (Figure 5.85d). As already presented in chapter 4.1.5, with site-selective emission in

the pre-edge region, additional features in XES line shape can be identified, which would not be detectable in non-resonant XES (compare Figure 4.6). Comparing the literature results for α -Fe₂O₃ with those shown in Figure 5.85, no shoulders in the peak shape were found. This might be due to lower resolution of the overall spectra, as different monochromators were applied during presented and reference measurements. This assumption is supported by comparison with analysis details found for Fe₃O₄ and α -Fe₂O₃ reference compounds were also no non-symmetric peak shapes were found. Using *PyMca* software, a split pseudo-Voigt fit function was used to characterize the XES signals. The fit results are summarized in Table 5.9 (compare also Table 5.4 and Table 9.4).

Table 5.9: XES fits of mesoporous ZnFe₂O₄ powders.

E_{ex} / eV	Sample	E_{em} / eV	$FWHM$ / eV	A_{rel} / %	E_{trans} / eV
7113	PLU 300 °C	6405.5	4.32	26.75	707.5
	PLU 500 °C 12h	6405.4	4.30	18.93	707.6
	PLU 600 °C 12h	6405.7	4.36	23.39	707.3
7114	PLU 300 °C	6405.8	3.78	30.19	708.2
	PLU 500 °C 12h	6405.6	3.86	17.06	708.4
	PLU 600 °C 12h	6406.0	4.02	20.98	708.1
7118	PLU 300 °C	6405.8	5.36	28.63	712.2
	PLU 500 °C 12h	6405.4	4.89	20.90	712.6
	PLU 600 °C 12h	6405.8	5.26	26.16	712.2

E_{ex} – excitation energy / E_{em} – emission energy / $FWHM$ – full width at half maximum / A_{rel} – peak area relative to Fe₃O₄ / E_{trans} – energy transfer

Figure 5.86: RIXS planes of a) mesoporous ZnFe₂O₄ powder calcined at 600 °C and b) its respective precursor gel.

The RIXS planes with marked excitation energies for site-selective XES are shown in Figure 5.86. From RIXS analysis, again a higher pre-edge intensity was found for the PLU-derived gel in comparison to the sample calcined at 600 °C. This matches findings from XANES and XES analysis (compare Figure 4.4 and Figure 5.85).

The pre-edge feature of the crystalline sample shows a clear diagonal trend, which is typical for materials with Fe³⁺ atoms in octahedral coordination.^[293] As in normal spinel ZnFe₂O₄, the majority of Fe³⁺ are located in the octahedral sites, this assumption is supported by RIXS measurement. Along this axis, a rather broad distribution around the maximum was found. In contrast, the pre-edge feature of the precursor gel is more concerted. There are some weak expansion in the horizontal direction additionally to the diagonal extension. This indicates different energy transfer at the same excitation energy. A less diagonal plot shape was already reported by de Groot *et al.*^[293] for Fe³⁺ in tetrahedral coordination. As such a preliminary conformation of the Fe³⁺ ions in the precursor gel was already assumed from XANES analysis (compare Figure 4.4), the results from RIXS measurements are in agreement with all previous measurements. The peak positions from maximum energy absorption and energy transfer were estimated as 7114.0 eV and 708.4 eV for the calcined sample and at 7114.2 eV and 708.2 eV for the precursor gel, respectively.

Finally, valence-to-core XES excitation (V2C) of the sample calcined at 600 °C was measured. The obtained spectrum and corresponding fit is shown in Figure 5.87a. Evident from this figure is the non-optimum measurement period. As the Kβ'' line has only very weak intensity (see also chapter 4.1.5), very long measuring time is needed. In this case, the period of analysis was around 8 hours. Still, a rather noisy spectrum was received. In Figure 5.87b, the V2C-XES spectrum and the corresponding XANES spectrum are shown together with their first derivatives. As can be seen, a minimum and maximum for the decay of the V2C shoulder and the rise of the pre-edge shoulder can be found. Again, only a noisy first derivative was gained from V2C-XES spectrum, which makes it difficult to proceed.

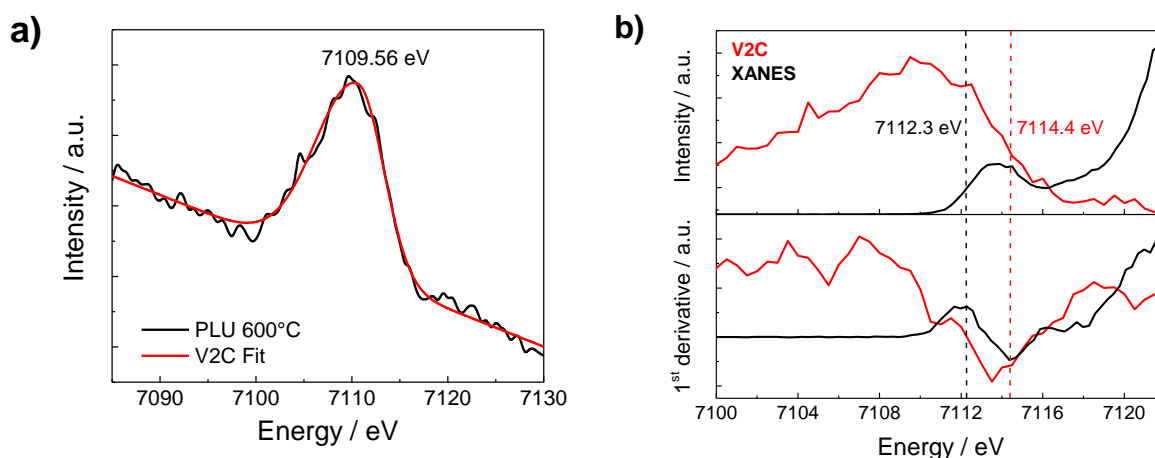


Figure 5.87: a) V2C-XES spectrum with fit and b) V2C-XES and XANES spectra with their first derivatives.

The horizontal markers were placed on the half maximum of the decay and the rise region, respectively. A value of 7112.3 eV for the onset of the pre-edge and 7114.4 eV for the V2C decay were obtained. The difference between those values, which is 2.1 eV, equals the band gap energy of the material. This values matches quite well with the indirect band gap calculated from UV-Vis analysis of ZnFe₂O₄ nanoparticles (compare Figure 5.1c-d). However, this is only a rough estimation due to limited data quality.

The overlap of the V2C and XANES signals in the pre-edge region is surprising, as the report by Nowakowski *et al.*^[312] stated only a minor overlap for α -Fe₂O₃. This was, so far, a good reference for the Fe³⁺ characteristics of ZnFe₂O₄. The difference is probably due to the calculated XANES spectra obtained at maximum K β intensity from RXES measurement. This shows narrower features compared to the measured, off-resonant HRFD-XAS spectrum.

6 Conclusion

At the beginning of this work, a vast number of publications concerning the band gaps, band positions as well as the photoelectrochemical and photocatalytic performance of MgFe_2O_4 , ZnFe_2O_4 and CaFe_2O_4 reported confusing and sometimes contradictory results. Due to the formation of by-phases or inappropriate phase analysis, the variety of experimental conditions, the partial lack of adequate reference experiments and the variation of multiple experimental parameters, literature results were found to be partly unreliable. Therefore, this work addressed the synthesis of highly phase pure, nanostructured MgFe_2O_4 , ZnFe_2O_4 and CaFe_2O_4 samples destined for detailed, systematic evaluation of their physicochemical, photocatalytic and photoelectrochemical properties.

The investigation of microwave-derived cubic spinel ferrite MgFe_2O_4 and ZnFe_2O_4 nanoparticles revealed phase-pure compounds with high monodispersity and spherical shape exhibiting indirect band gaps of 2.20 eV and 2.04 eV, respectively. This trend was also detected for the particle size of MgFe_2O_4 and ZnFe_2O_4 nanoparticles being 5 nm and 10 nm, respectively, which is consistent with the average crystallite size of 8.6 nm for ZnFe_2O_4 and 3.2 nm for MgFe_2O_4 calculated by Rietveld refinement. The difference in average crystallite size and particle size was assigned to the lower decomposition temperature of the zinc precursors, which leads to a higher oversaturation at the chosen reaction temperature of 275 °C. The synthesis period for both ferrites was found to be of minor impact. The synthesis of orthorhombic ferrite CaFe_2O_4 nanoparticles was not possible, which was accounted to the high decomposition temperature of the chosen precursor, exceeding the possible synthesis temperature. The influence of reaction setup for production of ZnFe_2O_4 nanoparticles was investigated, showing comparable results concerning the phase purity, average crystallite size, average microstrain and surface area. Post-synthetic heat treatment showed an increasing crystallite size and decreasing microstrain accompanied by a loss of surface area, which was attributed to nanoparticle sintering appearing at temperatures ≥ 500 °C. All as-synthesized and post-synthetically calcined nanoparticles showed heavy agglomeration, which reduces the accessible surface area during photocatalysis. Therefore, multiple approaches for colloidal stabilization of as-synthesized MgFe_2O_4 and ZnFe_2O_4 nanoparticles in non-polar and polar solvents were developed. Furthermore, surface-functionalized MgFe_2O_4 and ZnFe_2O_4 nanoparticles were investigated concerning their photocatalytic properties. It was shown, that not only a low degree of agglomeration but also the nature of the surfactant could influence the photocatalytic degradation of model compounds. This represents the first study on the interplay of colloidal stability, the nature of surfactants and the resulting photocatalytic efficiency of degradation processes.

Besides, a so-gel-based synthesis approach for mesoporous ferrite thin films, which was previously reported by Haetge *et al.*, was optimized for the synthesis of mesoporous ZnFe_2O_4 , MgFe_2O_4 and

CaFe₂O₄ thin film photoelectrodes. For generation of mesopores, different block-copolymers were used as soft templates.

The impact of pore morphology and crystallinity of mesoporous ZnFe₂O₄ thin films on their photoelectrochemical performance was studied systematically by variation of calcination temperature (500 °C – 600 °C) and calcination period (0 min – 12 hours) used during the synthesis. Furthermore, the infiltration with SiO₂ prior to the calcination was chosen to see if smaller mesopores, which come along with a higher surface area, could be maintained during the developed synthesis. It was shown, that the photoelectrochemical performance of these hard-templated films depends on the grain size formed during sintering, leading to the assumption that the PEC performance of mesoporous ZnFe₂O₄ depends rather on the size of crystalline domains than on the morphology of the pores. This is, so far, the first systematic study on the influence of pore morphology and crystallinity on the PEC performance of nanostructured thin film photoelectrodes.

For MgFe₂O₄, ultrathin mesoporous thin films were prepared by a polymer-templated dip coating approach. A need for higher temperatures starting from 600 °C was identified for development of crystalline mesoporous MgFe₂O₄ thin films. As already seen for mesoporous ZnFe₂O₄ photoelectrodes, the extension of the calcination period increases the achievable photocurrent. A MgCO₃ surface layer was detected by XPS analysis, which might be accountable for the limited PEC performance.

After intensive investigation, the synthesis procedure was also transferred to CaFe₂O₄ resulting in mesoporous thin films with hierarchical pore structure. By this means, production of mesoporous CaFe₂O₄ photocathodes at synthesis temperatures below 800 °C was possible for the first time. Similar to MgFe₂O₄, XPS analysis revealed the presence of a CaCO₃ surface layer on mesoporous CaFe₂O₄ thin films, which might limit the PEC performance. The tendency for carbonate formation of Mg- and Ca-based ferrites during calcination in air was accounted to the highly negative Gibbs free formation enthalpy of MgCO₃ and CaCO₃.

Comparison with nanoparticle-derived mesoporous ZnFe₂O₄ thin films gave insights into the charge carrier diffusion and influence of grain boundaries underlining the aforementioned necessity for crystalline materials. Nanoparticle-based ZnFe₂O₄ thin films were produced by spin coating of an ethanol-based solution of PVP-encapsulated ZnFe₂O₄ nanoparticles. The film thickness was easily adjustable by multiple consecutive coating steps. The average crystallite size and mesopore morphology were influenced by changing the calcination procedure of the as-synthesized thin films as shown by SEM and Rietveld analysis. The PEC performance under simulated solar light showed a significant difference between foreside and backside irradiation, which was accounted to an increased transport limitation of the charge carriers inside the mesoporous structure.

Finally, mesoporous ZnFe₂O₄ powders were produced as a third example of nanostructured ZnFe₂O₄ samples. Based on the precursor gels produced with different polymer templates, phase-pure

ZnFe₂O₄ powders were obtained after calcination temperatures between 500 °C and 600 °C, which was verified by XRD and Raman analysis. During post-synthetic heat treatment, the average pore sizes of 8.6 nm in the precursor gels increased to about 25 nm. Different crystallite sizes were found after the calcination step, increasing with rising calcination temperature according to Rietveld refinement. They were in agreement with the values found for equally treated mesoporous ZnFe₂O₄ thin films. TEM analysis confirmed a porous, connected network of ZnFe₂O₄ single crystals in the range of the calculated average crystallite size. By synchrotron-based X-ray absorption techniques, deeper insight into the distribution of Fe³⁺ ions in the spinel structure were obtained, indicating a low degree of inversion as already found for ZnFe₂O₄ nanoparticles. Applying XANES and valence-to-core emission analysis, a band gap of 2.1 eV was determined, which matches well with the value found during DR-UV-Vis analysis. This is, so far, the first systematic analysis using synchrotron techniques of an iron-oxide-based mesoporous powder concerning the band structure, electronic states and degree of inversion.

The obtained results on MgFe₂O₄, ZnFe₂O₄ and CaFe₂O₄ rule out contradictory literature reports, clarifying the band positions and semiconductor types. This allows inferences on their possible application in photocatalysis and photoelectrochemistry, suggesting MgFe₂O₄ and ZnFe₂O₄ as photoanode materials for oxidation reactions and CaFe₂O₄ as photocathode material. A strong impact of the crystallinity in nanostructured samples was identified and a dependence of the PEC performance of mesoporous ZnFe₂O₄ thin films on the synthesis method was revealed. Furthermore, for the first time, colloidal stability and the nature of surfactants was related to the photocatalytic efficiency of degradation processes.

7 Outlook

In the future, different topics could be addressed to further understand and improve the photocatalytic and photoelectrochemical performance of the studied systems.

In principal, the synthesis developed for ZnFe₂O₄ nanoparticles^[4] and adapted for MgFe₂O₄ nanoparticles^[1] should be applicable to other cubic spinel ferrites, too, allowing a fast and easy synthesis of phase-pure, uniform nanocrystals.

As already examined, the synthesis was not adaptable for non-cubic ferrite material CaFe₂O₄. Therefore, no CaFe₂O₄ nanoparticles were producible for photocatalytic investigation. Concerning this, the development of a solution-based synthesis approach for CaFe₂O₄ nanoparticles is highly desirable and should be targeted in the future. To achieve this, the application of different precursors, solvents or reaction setups would be imaginable.

In addition, the *in situ* stabilization of PVP could be applied to other solution-based synthesis approaches operating at temperatures between 200 °C and 300 °C. This would offer the possibility of direct synthesis of water-based colloidal solutions. Furthermore, these colloids could be used for production of mesoporous thin films *via* spin coating as described in chapter 3.2.4. Possibly, PVP-encapsulated nanoparticles could be applicable for dip-coating synthesis of mesoporous thin films, too. As shown for mesoporous ZnFe₂O₄ thin film photoanodes, the use of microwave-assisted formation of monocrystalline nanoparticle precursors can lead to higher photocurrent densities at similar film thicknesses and surface area compared to sol-gel based approaches.

The stabilization of small nanoparticles with betaine hydrochloride or citric acid might also be applicable to other ferrite or metal oxide nanoparticles, although adjustment of the surfactant ratio could be necessary in the latter case due to different faceting of the oxide surfaces.

The morphological impact of soft templating with different block-copolymers followed by tailored calcination procedures should be transferrable to other ferrite and iron oxide materials and might be applicable for other metal oxide semiconductors with a comparable sol-gel chemistry.

For mesoporous thin films, the impact of film thickness was not investigated so far. As the thickness of the thin film absorber correlates with the absorption of incident light, an optimum in film thickness could lead to an improved PEC performance. Besides, the increase of film thickness is accompanied by the increase of photocatalyst amount, which would allow conclusions on the change of PEC characteristics concerning the variation of the amount of active mass of the photocatalyst.

Furthermore, the conservation of original pore structure by infiltration with a hard template was only briefly addressed in chapter 5.3.1.3 for mesoporous ZnFe₂O₄ thin films. This approach could be transferred to mesoporous MgFe₂O₄ and CaFe₂O₄ thin film photoelectrodes and might help to reduce the amount of carbonate formed during calcination. As the carbonate surface layers are assumed to

act as passivation layers, their reduction or complete elimination could improve the PEC performance. Especially concerning MgFe_2O_4 thin films, the optimum conditions for generation of high-performing photoanodes have not been found yet, which is why further adjustment of the dip coating and calcination procedure would be necessary.

Furthermore, the generation of larger pores by application of novel polymers could improve the mass transport and gas diffusion inside the thin films. In 2016, the generation of 30 nm sized mesopores in Ta_2O_5 and CsTaWO_6 by a tailored drying and calcination process in the presence of ISO polymer has been reported.^[112,143] A transfer of this process to the developed sol-gel approach for ferrite thin film synthesis could lead to an ordered porosity in ferrite powders.

During the photoelectrochemical characterization of ZnFe_2O_4 , CaFe_2O_4 and MgFe_2O_4 photoelectrodes, difficulties in the charge transfer into the solution were observed. This can be accounted to problems with hole accumulation, the presence of surface trap states and a low charge carrier mobility. These points could be addressed by deposition of suitable co-catalysts (*e.g.* CoO(OH) , FeO(OH) or IrO_2)^[152,380,381], the addition of a passivation layer (*e.g.* SnO_2 , Al_2O_3 or Fe_2TiO_5)^[382–384] and doping^[385–387] or post-synthetic treatment as reported by Kim *et al.*^[107,232].

With the STH efficiency of PEC tandem cells depending on the band gap of the included absorber materials, visible-light-absorbing materials have been identified as desirable components. With the aim of 10 % STH efficiency, ZnFe_2O_4 and MgFe_2O_4 exhibiting band gaps around 2 eV could be suitable absorber materials for dual-absorber tandem cells in combination with silicon.^[43,44] So far, mostly hematite-silicon-tandem approaches have been reported.^[388] Therefore, the combination of ZnFe_2O_4 and MgFe_2O_4 as photoanode materials with either a CaFe_2O_4 or a silicon photocathode to construct a tandem cell will be a challenging goal for the future.

8 References

- [1] K. Kirchberg, A. Becker, A. Bloesser, T. Weller, J. Timm, C. Suchomski, R. Marschall, *J. Phys. Chem. C* **2017**, *121*, 27126–27138.
- [2] J. Cao, J. Xing, Y. Zhang, H. Tong, Y. Bi, T. Kako, M. Takeguchi, J. Ye, *Langmuir* **2013**, *29*, 3116–3124.
- [3] H. G. Kim, P. H. Borse, J. S. Jang, E. D. Jeong, O. S. Jung, Y. J. Suh, J. S. Lee, *Chem. Commun.* **2009**, 5889–5891.
- [4] C. Suchomski, B. Breitung, R. Witte, M. Knapp, S. Bauer, T. Baumbach, C. Reitz, T. Brezesinski, **2016**, *7*, 1350–1360.
- [5] J. Haetge, C. Suchomski, T. Brezesinski, *Inorg. Chem.* **2010**, *49*, 11619–11626.
- [6] L. Lin, A. Gettelman, Q. Fu, Y. Xu, *Clim. Change* **2018**, *146*, 407–422.
- [7] B. I. Cook, J. E. Smerdon, R. Seager, S. Coats, *Clim. Dyn.* **2014**, *43*, 2607–2627.
- [8] A. Dai, *Wiley Interdiscip. Rev. Clim. Chang.* **2011**, *2*, 45–65.
- [9] J. Hansen, M. Sato, R. Ruedy, K. Lo, D. W. Lea, M. Medina-Elizade, *Proc. Natl. Acad. Sci. U. S. A.* **2006**, *103*, 14288–14293.
- [10] G. Koneswaran, D. Nierenberg, *Environ. Health Perspect.* **2008**, *116*, 578–582.
- [11] A. Amtout, R. Leonelli, *Phys. Rev. B* **1995**, *51*, 6842–6851.
- [12] H. Tang, H. Berger, P. E. Schmid, F. Lévy, G. Burri, *Solid State Commun.* **1993**, *87*, 847–850.
- [13] X. Chen, S. Shen, L. Guo, S. S. Mao, *Chem. Rev.* **2010**, *110*, 6503–6570.
- [14] K. Van Benthem, C. Elsässer, R. H. French, *J. Appl. Phys.* **2001**, *90*, 6156–6164.
- [15] R. Abe, M. Higashi, K. Sayama, Y. Abe, H. Sugihara, *J. Phys. Chem. B* **2006**, *110*, 2219–2226.
- [16] J. Soldat, R. Marschall, M. Wark, *Chem. Sci.* **2014**, *00*, 1–7.
- [17] R. Dillert, D. H. Taffa, M. Wark, T. Bredow, D. W. Bahnemann, *APL Mater.* **2015**, *3*, 104001:1-15.
- [18] D. H. Taffa, R. Dillert, A. C. Ulpe, K. Bauerfeind, T. Bredow, D. Bahnemann, M. Wark, *J. Photonics Energy* **2016**, *7*, 1–24.
- [19] E. Casbeer, V. K. Sharma, X.-Z. Li, *Sep. Purif. Technol.* **2012**, *87*, 1–14.
- [20] P. Jing, J. Li, L. Pan, J. Wang, X. Sun, Q. Liu, *J. Hazard. Mater.* **2015**, *284*, 163–170.
- [21] H. Yang, J. Yan, Z. Lu, X. Cheng, Y. Tang, *J. Alloys Compd.* **2009**, *476*, 715–719.
- [22] P. H. Borse, C. R. Cho, K. T. Lim, Y. J. Lee, T. E. Hong, J. S. Bae, E. D. Jeong, H. J. Kim, H. G. Kim, *J. Korean Phys. Soc.* **2011**, *58*, 1672.
- [23] B. F. Decker, J. S. Kasper, *Acta Crystallogr.* **1957**, *10*, 332–337.
- [24] Y. Matsumoto, *J. Solid State Chem.* **1996**, *126*, 227–234.
- [25] R. Marschall, *Adv. Funct. Mater.* **2014**, *24*, 2421–2440.
- [26] K. O. Abdulwahab, M. A. Malik, P. O'Brien, G. A. Timco, *Mater. Sci. Semicond. Process.* **2014**, *27*, 303–308.
- [27] S. Sun, H. Zeng, D. B. Robinson, S. Raoux, P. M. Rice, S. X. Wang, G. Li, *J. Am. Chem. Soc.* **2004**, *126*, 273–279.
- [28] V. Šepelák, A. Feldhoff, P. Heitjans, F. Krumeich, D. Menzel, F. J. Litterst, I. Bergmann, K. D. Becker, *Chem. Mater.* **2006**, *18*, 3057–3067.
- [29] Z. Yan, J. Gao, Y. Li, M. Zhang, M. Guo, *RSC Adv.* **2015**, *5*, 92778–92787.
- [30] A. G. Hufnagel, K. Peters, A. Müller, C. Scheu, D. Fattakhova-Rohlfing, T. Bein, *Adv. Funct. Mater.* **2016**, *26*, 4435–4443.
- [31] D. Peeters, D. H. Taffa, M. M. Kerrigan, A. Ney, N. Jöns, D. Rogalla, S. Cwik, H. W. Becker, M. Grafen, A. Ostendorf, et al., *ACS Sustain. Chem. Eng.* **2017**, *5*, 2917–2926.
- [32] S. Ida, K. Yamada, T. Matsunaga, H. Hagiwara, Y. Matsumoto, T. Ishihara, *J. Am. Chem. Soc.* **2010**, *132*, 17343–17345.
- [33] M. Hanesch, *Geophys. J. Int.* **2009**, *177*, 941–948.
- [34] K. Kirchberg, S. Wang, L. Wang, R. Marschall, *ChemPhysChem* **2018**, *19*, 2313–2320.
- [35] Agency for Natural Resources and Energy, *Key World Energy Statistics*, **2017**.
- [36] D. a Lashof, D. R. Ahuja, *Nature* **1990**, *344*, 529–531.

- [37] United Nations Climate Change Secretariat, *Yearbook of Global Climate Action 2017*, Bonn, **2017**.
- [38] United Nations Framework Convention on Climate Change, *Adoption of the Paris Agreement*, **2015**.
- [39] R. Perez, M. Perez, *Int. Energy Agency SHC Program. Sol. Updat.* **2015**, *62*, 4–6.
- [40] Fraunhofer Institute for Solar Energy Systems, *Photovoltaics Report*, **2018**.
- [41] J. Chen, D. Yang, D. Song, J. Jiang, A. Ma, M. Z. Hu, C. Ni, *J. Power Sources* **2015**, *280*, 649–666.
- [42] Z. Li, W. Luo, M. Zhang, J. Feng, Z. Zou, *Energy Environ. Sci.* **2013**, *6*, 347–370.
- [43] A. J. Bard, M. A. Fox, *Acc. Chem. Res.* **1995**, *28*, 141–145.
- [44] M. S. Prévot, K. Sivula, *J. Phys. Chem. C* **2013**, *117*, 17879–17893.
- [45] J. Juodkazytė, G. Seniutinas, B. Šebeka, I. Savickaja, T. Malinauskas, K. Badokas, K. Juodkakis, S. Juodkakis, *Int. J. Hydrogen Energy* **2016**, *41*, 11941–11948.
- [46] K. Takanabe, *ACS Catal.* **2017**, *7*, 8006–8022.
- [47] F. E. Osterloh, *ACS Energy Lett.* **2017**, *2*, 445–453.
- [48] N. Serpone, A. Salinaro, A. Emeline, V. Ryabchuk, *J. Photochem. Photobiol. A Chem.* **2000**, *130*, 83–94.
- [49] R. Brimiouille, D. Lenhart, M. M. Maturi, T. Bach, *Angew. Chemie - Int. Ed.* **2015**, *54*, 3872–3890.
- [50] J. Du, K. L. Skubi, D. M. Schultz, T. P. Yoon, *Science (80-.)*. **2014**, *344*, 392–396.
- [51] G. Knör, *Coord. Chem. Rev.* **2015**, *304–305*, 102–108.
- [52] D. Gust, T. A. Moore, A. L. Moore, *Acc. Chem. Res.* **2009**, *42*, 1890–1898.
- [53] A. Duret, M. Grätzel, *J. Phys. Chem. B* **2005**, *109*, 17184–17191.
- [54] A. Kudo, Y. Miseki, *Chem. Soc. Rev.* **2009**, *38*, 253–278.
- [55] D. Bahnemann, *Sol. Energy* **2004**, *77*, 445–459.
- [56] A. Fujishima, K. Honda, *Nature* **1972**, *238*, 37–38.
- [57] S. Dutta, *Int. J. Hydrogen Energy* **1990**, *15*, 379–386.
- [58] A. J. Nozik, in *Photoelectrochem. Water Split. Mater. Process. Archit.*, **2013**, pp. 359–388.
- [59] M. F. Weber, M. J. Dignam, *J. Electrochem. Soc.* **1984**, *131*, 1258–1265.
- [60] J. R. Bolton, S. J. Strickler, J. S. Connolly, *Nature* **1985**, *316*, 495–500.
- [61] S. Hu, C. Xiang, S. Haussener, A. D. Berger, N. S. Lewis, *Energy Environ. Sci.* **2013**, *6*, 2984–2993.
- [62] F. F. Abdi, L. Han, A. H. M. Smets, M. Zeman, B. Dam, R. Van De Krol, *Nat. Commun.* **2013**, *4*, 1–7.
- [63] S. Y. Reece, J. A. Hamel, K. Sung, T. D. Jarvi, A. J. Esswein, H. Pijpers, J. J., D. G. Nocera, *Science (80-.)*. **2011**, *334*, 645–648.
- [64] Gurudayal, D. Sabba, M. H. Kumar, L. H. Wong, J. Barber, M. Grätzel, N. Mathews, *Nano Lett.* **2015**, *15*, 3833–3839.
- [65] Gurudayal, R. A. John, P. P. Boix, C. Yi, C. Shi, M. C. Scott, S. A. Veldhuis, A. M. Minor, S. M. Zakeeruddin, L. H. Wong, et al., *ChemSusChem* **2017**, *10*, 2449–2456.
- [66] J. Luo, Z. Li, S. Nishiwaki, M. Schreier, M. T. Mayer, P. Cendula, Y. H. Lee, K. Fu, A. Cao, M. K. Nazeeruddin, et al., *Adv. Energy Mater.* **2015**, *5*, 1501520.
- [67] E. L. Miller, R. E. Rocheleau, X. M. Deng, *Int. J. Hydrogen Energy* **2003**, *28*, 615–623.
- [68] Y. Yang, J. Wang, J. Zhao, B. A. Nail, X. Yuan, Y. Guo, F. E. Osterloh, *ACS Appl. Mater. Interfaces* **2015**, *7*, 5959–5964.
- [69] Y. S. Chen, J. S. Manser, P. V. Kamat, *J. Am. Chem. Soc.* **2015**, *137*, 974–981.
- [70] L. Peter, in *Photoelectrochem. Water Split. Mater. Process. Archit.*, **2013**, pp. 19–51.
- [71] S. Giménez, J. Bisquert, *Photoelectrochemical Solar Fuel Production*, **2016**.
- [72] A. J. Bard, A. B. Bocarsly, F. R. F. Fan, E. G. Walton, M. S. Wrighton, *J. Am. Chem. Soc.* **1980**, *102*, 3671–3677.
- [73] J. Bardeen, *Phys. Rev.* **1947**, *71*, 717–727.
- [74] W. W. Gärtner, *Phys. Rev.* **1959**, *116*, 84–87.
- [75] J. Reichman, *Appl. Phys. Lett.* **1980**, *36*, 574–577.
- [76] F. El Guibaly, K. Colbow, *J. Appl. Phys.* **1982**, *53*, 1737–1740.
- [77] M. Sharon, *An Introduction to the Physics and Electrochemistry of Semiconductors*, **2016**.
- [78] X. Xu, A. K. Azad, J. T. S. Irvine, *Catal. Today* **2013**, *199*, 22–26.

- [79] M. A. Henderson, *Surf. Sci. Rep.* **2011**, *66*, 185–297.
- [80] L. Brus, *J. Phys. Chem.* **1986**, *90*, 2555–2560.
- [81] C. Kormann, D. W. Bahnemann, M. R. Hoffmann, *J. Phys. Chem.* **1988**, *92*, 5196–5201.
- [82] A. Hellman, in *Photoelectrochem. Water Split. Mater. Process. Archit.*, **2013**, pp. 266–288.
- [83] M. D. Archer, A. J. Nozik, *Nanostructured and Photoelectrochemical Systems for Solar Photon Conversion*, Imperial College Press, London, **2008**.
- [84] R. Marschall, L. Wang, *Catal. Today* **2014**, *225*, 111–135.
- [85] M. Khairy, W. Zakaria, *Egypt. J. Pet.* **2014**, *23*, 419–426.
- [86] L. Brus, *Appl. Phys. A Solids Surfaces* **1991**, *53*, 465–474.
- [87] B. O'Regan, M. Grätzel, *Nature* **1991**, *353*, 737–740.
- [88] R. J. D. Tilley, *Defects in Solids*, **2008**.
- [89] K. Sivula, F. Le Formal, M. Grätzel, *ChemSusChem* **2011**, *4*, 432–449.
- [90] T. Weller, J. Sann, R. Marschall, *Adv. Energy Mater.* **2016**, *6*, 1600208.
- [91] S. D. Tilley, M. Cornuz, K. Sivula, M. Grätzel, *Angew. Chemie - Int. Ed.* **2010**, *49*, 6405–6408.
- [92] A. Biswas, I. S. Bayer, A. S. Biris, T. Wang, E. Dervishi, F. Faupel, *Adv. Colloid Interface Sci.* **2012**, *170*, 2–27.
- [93] X. Zhang, C. Sun, N. Fang, *J. Nanoparticle Res.* **2004**, *6*, 125–130.
- [94] W. Chern, K. Hsu, I. S. Chun, B. P. D. Azeredo, N. Ahmed, K. H. Kim, J. M. Zuo, N. Fang, P. Ferreira, X. Li, *Nano Lett.* **2010**, *10*, 1582–1588.
- [95] T. Prasad Yadav, R. Manohar Yadav, D. Pratap Singh, *Nanosci. Nanotechnol.* **2012**, *2*, 22–48.
- [96] A. A. Tseng, K. Chen, C. D. Chen, K. J. Ma, *IEEE Trans. Electron. Packag. Manuf.* **2003**, *26*, 141–149.
- [97] V. K. LaMer, R. H. Dinegar, *J. Am. Chem. Soc.* **1950**, *72*, 4847–4854.
- [98] C. Wagner, *Zeitschrift für Elektrochemie, Berichte der Bunsengesellschaft für Phys. Chemie* **1961**, *65*, 581–591.
- [99] M. W. Louie, A. T. Bell, *J. Am. Chem. Soc.* **2013**, *135*, 12329–12337.
- [100] N. C. Hildebrandt, J. Soldat, R. Marschall, *Small* **2015**, *11*, 2051–2057.
- [101] A. Bloesser, P. Voepel, M. O. Loeh, A. Beyer, K. Volz, R. Marschall, *J. Mater. Chem. A* **2018**, *6*, 1971–1978.
- [102] L. Schwertmann, M. Wark, R. Marschall, *RSC Adv.* **2013**, *3*, 18908.
- [103] S. Diodati, L. Pandolfo, A. Caneschi, S. Gialanella, S. Gross, *Nano Res.* **2014**, *7*, 1027–1042.
- [104] A. Antonello, G. Jakob, P. Dolcet, R. Momper, M. Kokkinopoulou, K. Landfester, R. Muñoz-Espí, S. Gross, *Chem. Mater.* **2017**, *29*, 985–997.
- [105] J. de Vicente, A. V. Delgado, R. C. Plaza, J. D. G. Durán, F. González-Caballero, *Langmuir* **2000**, *16*, 7954–7961.
- [106] C. Suchomski, B. Breitung, R. Witte, M. Knapp, S. Bauer, T. Baumbach, C. Reitz, T. Brezesinski, *Beilstein J. Nanotechnol.* **2016**, *7*, 1350–1360.
- [107] J. H. Kim, Y. J. Jang, J. H. Kim, J. Jang, S. H. Choi, J. S. Lee, *Nanoscale* **2015**, *7*, 19144–19151.
- [108] H. S. Han, S. Shin, D. H. Kim, I. J. Park, J. S. Kim, P.-S. Huang, J.-K. Lee, I. S. Cho, X. Zheng, *Energy Environ. Sci.* **2018**, *11*, 1299–1306.
- [109] G. S. Parkinson, *Surf. Sci. Rep.* **2016**, *71*, 272–365.
- [110] H. G. Yang, C. H. Sun, S. Z. Qiao, J. Zou, G. Liu, S. C. Smith, H. M. Cheng, G. Q. Lu, *Nature* **2008**, *453*, 638–641.
- [111] A. Ruplecker, F. Kleitz, E. L. Salabas, F. Schüth, *Chem. Mater.* **2007**, *19*, 485–496.
- [112] M. Weiss, S. Waitz, R. Ellinghaus, T. Weller, R. Marschall, *RSC Adv.* **2016**, *6*, 79037–79042.
- [113] H. Wang, H. Y. Jeong, M. Imura, L. Wang, L. Radhakrishnan, N. Fujita, T. Castle, O. Terasaki, Y. Yamauchi, *J. Am. Chem. Soc.* **2011**, *133*, 14526–14529.
- [114] L. Chuenchom, R. Kraehnert, B. M. Smarsly, S. Matter, *Soft Matter* **2012**, *8*, 10801–10812.
- [115] L. Borchardt, M. Oschatz, M. Lohe, V. Presser, Y. Gogotsi, S. Kaskel, *Carbon N. Y.* **2012**, *50*, 3987–3994.
- [116] A. Lehoux, L. Ramos, P. Beaunier, D. B. Uribe, P. Dieudonné, F. Audonnet, A. Etcheberry, M. José-Yacamán, H. Remita, *Adv. Funct. Mater.* **2012**, *22*, 4900–4908.
- [117] C. Reitz, J. Haetge, C. Suchomski, T. Brezesinski, *Chem. Mater.* **2013**, *25*, 4633–4642.

- [118] K. Schulz, R. Schmack, H. W. Klemm, A. Kabelitz, T. Schmidt, F. Emmerling, R. Kraehnert, *Chem. Mater.* **2017**, *29*, 1724–1734.
- [119] M. Su, C. He, V. K. Sharma, M. Abou Asi, D. Xia, X. Li, H. Deng, Y. Xiong, *J. Hazard. Mater.* **2012**, *211–212*, 95–103.
- [120] J. Brillet, M. Grätzel, K. Sivula, *Nano Lett.* **2010**, *10*, 4155–4160.
- [121] Y. Zhang, A. Weidenkaff, A. Reller, *Mater. Lett.* **2002**, *54*, 375–381.
- [122] B. Ahmmad, K. Leonard, M. Shariful Islam, J. Kurawaki, M. Muruganandham, T. Ohkubo, Y. Kuroda, *Adv. Powder Technol.* **2013**, *24*, 160–167.
- [123] R. Guillet-Nicolas, R. Ahmad, K. A. Cychosz, F. Kleitz, M. Thommes, *New J. Chem.* **2016**, *40*, 4351–4360.
- [124] M. Kurahashi, K. Kanamori, K. Takeda, H. Kaji, K. Nakanishi, *RSC Adv.* **2012**, *2*, 7166–7173.
- [125] P. Bahadur, G. Riess, *Tenside, Surfactants, Deterg.* **1991**, *28*, 173–179.
- [126] P. Alexandridis, T. Alan Hatton, *Colloids Surfaces A Physicochem. Eng. Asp.* **1995**, *96*, 1–46.
- [127] R. H. Goncalves, B. H. R. Lima, E. R. Leite, *J. Am. Chem. Soc.* **2011**, *133*, 6012–6019.
- [128] H. Zheng, S. Huang, J. Liu, F. Chen, X. Yang, W. Xu, X. Liu, *J. Dispers. Sci. Technol.* **2017**, *38*, 979–984.
- [129] N. Inoue, M. Kikuchi, T. Shima, M. Iwase, Y. Nishi, *Phys. Lett. A* **1991**, *157*, 299–300.
- [130] E. Yu, S. C. Kim, H. J. Lee, K. H. Oh, M. W. Moon, *Sci. Rep.* **2015**, *5*:9362, 1–6.
- [131] C. J. Brinker, Y. Lu, A. Sellinger, H. Fan, *Adv. Mater.* **1999**, *11*, 579–585.
- [132] L. Mahoney, R. T. Koodali, *Materials (Basel)*. **2014**, *7*, 2697–2746.
- [133] M. Kakihana, *J. Sol-Gel Sci. Technol.* **1996**, *6*, 7–55.
- [134] A. E. Danks, S. R. Hall, Z. Schnepf, *Mater. Horizons* **2016**, *3*, 91–112.
- [135] C. Jo, K. Kim, R. Ryoo, *Microporous Mesoporous Mater.* **2009**, *124*, 45–51.
- [136] Y. Wan, D. Zhao, *Chem. Rev.* **2007**, *107*, 2821–2860.
- [137] A. Taguchi, F. Schüth, *Microporous Mesoporous Mater.* **2005**, *77*, 1–45.
- [138] J. Brillet, M. Grätzel, K. Sivula, *Nano Lett.* **2010**, *10*, 4155–4160.
- [139] P. Yang, D. Zhao, D. I. Margolese, B. F. Chmelka, G. D. Stucky, *Chem. Mater.* **1999**, *11*, 2813–2826.
- [140] T. Brezesinski, M. Groenewolt, M. Antonietti, B. Smarsly, *Angew. Chemie - Int. Ed.* **2006**, *45*, 781–784.
- [141] L. Wang, W. Ding, Y. Sun, *Mater. Res. Bull.* **2016**, *83*, 230–249.
- [142] R. Marschall, I. Bannat, A. Feldhoff, L. Wang, G. Q. Lu, M. Wark, *Small* **2009**, *5*, 854–859.
- [143] A. S. Cherevan, S. Robbins, D. Dieterle, P. Gebhardt, U. Wiesner, D. Eder, *Nanoscale* **2016**, *8*, 16694–16701.
- [144] C. Zhu, D. Du, A. Eychmüller, Y. Lin, *Chem. Rev.* **2015**, *115*, 8896–8943.
- [145] M. Quintard, S. Whitaker, *Chem. Eng. Sci.* **1993**, *48*, 2537–2564.
- [146] T. Limnell, H. A. Santos, E. Mäkilä, T. Heikkilä, J. Salonen, D. Y. Murzin, N. Kumar, T. Laaksonen, L. Peltonen, J. Hirvonen, *J. Pharm. Sci.* **2011**, *100*, 3294–3306.
- [147] T. Zhao, Y. Ren, J. Yang, L. Wang, W. Jiang, A. A. Elzatahry, A. Alghamdi, Y. Deng, D. Zhao, W. Luo, *J. Mater. Chem. A* **2016**, *4*, 16446–16453.
- [148] X. Zhu, N. Kosinov, A. V. Kubarev, A. Bolshakov, B. Mezari, I. Valastyan, J. P. Hofmann, M. B. J. Roefsaers, E. Sarkadi-Pribóczy, E. J. M. Hensen, *ChemCatChem* **2017**, *9*, 3470–3477.
- [149] C. J. Jia, Y. Liu, M. Schwickardi, C. Weidenthaler, B. Spliethoff, W. Schmidt, F. Schüth, *Appl. Catal. A Gen.* **2010**, *386*, 94–100.
- [150] L. Liu, Z. Ji, W. Zou, X. Gu, Y. Deng, F. Gao, C. Tang, L. Dong, *ACS Catal.* **2013**, *3*, 2052–2061.
- [151] M. G. Ahmed, T. A. Kandiel, A. Y. Ahmed, I. Kretschmer, F. Rashwan, D. Bahnemann, *J. Phys. Chem. C* **2015**, *119*, 5864–5871.
- [152] L. Wang, D. Mitoraj, S. Turner, O. V. Khavryuchenko, T. Jacob, R. K. Hocking, R. Beranek, *ACS Catal.* **2017**, *7*, 4759–4767.
- [153] A. L. Linsebigler, G. Lu, J. T. Yates, *Chem. Rev.* **1995**, *95*, 735–758.
- [154] J. B. Joo, R. Dillon, I. Lee, Y. Yin, C. J. Bardeen, F. Zaera, *Proc. Natl. Acad. Sci.* **2014**, *111*, 7942–7947.
- [155] A. J. Bard, L. R. Faulkner, *Electrochemical Methods – Fundamental and Applications*, John Wiley

- & Sons, Inc., New York, **2001**.
- [156] K. Fujihara, T. Ohno, M. Matsumura, *J. Chem. Soc. - Faraday Trans.* **1998**, *94*, 3705–3709.
- [157] R. Dom, H. G. Kim, P. H. Borse, *ChemistrySelect* **2017**, *2*, 2556–2564.
- [158] A. A. Ismail, D. W. Bahnemann, *J. Phys. Chem. C* **2011**, *115*, 5784–5791.
- [159] K. C. Christoforidis, P. Fornasiero, *ChemCatChem* **2017**, *9*, 1523–1544.
- [160] X. Fu, J. Long, X. Wang, D. Y. C. Leung, Z. Ding, L. Wu, Z. Zhang, Z. Li, X. Fu, *Int. J. Hydrogen Energy* **2008**, *33*, 6484–6491.
- [161] E. Selli, G. L. Chiarello, E. Quartarone, P. Mustarelli, I. Rossetti, L. Forni, *Chem. Commun.* **2007**, 5022–5024.
- [162] R. Liu, J. Ren, D. Zhao, J. Ning, Z. Zhang, Y. Wang, Y. Zhong, C. Zheng, Y. Hu, *Inorg. Chem. Front.* **2017**, *4*, 2045–2054.
- [163] K. Hara, K. Sayama, H. Arakawa, *Appl. Catal. A Gen.* **1999**, *189*, 127–137.
- [164] A. Kudo, K. Ueda, H. Kato, I. Mikami, *Catal. Letters* **1998**, *53*, 229–230.
- [165] J. Schneider, D. W. Bahnemann, *J. Phys. Chem. Lett.* **2013**, *4*, 3479–3483.
- [166] M. Fischer, P. Warneck, *J. Phys. Chem.* **1996**, *100*, 15111–15117.
- [167] A. A. Ismail, D. W. Bahnemann, *Sol. Energy Mater. Sol. Cells* **2014**, *128*, 85–101.
- [168] A. Y. Ahmed, T. A. Kandiel, I. Ivanova, D. Bahnemann, *Appl. Surf. Sci.* **2014**, *319*, 44–49.
- [169] T. Rajh, A. E. Ostafin, O. I. Micic, D. M. Tiede, M. C. Thurnauer, *J. Phys. Chem.* **1996**, *100*, 4538–4545.
- [170] V. N. H. Nguyen, R. Amal, D. Beydoun, *Chem. Eng. Sci.* **2003**, *58*, 4429–4439.
- [171] M. C. Blount, J. A. Buchholz, J. L. Falconer, *J. Catal.* **2001**, *197*, 303–314.
- [172] S. Zinoviev, F. Müller-Langer, P. Das, N. Bertero, P. Fornasiero, M. Kaltschmitt, G. Centi, S. Miertus, *ChemSusChem* **2010**, *3*, 1106–1133.
- [173] B. Parkinson, J. Turner, in *Photoelectrochem. Water Split. Mater. Process. Archit.*, **2013**, pp. 1–18.
- [174] Z. Zhang, W. Wang, *Mater. Lett.* **2014**, *133*, 212–215.
- [175] A. M. Khan, A. Mehmood, M. Sayed, M. F. Nazar, B. Ismail, R. A. Khan, H. Ullah, H. M. Abdur Rehman, A. Y. Khan, A. R. Khan, *J. Mol. Liq.* **2017**, *236*, 395–403.
- [176] M. Kurian, D. S. Nair, A. M. Rahnamol, *React. Kinet. Mech. Catal.* **2013**, *111*, 591–604.
- [177] S. Bae, S. Kim, S. Lee, W. Choi, *Catal. Today* **2014**, *224*, 21–28.
- [178] International Organization for Standardization, *ISO 10678:2010*, **2010**.
- [179] D. Wöhrle, M. W. Tausch, W.-D. Stohrer, *Photochemie: Konzepte, Methoden, Experimente*, **1998**.
- [180] H. J. Kuhn, S. E. Braslavsky, R. Schmidt, *Pure Appl. Chem.* **2004**, *76*, 2105–2146.
- [181] X. Yao, R. Zhao, L. Chen, J. Du, C. Tao, F. Yang, L. Dong, *Appl. Catal. B Environ.* **2017**, *208*, 82–93.
- [182] W. Kim, T. Tachikawa, G. H. Moon, T. Majima, W. Choi, *Angew. Chemie - Int. Ed.* **2014**, *53*, 14036–14041.
- [183] T. Ohno, K. Tokieda, S. Higashida, M. Matsumura, *Appl. Catal. A Gen.* **2003**, *244*, 383–391.
- [184] K. Xiong, K. Wang, L. Chen, X. Wang, Q. Fan, J. Courtois, Y. Liu, X. Tuo, M. Yan, *Nano-Micro Lett.* **2018**, *10:17*, 1–11.
- [185] F. Wang, J. Jiu, L. Pei, K. Nakagawa, S. Isoda, M. Adachi, *Mater. Lett.* **2007**, *61*, 488–490.
- [186] Z. Wu, Y. Wang, L. Sun, Y. Mao, M. Wang, C. Lin, *J. Mater. Chem. A* **2014**, *2*, 8223.
- [187] X. Wang, S. Meng, X. Zhang, H. Wang, W. Zhong, Q. Du, *Chem. Phys. Lett.* **2007**, *444*, 292–296.
- [188] S. Livraghi, M. R. Chierotti, E. Giamello, G. Magnacca, M. C. Paganini, G. Cappelletti, C. L. Bianchi, *J. Phys. Chem. C* **2008**, *112*, 17244–17252.
- [189] Z. Liu, Z.-G. Zhao, M. Miyauchi, *J. Phys. Chem. C* **2009**, *113*, 17132–17137.
- [190] K. Villa, S. Murcia-López, T. Andreu, J. R. Morante, *Appl. Catal. B Environ.* **2014**, *163*, 150–155.
- [191] D. Dorfs, A. Eychmüller, in *Semicond. Nanocrystal Quantum Dots Synth. Assem. Spectrosc. Appl.*, **2008**.
- [192] P. Adel, A. Wolf, T. Kodanek, D. Dorfs, *Chem. Mater.* **2014**, *26*, 3121–3127.
- [193] S. Naskar, F. Lübke, S. Hamid, A. Freytag, A. Wolf, J. Koch, I. Ivanova, H. Pfnür, D. Dorfs, D. W. Bahnemann, et al., *Adv. Funct. Mater.* **2017**, *27*, 1604685.
- [194] S. Sánchez-Paradinas, D. Dorfs, S. Friebe, A. Freytag, A. Wolf, N. C. Bigall, *Adv. Mater.* **2015**, *27*,

- 6152–6156.
- [195] E. S. Kim, H. J. Kang, G. Magesh, J. Y. Kim, J. W. Jang, J. S. Lee, *ACS Appl. Mater. Interfaces* **2014**, *6*, 17762–17769.
- [196] X. She, Z. Zhang, M. Baek, K. Yong, *Appl. Surf. Sci.* **2018**, *429*, 29–36.
- [197] N. Srinivasan, E. Sakai, M. Miyauchi, *ACS Catal.* **2016**, *6*, 2197–2200.
- [198] Y. Pihosh, I. Turkevych, K. Mawatari, J. Uemura, Y. Kazoe, S. Kosar, K. Makita, T. Sugaya, T. Matsui, D. Fujita, et al., *Sci. Rep.* **2015**, *5*:11141, 1–10.
- [199] M. Rohloff, B. Anke, S. Zhang, U. Gernert, C. Scheu, M. Lerch, A. Fischer, *Sustain. Energy Fuels* **2017**, 1830–1846.
- [200] S. Wang, P. Chen, J. H. Yun, Y. Hu, L. Wang, *Angew. Chemie - Int. Ed.* **2017**, *4072*, 8500–8504.
- [201] M. Zhong, T. Hisatomi, Y. Kuang, J. Zhao, M. Liu, A. Iwase, Q. Jia, H. Nishiyama, T. Minegishi, M. Nakabayashi, et al., *J. Am. Chem. Soc.* **2015**, *137*, 5053–5060.
- [202] D. Eisenberg, H. S. Ahn, A. J. Bard, *J. Am. Chem. Soc.* **2014**, *136*, 14011–14014.
- [203] C. Zachäus, F. F. Abdi, L. M. Peter, R. van de Krol, *Chem. Sci.* **2017**, *8*, 3712–3719.
- [204] K. Sivula, R. van de Krol, *Nat. Rev. Mater.* **2016**, *1*, 15010.
- [205] R. Sahoo, S. Santra, C. Ray, A. Pal, Y. Negishi, S. K. Ray, T. Pal, *New J. Chem.* **2016**, *40*, 1861–1871.
- [206] H. Qiao, Y. Fei, K. Chen, R. Cui, Q. Wei, *Ionics (Kiel)*. **2016**, *22*, 967–974.
- [207] C. Cai, J. Liu, Z. Zhang, Y. Zheng, H. Zhang, *Sep. Purif. Technol.* **2016**, *165*, 42–52.
- [208] S. Zhu, B. Dong, Y. Yu, L. Bu, J. Deng, S. Zhou, *Chem. Eng. J.* **2017**, *328*, 527–535.
- [209] Z. Cao, M. Qin, Y. Gu, B. Jia, P. Chen, X. Qu, *Mater. Res. Bull.* **2016**, *77*, 41–47.
- [210] F. J. Morin, *Phys. Rev.* **1951**, *83*, 1005–1010.
- [211] A. J. Bosman, H. J. van Daal, *Adv. Phys.* **1970**, *19*, 1–117.
- [212] N. J. Cherepy, D. B. Liston, J. A. Lovejoy, H. Deng, J. Z. Zhang, *J. Phys. Chem. B* **1998**, *102*, 770–776.
- [213] M. Barroso, S. R. Pendlebury, A. J. Cowan, J. R. Durrant, *Chem. Sci.* **2013**, *4*, 2724–2734.
- [214] H. Han, F. Riboni, F. Karlicky, S. Kment, A. Goswami, P. Sudhagar, J. Yoo, L. Wang, O. Tomanec, M. Petr, et al., *Nanoscale* **2017**, *9*, 134–142.
- [215] Z. Wang, P. Lazor, S. K. Saxena, H. S. C. O'Neill, *Mater. Res. Bull.* **2002**, *37*, 1589–1602.
- [216] Z. Wang, D. Schiferl, Y. Zhao, H. S. C. O'Neill, *J. Phys. Chem. Solids* **2003**, *64*, 2517–2523.
- [217] A. Milutinović, Z. Lazarević, Č. Jovalekić, I. Kuryliszyn-Kudelska, M. Romčević, S. Kostić, N. Romčević, *Mater. Res. Bull.* **2013**, *48*, 4759–4768.
- [218] F. S. Li, L. Wang, J. B. Wang, Q. G. Zhou, X. Z. Zhou, H. P. Kunkel, G. Williams, *J. Magn. Magn. Mater.* **2004**, *268*, 332–339.
- [219] R. Sai, S. D. Kulkarni, S. S. M. Bhat, N. G. Sundaram, N. Bhat, S. A. Shivashankar, *RSC Adv.* **2015**, *5*, 10267–10274.
- [220] S. Zhai, Y. Yin, S. R. Shieh, S. Shan, W. Xue, C. P. Wang, K. Yang, Y. Higo, *Phys. Chem. Miner.* **2016**, *43*, 307–314.
- [221] L. Smart, E. Moore, *Solid State Chemistry*, **1995**.
- [222] C. Kittel, *Phys. Rev.* **1946**, *70*, 965–971.
- [223] B. Ren, Y. Huang, C. Han, M. N. Nadagouda, D. D. Dionysiou, in *Ferrites Ferrates Chem. Appl. Sustain. Energy Environ. Remediat.*, American Chemical Society, **2016**, pp. 79–112.
- [224] A. K. Gupta, M. Gupta, *Biomaterials* **2005**, *26*, 3995–4021.
- [225] S. M. Hoque, M. S. Hossain, S. Choudhury, S. Akhter, F. Hyder, *Mater. Lett.* **2016**, *162*, 60–63.
- [226] A. Goldman, *Modern Ferrite Technology*, Springer, Pittsburgh, **2006**.
- [227] Q. Song, Z. J. Zhang, *J. Am. Chem. Soc.* **2004**, *126*, 6164–6168.
- [228] S. V. Jadhav, K. M. Jinka, H. C. Bajaj, *Catal. Today* **2012**, *198*, 98–105.
- [229] K. Mukherjee, S. B. Majumder, *J. Appl. Phys.* **2009**, *106*, 0649121 1–10.
- [230] J. Liu, J. Xiao, X. Zeng, P. Dong, J. Zhao, Y. Zhang, X. Li, *J. Alloys Compd.* **2017**, *699*, 401–407.
- [231] Y. Pan, Y. Zhang, X. Wei, C. Yuan, J. Yin, D. Cao, G. Wang, *Electrochim. Acta* **2013**, *109*, 89–94.
- [232] J. H. Kim, J. H. Kim, J. W. Jang, J. Y. Kim, S. H. Choi, G. Magesh, J. Lee, J. S. Lee, *Adv. Energy Mater.* **2015**, *5*, 1–9.
- [233] C. Nan, G. Fan, J. Fan, F. Li, *Mater. Lett.* **2013**, *106*, 5–7.

- [234] Y. Lu, Y. Feng, F. Wang, X. Zou, Z. F. Chen, P. Chen, H. Liu, Y. Su, Q. Zhang, G. Liu, *J. Photochem. Photobiol. A Chem.* **2018**, *353*, 10–18.
- [235] J. Qiu, C. Wang, M. Gu, *Mater. Sci. Eng. B* **2004**, *112*, 1–4.
- [236] M. Singh, H. S. Dosanjh, H. Singh, *J. Water Process Eng.* **2016**, *11*, 152–161.
- [237] E. Skliri, J. Miao, J. Xie, G. Liu, T. Salim, B. Liu, Q. Zhang, G. S. Armatas, *Appl. Catal. B Environ.* **2018**, *227*, 330–339.
- [238] Y. Tingting, X. Jiawei, T. Hao, X. Anjian, L. Shikuo, Y. Wensheng, S. Yuhua, *J. Mater. Chem. A* **2017**, *6*, 1210–1218.
- [239] E. S. Kim, N. Nishimura, G. Magesh, J. Y. Kim, J. W. Jang, H. Jun, J. Kubota, K. Domen, J. S. Lee, *J. Am. Chem. Soc.* **2013**, *135*, 5375–5383.
- [240] A. A. Tahir, K. G. U. Wijayantha, *J. Photochem. Photobiol. A Chem.* **2010**, *216*, 119–125.
- [241] Y. Matsumoto, M. Omae, K. Sugiyama, E. Sato, *J. Phys. Chem.* **1987**, *91*, 577–581.
- [242] J. Cao, T. Kako, P. Li, S. Ouyang, J. Ye, *Electrochem. commun.* **2011**, *13*, 275–278.
- [243] N. ul Ain, W. Shaheen, B. Bashir, N. M. Abdelsalam, M. F. Warsi, M. A. Khan, M. Shahid, *Ceram. Int.* **2016**, *42*, 12401–12408.
- [244] W. Fan, M. Li, H. Bai, D. Xu, C. Chen, C. Li, Y. Ge, W. Shi, *Langmuir* **2016**, *32*, 1629–1636.
- [245] J. Jiang, W. Fan, X. Zhang, H. Bai, Y. Liu, S. Huang, B. Mao, S. Yuan, C. Liu, W. Shi, *New J. Chem.* **2016**, *40*, 538–544.
- [246] N. Guijarro, P. Borno, M. S. Prévot, X. Yu, X. Zhu, M. Johnson, X. A. Jeanbourquin, F. Le Formal, K. Sivula, *Sustain. Energy Fuels* **2018**, *2*, 103–117.
- [247] W.-H. Xu, L. Wang, J. Wang, G.-P. Sheng, J.-H. Liu, H.-Q. Yu, X.-J. Huang, *CrystEngComm* **2013**, *15*, 7895.
- [248] M. Bagheri, M. A. Bahrevar, A. Beitollahi, *Ceram. Int.* **2015**, *41*, 11618–11624.
- [249] A. Pradeep, G. Chandrasekaran, *Mater. Lett.* **2006**, *60*, 371–374.
- [250] S. I. Hussein, A. S. Elkady, M. M. Rashad, A. G. Mostafa, R. M. Megahid, *J. Magn. Magn. Mater.* **2015**, *379*, 9–15.
- [251] D. Chen, Y. Zhang, C. Tu, *Mater. Lett.* **2012**, *82*, 10–12.
- [252] V. Šepelák, I. Bergmann, D. Menzel, A. Feldhoff, P. Heitjans, F. J. Litterst, K. D. Becker, *J. Magn. Magn. Mater.* **2007**, *316*, 764–767.
- [253] L. J. Berchmans, M. Myndyk, K. L. Da Silva, A. Feldhoff, J. Šubrt, P. Heitjans, K. D. Becker, V. Šepelák, *J. Alloys Compd.* **2010**, *500*, 68–73.
- [254] S. Verma, P. A. Joy, Y. B. Kholam, H. S. Potdar, S. B. Deshpande, *Mater. Lett.* **2004**, *58*, 1092–1095.
- [255] T. Sasaki, S. Ohara, T. Naka, J. Vejpravova, V. Sechovsky, M. Umetsu, S. Takami, B. Jeyadevan, T. Adschiri, *J. Supercrit. Fluids* **2010**, *53*, 92–94.
- [256] C. Karunakaran, S. SakthiRaadha, P. Gomathisankar, P. Vinayagamoorthy, *RSC Adv.* **2013**, *3*, 16728–16738.
- [257] S. Ilhan, S. G. Izotova, A. A. Komlev, *Ceram. Int.* **2015**, *41*, 577–585.
- [258] S. Munjal, N. Khare, in *AIP Conf. Proc.*, **2016**.
- [259] R. Dom, R. Subasri, N. Y. Hebalkar, A. S. Chary, P. H. Borse, *RSC Adv.* **2012**, *2*, 12782–12791.
- [260] Y. Xu, J. Sherwood, Y. Qin, R. A. Holler, Y. Bao, *Nanoscale* **2015**, *7*, 12641–12649.
- [261] E. V. Groman, J. C. Bouchard, C. P. Reinhardt, D. E. Vaccaro, *Bioconjug. Chem.* **2007**, *18*, 1763–1771.
- [262] D. Arndt, V. Zielasek, W. Dreher, M. Bäumer, *J. Colloid Interface Sci.* **2014**, *417*, 188–198.
- [263] K. Ashwini, K. S. Anantha Raju, P. Adinarayan Reddy, S. C. Sharma, H. Nagabhushana, K. Raghava Reddy, **2015**, *1*, 1–6.
- [264] K. Raj, B. Moskowitz, R. Casciari, *J. Magn. Magn. Mater.* **1995**, *149*, 174–180.
- [265] S. Odenbach, *Colloidal Magnetic Fluids: Basics, Development and Application of Ferrofluids*, Springer, Berlin Heidelberg, **2009**.
- [266] D. Carta, M. F. Casula, P. Floris, A. Falqui, G. Mountjoy, A. Boni, C. Sangregorio, A. Corrias, *Phys. Chem. Chem. Phys.* **2010**, *12*, 5074–5083.
- [267] D. Maiti, A. Saha, P. S. Devi, *Phys. Chem. Chem. Phys.* **2016**, *18*, 1439–1450.
- [268] H. Zeng, P. M. Rice, S. X. Wang, S. Sun, *J. Am. Chem. Soc.* **2004**, *126*, 11458–11459.

- [269] L. I. Cabrera, Á. Somoza, J. F. Marco, C. J. Serna, M. Puerto Morales, *J. Nanoparticle Res.* **2012**, *14*:873, 1–14.
- [270] M. Lattuada, T. A. Hatton, *Langmuir* **2007**, *23*, 2158–2168.
- [271] S. Munjal, N. Khare, C. Nehate, V. Koul, *J. Magn. Magn. Mater.* **2016**, *404*, 166–169.
- [272] H. Zhao, R. Liu, Q. Zhang, Q. Wang, *Mater. Res. Bull.* **2016**, *75*, 172–177.
- [273] J. Chandradass, A. H. Jadhav, H. Kim, *Appl. Surf. Sci.* **2012**, *258*, 3315–3320.
- [274] S. M. Hoque, M. A. Hakim, A. Mamun, S. Akhter, M. T. Hasan, D. P. Paul, K. Chattopadhyay, *Mater. Sci. Appl.* **2011**, *02*, 1564–1571.
- [275] M. Goodarz Naseri, M. H. M. Ara, E. B. Saion, A. H. Shaari, *J. Magn. Magn. Mater.* **2014**, *350*, 141–147.
- [276] J. M. Kremsner, A. Stadler, *A Chemist's Guide to Microwave Synthesis*, Anton Paar GmbH, Graz, **2013**.
- [277] R. M. Patil, P. B. Shete, N. D. Thorat, S. V. Otari, K. C. Barick, A. Prasad, R. S. Ningthoujam, B. M. Tiwale, S. H. Pawar, *RSC Adv.* **2014**, *4*, 4515–4522.
- [278] M. Ogawa, N. Shimura, A. Ayrál, *Chem. Mater.* **2006**, *18*, 1715–1718.
- [279] “Chrystallography Open Database,” can be found under (www.crystallography.net/cod/index.php), **2018**.
- [280] A. L. Patterson, *Phys. Rev.* **1939**, *56*, 978.
- [281] J. Rodríguez-Carvajal, *An Introduction to the Program FULLPROF: Refinement of Crystal and Magnetic Structures from Powder and Single Crystal Data*, **2001**.
- [282] L. B. McCusker, R. B. Von Dreele, D. E. Cox, D. Louër, P. Scardi, *J. Appl. Crystallogr.* **1999**, *32*, 36–50.
- [283] S. R. Hall, F. H. Allen, I. D. Brown, *Acta Crystallogr. Sect. A* **1991**, *47*, 655–685.
- [284] E. Solano, C. Frontera, T. Puig, X. Obradors, S. Ricart, J. Ros, *J. Appl. Crystallogr.* **2014**, *47*, 414–420.
- [285] A. Nakatsuka, H. Ueno, N. Nakayama, T. Mizota, H. Maekawa, *Phys. Chem. Miner.* **2004**, *31*, 278–287.
- [286] D. J. Miller, M. C. Biesinger, N. S. McIntyre, *Surf. Interface Anal.* **2002**, *33*, 299–305.
- [287] “Rossendorf Beamline (ROBL),” can be found under www.hzdr.de/db/Cms?pNid=247, **2018**.
- [288] S. Calvin, *XAFS for Everyone*, CRC Press, Boca Raton, **2013**.
- [289] V. A. Solé, E. Papillon, M. Cotte, P. Walter, J. Susini, *Spectrochim. Acta - Part B At. Spectrosc.* **2007**, *62*, 63–68.
- [290] T. E. Westre, P. Kennepohl, J. G. DeWitt, B. Hedman, K. O. Hodgson, E. I. Solomon, *J. Am. Chem. Soc.* **1997**, *119*, 6297–6314.
- [291] A. H. De Vries, L. Hozoi, R. Broer, *Int. J. Quantum Chem.* **2002**, *91*, 57–61.
- [292] G. Peng, F. M. F. DeGroot, K. Hämäläinen, J. A. Moore, X. Wang, M. M. Grush, J. B. Hastings, D. P. Siddons, W. H. Armstrong, O. C. Mullins, et al., *J. Am. Chem. Soc.* **1994**, *116*, 2914–2920.
- [293] F. de Groot, *17th Int. Conf. x-ray Inn. Process.* **1997**, *389*, 497–520.
- [294] G. A. Waychunas, *Am. Mineral.* **1987**, *72*, 89–101.
- [295] G. Calas, G. E. Brown Jr., G. A. Waychunas, J. Petiau, *Phys. Chem. Miner.* **1987**, *15*, 19–29.
- [296] U. Bergmann, P. Glatzel, *Photosynth. Res.* **2009**, *102*, 255–266.
- [297] J. A. van Bokhoven, C. Lamberti, *Emission Spectroscopy X-Ray Absorption and X-Ray Theory and Applications*, Wiley, West Sussex, United Kingdom, **2016**.
- [298] F. M. F. De Groot, P. Glatzel, U. Bergmann, P. A. Van Aken, R. A. Barrea, S. Klemme, M. Hävecker, A. Knop-Gericke, W. M. Heijboer, B. M. Weckhuysen, *J. Phys. Chem. B* **2005**, *109*, 20751–20762.
- [299] P. Glatzel, U. Bergmann, *Coord. Chem. Rev.* **2005**, *249*, 65–95.
- [300] F. De Groot, *Chem. Rev.* **2001**, *101*, 1779–1808.
- [301] S. Bare, *APS XAFS Sch.* **2008**.
- [302] M. L. Baker, M. W. Mara, J. J. Yan, K. O. Hodgson, B. Hedman, E. I. Solomon, *Coord. Chem. Rev.* **2017**, *345*, 182–208.
- [303] W. A. Caliebe, C. C. Kao, J. B. Hastings, M. Taguchi, T. Uozumi, F. M. F. de Groot, *Phys. Rev. B* **1998**, *58*, 13452–13458.
- [304] B. Ravel, M. Newville, *J. Synchrotron Radiat.* **2005**, *12*, 537–541.

- [305] U. Bergmann, C. R. Horne, T. J. Collins, J. M. Workman, S. P. Cramer, *Chem. Phys. Lett.* **1999**, *302*, 119–124.
- [306] S. A. Pizarro, P. Glatzel, H. Visser, J. H. Robblee, G. Christou, U. Bergmann, V. K. Yachandra, *Phys. Chem. Chem. Phys.* **2004**, *6*, 4864–4870.
- [307] H. Visser, E. Anxolabéhère-Mallart, U. Bergmann, P. Glatzel, J. H. Robblee, S. P. Cramer, J. J. Girerd, K. Sauer, M. P. Klein, V. K. Yachandra, *J. Am. Chem. Soc.* **2001**, *123*, 7031–7039.
- [308] E. Gallo, P. Glatzel, *Adv. Mater.* **2014**, *26*, 7730–7746.
- [309] G. Smolentsev, A. V. Soldatov, J. Messinger, K. Merz, T. Weyhermüller, U. Bergmann, Y. Pushkar, J. Yano, V. K. Yachandra, P. Glatzel, *J. Am. Chem. Soc.* **2009**, *131*, 13161–13167.
- [310] F. M. F. de Groot, *Top. Catal.* **2000**, *10*, 179–186.
- [311] P. E. Best, *J. Chem. Phys.* **1966**, *44*, 3248–3253.
- [312] M. Nowakowski, J. Czapla-Masztafiak, J. Szlachetko, W. M. Kwiatek, *Chem. Phys.* **2017**, *493*, 49–55.
- [313] M. Sikora, A. Juhin, T. C. Weng, P. Saintavit, C. Detlefs, F. De Groot, P. Glatzel, *Phys. Rev. Lett.* **2010**, *105*, 037202 1-4.
- [314] M. Hesse, H. Meier, B. Zeeh, *Spektroskopische Methoden in Der Organischen Chemie*, Georg Thieme Verlag KG, Stuttgart, **2012**.
- [315] C. V. Raman, *Nature* **1928**, *121*, 619.
- [316] E. Smith, G. Dent, *Modern Raman Spectroscopy: A Practical Approach*, John Wiley & Sons, Inc., Chichester, **2005**.
- [317] D. L. A. de Faria, S. Venâncio Silva, M. T. de Oliveira, *J. Raman Spectrosc.* **1997**, *28*, 873–878.
- [318] J. Tauc, R. Grigorovici, A. Vancu, *Phys. Status Solidi* **1966**, *15*, 627–637.
- [319] W. Rasband, “The ImageJ User Guide,” can be found under <https://imagej.net/docs/guide>, **2010**.
- [320] J. Rouquerol, D. Avnir, C. W. Fairbridge, D. H. Everett, J. M. Haynes, N. Pernicone, J. D. F. Ramsay, K. S. W. Sing, K. K. Unger, *Pure Appl. Chem.* **1994**, *66*, 1739–1758.
- [321] M. Thommes, K. Kaneko, A. V. Neimark, J. P. Olivier, F. Rodriguez-Reinoso, J. Rouquerol, K. S. W. Sing, *Pure Appl. Chem.* **2015**, *87*, 1051–1069.
- [322] S. Brunauer, P. H. Emmett, E. Teller, *J. Am. Chem. Soc.* **1938**, *60*, 309–319.
- [323] P. A. Webb; C. Orr, *Analytical Methods in Fine Particle Technology*, Micromeritics Instrument Corp., Norcross, **1997**.
- [324] F. Rouquerol, J. Rouquerol, K. S. W. Sing, P. Llewellyn, G. Maurin, *Adsorption by Powders and Porous Solids: Principles, Methodology and Applications*, **2014**.
- [325] M. Thommes, K. A. Cychoz, *Adsorption* **2014**, *20*, 233–250.
- [326] W. Ostwald, *Die Welt Der Vernachlässigten Dimensionen: Eine Einführung in Die Kolloidchemie, Mit Besonderer Berücksichtigung Ihrer Anwendungen.*, Theodor Steinkopff, Dresden Leipzig, **1920**.
- [327] H. Staudinger, *Nobel Lect.* **1953**.
- [328] H. Sahabi, M. Kind, *Polymers (Basel)*. **2011**, *3*, 2156–2171.
- [329] B. Derjaguin, L. Landau, *Prog. Surf. Sci.* **1993**, *43*, 30–59.
- [330] E. J. W. Verwey, J. T. G. Overbeek, *J. Phys. Colloid Chem.* **1948**, *51*, 631–636.
- [331] R. Everaers, M. R. Ejtehadi, *Phys. Rev. E - Stat. Physics, Plasmas, Fluids, Relat. Interdiscip. Top.* **2003**, *67*, 8.
- [332] Malvern Instruments, *Zeta Potential: An Introduction in 30 Minutes*, Worchester, **2011**.
- [333] O. Stern, *Zeitschrift für Elektrochemie Angew. Phys. Chemie* **1924**, *30*, 508–516.
- [334] J. T. G. Overbeek, *Pure Appl. Chem.* **1980**, *52*, 1151–1161.
- [335] S. S. Batsanov, E. D. Ruchkin, I. A. Poroshina, *Refractive Indices of Solids*, Springer, Pittsburgh, **2016**.
- [336] Zahner-elektrik GmbH & Co KG, “PEC Cells,” can be found under <http://zahner.de/products/photoelectrochemistry/pec-cells.html>, **2018**.
- [337] Ž. Cvejić, S. Rakić, S. Jankov, S. Skuban, A. Kapor, *J. Alloys Compd.* **2009**, *480*, 241–245.
- [338] V. Bhingardive, T. Woldu, S. Biswas, G. P. Kar, S. Thomas, N. Kalarikkal, S. Bose, *ChemistrySelect* **2016**, *1*, 4747–4752.

- [339] A. Becker, *Mikrowellenuntersützte Synthese Und Charakterisierung von Magnesiumferrit-Nanopartikeln*, **2016**.
- [340] S. Thota, S. C. Kashyap, S. K. Sharma, V. R. Reddy, *J. Phys. Chem. Solids* **2016**, *91*, 136–144.
- [341] B. Antic, N. Jovic, M. B. Pavlovic, A. Kremenovic, D. Manojlovic, M. Vucinic-Vasic, A. S. Nikolic, *J. Appl. Phys.* **2010**, *107*, 1–8.
- [342] P. H. Borse, J. . Jang, S. J. Hong, J. . Lee, J. H. Jung, T. E. Hong, C. W. Ahn, E. D. Jeong, K. S. Hong, J. H. Yoon, et al., *J. Korean Phys. Soc.* **2009**, *55*, 1472.
- [343] N. Kislov, S. S. Srinivasan, Y. Emirov, E. K. Stefanakos, *Mater. Sci. Eng. B Solid-State Mater. Adv. Technol.* **2008**, *153*, 70–77.
- [344] U. a. Agú, M. I. Oliva, S. G. Marchetti, A. C. Heredia, S. G. Casuscelli, M. E. Crivello, *J. Magn. Magn. Mater.* **2014**, *369*, 249–259.
- [345] P. A. Vinosha, L. A. Mely, J. E. Jeronsia, S. Krishnan, S. J. Das, *Optik (Stuttg)*. **2017**, *134*, 99–108.
- [346] S. Il Choi, *Adv. Powder Technol.* **2016**, *27*, 1862–1867.
- [347] M. Devaraj, R. Saravanan, R. Deivasigamani, V. K. Gupta, F. Gracia, S. Jayadevan, *J. Mol. Liq.* **2016**, *221*, 930–941.
- [348] P. Saravanan, G. Venkata Ramana, K. Srinivasa Rao, B. Sreedhar, V. T. P. Vinod, V. Chandrasekaran, *J. Magn. Magn. Mater.* **2011**, *323*, 2083–2089.
- [349] R. M. Patil, P. B. Shete, N. D. Thorat, S. V. Otari, K. C. Barick, A. Prasad, R. S. Ningthoujam, B. M. Tiwale, S. H. Pawar, *RSC Adv.* **2014**, *4*, 4515–4522.
- [350] A. Becker, *Photokatalytische Studien an Ferritischen Nanopartikel-Dispersionen*, **2016**.
- [351] S. M. Tsimbler, L. L. Shevchenko, V. V. Grigor'eva, *J. Appl. Spectrosc.* **1969**, *11*, 1096–1101.
- [352] A. Freytag, S. Sánchez-Paradinas, S. Naskar, N. Wendt, M. Colombo, G. Pugliese, J. Poppe, C. Demirci, I. Kretschmer, D. W. Bahnemann, et al., *Angew. Chemie - Int. Ed.* **2016**, *55*, 1200–1203.
- [353] A. Freytag, M. Colombo, N. C. Bigall, *Zeitschrift für Phys. Chemie* **2017**, *231*, 1–13.
- [354] J. A. Gomes, G. M. Azevedo, J. Depeyrot, J. Mestnik-Filho, G. J. Da Silva, F. A. Tourinho, R. Perzynski, *J. Magn. Magn. Mater.* **2011**, *323*, 1203–1206.
- [355] M. Sikora, A. Juhin, G. Simon, M. Zajc, K. Biernacka, C. Kapusta, L. Morellon, M. R. Ibarra, P. Glatzel, *J. Appl. Phys.* **2012**, *111*, 2010–2013.
- [356] C. M. B. Henderson, J. M. Charnock, D. A. Plant, *J. Phys. Condens. Matter* **2007**, *19*, 076214 1–25.
- [357] G. Redden, J. Bargar, R. Bencheikh-Latmani, *J. Colloid Interface Sci.* **2001**, *244*, 211–219.
- [358] L. Shao, Z. Ren, G. Zhang, L. Chen, *Mater. Chem. Phys.* **2012**, *135*, 16–24.
- [359] P. Atkins, J. de Paula, *Physical Chemistry*, Oxford University Press, Oxford, **2006**.
- [360] S. K. Srinivasan, S. Ganguly, *Catal. Letters* **1991**, *10*, 279–287.
- [361] S. Wang, P. Chen, J.-H. Yun, Y. Hu, L. Wang, *Angew. Chemie* **2017**, *129*, 8620–8624.
- [362] G. Wang, Y. Yang, Y. Ling, H. Wang, X. Lu, Y.-C. Pu, J. Z. Zhang, Y. Tong, Y. Li, *J. Mater. Chem. A* **2016**, *4*, 2849–2855.
- [363] E. Paparazzo, *J. Phys. D. Appl. Phys.* **1987**, *20*, 1091–1094.
- [364] E. Puppini, I. Lindau, I. Abbati, *Solid State Commun.* **1991**, *77*, 983–986.
- [365] Z. Wang, P. Lazor, S. K. Saxena, H. St, C. O. Neill, *Mater. Res. Bull.* **2002**, *37*, 1589–1602.
- [366] S. Baranovski, O. Rubel, in *Charg. Transp. Disord. Solids with Appl. Electron.* (Ed.: S. Baranovski), John Wiley & Sons, Inc., Chichester, **2006**.
- [367] M. Santamaria, F. Di Quarto, S. Zanna, P. Marcus, *Electrochim. Acta* **2007**, *53*, 1314–1324.
- [368] M. C. Biesinger, B. P. Payne, A. P. Grosvenor, L. W. M. Lau, A. R. Gerson, R. S. C. Smart, *Appl. Surf. Sci.* **2011**, *257*, 2717–2730.
- [369] D. Tie, F. Feyerabend, N. Hort, R. Willumeit, D. Hoeche, *Adv. Eng. Mater.* **2010**, *12*, 699–704.
- [370] K. Kirchberg, R. Marschall, *Sustain. Energy Fuels* **2019**, DOI 10.1039/C8SE00627J.
- [371] K. T. Jacob, N. Dasgupta, Y. Waseda, *Zeitschrift für Met.* **1999**, *90*, 486–490.
- [372] Q. Ma, H. He, *Atmos. Environ.* **2012**, *50*, 97–102.
- [373] N. Kolev, M. N. Iliev, V. N. Popov, M. Gospodinov, *Solid State Commun.* **2003**, *128*, 153–155.
- [374] A. Piovano, M. Ceretti, M. R. Johnson, G. Agostini, W. Paulus, C. Lamberti, *J. Phys. Condens. Matter* **2015**, *27*, 225403 1-11.
- [375] H. Dotan, K. Sivula, M. Grätzel, A. Rothschild, S. C. Warren, *Energy Environ. Sci.* **2011**, *4*, 958–

- 964.
- [376] D. J. Miller, M. C. Biesinger, N. S. McIntyre, *Surf. Interface Anal.* **2002**, *33*, 299–305.
- [377] D. R. Baer, D. L. Blanchard, M. H. Engelhard, J. M. Zachara, *Surf. Interface Anal.* **1991**, *17*, 25–30.
- [378] B. Demri, D. Muster, *J. Mater. Process. Technol.* **1995**, *55*, 311–314.
- [379] P. R. Couchman, W. A. Jesser, D. Kuhlmann-Wilsdorf, J. P. Hirth, *Surf. Sci.* **1972**, *33*, 429–436.
- [380] W. Liu, H. Liu, L. Dang, H. Zhang, X. Wu, B. Yang, Z. Li, X. Zhang, L. Lei, S. Jin, *Adv. Funct. Mater.* **2017**, *27*, 1603904.
- [381] R. Abe, M. Higashi, K. Domen, *J. Am. Chem. Soc.* **2010**, *132*, 11828–11829.
- [382] F. Le Formal, N. Tétreault, M. Cornuz, T. Moehl, M. Grätzel, K. Sivula, *Chem. Sci.* **2011**, *2*, 737–743.
- [383] L. Wang, N. T. Nguyen, P. Schmuki, *ChemSusChem* **2016**, *9*, 2048–2053.
- [384] W. M. Carvalho, F. L. Souza, *ChemPhysChem* **2016**, *17*, 2710–2717.
- [385] K. Sekizawa, T. Nonaka, T. Arai, T. Morikawa, *ACS Appl Mater Interfaces* **2014**, *6*, 10969–10973.
- [386] Y. Matsumoto, K. Sugiyama, E. I. Sato, *J. Solid State Chem.* **1988**, *74*, 117–125.
- [387] K. J. McDonald, K.-S. Choi, *Chem. Mater.* **2011**, *23*, 4863–4869.
- [388] X. Wang, K. Q. Peng, Y. Hu, F. Q. Zhang, B. Hu, L. Li, M. Wang, X. M. Meng, S. T. Lee, *Nano Lett.* **2014**, *14*, 18–23.
- [389] A. Becker, *Stabilisierung Und Keimunterstütztes Wachstum von Magnesiumferrit-Nanopartikeln*, **2016**.

9 Appendix

Table 9.1: Parameters obtained from Rietveld refinement of XRD data from all discussed samples.

Matrix	Sample	χ^2_{global}	$a/\text{\AA}$	L_a/nm	$\eta/\%$
Thin films	ZFO PLU 500 °C 0 min	1.23	8.43536	10.78 ± 0.51	58.5
	ZFO PLU 500 °C 10 min	1.42	8.43288	10.42 ± 0.39	43.6
	ZFO PLU 500 °C 12 h	1.25	8.4421	13.00 ± 1.10	46.4
	ZFO PLU 550 °C 0 min	1.32	8.43394	9.08 ± 0.24	51.0
	ZFO PLU 550 °C 10 min	1.28	8.43518	8.50 ± 0.27	40.1
	ZFO PLU 550 °C 12 h	1.77	8.4421	17.85 ± 1.14	34.0
	ZFO PLU 600 °C 0 min	1.29	8.44268	11.12 ± 0.14	44.7
	ZFO PLU 600 °C 10 min	1.24	8.43456	10.83 ± 0.38	49.1
	ZFO PLU 600 °C 12 h	1.52	8.4421	20.13 ± 1.19	31.0
	ZFO PIB 500 °C 0 min	1.24	8.43555	9.48 ± 0.44	52.8
	ZFO PIB 500 °C 10 min	1.41	8.43296	8.03 ± 0.23	38.6
	ZFO PIB 500 °C 12 h	1.80	8.4421	17.05 ± 1.60	30.0
	ZFO PIB 550 °C 0 min	1.10	8.43236	9.25 ± 0.87	41.8
	ZFO PIB 550 °C 10 min	1.87	8.43714	8.12 ± 0.62	70.3
	ZFO PIB 550 °C 12 h	1.38	8.4421	21.36 ± 0.90	21.9
	ZFO PIB 600 °C 0 min	1.43	8.4421	10.03 ± 0.22	39.2
	ZFO PIB 600 °C 10 min	1.33	8.442	10.52 ± 0.56	44.4
	ZFO PIB 600 °C 12 h	2.90	8.44599	21.03 ± 0.97	7.8
	MFO PLU 600 °C 12 h	1.35	8.38483	4.323 ± 0.874	33.7
	Nanoparticles	ZFO MW as-syn	1.60	8.43215	10.49 ± 0.87
ZFO Batch 206 °C		1.59	8.40485	8.82 ± 1.05	35.0
ZFO PVP		1.56	8.4421	14.07 ± 0.54	18.8
ZFO MW 400 °C		1.86	8.4421	10.03 ± 0.51	24.9
ZFO MW 500 °C		1.70	8.43738	13.35 ± 0.39	23.9
ZFO MW 600 °C		2.07	8.44006	17.37 ± 0.91	18.2
ZFO MW 30 min		3.00	8.43501	8.62 ± 0.89	44.1
ZFO MW 20 min		2.09	8.4323	8.34 ± 0.91	58.2
ZFO MW 15 min		1.03	8.4299	9.41 ± 0.89	51.6
ZFO MW 10 min		1.74	8.4283	7.22 ± 0.72	60.1
MFO MW 30 min		1.14	8.37738	3.196 ± 0.16	59.3
MFO MW 20 min		1.23	8.38597	2.553 ± 0.21	10.8

	MFO MW 15 min	1.24	8.38413	2.913 ± 0.38	60.4
	MFO MW 10 min	1.77	8.3873	1.584 ± 0.11	46.4
	MFO PVP	1.10	8.3900	4.415 ± 0.146	61.3
Mesoporous powders	ZFO PLU 500 °C 12 h	1.6	8.43985	16.05 ± 1.19	22.9
	ZFO PLU 550 °C 12 h	1.78	8.43698	19.70 ± 1.74	20.9
	ZFO PLU 600 °C 12 h	1.74	8.44266	21.34 ± 1.48	17.1
	ZFO PIB 600 °C 12 h	2.9	8.44599	21.03 ± 0.97	7.8

$\chi^2_{\text{global}} = / a = \text{lattice parameter} / L_a = \text{average crystallite size} / \eta = \text{average microstrain}$

Table 9.2: Results from NLDFT and Langmuir analysis of N₂ physisorption on ZnFe₂O₄ powders.

Sample	$V_p / \text{cm}^3\text{g}^{-1}$	$d_p \text{ (NLDFT}_{\text{ads}}) / \text{nm}$	$S_L / \text{m}^2\text{g}^{-1}$	$\sigma \text{ (NLDFT}_{\text{ads}}) / \%$	K_L
ZFO PLU 300 °C	0.374	6.8	252.0	2.5	0.995
ZFO PIB 300 °C	0.286	6.8	168.1	1.8	0.995
ZFO PLU 500 °C	0.180	24.6	66.0	1.5	0.997
ZFO PLU 550 °C	0.109	25.5	44.2	1.7	0.999
ZFO PLU 600 °C	0.094	24.6	32.0	1.8	0.997
ZFO PIB 600 °C	0.063	25.5	34.0	1.0	0.997
ZFO MW as-syn	0.110	7.0	117.4	4.0	0.998
ZFO MW 400 °C	0.114	9.1	80.5	2.7	0.997
ZFO MW 500 °C	0.123	12.6	53.7	5.1	0.997
ZFO MW 600 °C	0.094	18.6	25.8	7.3	1.000

$V_p = \text{pore volume} / d_p = \text{pore diameter} / S_L = \text{Langmuir surface area} / \sigma = \text{fitting error} / K_L = \text{Langmuir sorption coefficient}$

Table 9.3: XANES pre-edge fits.

Sample	x_1 / eV	$FWHM_1$ / eV	A_1	x_2 / eV	$FWHM_2$ / eV	A_2	E_0 / eV
ZnFe ₂ O ₄ PLU 300 °C	7113.64	0.99	0.32	7116.07	1.51	0.20	7122.90
ZnFe ₂ O ₄ PLU 500 °C 12 h	7113.56	0.83	0.10	7115.87	2.60	0.34	7123.05
ZnFe ₂ O ₄ PLU 550 °C 12 h	7113.59	1.05	0.13	7116.23	2.42	0.26	7123.05
ZnFe ₂ O ₄ PLU 600 °C 12 h	7113.60	1.02	0.16	7116.32	2.53	0.25	7122.84
ZnFe ₂ O ₄ Batch	7113.74	1.08	0.30	7116.61	1.19	0.12	7123.02
ZnFe ₂ O ₄ MW as-syn	7113.68	1.11	0.29	7116.74	1.76	0.19	7122.37
ZnFe ₂ O ₄ MW 400 °C	7113.72	1.10	0.29	7116.70	1.71	0.19	7122.74
ZnFe ₂ O ₄ MW 500 °C	7113.68	1.17	0.28	7116.78	1.79	0.19	7122.93
ZnFe ₂ O ₄ MW 600 °C	7113.70	1.08	0.24	7116.60	1.84	0.19	7122.91
ZnFe ₂ O ₄ PVP	7113.76	1.11	0.29	7116.61	1.19	0.12	7122.91
MgFe ₂ O ₄ PVP	7113.73	1.11	0.64	7117.24	1.18	0.21	7121.91
Fe ₃ O ₄	7113.5	1.02	0.38	7116.4	1.35	0.15	7120.8
α -Fe ₂ O ₃	7113.6	2.14	0.36	7116.3	0.82	0.06	7121.7

x – peak position / $FWHM$ – full width at half maximum / A – peak area / E_0 –edge energy

Table 9.4: XES fits of analyzed compounds.

$E_{\text{ex}} / \text{eV}$	Sample	$E_{\text{em}} / \text{eV}$	$FWHM / \text{eV}$	A	$E_{\text{trans}} / \text{eV}$
7113	ZnFe ₂ O ₄ PLU 300 °C	6405.5	4.32	0.000193	707.5
	ZnFe ₂ O ₄ PLU 500 °C 12 h	6405.4	4.30	0.000137	707.6
	ZnFe ₂ O ₄ PLU 600 °C 12 h	6405.7	4.36	0.000169	707.3
	ZnFe ₂ O ₄ Batch	6405.3	4.37	0.000242	707.7
	ZnFe ₂ O ₄ MW as-syn	6405.6	4.20	0.000284	707.4
	ZnFe ₂ O ₄ MW 400 °C	6405.5	4.33	0.000177	707.5
	ZnFe ₂ O ₄ MW 500 °C	6405.7	4.22	0.000137	707.3
	ZnFe ₂ O ₄ MW 600 °C	6405.8	4.20	0.000142	707.2
	MgFe ₂ O ₄ PVP	6405.3	4.05	0.000439	707.7
	Fe ₃ O ₄	6405.4	3.94	0.000722	707.6
	α -Fe ₂ O ₃	6405.4	3.96	0.000270	707.6
7114	ZnFe ₂ O ₄ PLU 300 °C	6405.8	3.78	0.000361	708.2
	ZnFe ₂ O ₄ PLU 500 °C 12 h	6405.6	3.86	0.000204	708.4
	ZnFe ₂ O ₄ PLU 600 °C 12 h	6406.0	4.02	0.000251	708.1
	ZnFe ₂ O ₄ Batch	6405.8	4.07	0.000467	708.2
	ZnFe ₂ O ₄ MW as-syn	6405.9	3.85	0.000467	708.1
	ZnFe ₂ O ₄ MW 400 °C	6405.5	3.86	0.000294	708.5
	ZnFe ₂ O ₄ MW 500 °C	6406.0	3.80	0.000216	708.0
	ZnFe ₂ O ₄ MW 600 °C	6406.0	3.90	0.000208	708.0
	MgFe ₂ O ₄ PVP	6405.8	3.71	0.000837	708.2
	Fe ₃ O ₄	6405.8	3.78	0.001195	708.2
	α -Fe ₂ O ₃	6405.8	3.64	0.000522	708.2
7118	ZnFe ₂ O ₄ PLU 300 °C	6405.8	5.36	0.000148	712.2
	ZnFe ₂ O ₄ PLU 500 °C 12 h	6405.4	4.89	0.000108	712.6
	ZnFe ₂ O ₄ PLU 600 °C 12 h	6405.8	5.26	0.000135	712.2
	ZnFe ₂ O ₄ Batch	6405.7	6.04	0.000190	712.3
	ZnFe ₂ O ₄ MW as-syn	6405.9	5.75	0.000224	712.1
	ZnFe ₂ O ₄ MW 400 °C	/	/	/	/
	ZnFe ₂ O ₄ MW 500 °C	6405.9	5.12	0.000110	712.2
	ZnFe ₂ O ₄ MW 600 °C	6406.0	5.36	0.000113	712.0
	MgFe ₂ O ₄ PVP	6405.7	6.20	0.000269	712.3
	Fe ₃ O ₄	6405.5	5.33	0.000516	712.5
	α -Fe ₂ O ₃	6405.6	4.63	0.000190	712.4

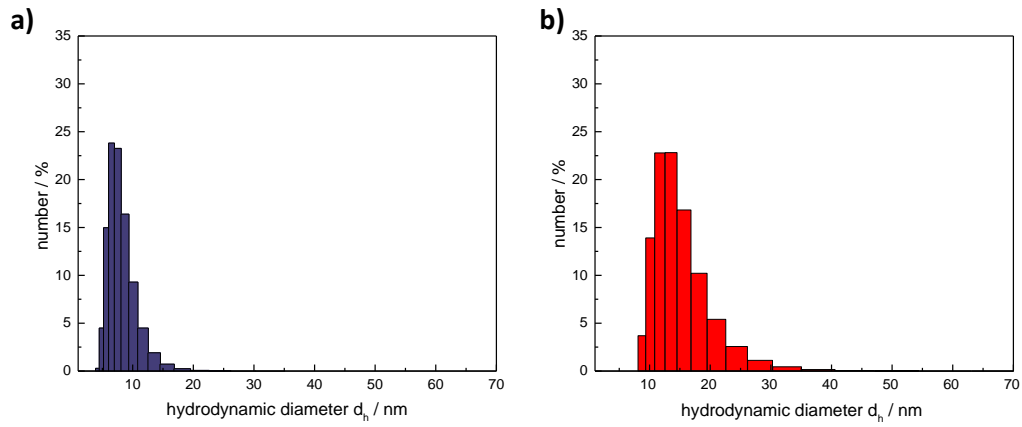


Figure 9.1: DLS measurement of *in situ* OLA/OA-stabilized $MgFe_2O_4$ nanoparticles synthesized a) by adapting a procedure reported by Sun *et al.*, and b) by adding OLA and OA to the standard synthesis mixture (from A. Becker).^[389]

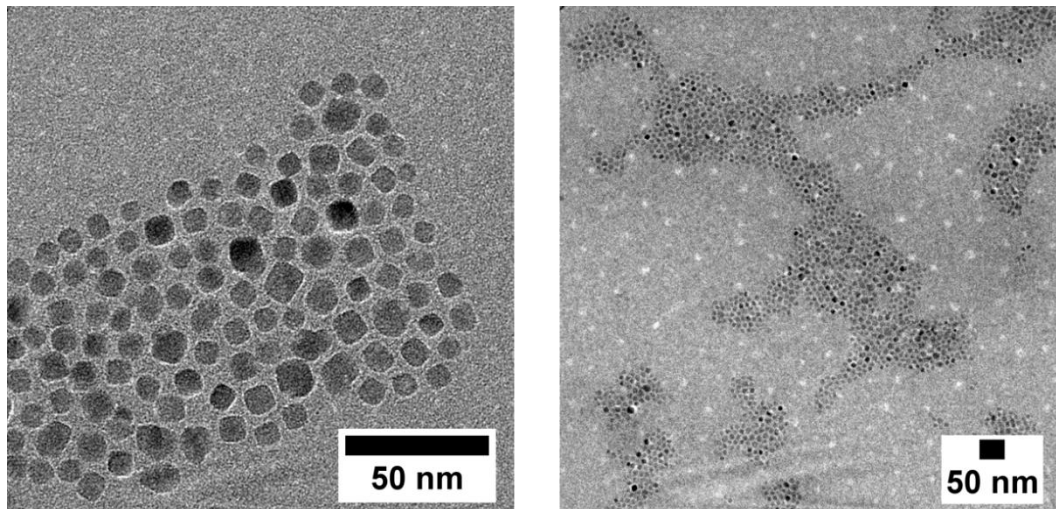


Figure 9.2: TEM images of *in situ* OLA/OA-stabilized $MgFe_2O_4$ nanoparticles synthesized a) by adapting a procedure reported by Sun *et al.* (adapted from A. Becker).^[389]

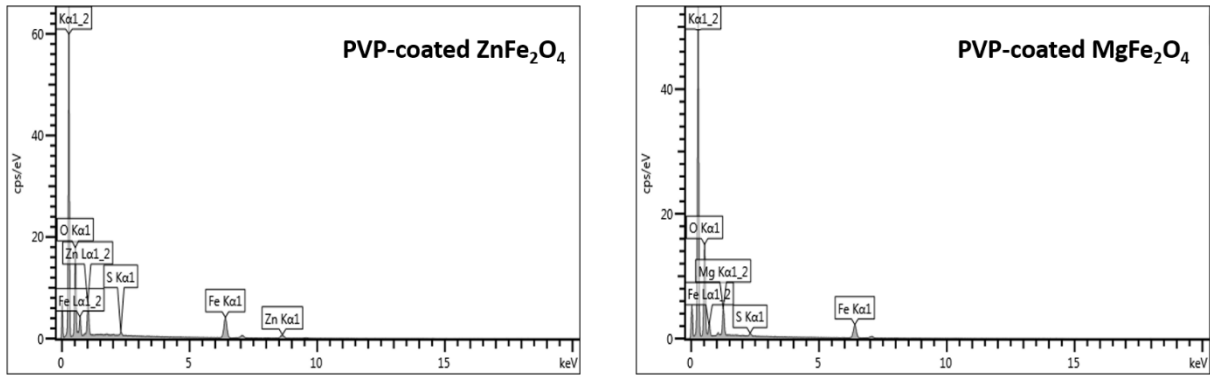


Figure 9.3: EDX spectra of PVP-coated a) ZnFe₂O₄ and b) MgFe₂O₄ nanoparticles.

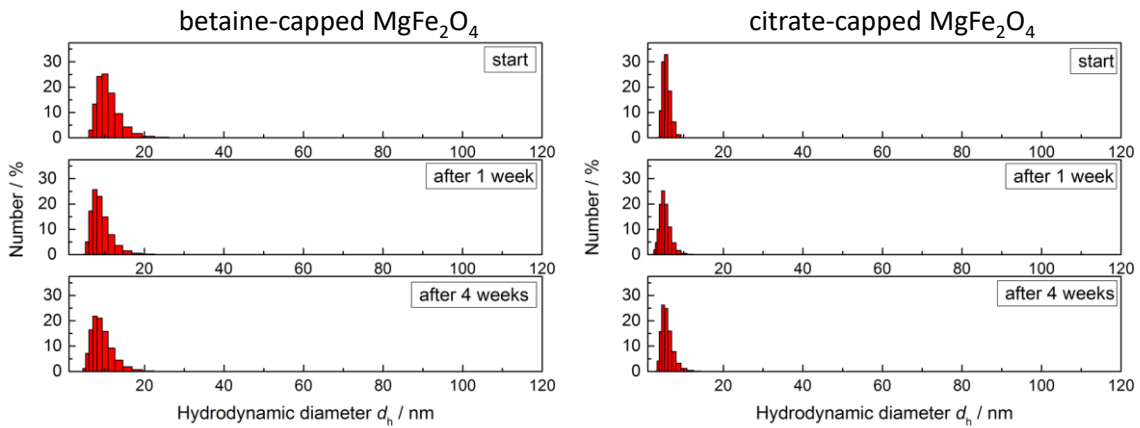


Figure 9.4: DLS measurements for betaine- and citrate-capped MgFe₂O₄ nanoparticles recorded immediately, 1 week and 4 weeks after the synthesis.^[1,350]

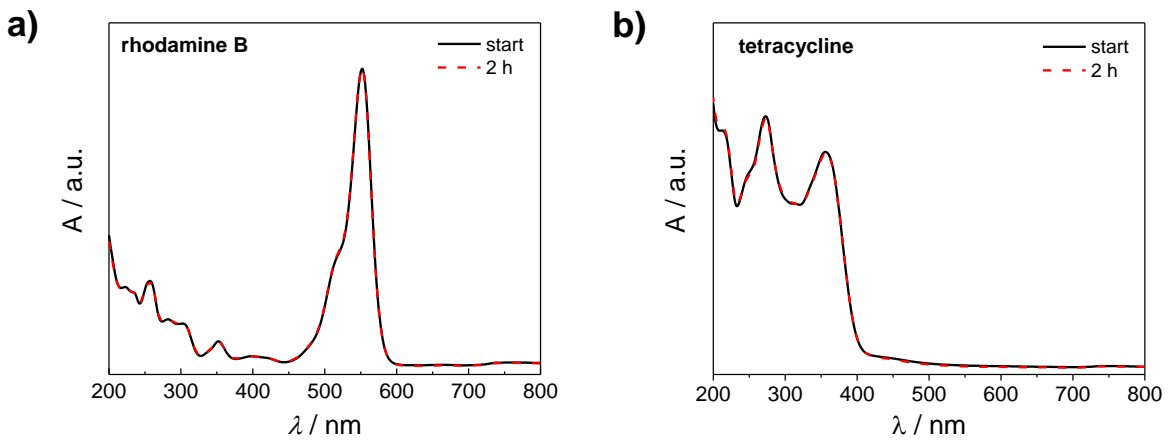


Figure 9.5: UV-Vis spectra collected of aqueous solution of a) rhodamine B and b) tetracycline under simulated sunlight irradiation (adapted from A. Becker).^[350]

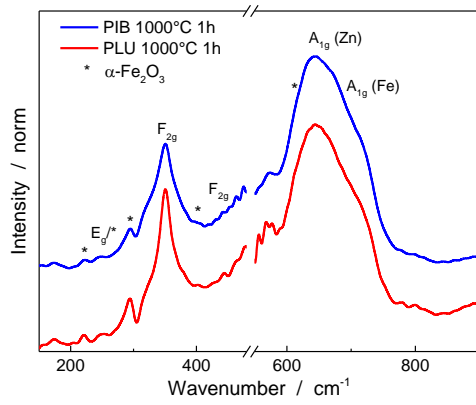


Figure 9.6: Raman spectra of mesoporous ZnFe₂O₄ thin films template with Pluronic® F127 (red) and PIB3000 (blue) calcined at 1000 °C for 1 h (heating rate 10 °C min⁻¹) showing α-Fe₂O₃ impurities (marked with *).^[34]

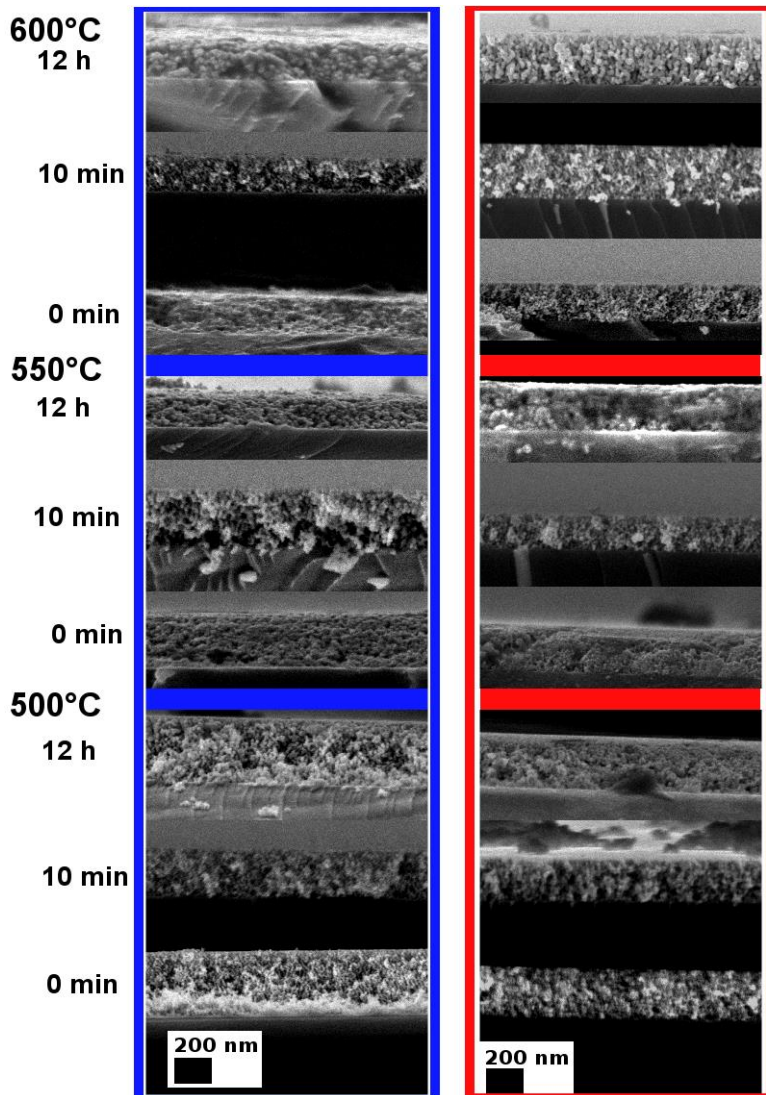
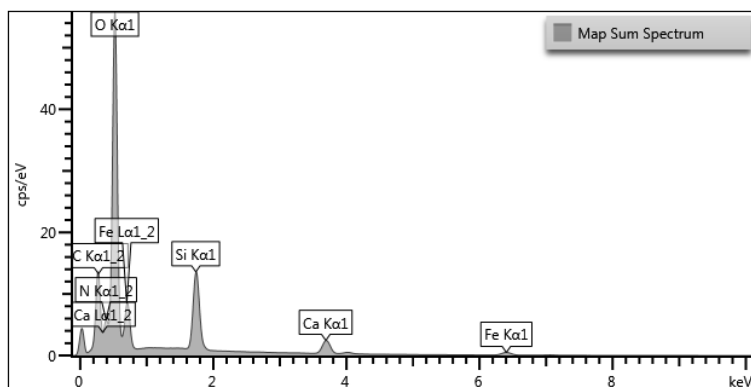


Figure 9.7: Cross section SEM images of PIB-derived (blue) and PLU-derived mesoporous ZnFe₂O₄ thin films.^[34]

Table 9.5: Raman signals of CaFe_2O_4 thin films compared to literature values.

CaFe_2O_4 700 °C 1h (on Si at 300 K)	CaFe_2O_4 700 °C 4h (on Si at 300 K)	CaFe_2O_4 (single crystal) calculated (measured) ^[373]	$\text{Ca}_2\text{Fe}_2\text{O}_5$ (single crystal) calculated (measured) ^[374]
119	120	84 (121) A_g	-
159	146	155 B_{2g}	-
176	180	183 B_{2g}	-
203	205	210 A_g	-
217	222	224 B_{2g}	226 (251) A_g
-	244	249 A_g	246 (261) A_g
269	272	267 (274) A_g	-
288	292	290 or 298 A_g	297 (292) A_g
-	308	298 (302) B_{2g}	310 (313) A_g
337	341	337 B_{2g}	-
363	364	367 B_{1g} or B_{3g}	350 (380) A_g
-	377	407 (371) A_g	-
400	406	406 A_g	400 (397) A_g
439	437	428 or 431 A_g or B_{2g}	435 (428) A_g
-	451	451 A_g	-
582	580	578 or 588 A_g or B_{2g}	596 (558) A_g
643	646	653 (648) A_g	618 (595) A_g
-	679	-	668 (705) A_g

Figure 9.8: EDX spectrum of a non-stoichiometric CaFe_2O_4 precursor gel.

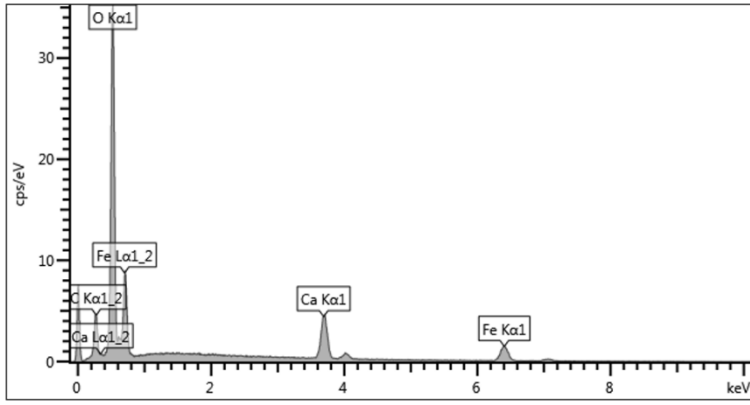


Figure 9.9: EDX spectrum of a stoichiometric CaFe_2O_4 precursor gel.

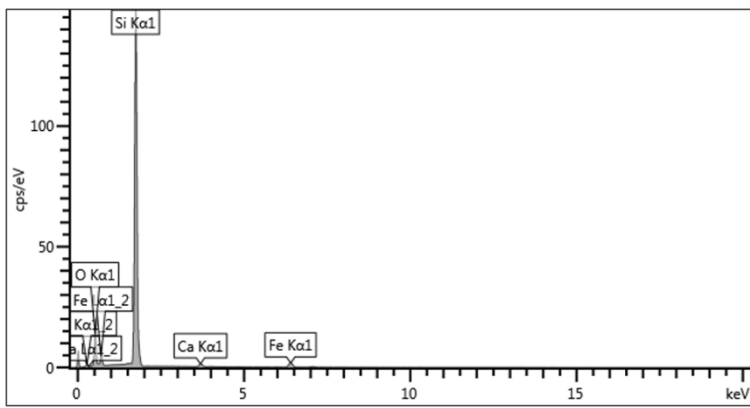


Figure 9.10: EDX spectrum of a CaFe_2O_4 thin film calcined at 800 °C in synthetic air.

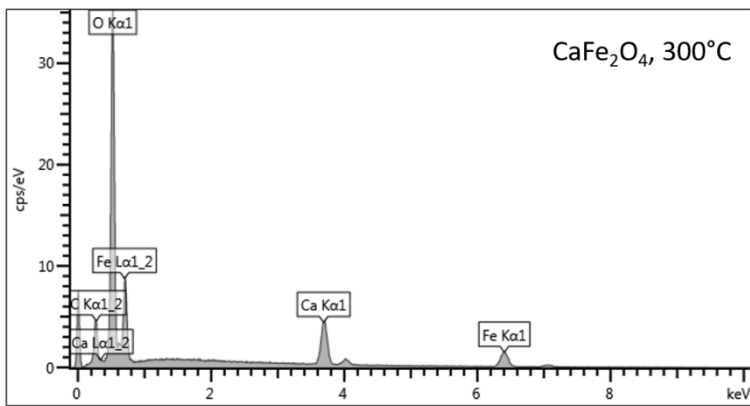


Figure 9.11: EDX spectrum of a stoichiometric CaFe_2O_4 precursor gel treated at 300 °C.

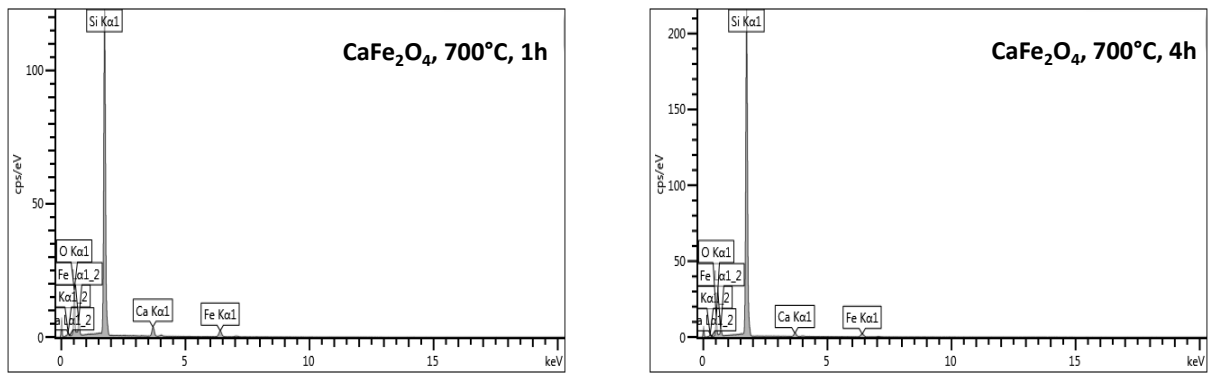


Figure 9.12: EDX spectrum of a CaFe₂O₄ thin film calcined at 700 °C for 1 hour (left) and 4 hours (right) in air.

10 List of Abbreviations and Symbols

Abbreviation	Meaning	Abbreviation	Meaning
1-PE	1-phenylethanol	DTG	differential thermogravimetry
2-ME	2-methoxyethanol	e ⁻	electron
acac	acetylacetonate	EQE	external quantum efficiency
ALD	atomic layer deposition	ESRF	European Synchrotron Radiation Facility
AM 1.5G	global standard spectrum	Et ₂ O	diethyl ether
as-syn	as-synthesized	EtOH	ethanol
BET	Brunauer, Emmett, Teller	EQE	external quantum efficiency
BETA	betaine hydrochloride	EXAFS	extended X-ray absorption fine structure
BJH	Barrett, Joyner and Halenda	FE-SEM	field emission scanning electron microscope
C ₁₆ TAC	hexadecyltrimethyl ammonium chloride	FTO	flourine-doped tin oxide
CB	conduction band	FWHM	full width at half maximum
ccc	critical coagulation concentration	GIXRD	gracing incidence X-ray diffraction
CIF	Crystallographic Information File	h ⁺	hole
CIT	citric acid	H ₂ O ₂	hydrogen peroxide
CMC	critical micelle concentration	HER	hydrogen evolution reaction
COD	Crystallography Open Database	HRFD	high resolution fluorescence detection
CVD	chemical vapor deposition	IEP	isoelectric point
DFT	density functional theory	IPCE	incident photon to current conversion efficiency
DHS	domed hot stage	IR	infrared light
DLS	Dynamic Light Scattering	IRF	instrumental resolution file
DLVO	Derjaguin, Landau, Verwey, Overbeek	ITO	indium tin oxide
DR	diffuse reflectance	IUPAC	International Union of Pure and Applied Chemistry

Abbreviation	Meaning	Abbreviation	Meaning
JCPDS	Joint Committee on Powder Diffraction Standards	SCE	saturated calomel electrode
m/z	mass to charge ratio	SEM	scanning electron microscopy
MeOH	methanol	STH	solar-to-hydrogen transmission electron microscopy
MW	microwave	TEM	transmission electron microscopy
ND	donor density	TEOS	tetraethyl orthosilicate
NHE	normal hydrogen electrode	TG	thermogravimetry
NLDFT	non-local density functional theory	TGA	thermogravimetric analysis
NLDFT	non-local density functional theory	TG-MS	thermogravimetry coupled with mass spectrometry
OA	oleic acid	TMOS	tetramethyl orthosilicate
OER	oxygen evolution reaction	TOC	total organic carbon
OLA	oleylamine	ToF-SIMS	time of flight secondary mass spectrometry
PEC	photoelectrochemical	TON	turn over number
PEO	polyethylene oxide	TR	transmission
PIB	short for PIB3000	UV	ultraviolet
PLD	pulsed laser deposition	UV-Vis	ultraviolet and visible light
PLU	Pluronic® F-127	V2C	valence-to-core
PPO	polypropylene oxide	VB	valence band
PTFE	polytetrafluoroethylene	wt%	weight percent
PV	photovoltaic	XANES	X-ray absorption near-edge spectroscopy
PVP	polyvinylpyrrolidone	XAS	X-ray absorption spectroscopy
RHE	reversible hydrogen electrode	XES	X-ray emission spectroscopy
rpm	rounds per minute	XPS	X-ray photoelectron spectroscopy
SAED	selected area electron diffraction	XRD	X-Ray Diffraction
SC	space charge		

Symbol	Meaning	Symbol	Meaning
A	peak area	E_{VB}	valence band energy
a	lattice constant	$f(E)$	Fermi Dirac function
B	Debye-Waller factor	h_{surf}	surface holes
C	C constant	I_0	incident photon flux
c	velocity of light	I_{XAS}	X-ray absorption intensity
C_0	starting concentration	J_0	initial photocurrent
ccp	cubic closed package	J_{charge}	charging current
$C_{critical}$	critical concentration minimum nucleation	J_{rec}	recombination current
C_{min}	concentration	J_S	steady state photocurrent
C_{rel}	relative concentration saturation	J_{tr}	charge transfer current
$C_{saturation}$	concentration	k	rate constant
C_{SC}	local capacity	k_B	Boltzmann constant
D	interparticle distance	K_{Bragg}	Bragg constant Langmuir sorption
d	dipole coupling hydrodynamic	K_L	coefficient rate constant for
d_h	diameter	k_{rec}	recombination reaction rate constant for transfer
d_p	pore diameter	k_{tr}	reaction
E	energy	L	mean free diffusion length
E°_{ox}	oxidation potential	L_a	average crystallite size mean free diffusion length
E°_{red}	reduction potential	L_h	of holes
E_0	edge energy conduction band	m_r^*	reduced effective mass
E_{CB}	energy	m^*	reduced mass
E_{diss}	dissociation energy	m_e^*	effective mass of electrons
E_{em}	emission energy	m_h^*	effective mass of holes
E_{ex}	excitation energy energy of the final	m_{red}	reduced mass
E_f	state	N	degrees of freedom
E_F	Fermi energy quasi Fermi level of	n_A	amount of substance A
$E_F(e^-)$	electrons quasi Fermi level of	N_A	Avogadro constant
$E_F(h^+)$	holes	n_B	amount of substance B
E_g	bandgap energy quantum localization	N_D	donor density density of states of
E_i	energy	N_e	photogenerated electrons
E_{trans}	energy transfer		

Symbol	Meaning	Symbol	Meaning
N_h	density of states of photogenerated holes	$\Delta_f H^\circ$	formation enthalpy
p	pressure	Δk	wave vector difference
P_λ	power of the light source	Δ_o	ligand field splitting energy in octahedral geometry
q	charge	$\Delta_R G^\circ$	Gibbs free enthalpy
R	reflectance	Δ_T	ligand field splitting energy in tetrahedral geometry
r	particle radius	$\Delta\Phi_{SC}$	potential drop across the SC region
r_{anion}	radius of a anion	ϵ	dielectric constant of the material
r_{cation}	radius of a cation	ϵ_0	dielectric constant of the vacuum
S	surface area	ζ	Zeta potential
S_{BET}	BET surface area	η	average microstrain
S_L	Langmuir surface area	η_a	overpotential
t_{syn}	synthesis period	θ	diffraction angle
U	potential	κ	inverse screening length
U_{FB}	flat band potential	λ	wavelength
U_{Gauss}, V_{Gauss}	Gaussian parameter	μ	charge carrier mobility
W_{Gauss}, Y_{Gauss}	for FWHM	μ_h	hole mobility
V	volume	ν	frequency
V_{ads}	adsorbed volume	ν_{in}	frequency of the incident photon
V_m	volume of the monolayer	ν_{osc}	vibrational frequency
V_{RHE}	volt vs. the reversible hydrogen electrode	ξ	photonic efficiency
w_{SC}	size of SC region/depletion region	σ_m	area of gas molecule inside a monolayer
x	peak position	τ_h	lifetime of the holes
z	number of fundamental vibrations	τ_{hole}	core-hole lifetime
α	absorption coefficient	τ_L	lifetime of charge carriers
Γ	Lorentzian shape broadening	φ	emission energy
δ	degree of inversion		
Symbol	Meaning	Symbol	Meaning

10 List of Abbreviations and Symbols

Φ	light intensity	ϕ_L	Lennard Jones potential
	potential of attractive		potential of repulsive
ϕ_A	forces	ϕ_R	forces
ϕ_{DLVO}	DLVO potential	χ^2	goodness of fit
	electrostatic repulsion		
ϕ_{EL}	potential	ψ	surface potential
	final state of the deep		
Φ_f	core hole	ω	wavenumber
	initial state of the		
Φ_i	deep core hole	Ω	excitation energy

11 List of Tables

Table 3.1: List of organic solid chemicals.	39
Table 3.2: List of inorganic solid chemicals.	40
Table 3.3: List of inorganic and organic liquid chemicals.	40
Table 3.4: List of polymers.	41
Table 3.5: Reaction conditions for batch synthesis of AFe_2O_4 nanoparticles.	42
Table 3.6: Reaction conditions for microwave-assisted synthesis of AB_2O_4 nanoparticles.	43
Table 3.7: Precursor mixture for mesoporous $ZnFe_2O_4$ film synthesis.	47
Table 3.8: Precursor mixture for mesoporous $MgFe_2O_4$ film synthesis.	47
Table 3.9: Precursor mixture for mesoporous $CaFe_2O_4$ film synthesis.	47
Table 5.1: XANES fits of reference compounds.	99
Table 5.2: XES fits of reference compounds.	100
Table 5.3: XANES fits of $ZnFe_2O_4$ nanoparticles.	103
Table 5.4: XES fits of $ZnFe_2O_4$ nanoparticles.	105
Table 5.5: XANES fits of PVP-coated ferrite nanoparticles.	107
Table 5.6: XES fits of $MgFe_2O_4$ nanoparticles.	107
Table 5.7: Parameters obtained from Rietveld refinement of XRD data from $ZnFe_2O_4$ powders.	155
Table 5.8: XANES fits of mesoporous $ZnFe_2O_4$ powders.	158
Table 5.9: XES fits of mesoporous $ZnFe_2O_4$ powders.	160
Table 9.1: Parameters obtained from Rietveld refinement of XRD data from all discussed samples.	179
Table 9.2: Results from NLDFT and Langmuir analysis of N_2 physisorption on $ZnFe_2O_4$ powders.	180
Table 9.3: XANES pre-edge fits.	181
Table 9.4: XES fits of analyzed compounds.	182
Table 9.5: Raman signals of $CaFe_2O_4$ thin films compared to literature values.	186

12 List of Figures

Figure 2.1: Worldwide CO ₂ emission from fuel combustion in between 1971 and 2015. ^[35]	6
Figure 2.2: World's total energy supply by fuels in 1973 (left) and 2015 (right). ^[37]	6
Figure 2.3: Potential energy reserves of renewable and finite resources. ^[40]	7
Figure 2.4: STH efficiency and solar photocurrent density generated under AM1.5G illumination correlated to the semiconductor band gap. ^[43]	8
Figure 2.5: Schematic illustration of the photo-catalytic process.....	9
Figure 2.6: PEC water splitting in a semiconductor tandem cell.....	11
Figure 2.7: Maximum theoretical STH efficiencies and photocurrent densities under solar irradiation correlated to the band gap of the applied photoanode material in combination with a photocathode exhibiting a band gap of < 1.5 eV; inset shows the band positions of the exemplary absorber materials with respect to the redox potentials for OER and HER in water (from Prévot et al.) ^[45]	12
Figure 2.8: Direct and indirect band gap semi-conductors.	13
Figure 2.9: Fermi level positions in case of undoped, p-doped and n-doped semiconductor.....	13
Figure 2.10: Schematic illustration of the interplay between space charge, electrical field, potential and band bending. ^[71]	15
Figure 2.11: Energy diagram of a biased n-type photoelectrode with Fermi level splitting. ^[72]	16
Figure 2.12: LaMer diagram showing nanoparticle evolution during bottom-up synthesis.....	19
Figure 2.13: Schematic illustration of micelle formation.	20
Figure 2.14: a) Pluronic F127, b) PIB3000, c) "Pluronic grid" illustrating the variation in composition of PEO-PPO-PEO block-copolymers and their state of matter with a liquid phase (L, pale grey), a paste-like phase (P, grey) and a solid phase (F, dark grey) adapted from literature ^[127-129]	21
Figure 2.15: Mechanisms of hydrogen evolution on a semiconductor surface decorated with HER-co-catalysts acting as electron trap (left) and hydrogen atom recombination site (right).	24
Figure 2.16: Oxidation potentials for different organic sacrificial agents in regard to the redox potentials for the water splitting half reactions. ^[164]	27
Figure 2.17: Shape of photocurrent curves under ideal conditions and with recombination in the SC layer (from S. Giménez <i>et al.</i>). ^[71]	28
Figure 2.18: Current flowing at the semiconductor-electrolyte interface during illumination (left) and resulting transient photocurrent response (from Giménez <i>et al.</i>). ^[71]	28
Figure 2.19: Band positions of various metal oxide semiconductors in relation to the redox potentials for water splitting (adapted from K. Sivula & R. van de Krol). ^[209]	32
Figure 2.20: Ligand field splitting of Fe ²⁺ and Fe ³⁺ 3d orbitals.	33
Figure 2.21: Structure of (a) normal spinel, (b) inverse spinel and (c) orthorhombic ferrites. ^[18]	34
Figure 2.22: Band positions reported for different ferrite compounds. ^[18]	35
Figure 3.1: Reaction setup for standard reflux synthesis.....	42
Figure 3.2: Heat distribution in conventional heating and microwave heating. ^[278]	43

Figure 3.3: Schematic dip coating synthesis of mesoporous ferrite thin films.	46
Figure 3.4: Schematic spin coating synthesis of mesoporous ZnFe ₂ O ₄ thin films.	48
Figure 4.1: Beamline optics of the Rossendorf beamline (BM20) at ESRF. ^[289]	52
Figure 4.2: X-ray absorption and emission processes for Fe ³⁺	53
Figure 4.3: X-ray absorption spectrum with marked XANES and EXAFS regions (adapted from S. Bare). ^[303]	55
Figure 4.4: XANES pre-edge fits of mesoporous ZnFe ₂ O ₄ powders.	56
Figure 4.5: Origin of XES emission lines.	57
Figure 4.6: K-edge absorption spectrum (top) and corresponding K α XES of α -Fe ₂ O ₃ . ^[305]	58
Figure 4.7: Measured XES spectra of Fe ₃ O ₄ and respective fits.	59
Figure 4.8: Examples of IR-ative and Raman-active vibrations.	62
Figure 4.9: Processes during Raman spectroscopy.	64
Figure 4.10: Different types of physisorption isotherms according to the IUPAC classification. ^[324]	68
Figure 4.11: Different types of hysteresis loops according to the IUPAC classification. ^[324]	69
Figure 4.12: Fitting comparison (NLDFT adsorption model) of N ₂ physisorption data for ZnFe ₂ O ₄ porous powders calcined at a) 300 °C and b) 600 °C.	72
Figure 4.13: Potential curve according to DLVO theory adapted from Sahabi et al. ^[331]	73
Figure 4.14: Steric and electrostatic stabilization in dispersoid colloids.	74
Figure 4.15: Formation of electric double layer.	75
Figure 4.16: Experimental setup used for photocatalytic degradation of model compounds.	77
Figure 4.17: PEC cell (adapted from ZAHNER). ^[340]	78
Figure 5.1: a) XRD patterns, b) Raman spectra and c-d) DR-UV/Vis spectra recorded for ZnFe ₂ O ₄ and MgFe ₂ O ₄ nanoparticles obtained from microwave-assisted synthesis (d) adapted from literature) ^[5] . 80	
Figure 5.2: TEM images of microwave-derived a) ZnFe ₂ O ₄ and b) MgFe ₂ O ₄ nanoparticles.	81
Figure 5.3: TG, DTG and MS traces of a) Fe(acac) ₃ , b) Zn(acac) ₂ , c) Mg(acac) ₂ and d) Ca(acac) ₂	82
Figure 5.4: a) XRD patterns as well as b) crystallite sizes (above) and microstrain values (below) of microwave-derived ZnFe ₂ O ₄ and MgFe ₂ O ₄ nanoparticles obtained after different synthesis periods. 84	
Figure 5.5: Rietveld refinements of a) microwave-derived and b) batch-synthesized ZnFe ₂ O ₄ (* marks a reflection caused by the sample holder) as well as their c) Raman spectra and d) IR patterns.	85
Figure 5.6: TEM images of batch-synthesized ZnFe ₂ O ₄ nanoparticles.	85
Figure 5.7: a) XRD patterns, b) average crystallite size and microstrain, c) physisorption isotherms and d) Raman spectra of microwave-derived, as-synthesized and calcined ZnFe ₂ O ₄ nanoparticles.	87
Figure 5.8: Surface functionalization approaches for ferrite nanoparticles.	88
Figure 5.9: ZnFe ₂ O ₄ nanoparticles obtained after a) Sun reflux approach, b) Sun microwave approach and c) addition of OLA/OA to the standard microwave synthesis.	89
Figure 5.10: DLS measurements of <i>in situ</i> OLA/OA-capped ZnFe ₂ O ₄ nanoparticles in toluene.	89

Figure 5.11: XRD patterns of <i>in situ</i> OLA/OA- functionalized a) ZnFe ₂ O ₄ and b) MgFe ₂ O ₄ nanoparticles and Raman spectra of <i>in situ</i> OLA/OA- functionalized c) ZnFe ₂ O ₄ and d) MgFe ₂ O ₄ nanoparticles synthesized by different approaches (c and d adapted from literature). ^[5]	90
Figure 5.12: a) IR and b) DLS of post-synthetically OLA/OA-capped ZnFe ₂ O ₄ and MgFe ₂ O ₄ nanoparticles (data for MgFe ₂ O ₄ adapted from literature). ^[5]	91
Figure 5.13: a-b) Rietveld refinements (* marks artefact of sample holder), c-d) Raman spectra, e) IR spectra and f) DLS measurements of PVP-encapsulated MgFe ₂ O ₄ and ZnFe ₂ O ₄ nanoparticles.	93
Figure 5.14: TEM images of PVP-coated a) ZnFe ₂ O ₄ and b) MgFe ₂ O ₄ nanoparticles.	94
Figure 5.15: a) Hydrodynamic radii and b) IR spectra of PVP-encapsulated ZnFe ₂ O ₄ nanoparticles with different amounts of PVP added to the synthesis mixture.	94
Figure 5.16: a) ZnFe ₂ O ₄ and b) MgFe ₂ O ₄ betaine hydrochloride functionalized nanoparticles.	95
Figure 5.17: DLS measurements of a) betaine-capped MgFe ₂ O ₄ nanoparticles with a molar ratio of 4 mg wt% ⁻¹ and b) betaine-capped MgFe ₂ O ₄ nanoparticles with a molar ratio of 16 mg wt% ⁻¹ (adapted from A. Becker). ^[355]	96
Figure 5.18: a) DLS size distributions and b) IR patterns as well as TEM images of citrate-functionalized c) ZnFe ₂ O ₄ and d) MgFe ₂ O ₄ nanoparticles (data for MgFe ₂ O ₄ adapted from literature) ^[5]	97
Figure 5.19: a) Full and b) pre-edge XANES spectra of Fe ₃ O ₄ and α-Fe ₂ O ₃ nanoparticles.	98
Figure 5.20: XES spectra of a) Fe ₃ O ₄ and b) α-Fe ₂ O ₃	99
Figure 5.21: RIXS counter plots of a) Fe ₃ O ₄ and b) α-Fe ₂ O ₃	101
Figure 5.22: Full and pre-edge XANES spectra of a-b) freshly synthesized and c-d) calcined, microwave-derived ZnFe ₂ O ₄ nanoparticles.	102
Figure 5.23: a-c) XES spectra of ZnFe ₂ O ₄ nanoparticles and d) relative peak areas A _{rel} obtained by spectra fitting.	104
Figure 5.24: RIXS planes of a) batch-synthesized, b) microwave-derived and c) calcined ZnFe ₂ O ₄ nanoparticles.	105
Figure 5.25: a) Full and b) pre-edge XANES spectra of PVP-coated MgFe ₂ O ₄ and ZnFe ₂ O ₄ nanoparticles.	106
Figure 5.26: Site-selective XES spectra of PVP-coated MgFe ₂ O ₄ nanoparticles.	107
Figure 5.27: RIXS plane of PVP-coated MgFe ₂ O ₄ nanoparticles.	108
Figure 5.28: UV-Vis spectra collected during rhodamine B degradation experiments under simulated sunlight (AM1.5G) using a) non-functionalized ZnFe ₂ O ₄ nanoparticles, b) non-functionalized MgFe ₂ O ₄ nanoparticles, c) betaine-capped MgFe ₂ O ₄ nanoparticles, and d) citrate-capped MgFe ₂ O ₄ nanoparticles (adapted from literature). ^[5,355]	109
Figure 5.29: a) Calculated relative concentrations c _{rel} and b) kinetic evaluation of rhodamine B in the presence of non-functionalized (NF, black), betaine-capped (BETA, red) and citrate-capped (CIT, blue) MgFe ₂ O ₄ nanoparticles (adapted from literature). ^[5]	110
Figure 5.30: UV-Vis spectra of tetracycline degradation experiments under simulated sunlight (AM1.5G) using non-functionalized ZnFe ₂ O ₄ nanoparticles (adapted from A. Becker). ^[355]	111
Figure 5.31: UV-Vis spectra collected during tetracycline degradation experiments under simulated sunlight (AM1.5G) using a) non-functionalized MgFe ₂ O ₄ nanoparticles ,b) betaine-capped MgFe ₂ O ₄	

nanoparticles, and TOC measurements of tetracycline degradation in the presence of c) non-functionalized MgFe_2O_4 nanoparticles and d) betaine-capped MgFe_2O_4 nanoparticles (adapted from A. Becker). ^[355]	112
Figure 5.32: TG-MS measurements of a) Pluronic® F127 and b) PIB3000 polymer. ^[34]	113
Figure 5.33: TG-MS data of the used metal nitrate precursors (Figures a) and b) also presented elsewhere) ^[34]	114
Figure 5.34: TG-MS measurements and IR patterns of a+c) PLU-derived and b+d) PIB-derived ZnFe_2O_4 precursor gels pre-dried at 100 °C. ^[34]	116
Figure 5.35: GIXRD measurements during <i>in situ</i> heating of a) PLU-derived and b) PIB-derived mesoporous ZnFe_2O_4 thin films. ^[34]	117
Figure 5.36: GIXRD patterns of a) PLU-derived and b) PIB-derived obtained after <i>in situ</i> calcination of ZnFe_2O_4 gel films. ^[34]	117
Figure 5.37: GIXRD measurements of a) PLU-derived and b) PIB-derived as well as Raman spectra of c) PLU-derived and d) PIB-derived and UV-Vis spectra of e) PLU-derived and f) PIB-derived mesoporous ZnFe_2O_4 thin films. ^[34]	118
Figure 5.38: a) Average crystallite sizes and b) average microstrain of mesoporous ZnFe_2O_4 thin films calcined at 600 °C. ^[34]	119
Figure 5.39: SEM images of PLU-templated (left, red half-circle) and PIB-templated (right, blue half-circle) samples obtained after different calcination procedures. ^[34]	120
Figure 5.40: Kr BET measurements of PIB- and PLU-derived ZnFe_2O_4 thin films. ^[34]	121
Figure 5.41: Photocurrent values at 1.23 V_{RHE} of PLU- and PIB-derived mesoporous ZnFe_2O_4 photoanodes measured in 1M NaOH/1M Na_2SO_3 electrolyte. ^[34]	122
Figure 5.42: PEC densities at 1.23 V_{RHE} PIB- and PLU-derived samples calcined for 12 hours calculated in respect to different photoelectrode features. ^[34]	123
Figure 5.43: Photocurrent densities under front side and back side solar irradiation and b) calculated donor densities of PIB-templated (blue) and PLU-templated (red) mesoporous ZnFe_2O_4 thin films calcined for 12 hours. ^[34]	124
Figure 5.44: a) Mott-Schottky plots and b) photocurrent measurements with intermittent irradiation with simulated solar light of PLU- and PIB-derived mesoporous ZnFe_2O_4 thin films calcined at 600 °C with 12 hours holding time. ^[34]	124
Figure 5.45: ToF-SIMS depth profile of mesoporous ZnFe_2O_4 thin films derived from a) PLU and b) PIB template.	125
Figure 5.46: a) Photocurrent density and b) IPCE measurements of a mesoporous PLU-derived ZnFe_2O_4 photoelectrode calcined at 600 °C for 12 hours in 1 M NaOH (bright red) and in 1 M NaOH with 1 M Na_2SO_3 (dark red).	126
Figure 5.47: XPS measurements of ZnFe_2O_4 thin films with and without SiO_2 scaffold. ^[34]	127
Figure 5.48: SEM images of PIB-derived (upper) and PLU-derived (lower) ZnFe_2O_4 samples with and without SiO_2 scaffold. ^[34]	128
Figure 5.49: PEC performance of (a) PIB-derived and (b) PLU-derived samples with and without SiO_2 hard templating. ^[34]	128
Figure 5.50: TG-MS data and b) IR pattern of precursor gel.	129

Figure 5.51: SEM top view (above) and cross section (below) images of MgFe_2O_4 thin films calcined at 600 °C for 0 min (left) and 12 hours (right).	130
Figure 5.52: Transmission UV-Vis spectra of MgFe_2O_4 thin films.....	130
Figure 5.53: a) GIXRD patterns and b) Raman spectra of mesoporous MgFe_2O_4 thin films calcined at 600 °C.	131
Figure 5.54: Photocurrent density measurements of mesoporous MgFe_2O_4 thin films calcined at 600 °C with a holding time at T_{max} of a) 0 min and b) 12 h as well as c) Mott Schottky plots and d) IPCE measurements.....	132
Figure 5.55: Photocurrent measurement of mesoporous MgFe_2O_4 during front and backside illumination with simulated solar light.....	133
Figure 5.56: Photocurrent densities at 1.23 V_{RHE} normalized to (1) 1 cm^2 irradiated area (2) irradiated surface area (3) irradiated absorber loading (4) irradiated area and absorber loading.	134
Figure 5.57: XPS spectra for the a) C 1s and b) O 1s emission line of MgFe_2O_4 photoelectrode calcined for 12 hours.	134
Figure 5.58: a) TG-MS data and b) IR patterns of precursor gels.....	135
Figure 5.59: a) SEM images and b) GIXRD patterns of CaFe_2O_4 films produced with soft templates of different molecular weight (* marks artefact of sample holder).....	136
Figure 5.60: Left: SEM images of CaFe_2O_4 thin films calcined at different temperatures without holding time; right: respective GIXRD patterns.	137
Figure 5.61: Left: top view and cross section SEM images of CaFe_2O_4 thin film calcined at 850 °C without holding time; right: respective GIXRD pattern.	138
Figure 5.62: GIXRD pattern and Raman spectrum of PIB-templated CaFe_2O_4 thin film calcined at 800 °C in air for 4h.....	138
Figure 5.63: a) GIXRD patterns and b) Raman spectra of CaFe_2O_4 precursor gel and obtained after calcination at 600 °C.....	139
Figure 5.64: GIXRD measurements during <i>in situ</i> heating of mesoporous CaFe_2O_4 thin films at (a) 600 °C and (b) 700 °C.....	140
Figure 5.65: SEM images of CaFe_2O_4 thin films calcined in air at different temperatures with 4 hours holding time.	140
Figure 5.66: a) GIXRD patterns and b) Raman spectra of CaFe_2O_4 thin films calcined in air at different temperatures with 4 hours holding time.	141
Figure 5.67: a) GIXRD patterns and b) Raman spectra of CaFe_2O_4 thin films calcined in different gas atmospheres for 4 hours.....	142
Figure 5.68: a) GIXRD patterns (* marks artefacts of CaFe_2O_5) b) Raman spectra of CaFe_2O_4 thin films synthesized with 30 % Ca precursor excess.	142
Figure 5.69: a) UV-Vis spectra, b) SEM top view (above) and cross section (below) images of CaFe_2O_4 thin films calcined at 700 °C.	143
Figure 5.70: a) Mott Schottky plot and b) photocurrent measurement in Ar-purged 0.1 M Na_2SO_4 during intermittent irradiation of CaFe_2O_4 photoelectrode calcined at 850 °C with 0 min holding time.	144

Figure 5.71: Photocurrent measurements under intermittent illumination a) in the absence of sacrificial agents and b) with methanol, as well as c) Mott Schottky and d) IPCE measurements of porous CaFe_2O_4 thin films calcined at 700 °C; measurements conducted in a+c) Ar-purged 0.1 M Na_2SO_4 , b+d) Ar-purged 0.1 M Na_2SO_4 with 10 % MeOH.	145
Figure 5.72: Photocurrent measurements in 0.1 M Na_2SO_4 under simulated solar light (AM 1.5G) in the absence (green) and presence (blue) of H_2O_2 under a) dark conditions and illumination from the front and backside, and b) under intermittent front side illumination.	147
Figure 5.73: Charge separation efficiency (upper, black) and charge injection efficiency (lower, grey) calculated according to a procedure reported by Dotan <i>et al.</i> ^[381]	147
Figure 5.74: XPS spectra of the CaFe_2O_4 thin film calcined for 1 hour at 700 °C: a) survey spectrum, b) C 1s spectrum, c) O 1s spectrum and d) Ca 2p spectrum.....	148
Figure 5.75: TG-DTG of PVP-coated ZnFe_2O_4 nanoparticles.....	149
Figure 5.76: Rietveld refinement of XRD patterns obtained for nanoparticle-derived ZnFe_2O_4 thin films.	150
Figure 5.77: SEM images of heat-treated mesoporous thin films prepared from PVP-coated ZnFe_2O_4 nanoparticles.....	151
Figure 5.78: Dependence of the film thickness on the number of coating steps.	151
Figure 5.79: PEC performance under a) intermittent illumination, b) front and backside illumination, c) Mott Schottky plot and d) IPCE of the nanoparticle-derived ZnFe_2O_4 thin film.....	152
Figure 5.80: XRD data and b) Raman spectra of mesoporous ZnFe_2O_4 powders.....	154
Figure 5.81: N_2 physisorption isotherms of ZnFe_2O_4 powders synthesized with a) Pluronic® F127 and b) PIB3000 soft template.....	155
Figure 5.82: IR patterns of mesoporous ZnFe_2O_4 powders.....	156
Figure 5.83: TEM images of PLU-derived ZnFe_2O_4 powders calcined at a+d) 600 °C, b+e) 550 °C and c+f) 500 °C.	157
Figure 5.84: a) Full XANES spectra and b) XANES pre-edge features of PLU-derived mesoporous ZnFe_2O_4 powders.....	158
Figure 5.85: K-edge absorption spectrum of PLU with corresponding excitation energies for b-d) the corresponding X-ray emission spectra of mesoporous ZnFe_2O_4 powders.....	159
Figure 5.86: RIXS planes of a) mesoporous ZnFe_2O_4 powder calcined at 600 °C and b) its respective precursor gel.....	160
Figure 5.87: a) V2C-XES spectrum with fit and b) V2C-XES and XANES spectra with their first derivatives.	161
Figure 9.1: DLS measurement of <i>in situ</i> OLA/OA-stabilized MgFe_2O_4 nanoparticles synthesized a) by adapting a procedure reported by Sun <i>et al.</i> , and b) by adding OLA and OA to the standard synthesis mixture (from A. Becker). ^[395]	183
Figure 9.2: TEM images of <i>in situ</i> OLA/OA-stabilized MgFe_2O_4 nanoparticles synthesized a) by adapting a procedure reported by Sun <i>et al.</i> (adapted from A. Becker). ^[395]	183
Figure 9.3: EDX spectra of PVP-coated a) ZnFe_2O_4 and b) MgFe_2O_4 nanoparticles.....	184
Figure 9.4: DLS measurements for betaine- and citrate-capped MgFe_2O_4 nanoparticles recorded immediately, 1 week and 4 weeks after the synthesis. ^[5,355]	184

Figure 9.5: UV-Vis spectra collected of aqueous solution of a) rhodamine B and b) tetracycline under simulated sunlight irradiation (adapted from A. Becker). ^[355]	184
Figure 9.6: Raman spectra of mesoporous ZnFe ₂ O ₄ thin films template with Pluronic® F127 (red) and PIB3000 (blue) calcined at 1000 °C for 1 h (heating rate 10 °C min ⁻¹) showing α-Fe ₂ O ₃ impurities (marked with *). ^[34]	185
Figure 9.7: Cross section SEM images of PIB-derived (blue) and PLU-derived mesoporous ZnFe ₂ O ₄ thin films.	185
Figure 9.8: EDX spectrum of a non-stoichiometric CaFe ₂ O ₄ precursor gel.	186
Figure 9.9: EDX spectrum of a stoichiometric CaFe ₂ O ₄ precursor gel.	187
Figure 9.10: EDX spectrum of a CaFe ₂ O ₄ thin film calcined at 800 °C in synthetic air.	187
Figure 9.11: EDX spectrum of a stoichiometric CaFe ₂ O ₄ precursor gel treated at 300 °C.	187
Figure 9.12: EDX spectrum of a CaFe ₂ O ₄ thin film calcined at 700 °C for 1 hour (left) and 4 hours (right) in air.	188

13 List of Publications, Contributions and Research Visits

13.1 Peer-Reviewed Journals

- K. Kirchberg, A. Becker, A. Blößer, T. Weller, J. Timm, C. Suchomski, R. Marschall „Stabilization of Monodisperse, Phase-Pure MgFe_2O_4 Nanoparticles in Aqueous and Nonaqueous Media and Their Photocatalytic Behavior“, *J. Phys. Chem. C*, 2017, **121** (48), 27126 – 27138; DOI: 10.1021/acs.jpcc.7b08780.
- K. Kirchberg, S. Wang, L. Wang, R. Marschall „Mesoporous ZnFe_2O_4 Photoanodes with Template-tailored Mesopores and Temperature-dependent Photocurrents“, *ChemPhysChem* 2018, **9** (18), 2313 – 2320; DOI: 10.1002/cphc.201800506.
- K. Kirchberg, R. Marschall „Sol-gel synthesis of mesoporous CaFe_2O_4 photocathodes with hierarchical pore morphology“, *Sustainable Energy Fuels* 2019, Advance Artikel; DOI: 10.1039/C8SE00627J.

13.2 Poster and Talk Contributions

- “Solar Hydrogen Production using MgFe_2O_4 Nanoparticles“, K. Kirchberg, A. Becker, R. Marschall, *Sustainability – renew, resource and rethink @ Achema 2018*, Mainz, Germany, 10. – 11.06.2018, 1st poster prize for best poster presentation.
- “Temperature matters: How the calcination procedure influences the photoelectrochemical performance of ZnFe_2O_4 “, K. Kirchberg, P. Timmer, R. Marschall, *12th Materialforschungstag Mittelhessen 2018*, Marburg, Germany, 16.05.2018, poster contribution.
- “Photocatalytic Pollutant Degradation by Colloidal Magnesium Ferrite Nanoparticles“, Kristin Kirchberg, Anna Becker, A. Blößer, T. Weller, J. Timm, C. Suchomski, R. Marschall, *20th Frühjahrssymposium*, Constance, Germany, 21. – 24.03.2018, oral contribution.
- “Temperature matters: How the calcination procedure influences the photoelectrochemical performance of ZnFe_2O_4 “, K. Kirchberg, P. Timmer, R. Marschall, *6th International Conference on Semiconductor Photochemistry (SP6)*, Oldenburg, Germany, 10. – 14.09.2017, flash talk and poster contribution.

- “Solar Hydrogen Production using MgFe₂O₄ Nanoparticles“, K. Kirchberg, A. Becker, R. Marschall, *2nd International Solar Fuels Conference (ISF-2)*, San Diego, USA, 06. – 11.07.2017, poster contribution.
- “Influence of pore morphologies on photoelectrochemical performance of mesoporous zinc ferrite thin films“, K. Kirchberg, P. Timmer, R. Marschall, *19th Frühjahrssymposium*, Mainz, Germany, oral contribution.
- “Influence of pore morphologies on photoelectrochemical performance of mesoporous zinc ferrite thin films“, K. Kirchberg, P. Timmer, R. Marschall, *5th International Conference on Multifunctional and Hybrid Materials (HYMA5)*, Lisbon, Portugal, 06. – 11.03.2017, poster contribution.
- “Studies on mesoporous ZnFe₂O₄ thin films with different pore morphologies for photoelectrochemical applications“, K. Kirchberg, P. Timmer, R. Marschall, *20th Deutsche Zeolith-Tagung (DZT)*, Frankfurt, Germany, 01. – 03.03.2017, poster contribution.
- “Nanostructured Ferrite Materials for Photoelectrochemical Water Splitting“, K. Kirchberg, P. Timmer, R. Marschall, *21st International Conference on Conversion and Storage of Solar Energy (IPS21)*, St. Petersburg, Russia, 24. – 29.07.2016, poster contribution.
- “Nanostructured Ferrite Materials for Photoelectrochemical Water Splitting“, C. Suchomski, K. Kirchberg, J. Keppner, R. Marschall, *9th European Meeting on Solar Chemistry and Photocatalysis: Environmental Application (SPEA9)*, Strassbourg, France, 13. – 17.06.2016, poster prize for best poster contribution.

13.3 Research Visits

- Four-week stay at the Australian Institute for Bioengineering and Nanotechnology (AIBN) in research group of Prof. Dr. Lianzhou Wang (University of Queensland, Brisbane, Australia) from 25th October to 25th November 2016.